UNIVERSIDAD AUTÓNOMA DE MADRID

ESCUELA POLITÉCNICA SUPERIOR

PROYECTO FIN DE CARRERA

DESIGN OF WIDEBAND ORTHOMODE TRANSDUCERS BASED ON THE TURNSTILE JUNCTION FOR SATELLITE COMMUNICATIONS

INGENIERÍA DE TELECOMUNICACIÓN

Ignacio Izquierdo Martínez

Noviembre de 2008

DESIGN OF WIDEBAND ORTHOMODE TRANSDUCERS BASED ON THE TURNSTILE JUNCTION FOR SATELLITE COMMUNICATIONS

AUTOR: Ignacio Izquierdo Martínez
TUTOR: Jorge A. Ruiz Cruz

Grupo de Sistemas de Radiocomunicaciones y Comunicaciones Ópticas
Dpto. de Ingeniería Informática
Escuela Politécnica Superior
Universidad Autónoma de Madrid
Noviembre de 2008

PROYECTO FIN DE CARRERA

Título: *Design of wideband orthomode transducers based on the Turnstile junction for satellite communications.*

Autor: D. Ignacio Izquierdo Martínez

Título: D. Jorge A. Ruiz Cruz

Tribunal:

Presidente: D. José Luis Masa Campos

Vocal: D. Jorge E. López de Vergara

Vocal secretario: D. Jorge A. Ruiz Cruz

Fecha de lectura:

Calificación:

Abstract

Orthomode Transducers (OMTs) are passive microwave devices whose function is to discriminate between the two orthogonal single signals received by dual-polarization antenna systems. In transmission, they combine these signals and route them to the antenna (typically a horn-type antenna with revolution symmetry). Satellite communication systems and radio astronomy are typical environments where OMTs are found. Their use in communication systems allows to double the capacity of the system, since two different signals can share the same frequency spectrum, as long as they are associated to different orthogonal polarizations.

This project is focused on OMTs in waveguide transmission systems. These devices have been developed over the last decades, though they are not widely dealt with in the literature. The design of these structures requires a good comprehension of some notions about electromagnetic theory and waveguides analysis. To set the framework of this project, a detailed bibliographic study of OMT components will be carried out.

One of the most typical structures found in wideband OMTs is the so-called Turnstile junction. This particular structure holds some symmetry properties that grant a broadband performance. Among all the aspects involved in the design of a Turnstile junction, the design of its internal matching obstacle is one of the key elements.

The aim of this project is to address an exhaustive study of all the components involved in the design of an OMT based on the Turnstile junction. For that reason, besides the theoretical study of electromagnetic concepts and the Turnstile junction, some routing structures such as bends, transformers and recombiners will be also studied and analyzed.

Two complete OMT designs will then be carried out: the first one will follow some typical OMT specifications and it will include a new internal obstacle for the Turnstile junction based on mitered bends, proposed for the first time in this project; the second one will represent an effort to improve existing wideband OMTs performance. For the latter, the addition of a new degree of freedom for the Turnstile junction will be proposed. It consists of a configuration of angled branches for the junction, using the same obstacle of the first design. The aforementioned will result in a more compact structure with even better performance.

Key words

Ortho-mode transducers, OMT, Turnstile junction, Waveguides, Polarization, S-parameters, S-Matrix, Generalized Scattering Matrix, Microwave Circuitry, Radio Frequency, Microwaves.

Resumen

Los Transductores de Modos Ortogonales (OMTs, Orthomode Transducers) son dispositivos pasivos de microondas cuya función es separar las dos señales individuales que son recibidas en sistemas de radiofrecuencia con antenas de doble polarización. A su vez, son capaces de combinar estas dos señales en transmisión y encaminarlas hacia la bocina. Son usados tanto en sistemas de comunicación por satélite como en aplicaciones de radioastronomía en el rango de los GHz, duplicando la capacidad del enlace.

Este proyecto se centra en los OMTs en tecnología de guía de onda. Este tipo de dispositivos, a pesar de haber sido desarrollados durante décadas, no son ampliamente tratados en la literatura. Su diseño requiere una buena comprensión de determinados conceptos teóricos pertenecientes al dominio del electromagnetismo, así como diversas consideraciones sobre circuitería de microondas.

Una de las estructuras típicas empleadas en el diseño de OMTs de banda ancha es la unión Turnstile. Este dispositivo pasivo posee ciertas propiedades de simetría que le confieren un comportamiento natural de banda ancha. Su diseño implica determinados aspectos entre los cuales cobra una gran importancia la topología del obstáculo interno de adaptación que se sitúa en la unión.

El objetivo de este proyecto es realizar un estudio exhaustivo de los componentes de un OMT basado en dicha unión con el fin de acometer su diseño completo de manera satisfactoria. Para ello, además del estudio teórico previo se realizarán estudios y análisis sobre los elementos de rutado típicos en estas estructuras como codos, transformadores o recombinadores.

Tras este estudio se realizarán dos diseños: el primero estará determinado por una serie de especificaciones típicas de un OMT, e incluirá un diseño propio para el obstáculo interno de la unión Turnstile basado en codos truncados, propuesto por primera vez en este proyecto; el segundo representará un intento por mejorar las prestaciones de este tipo de dispositivos. Para este segundo diseño se propondrá la adición de un nuevo grado de libertad para la unión Turnstile que consiste en la configuración en ángulo de sus ramas rectangulares, empleando el mismo obstáculo interno que el usado en el primer caso. Con ello se conseguirá un diseño del OMT más compacto, mejorando sus prestaciones.

Palabras clave

Ortomodo, Transductor de Modos Ortogonales, OMT, Unión Turnstile, Guías de Onda, Polarización, Parámetros-S, Matriz-S, Matriz de Dispersión Generalizada, Circuitería de Microondas, Radio Frecuencia, Microondas.

Agradecimientos

En primer lugar, quiero dar las gracias a mi tutor Jorge Alfonso Ruiz Cruz, por brindarme la oportunidad de realizar este Proyecto Fin de Carrera y por transmitirme su pasión por el mundo de las microondas. Han sido muchas horas de conversación y reflexión en las que en todo momento se ha mostrado dispuesto a enseñarme, ayudarme y aconsejarme, y es gracias a él que he podido completar este trabajo de una manera tan satisfactoria.

También quiero dar las gracias a todos los profesores de la Escuela Politécnica Superior que nos han aportado sus conocimientos durante todos estos años, colaborando para que todos nos sintiéramos cómodos y orgullosos de pertenecer a ella.

A mi familia y amigos, por todo el amor que me transmitís cada día, sin el cual todo se haría infinitamente más difícil. Gracias por vuestro apoyo incondicional, aun sin llegar a comprender exactamente qué es y para qué sirve eso que llamo Ortomodo.

Y a todos vosotros, compañeros, amigos y camaradas de la universidad, por todos los buenos momentos que hemos pasado juntos tanto en la escuela como fuera de ella, por hacer que me sienta parte de una gran familia que espero y deseo resista el paso del tiempo, un fuerte abrazo.

Ignacio Izquierdo Martínez
Noviembre de 2008.

Index of Contents

Index of Figures

Index of Tables

Chapter 1

Introduction

1.1 Motivation

Nowadays, there is an increasing number of applications in need of antenna systems operating over large bandwidths with great performance, ranging from radio astronomy to defense. These applications often require dual-polarization operation to satisfy their demands. With the development of high-performance feed horns capable of such a mode of operation comes the need of a device to carry out the task of separating or joining the two linearly or circularly polarized orthogonal signals received or sent by the system.

The **Orthomode Transducer (OMT)** is the key component which discriminates between the polarizations in those systems. Fig. 1.1 shows its location in an RF feed chain system typically used in telecommunications. Right after the antenna (for instance a horn), the two signals travel through the OMT, which discriminates between orthogonal components and serves different signals at its output ports. This feature of the OMT doubles the number of channels that can be served in a given frequency range. If the system operates over two frequency bands, as is usual in satellite communication links ranging from 1 GHz up to 30 GHz, subsequent diplexers discriminate between these bands, serving another two signals at their outputs. The overall system will then be serving four independent signals.

Fig. 1.6 shows typical frequency band designations for these systems.

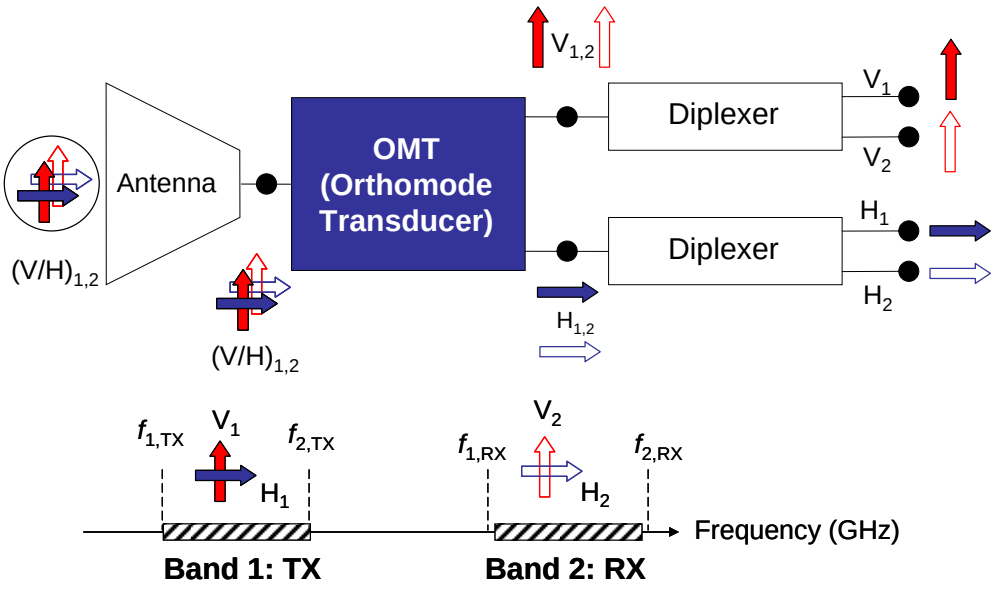

Fig. 1.1. Location of the OMT in a typical RF feed chain system operating over two frequency bands.

Radio astronomy applications generally need OMTs designed to cover as much bandwidth as possible but usually with more relaxed specifications in comparison with telecommunication systems, which may require, for example, much more stringent return or insertion losses. For that reason, wideband OMTs are one of the components of many telescopes found in several radio astronomy complexes. OMTs have been used to detect polarization state in many radio astronomy applications, such as the measure of the Cosmic Microwave Background (CMB). For example, [PII07] shows an OMT designed for CLOVER, an experiment focused on measuring angular polarization anisotropies of the CMB which is planned to be sited at Llano de Chajnantor, Chile, in the Atacama Desert, which is a very popular area for millimeter and sub-millimeter experiments such as APEX (Atacama Pathfinder Experiment, CBI (Cosmic Background Imager) or ALMA (Atacama Large Millimeter Array). The ALMA will be a huge radio astronomy station composed of up to 70 antennas. It is meant to replace the Very Large Telescope (VLT) complex at Cerro Paranal (Chile) as the most ambitious astronomic project ever built and it should be finished by 2012. [BVL05] shows another OMT designed for ALMA.

Fig. 1.2. Llano de Chajnantor, in the Atacama Desert, Chile. Image courtesy of "NRAO / AUI / NSF" from http://www.nrao.edu/.

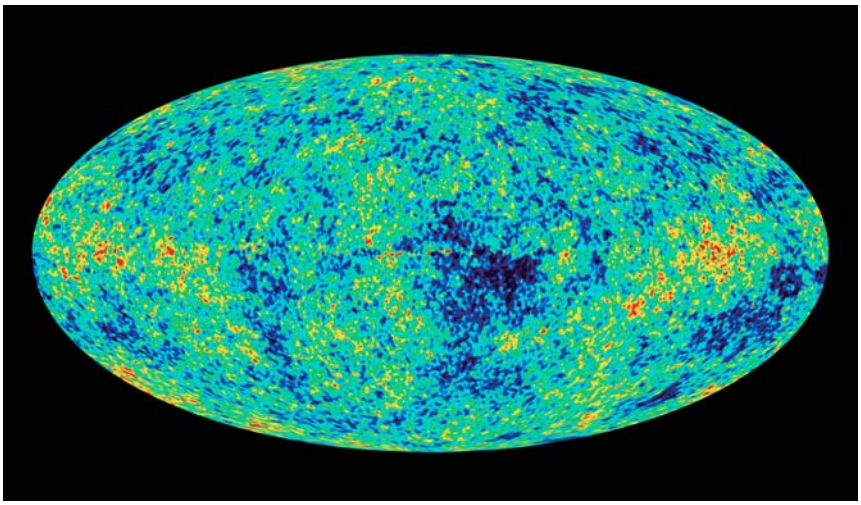

Fig. 1.3. WMAP (Wilkinson Microwave Anisotropy Probe) image of the Cosmic Microwave Background anisotropy. Image from http://map.gsfc.nasa.gov/.

As the working frequency of microwave applications increases (hundreds of GHz for radio astronomy) it gets more and more difficult to manufacture microwave devices with small components, as they become very unstable (their dimensions are on the order of inches). Certain structures, such as the **Turnstile junction** used in [BVL05] and [PII07], turn out to be suitable microwave networks at these frequencies, providing wideband operation because of their physical and electric properties.

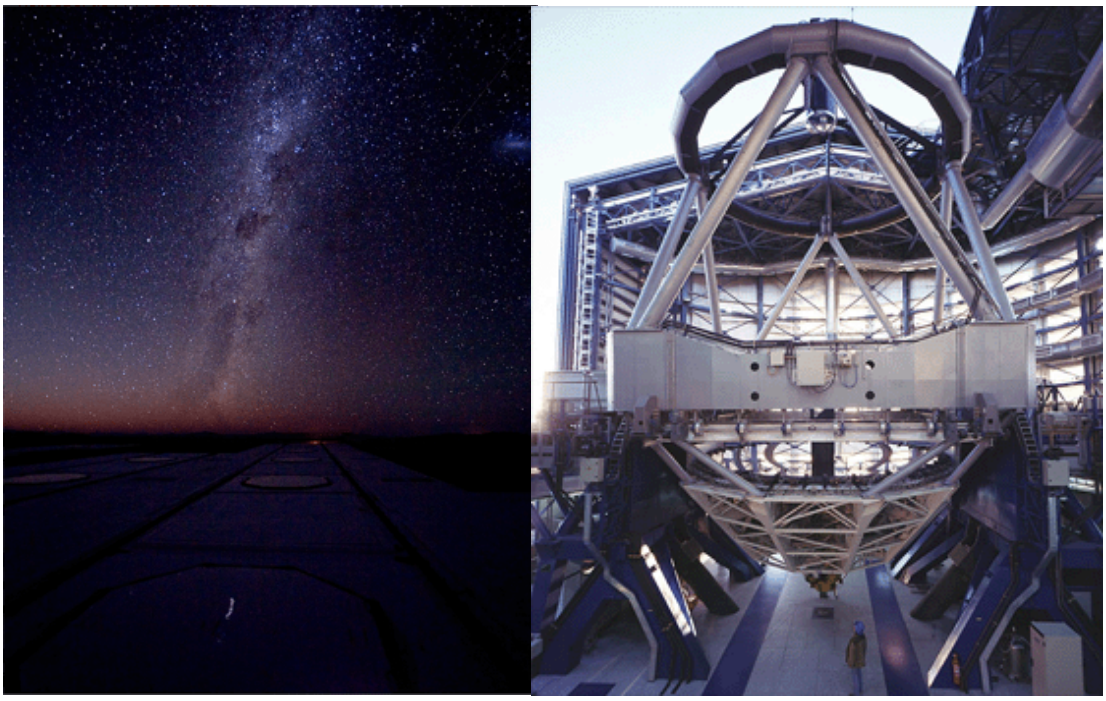

Fig. 1.4. Night sky at Paranal (Chile) and internal view of one of the telescopes of the VLT complex. Images from http://www.eso.cl/.

Fig. 1.5. Very Large Array (VLA) at Socorro, New Mexico, USA. Image courtesy of "NRAO / AUI / NSF" from http://www.nrao.edu/.

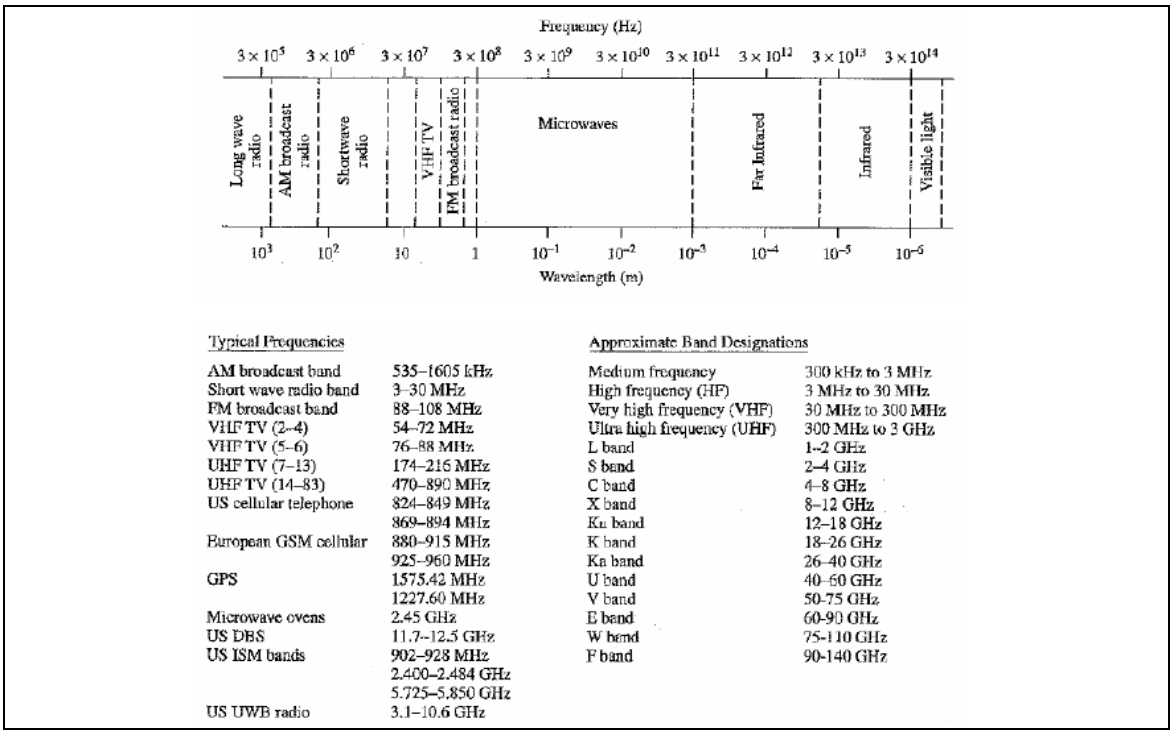

Typical Frequencies	
AM broadcast band	535–1605 kHz
Short wave radio band	3–30 MHz
FM broadcast band	88–108 MHz
VHF TV (2–4)	54–72 MHz
VHF TV (5–6)	76–88 MHz
UHF TV (7–13)	174–216 MHz
UHF TV (14–83)	470–890 MHz
US cellular telephone	824–849 MHz
	869–894 MHz
European GSM cellular	880–915 MHz
	925–960 MHz
GPS	1575.42 MHz
	1227.60 MHz
Microwave ovens	2.45 GHz
US DBS	11.7–12.5 GHz
US ISM bands	902–928 MHz
	2.400–2.484 GHz
	5.725–5.850 GHz
US UWB radio	3.1–10.6 GHz

Approximate Band Designations	
Medium frequency	300 kHz to 3 MHz
High frequency (HF)	3 MHz to 30 MHz
Very high frequency (VHF)	30 MHz to 300 MHz
Ultra high frequency (UHF)	300 MHz to 3 GHz
L band	1–2 GHz
S band	2–4 GHz
C band	4–8 GHz
X band	8–12 GHz
Ku band	12–18 GHz
K band	18–26 GHz
Ka band	26–40 GHz
U band	40–60 GHz
V band	50-75 GHz
E band	60-90 GHz
W band	75-110 GHz
F band	90-140 GHz

Fig. 1.6. Electromagnetic spectrum, typical frequencies for some applications and approximate frequency band designations. Image from [Poz05].

1.2 Objectives and organization of the document

The main objective of this project is to carry out a study of the OMT operation and its constituent components, in order to acquire enough knowledge to address the design of a particular type of a wideband OMT based on the Turnstile junction.

The first stage of this study is to address some electromagnetic concepts as waveguide modes, higher-order modes excitation or polarization states. Chapter 2 will present and summarize many of these concepts.

As OMTs are not widely treated in the literature, the survey in chapter 3 will be focused on these structures. It will present several OMT designs found in books and technical articles and it will try to present the reader some basic aspects of narrowband and wideband OMTs.

Following this, chapter 4 will give some details about the design cycle followed during this project, which is based on the joint use of Matlab and a commercial full-wave analysis software like HFSS (High Frequency Structure Simulator) or CST (Computer Simulation Technologies) Microwave Studio. It will also present basic notions about the optimization algorithms used during the design of the structures that compose the OMT.

Bends will be the first routing structures to be studied, along with waveguide transformers and recombinators. These are simple routing structures which can be very helpful to assimilate all the concepts seen in Ch. 2. Chapter 5 will present a study about mitered bends, which are very common in microwave circuitry, and some designs of transformers and recombinators developed during the project.

The next step will be to study in depth the junction that separates both polarizations, i.e., the Turnstile junction. Chapter 6 will focus on this structure, showing its usefulness as a component of a wideband OMT. It will also present some designs developed for this project which include a new internal obstacle and angled rectangular branches for the Turnstile junction, proposed for the first time in this project, to the best of the author's knowledge.

Chapter 7 will focus on the design of a complete OMT using some of the structures presented in the previous chapters. Different configurations will be discussed and two designs will be presented. The first one has some fixed specifications, while the second one represents an effort to improve existing wideband OMTs based on the Turnstile junction.

Finally, chapter 8 will show some final conclusions and future work related to this project.

The document also includes two Appendices. Appendix A will be focused on the explanation of some aspects related with the project and Appendix B will show the text of the published article [IR08].

Chapter 2

Theoretical Introduction

This theoretical introduction aims to present the background of the following chapters and sections. Its objective is not to present an in-depth study of electromagnetism, but to offer the reader a summary of electromagnetic waveguide development throughout their history and to explain some basic concepts related to electromagnetic waves, fields and waveguide theory.

2.1 Waveguides throughout history

Microwave engineering is not a young discipline. The fundamental concepts were developed over 100 years ago. The foundations of modern electromagnetic theory were formulated in 1861 by James Clerk Maxwell, who hypothesized wave propagation and light as a form of the same phenomenon: the electromagnetic field. Maxwell synthesized all previous observations from Ampère, Faraday, Gauss and some other physicists in the following differential, time-varying form (with units in the international system):

$$\nabla \times \overline{E} = -\frac{\partial \overline{B}}{\partial t} \tag{2.1}$$

$$\nabla \times \overline{H} = \frac{\partial \overline{D}}{\partial t} + \overline{J} \ . \tag{2.2}$$

Eqs. 2.1, 2.2 and the equation of the charge conservation principle,

$$\nabla \cdot \overline{J} + \frac{\partial \rho}{\partial t} = 0 \ , \tag{2.3}$$

constitute the basic equations of the electromagnetic field. Furthermore, two additional equations can be obtained combining Eqs. 2.1-2.3:

$$\nabla \cdot \overline{D} = \rho \tag{2.4}$$

$$\nabla \cdot \overline{B} = 0 \tag{2.5}$$

Fig. 2.2 shows a waveguide system. A very useful form of Maxwell's equations for this problem can be obtained by decomposing the equations into transverse and axial components and separating out the *z* dependence (along the longitudinal axis of the waveguide). The boundary conditions in these systems can be satisfied by fields that do not present all the components, i.e., some components along the *z* axis may be zero. The resolution of this set of equations yields three types of waves, classified according to the vector components for the electric and magnetic fields:

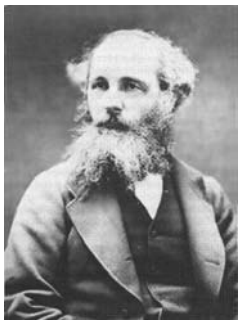

Fig. 2.1. James Clerk Maxwell.

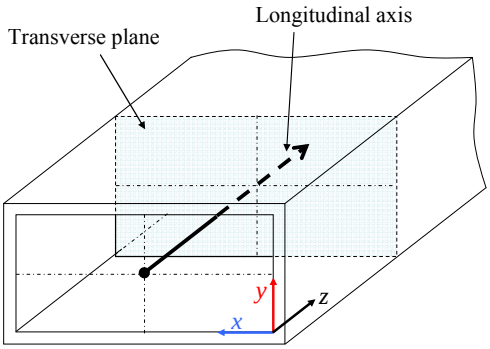

Fig. 2.2. Sketch of a waveguide (rectangular) and image of some waveguide sections and routing devices.

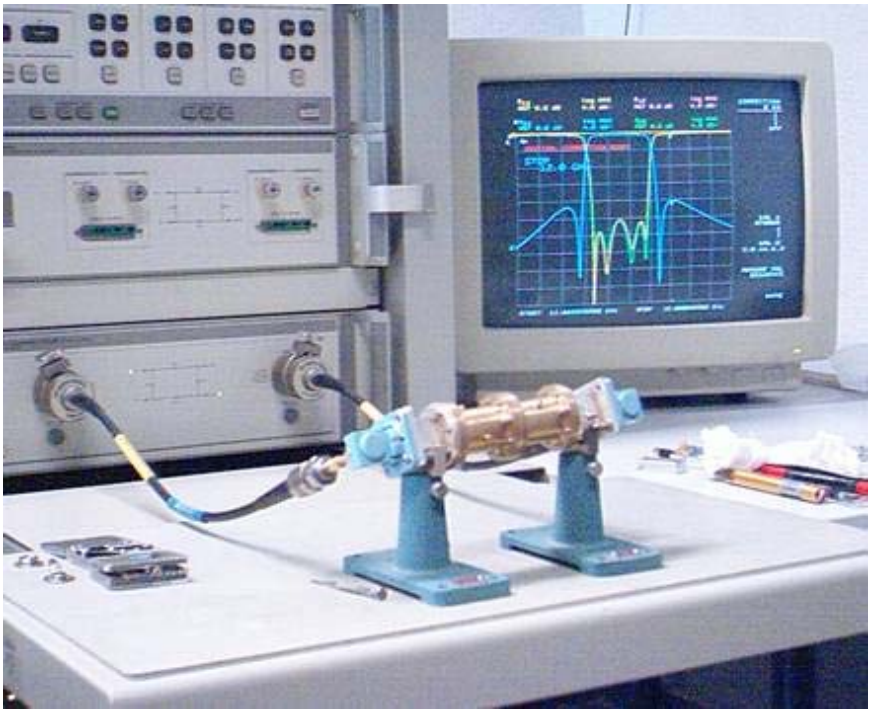

Fig. 2.3. Measurement of a microwave device.

- Transverse electromagnetic waves (*TEM*), without any longitudinal component.
- Transverse magnetic waves (*TM* or *E* Modes), with no longitudinal magnetic component.
- Transverse electric waves (*TE* or *H* Modes), with no longitudinal electric component.

This set of wave types was found by Rayleigh in 1897, during his attempt to demonstrate that waves could propagate within a hollow metallic cylinder. He stated that only a set of normal modes could exist inside them, one with a longitudinal component of the electric field and another with only a longitudinal magnetic component. Moreover, the propagation of these modes depended on a certain value of frequency (the cutoff frequency); below this frequency, propagation was not possible. This frequency was determined by the cross-sectional dimensions of the waveguide.

Practical difficulties to generate microwaves and probably the success of the experiments with long waves by Marconi pushed microwaves into the background for several years, until some investigators from the field of power transmission came out in the 30's showing the practical usefulness of microwaves for this purpose. It was not until the 40's during World War II that microwave engineering experimented a huge improvement. This resulted in waveguides getting a place among the most common and useful structures in the centimeter and millimeter wave ranges because of their low losses compared with coaxial cables and their great performance in presence of interferences.

2.2 Wave types

The details of the following analysis can be found in [Pag83]. The formulation assumes boundaries of perfect conductor ($\sigma = \infty$) and an homogeneous and isotropous dielectric inside the waveguide with no free charges nor currents ($\rho = 0$ and $\bar{J} = 0$). Therefore, the electromagnetic problem that will be analyzed from now on is governed by the following form of Maxwell equations, written now in the frequency domain:

$$\begin{aligned} \nabla \times \overline{E} &= -j\omega\mu\overline{H} \\ \nabla \times \overline{H} &= j\omega\varepsilon\overline{E} \\ \nabla \cdot \overline{E} &= 0 \\ \nabla \cdot \overline{H} &= 0 \end{aligned} \quad . \tag{2.6}$$

This set of equations can be transformed into three-dimensional vectorial Helmholtz equations by taking the curl in the first two expressions,

$$\begin{aligned} \nabla^2\overline{E} - \gamma_0^2\overline{E} &= 0 \\ \nabla^2\overline{H} - \gamma_0^2\overline{H} &= 0 \end{aligned} \tag{2.7}$$

with $\gamma_0^2 = -\omega^2\mu\varepsilon$. The solutions of this set of equations can be decomposed into transversal and longitudinal components for both electric and magnetic fields ($\overline{E} = \overline{E}_t + \overline{E}_z$, $\overline{H} = \overline{H}_t + \overline{H}_z$).

With these considerations, as each component must satisfy the Helmholtz equation it is possible to extract the axial component in order to apply separation of variables. For the electric field component, this process yields:

$$\nabla^2\overline{E}_z - \gamma_0^2\overline{E}_z = 0 \quad ; \quad \nabla^2\overline{E}_z = \left(\nabla^2 E_z\right)\hat{z} = \left(\nabla_t^2 E_z + \frac{\partial^2 E_z}{\partial z^2}\right)\hat{z} \quad ; \quad \nabla_t^2 E_z + \frac{\partial^2 E_z}{\partial z^2} - \gamma_0^2 E_z = 0$$

Now, $E_z = F_E(x,y)Z(z)$ is introduced in the above equations to find the solution for E_z:

$$\frac{\nabla_t^2 F_E}{F_E} + \frac{Z''}{Z} - \gamma_0^2 = 0 \tag{2.8}$$

with $\frac{Z''}{Z} = \gamma^2$ being a separation constant. The solution is:

$$E_z = F_E(x,y)\left(Ae^{\gamma z} + Be^{-\gamma z}\right) \tag{2.9}$$

The problem is thus reduced to find the scalar function $F_E(x,y)$ solution of the two-dimensional scalar Helmholtz equation $\nabla_t^2 F_E - \gamma_c^2 F_E = 0$ with $\gamma_c^2 = \gamma_0^2 - \gamma^2$ and appropriate boundary conditions. For the magnetic field, the same process could be followed, with $F_H(x,y)$ being an independent solution of $F_E(x,y)$.

From now on, γ represents the propagation constant of a mode, which is complex ($\gamma = \alpha + j\beta$) and depends on the frequency. Its real part (non-negative), α, is the attenuation constant and describes how the amplitude of the mode decreases as it travels through the guide. Its imaginary part (non-negative), β, is called the phase constant, and it describes the phase variation in the propagation along the *z*-axis. It could also be shown [Pag83] that γ_c^2 must be a real negative number. In many books the notation $k_c^2 = -\gamma_c^2$ is preferred, and therefore k_c must be a real positive number.

2.2.1 TE Modes

Transverse electric modes (also known as H modes) have $E_z = 0$, so the transverse components of the fields must be derived from the axial component of the magnetic field as follows:

$$\overline{H}_z = F_H(x,y)e^{-\gamma z}\hat{z} \tag{2.10. a}$$

$$\nabla_z \times \overline{E}_t = -j\omega\mu\overline{H}_t \tag{2.10. b}$$

$$\nabla_t \times \overline{H}_z + \nabla_z \times \overline{H}_t = j\omega\varepsilon\overline{E}_t . \tag{2.10. c}$$

The equation for $F_H(x,y)$, with homogeneous Neumann boundary conditions are

$$\nabla_t^2 F_H - \gamma_c^2 F_H = 0 \quad , \quad \left(\nabla_t F_H \cdot \hat{n}\right)\Big|_C = 0 \quad , \tag{2.11}$$

with C being the contour and *n* the normal to C. Multiplying now Eq. 2.10. c) by $-j\omega\mu$ and taking Eq. 2.10. a) into account:

$$\frac{\partial^2 \overline{E}_t}{\partial z^2} - \gamma_0^2\overline{E}_t = -j\omega\mu\nabla_t \times \overline{H}_z . \tag{2.12}$$

Rejecting the homogeneous solution (which would lead to a *TEM* mode):

$$\overline{E}_t = \frac{j\omega\mu}{\gamma}\overline{H}_t \times \hat{z} = Z_{TE}\overline{H}_t \times \hat{z} \tag{2.13}$$

$$\overline{H}_t = \frac{\gamma}{\gamma_c^2}\nabla_t \overline{H}_z = \frac{\gamma}{j\omega\mu}\hat{z} \times \overline{E}_t . \tag{2.14}$$

with $Z_{TE} = \frac{\hat{z} \times \overline{E}_t}{\overline{H}_t} = \frac{j\omega\mu}{\gamma}$ known as the *TE* mode wave impedance. For lossless dielectrics, it is real above the cutoff frequency and pure imaginary and positive under cutoff.

2.2.2 TM Modes

Transverse magnetic modes (also known as E modes) have $H_z = 0$, so this time the transverse components of the fields must be derived from the axial component of the electric field this time:

$$\overline{E}_z = F_E(x,y)e^{-\gamma z}\hat{z} \tag{2.15. a}$$

$$\nabla_t \times \overline{E}_z + \nabla_z \times \overline{E}_t = -j\omega\mu\overline{H}_t \tag{2.15. b}$$

$$\nabla_z \times \overline{H}_t = j\omega\varepsilon\overline{E}_t . \tag{2.15. c}$$

The equation for $F_E(x,y)$, with homogeneous Dirichlet boundary conditions are

$$\nabla_t^2 F_E - \gamma_c^2 F_E = 0 \quad , \quad F_E\big|_C = 0 \ , \tag{2.16}$$

with C being the contour and *n* the normal to C. Multiplying now Eq. 2.15. b) by $j\omega\varepsilon$ and taking Eq. 2.15. c) into account:

$$\frac{\partial^2 \overline{H}_t}{\partial z^2} - \gamma_0^2 \overline{H}_t = j\omega\varepsilon\nabla_t \times \overline{E}_z . \tag{2.17}$$

Rejecting again the homogeneous solution (*TEM* modes):

$$\overline{E}_t = \frac{\gamma}{\gamma_c^2}\nabla_t \overline{E}_z \ , \tag{2.18}$$

$$\overline{H}_t = \frac{j\omega\varepsilon}{\gamma}\hat{z} \times \overline{E}_t \ , \tag{2.19}$$

with $Z_{TM} = \frac{\hat{z} \times \overline{E}_t}{\overline{H}_t} = \frac{\gamma}{j\omega\varepsilon}$ known as the *TM* mode wave impedance. For lossless dielectrics, it is real above the cutoff frequency and pure imaginary and negative under cutoff.

2.3 Basic concepts

An electromagnetic **waveguide** is the structure already seen in Fig. 2.2. It is bounded by a conductor, and may include some others inside. The structure can be empty or filled with dielectric that for the theory exposed above must be homogeneous.

The electromagnetic field inside these waveguides may be represented as the superposition of an infinite number of **modes**, i.e., particular electromagnetic field solutions which could exist within the structure. Each one of these modes may be a **propagating mode** or an **evanescent mode** depending on the working frequency with respect to its **cutoff frequency**. For waveguides with lossless dielectrics, if the working frequency is below this value, the amplitude of the mode will attenuate along the waveguide as $e^{-\alpha z}$, dying away in a short distance. It is an **evanescent mode** (it is also said that is under cutoff). If the working frequency is over this value, the mode is propagating with variation along the *z* axis as $e^{-j\beta z}$.

The mode with the lowest cutoff frequency for a given waveguide is called the **dominant mode** of the structure. Waveguides are normally designed so that at the frequency of operation only the dominant mode can be propagating (although other evanescent modes may be excited by discontinuities). Therefore, the range of frequencies between this dominant mode and the next mode with the lowest cutoff frequency determines the **single-mode** or **monomode bandwidth** of the waveguide. This range may vary depending on the symmetry of the structure, as will be explained later in this chapter.

Modes with the same cutoff frequency but with different field distributions are called **degenerate modes** (e.g. the TE_{11}/TM_{11} from the rectangular waveguide).

Working at microwave frequencies (short wavelengths) means some design difficulties because of the reduced dimensions involved in microwave devices. However, as working frequency increases it is possible to achieve greater **absolute bandwidths**. For example, 6 MHz represent a 1% relative bandwidth at 600 MHz while at 60 GHz it corresponds with 600 MHz, i.e., a much greater absolute bandwidth. The **fractional bandwidth** of a device operating between f_L and f_H is defined as:

$$BW = 2\frac{f_H - f_L}{f_H + f_L} \times 100(\%) \ , \tag{2.20}$$

For example, if the design covers the range of frequencies between 12 and 18 GHz, it is covering a $BW = 2\frac{18-12}{18+12} \times 100 = 40\%$ fractional bandwidth.

2.4 Modes of the rectangular waveguide

Fig. 2.4 shows the cross section of a rectangular waveguide of sides *a* (along *x*) and *b* (along *y*). The conditions that the scalar function must fulfill in a rectangular waveguide are written as

$$\nabla_t^2 F + k_c^2 F = 0 \tag{2.21.a}$$

$$\left.\frac{\partial F_H}{\partial n}\right|_C = 0 \text{, for TE modes (H modes)} \tag{2.21.b}$$

$$F_E\big|_C = 0 \text{, for TM modes (E modes)} \ , \tag{2.21.c}$$

with C being the waveguide contour and *n* the normal to C. Note that the above mentioned change $k_c^2 = -\gamma_c^2$ is used here, and will be used from now on.

As the scalar function can be written as a function of two variables $F(x,y) = X(x)Y(y)$, Eq. 2.21.a) can be rewritten as $X''Y + XY'' + k_c^2 XY = 0$ to find its solutions:

$$\frac{X''}{X} + \frac{Y''}{Y} = -k_c^2 \ . \tag{2.22}$$

Two new separation constants k_x and k_y appear, and the functions *X*,*Y* are:

$$\frac{X''}{X} = -k_x^2 \ , \ \frac{Y''}{Y} = -k_y^2 \ , \tag{2.23}$$

$$\begin{aligned} X(x) &= A\sin(k_x x) + B\cos(k_x x) \\ Y(x) &= C\sin(k_y y) + D\cos(k_y y) \end{aligned} \ . \tag{2.24}$$

The next step is to apply boundary conditions for *TE* and *TM* modes to find their respective scalar function. For *TE* modes:

$$\begin{aligned} &\frac{\partial F_H}{\partial y} = X(x)k_y\left(C\cos(k_y y) - D\sin(k_y y)\right) && \frac{\partial F_H}{\partial x} = k_x\left(A\cos(k_x x) - B\sin(k_x x)\right)Y(y) \\ &\left.\frac{\partial F_H}{\partial y}\right|_{y=0} = 0 \Rightarrow C = 0 && \left.\frac{\partial F_H}{\partial x}\right|_{x=0} = 0 \Rightarrow A = 0 \\ &\left.\frac{\partial F_H}{\partial y}\right|_{y=b} = 0 \Rightarrow \sin(k_y b) = 0 \Rightarrow k_y = \frac{n\pi}{b} && \left.\frac{\partial F_H}{\partial x}\right|_{x=a} = 0 \Rightarrow \sin(k_x a) = 0 \Rightarrow k_x = \frac{m\pi}{a} \end{aligned} \ . \tag{2.25}$$

Fig. 2.4. Cross section and reference system of a rectangular waveguide.

Similarly, for *TM* modes:

$$\begin{aligned} &X(x)Y(y) = (A\sin(k_x x) + B\cos(k_x x))(C\sin(k_y y) + D\cos(k_y y)) \\ &F_E\big|_{x=0} = 0 \Rightarrow B = 0 \\ &F_E\big|_{x=a} = 0 \Rightarrow \sin(k_x a) = 0 \Rightarrow k_x = \frac{m\pi}{a} \\ &F_E\big|_{y=0} = 0 \Rightarrow D = 0 \\ &F_E\big|_{y=b} = 0 \Rightarrow \sin(k_y b) = 0 \Rightarrow k_y = \frac{n\pi}{b} \end{aligned} \quad . \tag{2.26}$$

The final expressions for the scalar functions are:

$$\underset{F_H = P\cos(k_x x)\cos(k_y y)}{\text{For TE modes:}} \quad , \quad \underset{F_E = Q\sin(k_x x)\sin(k_y y)}{\text{For TM modes:}} \tag{2.27}$$

with $P = BD$ and $Q = AC$, respectively. The components of electric and magnetic fields for *TE* and *TM* modes can be now easily obtained using equations from Sec. 2.2.1 and Sec. 2.2.2. It should be noted that all the expressions shown in Eq. 2.28 for the fields assume that the mode is propagating along the +z-axis. If it is needed to obtain the fields in time-domain for time-harmonic variation at a particular angular frequency $\omega = 2\pi f$, Eq. 2.28 have to be multiplied by $e^{j\omega t}$ and then to extract the real part.

$$\begin{array}{ll} \text{For } \mathrm{TE_{m,n}} \text{ modes } (\mathrm{P}=1): & \text{For } \mathrm{TM_{m,n}} \text{ modes } (\mathrm{Q}=1): \\ H_z = \cos(k_x x)\cos(k_y y)e^{-\gamma z} & E_z = \sin(k_x x)\sin(k_y y)e^{-\gamma z} \\ H_x = \frac{\gamma}{k_{c_{m,n}}^2} k_x \sin(k_x x)\cos(k_y y)e^{-\gamma z} & E_x = \frac{-\gamma}{k_{c_{m,n}}^2} k_x \cos(k_x x)\sin(k_y y)e^{-\gamma z} \\ H_y = \frac{\gamma}{k_{c_{m,n}}^2} k_y \cos(k_x x)\sin(k_y y)e^{-\gamma z} & E_y = \frac{-\gamma}{k_{c_{m,n}}^2} k_y \sin(k_x x)\cos(k_y y)e^{-\gamma z} \\ E_x = \frac{j\omega\mu}{k_{c_{m,n}}^2} k_y \cos(k_x x)\sin(k_y y)e^{-\gamma z} & H_x = \frac{j\omega\varepsilon}{k_{c_{m,n}}^2} k_y \sin(k_x x)\cos(k_y y)e^{-\gamma z} \\ E_y = \frac{-j\omega\mu}{k_{c_{m,n}}^2} k_x \sin(k_x x)\cos(k_y y)e^{-\gamma z} & H_y = \frac{-j\omega\varepsilon}{k_{c_{m,n}}^2} k_x \cos(k_x x)\sin(k_y y)e^{-\gamma z} \end{array} \quad . \tag{2.28}$$

For *TM* modes, both *m* and *n* must be non-zero integers. On the contrary, for *TE* modes, *m* and *n* may be zero but never both at the same time. These modes with *m* and *n* variations regarding *x* and *y* axis, respectively, are designated as TM_{mn} and TE_{mn}. Cutoff frequency for them is

$$f_{c_{m,n}} = \frac{\omega_{c_{m,n}}}{2\pi} \;\; ; \;\; \omega_{c_{m,n}} = \frac{k_{c_{m,n}}}{\sqrt{\mu\varepsilon}} = \frac{1}{\sqrt{\mu\varepsilon}}\left[\left(\frac{m\pi}{a}\right)^2 + \left(\frac{n\pi}{b}\right)^2\right]^{1/2} \quad . \tag{2.29}$$

The attenuation and phase constants of a mode with cutoff frequency $f_{c_{m,n}}$ are:

$$\alpha_{m,n} = k_{c_{m,n}}\sqrt{1 - \left(\frac{f}{f_{c_{m,n}}}\right)^2}, \quad f < f_{c_{m,n}} \quad , \tag{2.30}$$

$$\beta_{m,n} = \omega\sqrt{\mu\varepsilon}\sqrt{1 - \left(\frac{f_{c_{m,n}}}{f}\right)^2}, \quad f > f_{c_{m,n}} \quad . \tag{2.31}$$

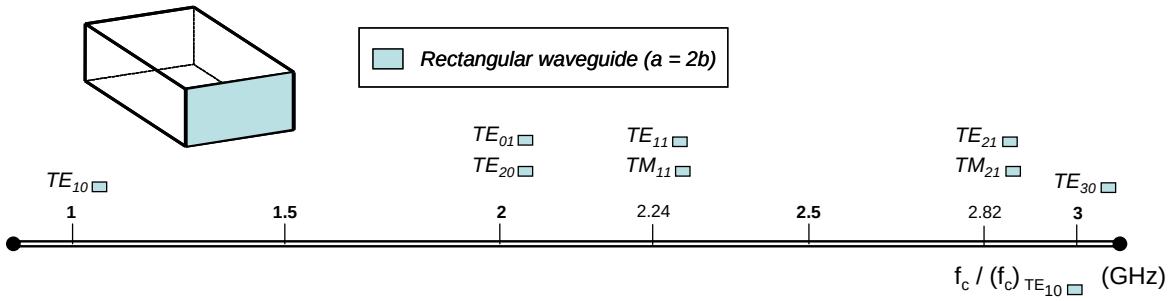

Fig. 2.5. Cutoff frequencies for the first higher-order modes of the rectangular waveguide with a=2b.

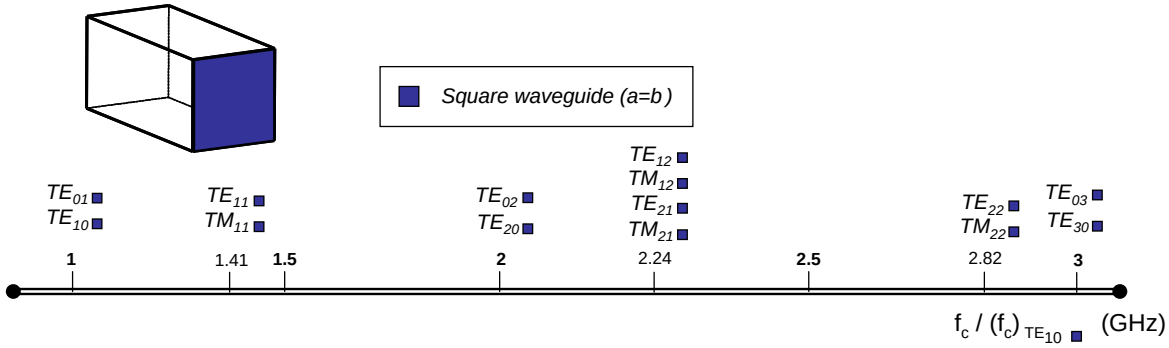

Fig. 2.6. Cutoff frequencies for the first higher-order modes of the square waveguide.

Fig. 2.5 shows a line diagram indicating the cutoff frequencies of some of the lowest-order modes referred to that of the fundamental TE_{10} mode for a waveguide with $a = 2b$. Note that the square waveguide is a rectangular waveguide with $a = b$, as it can be seen in Fig. 2.6.

2.5 Modes of the circular waveguide

Fig. 2.7 shows the cross section of a circular waveguide of radius a. In this case, the two-dimensional Helmholtz equation for the scalar function F (F_E or F_H) is expressed in circular or polar coordinates:

$$\frac{1}{r}\frac{\partial}{\partial r}\left(r\frac{\partial F}{\partial r}\right)+\frac{1}{r^2}\frac{\partial^2 F}{\partial \phi^2}+k_c^2 F=0 \tag{2.32.a}$$

$$\left.\frac{\partial F_H}{\partial r}\right|_{r=a}=0\text{, for TE modes (H }m\text{odes)} \tag{2.32.b}$$

$$F_E\big|_{r=a}=0\text{, for TM modes (E }m\text{odes)}\quad . \tag{2.32.c}$$

By setting $F(r,\phi)=R(r)H(\phi)$, it is possible to separate dependence over r and ϕ as follows:

$$r^2\frac{R''}{R}+\frac{rR'}{R}+k_c^2 r^2=\frac{-H''}{H}\quad . \tag{2.33}$$

Note that both sides of the equation must be equal for all values of r and ϕ, so they must equal a constant (let it be n). Then, two ordinary differential equations must be solved separately:

$$\frac{-H''}{H}=n,\ \text{ and }\ R''+\frac{1}{r}R'+\left(k_c^2-\frac{n^2}{r^2}\right)R=0\quad . \tag{2.34}$$

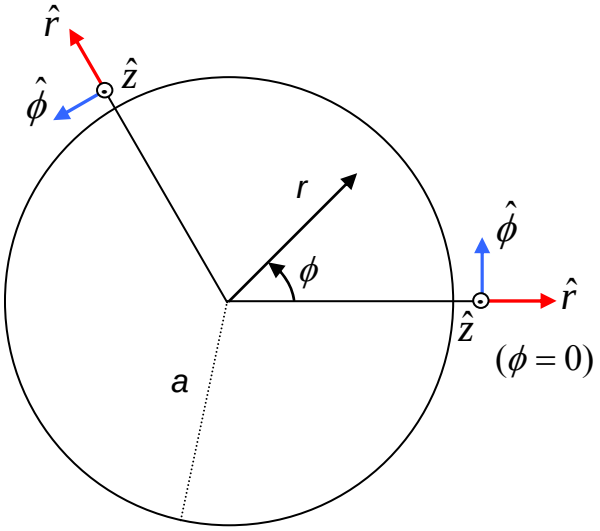

Fig. 2.7. Cross section and reference system for the circular waveguide.

These differential equations yield the following solutions,

$$\begin{aligned} H(\phi) &= A\sin(n\phi) + B\cos(n\phi) \\ R(r) &= CJ_n(k_c r) + DN_n(k_c r) \end{aligned} \tag{2.35}$$

with J_n and N_n being the *n*th-order Bessel functions of first and second kind, respectively. $N_n(k_c r)$ is infinite at *r=0* for any *n*, so it can not be included in the solution and *D* must be 0.

Note that the expression obtained for the variation of ϕ is the sum of two components $\sin(n\phi)$ and $\cos(n\phi)$ (if $n \neq 0$; for $n = 0$ there is only one solution). These two solutions are independent, leading to different modes (although with only a rotation of *90º/n* between their field patterns and with the same cutoff frequency, i.e., they will be degenerate modes). If not mentioned, a *TE/TM*$_{nl}$ mode will refer to both sine and cosine modes. Otherwise, the dependence with these functions will be indicated. With all these considerations, it is possible to apply boundary conditions to find the scalar function of a circular waveguide. For *TM* modes:

$$F_E\big|_{r=a} = CJ_n(k_c a) = 0 \Rightarrow J_n(k_c a) = 0 \Rightarrow k_c = \frac{p_{nl}}{a} \tag{2.36}$$

with p_{nl} being the *l*-th root of $J_n = 0$ (see Table 2.1). For *TE* modes:

$$\left.\frac{\partial F_H}{\partial r}\right|_{r=a} = CJ_n'(k_c a) = 0 \Rightarrow J_n'(k_c a) = 0 \Rightarrow k_c = \frac{p_{nl}'}{a} \tag{2.37}$$

with p_{nl}' being the *l*-th root of $J_n' = 0$ (see Table 2.2).

The final expressions for the scalar functions are:

$$\begin{aligned} &\text{For TE modes:} && \text{For TM modes:} \\ &F_H = PJ_n\left(\frac{p_{nl}'}{a}r\right)\begin{Bmatrix}\cos(n\phi)\\ \sin(n\phi)\end{Bmatrix} && F_E = QJ_n\left(\frac{p_{nl}}{a}r\right)\begin{Bmatrix}\cos(n\phi)\\ \sin(n\phi)\end{Bmatrix} \end{aligned} \tag{2.38}$$

with $P = Q = AC$ or BC. The components of electric and magnetic fields for *TE* and *TM* modes can be now obtained using equations from Sec. 2.2.1 and Sec. 2.2.2. The following fields are for a mode propagating along +*z*-axis:

$$\begin{array}{ll}
\text{For TE}_{n,l}\text{ modes (P = 1):} & \text{For TM}_{n,l}\text{ modes (Q = 1):} \\
H_z = e^{-\gamma z} J_n\left(\frac{p'_{nl}}{a} r\right)\begin{Bmatrix}\cos(n\phi)\\ \sin(n\phi)\end{Bmatrix} & E_z = e^{-\gamma z} J_n\left(\frac{p_{nl}}{a} r\right)\begin{Bmatrix}\cos(n\phi)\\ \sin(n\phi)\end{Bmatrix} \\
H_r = e^{-\gamma z} \frac{-\gamma}{k_c} J'_n\left(\frac{p'_{nl}}{a} r\right)\begin{Bmatrix}\cos(n\phi)\\ \sin(n\phi)\end{Bmatrix} & E_r = e^{-\gamma z} \frac{-\gamma}{k_c} J'_n\left(\frac{p_{nl}}{a} r\right)\begin{Bmatrix}\cos(n\phi)\\ \sin(n\phi)\end{Bmatrix} \\
H_\phi = e^{-\gamma z} \frac{-\gamma}{k_c^2}\frac{n}{r} J_n\left(\frac{p'_{nl}}{a} r\right)\begin{Bmatrix}-\sin(n\phi)\\ \cos(n\phi)\end{Bmatrix} & E_\phi = e^{-\gamma z} \frac{-\gamma}{k_c^2}\frac{n}{r} J_n\left(\frac{p_{nl}}{a} r\right)\begin{Bmatrix}-\sin(n\phi)\\ \cos(n\phi)\end{Bmatrix} \\
E_r = e^{-\gamma z} \frac{-j\omega\mu}{k_c^2}\frac{n}{r} J_n\left(\frac{p'_{nl}}{a} r\right)\begin{Bmatrix}-\sin(n\phi)\\ \cos(n\phi)\end{Bmatrix} & H_r = e^{-\gamma z} \frac{j\omega\varepsilon}{k_c^2}\frac{n}{r} J_n\left(\frac{p_{nl}}{a} r\right)\begin{Bmatrix}-\sin(n\phi)\\ \cos(n\phi)\end{Bmatrix} \\
E_\phi = e^{-\gamma z} \frac{j\omega\mu}{k_c} J'_n\left(\frac{p'_{nl}}{a} r\right)\begin{Bmatrix}\cos(n\phi)\\ \sin(n\phi)\end{Bmatrix} & H_\phi = e^{-\gamma z} \frac{-j\omega\varepsilon}{k_c} J'_n\left(\frac{p_{nl}}{a} r\right)\begin{Bmatrix}\cos(n\phi)\\ \sin(n\phi)\end{Bmatrix}
\end{array} \quad . \qquad (2.39)$$

Cutoff frequencies for the first higher-order modes of the circular waveguide are shown in Fig. 2.8.

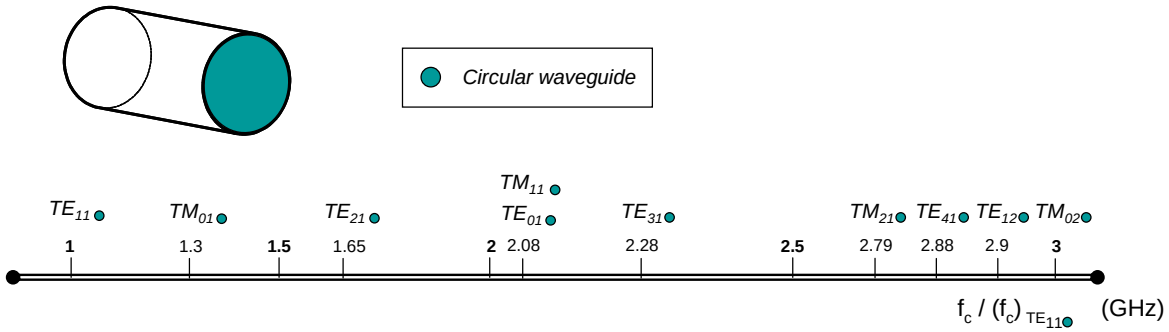

Fig. 2.8. Cutoff frequencies for the first higher-order modes of the circular waveguide.

l	p_{0l}	p_{1l}	p_{2l}	p_{3l}	p_{4l}	p_{5l}
1	2.405	3.832	5.136	6.38	7.59	8.77
2	5.52	7.016	8.417	9.76	11.06	12.34
3	8.654	10.173	11.62	13.02	14.37	15.7
4	11.79	13.32	14.8	16.22	17.62	18.98

Table 2.1. Zeros of Bessel functions.

l	p'_{0l}	p'_{1l}	p'_{2l}	p'_{3l}	p'_{4l}	p'_{5l}
1	3.831	1.841	3.054	4.201	5.317	6.415
2	7.015	5.331	6.706	8.015	9.282	10.519
3	10.173	8.536	9.969	11.346	12.682	13.987
4	13.324	11.706	13.17	14.585	15.964	17.312

Table 2.2. Zeros of derivatives of Bessel functions.

2.6 Field pattern and symmetry properties of the TE/TM modes

As it was discussed before, each mode has a unique cross-sectional distribution of its electric and magnetic field, which remains the same along the uniform waveguide (although its amplitude can vary). These unique field patterns hold certain symmetry properties which can be used to analyze if they will be excited in certain waveguide discontinuities.

As it is shown on Eq. 2.28 and Eq. 2.39, the components of the electric and magnetic fields of *TE* and *TM* modes can be written in terms of sines and cosines, which are odd and even functions respectively. Consequently, the field distribution of *TE* and *TM* modes will inherit these odd/even properties summarized in Table 2.3 and Table 2.4. The analysis of these symmetries is better explained with a reference system located at the center of the waveguide (see Fig. 2.9 to check the systems used in this section). The even/odd properties will be related to the *x*-axis (*xz*-plane) and the *y*-axis (*yz*-plane) of this new system.

It is important to clarify that the analytical expressions obtained for the fields of *TE* and *TM* modes in the previous sections depend on the reference system chosen for each case. For obtaining the expressions in the new coordinate system, the variable change $x_{new} = x_{old} - a/2$ and $y_{new} = y_{old} - b/2$ should be made (where x_{new}, y_{new} is the system in Fig. 2.9 and x_{old}, y_{old} the one in Fig. 2.4 and Eq. 2.27) .

There is another symmetry property which is more general than the even/odd one. It requires the explanation of two concepts: Perfect Electric Walls (PEW) and Perfect Magnetic Walls (PMW) symmetries. A mode is said to have a PEW symmetry with respect to a plane if the electric field is perpendicular to that plane (therefore the magnetic field will be inside that plane). Likewise, a mode has a PMW symmetry with respect to a plane if the magnetic field is perpendicular to that plane (therefore the electric field will be inside that plane). Moreover, electric and magnetic fields will be either symmetrical or antisymmetrical functions related to these walls.

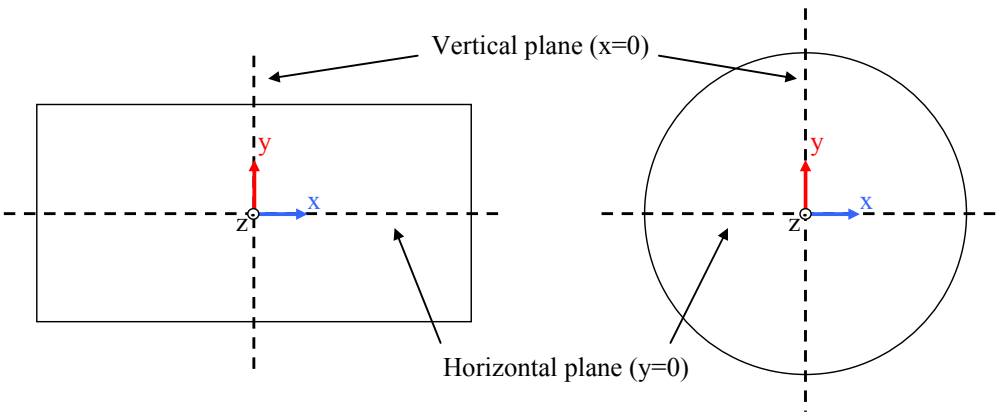

Fig. 2.9. Cross sections and symmetry planes of the rectangular and circular waveguides used to explain symmetry of its modes.

The next two tables summarize the symmetries of the modes in rectangular and circular waveguides. They can also be used to identify the modes excited by a discontinuity with certain symmetries. For example, assuming that only the fundamental mode propagates within the waveguide (i.e. the rectangular TE_{10} and the circular TE_{11}), if the discontinuity holds symmetry in both planes only modes with same symmetry properties of the fundamental modes will be generated, which reduces to modes of the first row of the tables for both waveguides. This will be further clarified in Sec. 2.7.

Rectangular Modes		**$E_x(x,y)$ & $H_y(x,y)$**	**$E_y(x,y)$ & $H_x(x,y)$**	**Horizontal wall (y=0)**	**Vertical wall (x=0)**
TE_{mn} m=1,3,5… n=0,2,4…	TM_{mn} m=1,3,5… n=2,4,6…	x: Odd y: Odd	x: Even y: Even	PEW $\overline{E}$ antisym. $\overline{H}$ sym.	PMW $\overline{E}$ sym. $\overline{H}$ antisym.
TE_{mn} m=0,2,4… n=0,2,4…	TM_{mn} m=2,4,6… n=2,4,6…	x: Even y: Odd	x: Odd y: Even	PEW $\overline{E}$ antisym. $\overline{H}$ sym.	PEW $\overline{E}$ antisym. $\overline{H}$ sym.
TE_{mn} m=0,2,4… n=1,3,5…	TM_{mn} m=2,4,6… n=1,3,5…	x: Even y: Even	x: Odd y: Odd	PMW $\overline{E}$ sym. $\overline{H}$ antisym.	PEW $\overline{E}$ antisym. $\overline{H}$ sym.
TE_{mn} m=1,3,5… n=1,3,5…	TM_{mn} m=1,3,5… n=1,3,5…	x: Odd y: Even	x: Even y: Odd	PMW $\overline{E}$ sym. $\overline{H}$ antisym.	PMW $\overline{E}$ sym. $\overline{H}$ antisym.

Table 2.3. Symmetry properties for the modes of the rectangular waveguide (reference system in Fig. 2.9).

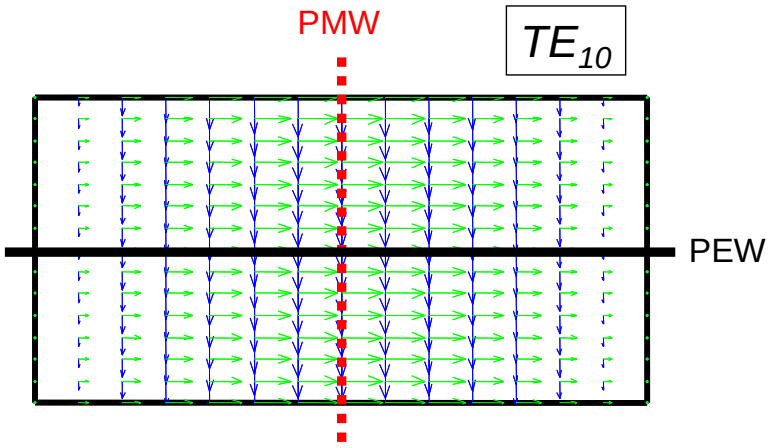

Fig. 2.10. Field pattern and symmetry properties of the TE_{10} rectangular fundamental mode.

Circular Modes		**$E_x(x,y)$ & $H_y(x,y)$**	**$E_y(x,y)$ & $H_x(x,y)$**	**Horizontal wall (y=0)**	**Vertical wall (x=0)**
$TE_{nl,cos}$ n=1,3,5… l=1,2,3…	$TM_{nl,sin}$ n=1,3,5… l=1,2,3…	x: Odd y: Odd	x: Even y: Even	PEW $\overline{E}$ antisym. $\overline{H}$ sym.	PMW $\overline{E}$ sym. $\overline{H}$ antisym.
$TE_{nl,cos}$ n=0,2,4… l=1,2,3…	$TM_{nl,sin}$ n=2,4,6… l=1,2,3…	x: Even y: Odd	x: Odd y: Even	PEW $\overline{E}$ antisym. $\overline{H}$ sym.	PEW $\overline{E}$ antisym. $\overline{H}$ sym.
$TE_{nl,sin}$ n=1,3,5… l=1,2,3…	$TM_{nl,cos}$ n=1,3,5… l=1,2,3…	x: Even y: Even	x: Odd y: Odd	PMW $\overline{E}$ sym. $\overline{H}$ antisym.	PEW $\overline{E}$ antisym. $\overline{H}$ sym.
$TE_{nl,sin}$ n=2,4,6… l=1,2,3…	$TM_{nl,cos}$ n=0,2,4… l=1,2,3…	x: Odd y: Even	x: Even y: Odd	PMW $\overline{E}$ sym. $\overline{H}$ antisym.	PMW $\overline{E}$ sym. $\overline{H}$ antisym.

Table 2.4. Symmetry properties for the modes of the circular waveguide (reference system in Fig. 2.9).

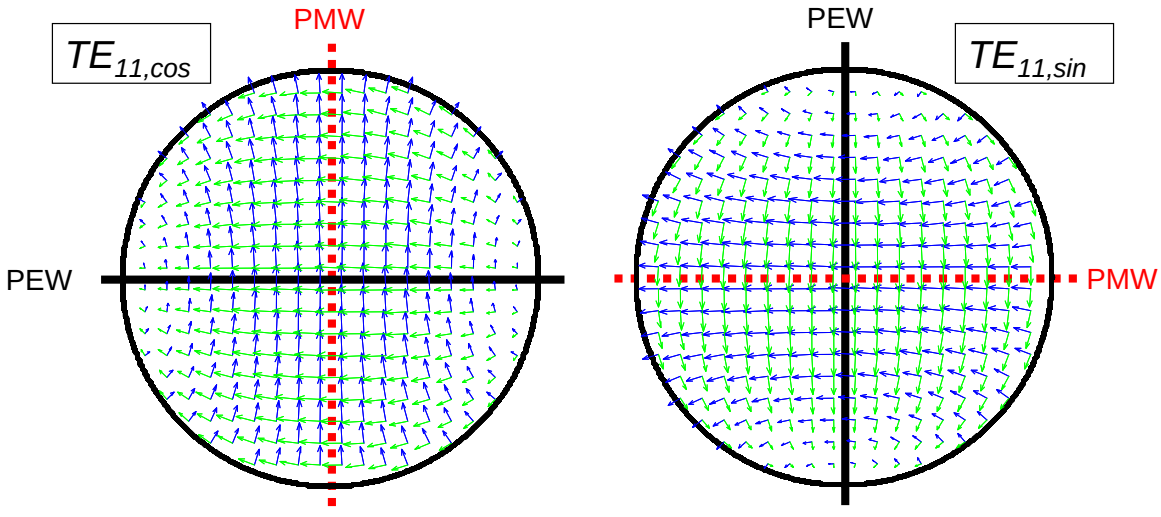

Fig. 2.11. Field pattern and symmetry properties of the TE_{11} circular fundamental mode.

Fig. 2.10 and Fig. 2.11 show the field pattern of both rectangular and circular fundamental modes. Figs. 2.12-2.18. show some examples of higher-order modes of the rectangular waveguide. Each one belongs to one of the rows from Table 2.3. The reader can identify each one of these modes and check their symmetry properties. Figs. 2.19-2.22 show some of the first higher-order modes of the circular waveguide. As it was mentioned before, circular modes are degenerate (sine, cosine, $n > 0$).

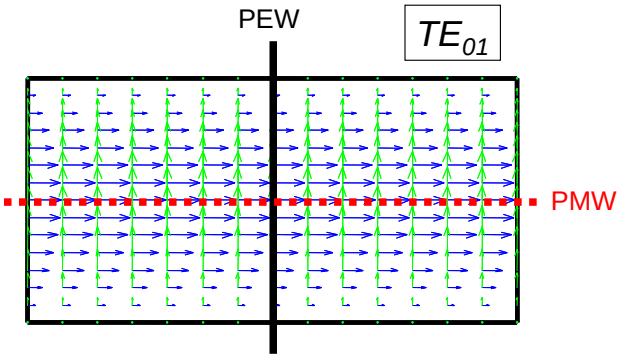

Fig. 2.12. Electric and magnetic fields pattern for the TE_{01} rectangular mode.

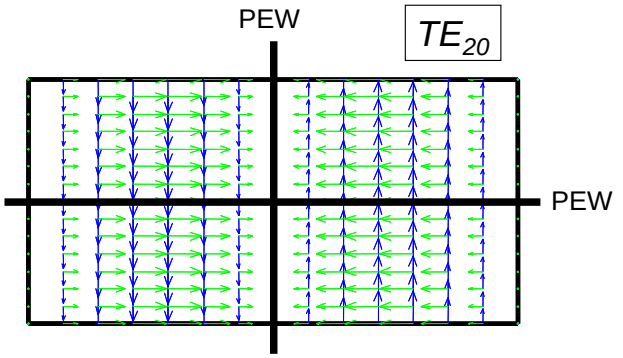

Fig. 2.13. Electric and magnetic fields pattern for the TE_{20} rectangular mode.

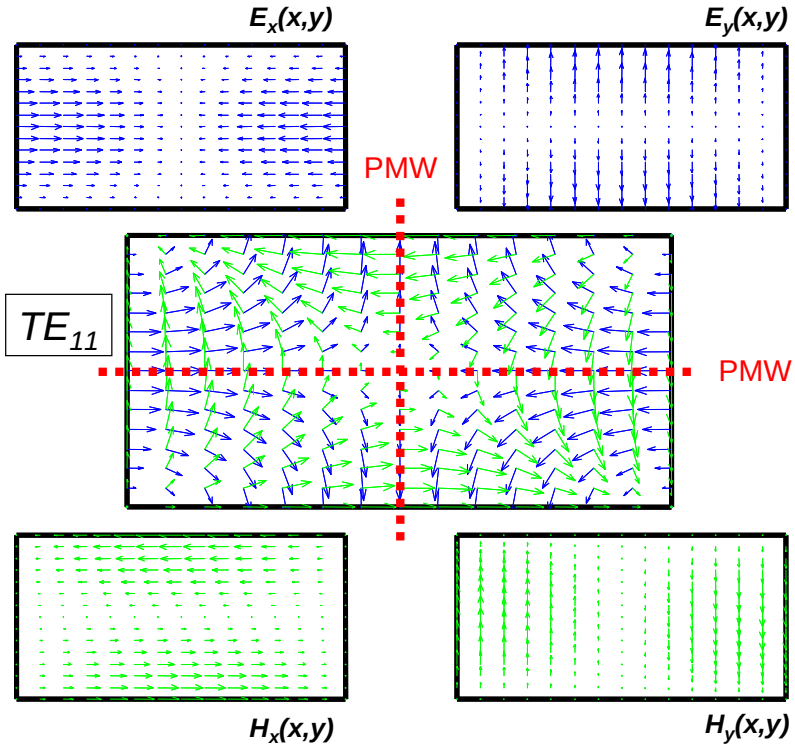

Fig. 2.14. Electric and magnetic fields pattern for the TE_{11} rectangular mode.

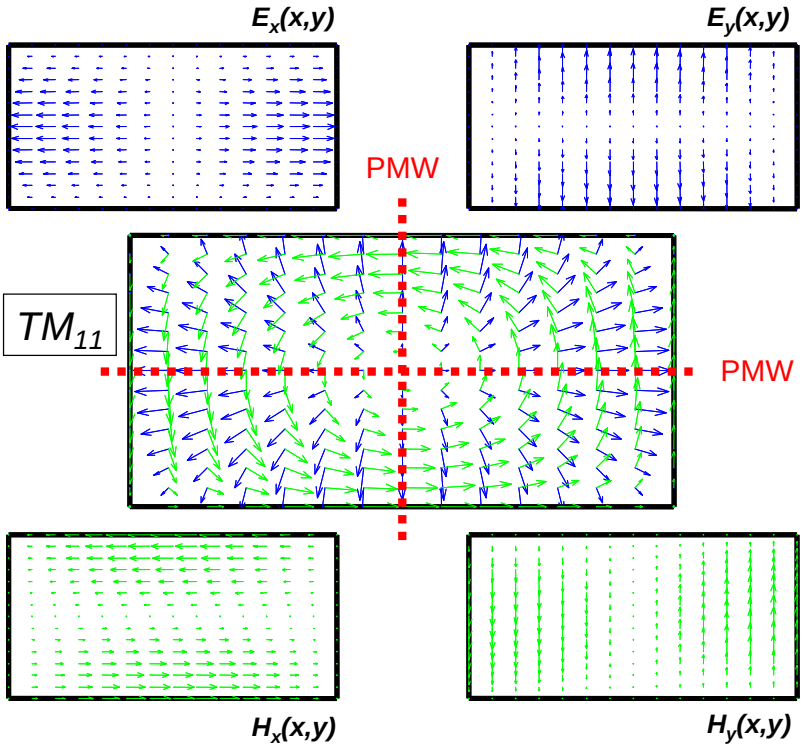

Fig. 2.15. Electric and magnetic fields pattern for the TM_{11} rectangular mode.

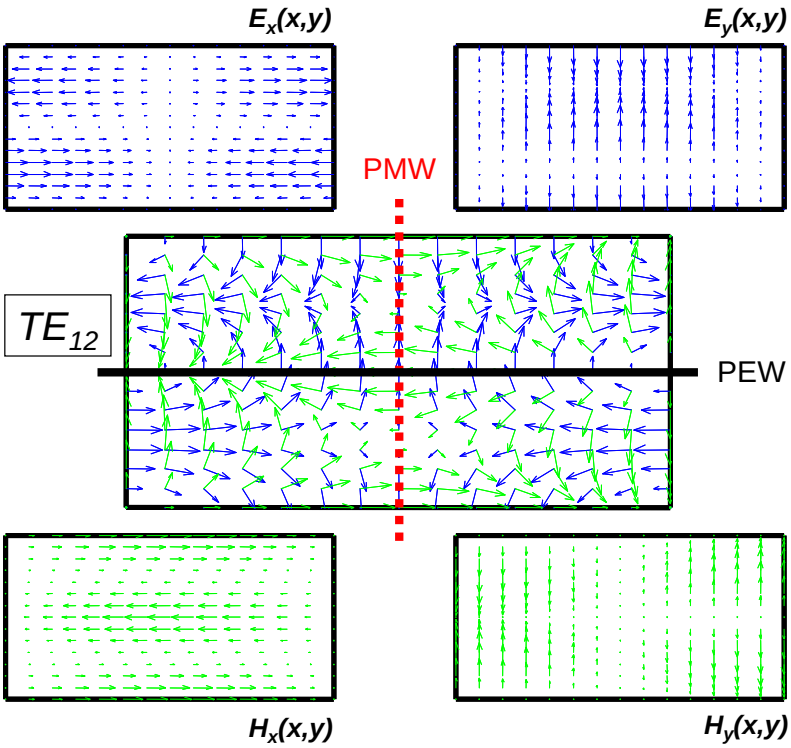

Fig. 2.16. Electric and magnetic fields pattern for the TE_{12} rectangular mode.

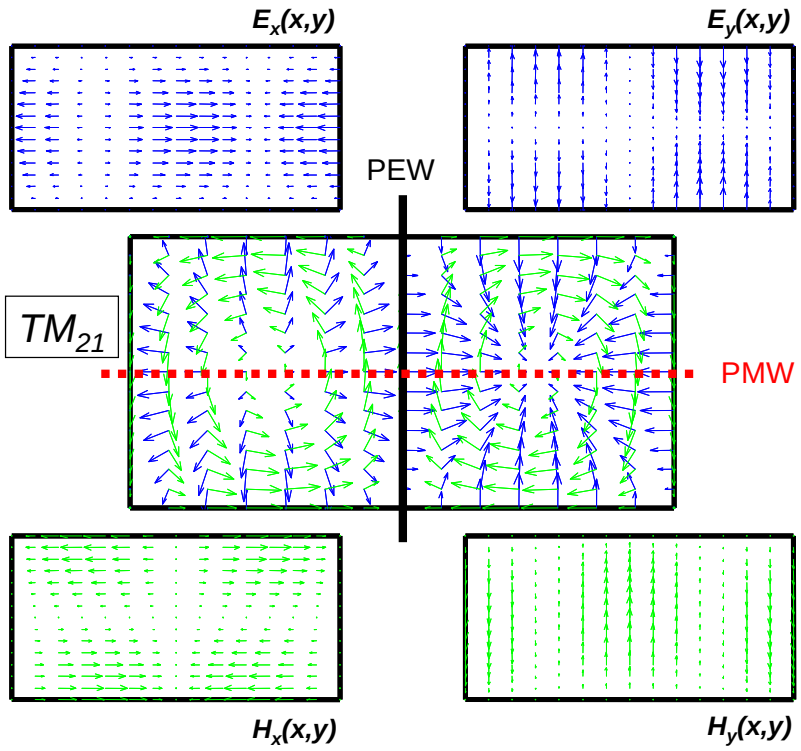

Fig. 2.17. Electric and magnetic fields pattern for the TM_{21} rectangular mode.

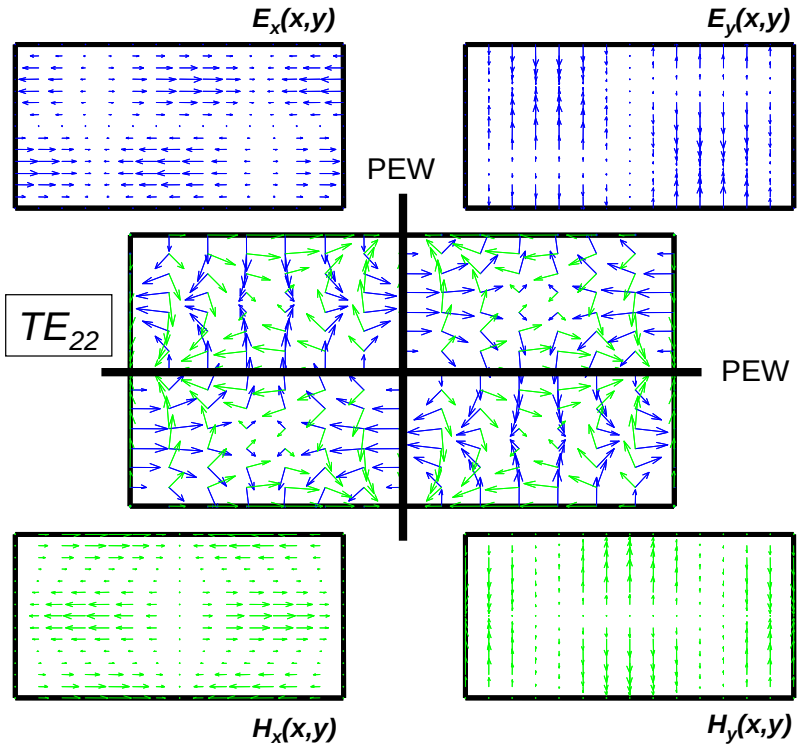

Fig. 2.18. Electric and magnetic fields pattern for the TE_{22} rectangular mode.

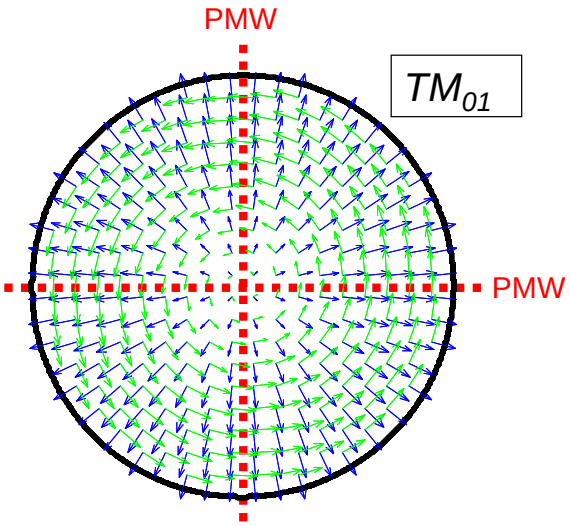

Fig. 2.19. Electric field pattern and symmetry properties for the TM_{01} circular mode.

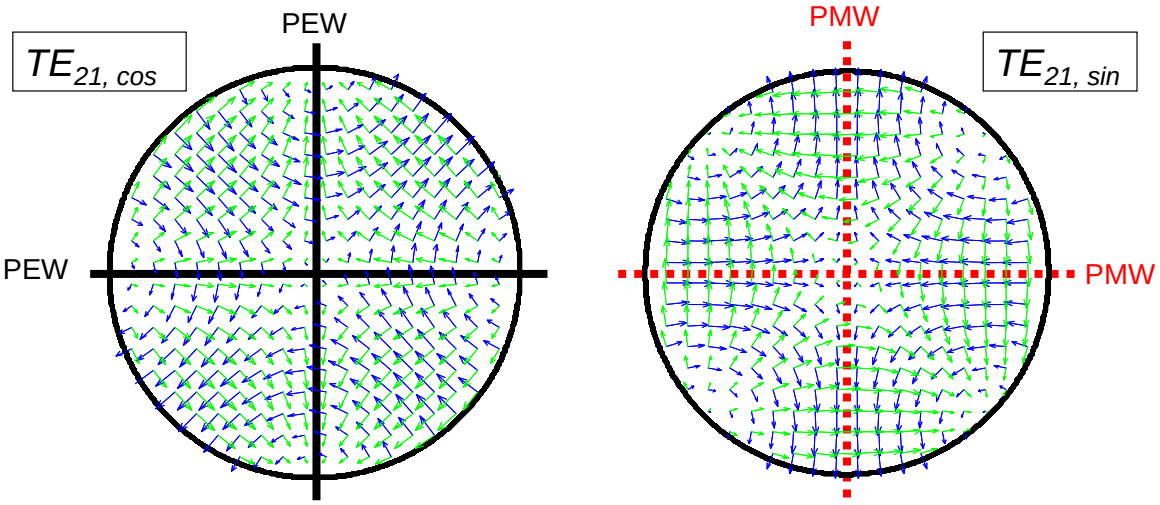

Fig. 2.20. Electric field pattern and symmetry properties for the two TE_{21} circular modes.

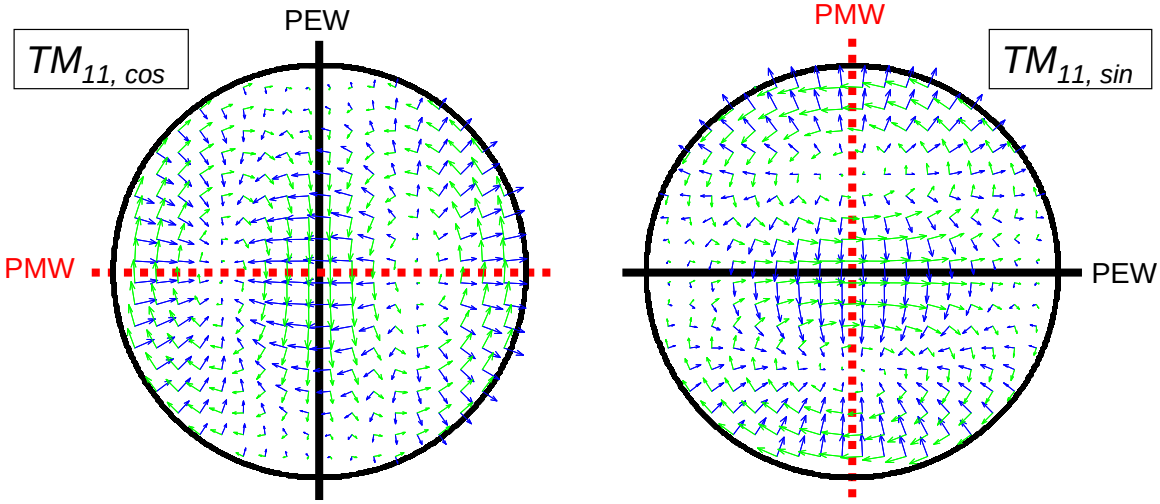

Fig. 2.21. Electric field pattern and symmetry properties for the two TM_{11} circular modes.

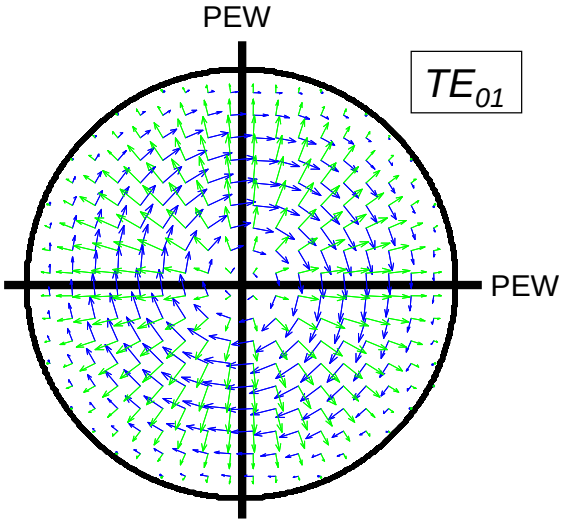

Fig. 2.22. Electric field pattern and symmetry properties for the TE_{01} circular mode.

2.7 Waveguide discontinuities. Some examples of higher-order modes generation

A microwave device may be composed of many waveguides with different cross-sections which are connected at certain planes. The surface where two waveguides of different cross-sections are connected is called a discontinuity. The discontinuity can be designed on purpose, or can be undesired (misalignment, manufacturing tolerances, ...). In any case, from an electromagnetic point of view, the discontinuity imposes specific boundary conditions which must be fulfilled by the electromagnetic field. These boundary conditions may not be accomplished by the individual electromagnetic field of the dominant modes of the waveguides. Therefore, the complete electromagnetic field around the discontinuity requires the contribution of other solutions to satisfy the boundary conditions of the problem, resulting in the excitation of higher-order modes.

When a higher-order mode is excited in a waveguide, the operating frequency determines if it is an evanescent mode or not. In the first case, it is contributing to the storage of electromagnetic energy in the vicinity of the discontinuity. Moreover, the amplitude of the mode will progressively decrease to zero as it travels within the waveguide. An accurate design must consider the attenuation level of these modes when the structure under analysis is cascaded with other components.

On the other hand, if a higher-order mode is excited and it is above cutoff, it will propagate freely inside the waveguide, carrying a portion (depending on the discontinuity) of the incident power. If this excitation is undesired, it will seriously affect the overall performance of the device.

The following examples will help the reader to understand how higher-order modes are generated by some discontinuities when the fundamental TE_{10} mode excites them.

Fig. 2.23-a and Fig. 2.23-b show a width discontinuity for a rectangular waveguide. The first one holds symmetry regarding both *yz* and *xz*-plane, so the TE_{10} mode will only excite $TE_{m0,\ m=1,3,5}$ modes. The second one only holds symmetry regarding *xz*-plane, so a subset of $TE_{m0,\ m=1,2,3...}$modes will be excited now. There is no height variation in the problem, so all the excited modes will preserve the height variation of the excitation, which is zero in this case.

Fig. 2.23-c and Fig. 2.23-d show a height discontinuity this time. Again, the first one holds symmetry regarding *yz* and *xz*-plane, so only a subset of $TE_{1n,\ n=0,2,4...}$ / $TM_{1n,\ n=2,4,6...}$ modes will be excited by the discontinuity. For the unsymmetrical height discontinuity, the modes $TE_{1n,\ n=0,1,2...}$ / $TM_{1n,\ n=1,2,3}$ will be excited. There is no width variation in the problem, so all the excited modes will preserve the width variation of the excitation, which is one in this case.

A third example at Fig. 2.23-e and Fig. 2.23-f shows the combination of width/height variation. The first one holds two planes of symmetry, thus exciting only a subset of $TE_{mn,\ m=1,3,5...\ ;\ n=0,2,4...}$ / $TM_{mn,\ m=1,3,5\ n=2,4,6...}$ modes. The last discontinuity breaks all the symmetries, so it excites all the modes TE_{mn} / TM_{mn}.

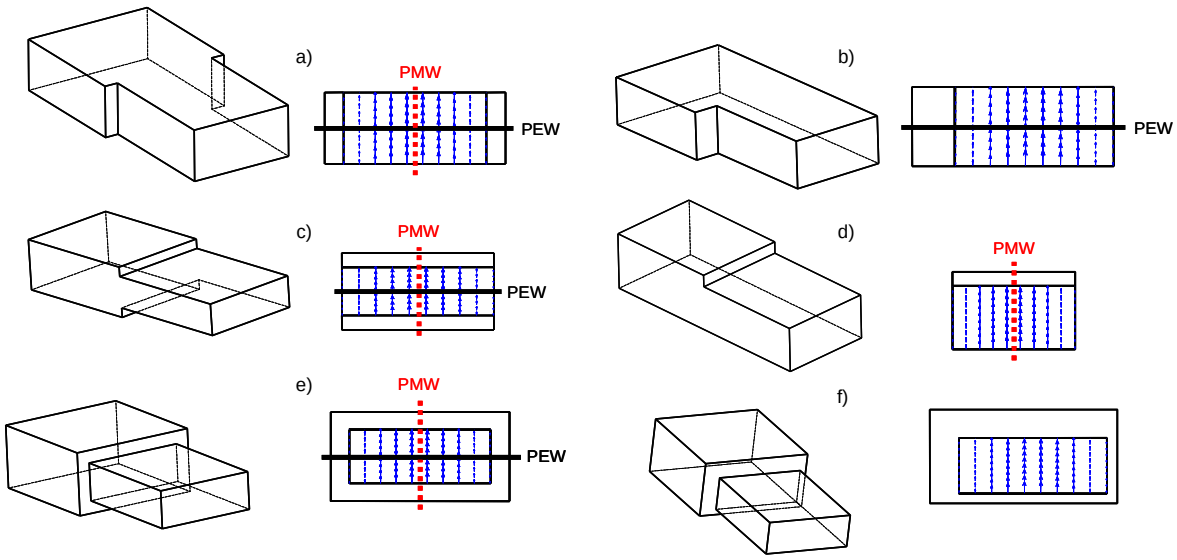

Fig. 2.23. Symmetries of some waveguide discontinuities.

2.8 General expression for the fields within a waveguide

So far, expressions for the individual TE, TM (and TEM) modes have been described in this chapter. It should be noted again that the total field in any point of the waveguide is in general obtained by summing up the individual fields of all the TE, TM (and TEM) modes traveling inside the waveguide in both directions:

$$\vec{E} = \sum_{i=1}^{\infty} \left\{ a_i \left(\vec{e}_i + e_{zi} \hat{z} \right) e^{-\gamma_i z} + b_i \left(\vec{e}_i - e_{zi} \hat{z} \right) e^{\gamma_i z} \right\} \tag{2.40.a}$$

$$\vec{H} = \sum_{i=1}^{\infty} \left\{ a_i \left(\vec{h}_i + h_{zi} \hat{z} \right) e^{-\gamma_i z} + b_i \left(-\vec{h}_i + h_{zi} \hat{z} \right) e^{\gamma_i z} \right\} \tag{2.40.b}$$

$$\vec{E}_t = \sum_{i=1}^{\infty} \left(a_i e^{-\gamma_i z} + b_i e^{\gamma_i z} \right) \vec{e}_i \tag{2.40.c}$$

$$\vec{H}_t = \sum_{i=1}^{\infty} \left(a_i e^{-\gamma_i z} - b_i e^{\gamma_i z} \right) \vec{h}_i \quad . \tag{2.40.d}$$

In these equations, a_i and b_i correspond to the complex amplitudes of the modes (index i can belong to a TE, TM or TEM mode) traveling in the positive and negative z directions, respectively. These amplitudes are determined by the excitation and load conditions applied to the waveguide and may vary with the frequency.

Once a reference system has been chosen, there is a change in the sign for the component of the field propagating in the negative direction which is necessary in order to grant that the field is solution of Maxwell's equations.

2.9 S parameters

Eqs. 2.40 represent a full solution for the problem of describing the electromagnetic field within a waveguide. This amount of information may be more detailed than what is really needed for designing microwave devices. Generally, the design problem only requires more global parameters like voltage and currents on the device terminals or flux density through them. Despite these considerations, it is very difficult to define unique voltages and currents for non-TEM based waveguides like the rectangular and circular waveguides analyzed in this chapter.

Moreover, classical network theory requires open and short circuit conditions to determine Y or Z matrices or to measure them, and such conditions become very unstable on microwave devices working at high frequencies and may result in radiations or even destroy the device.

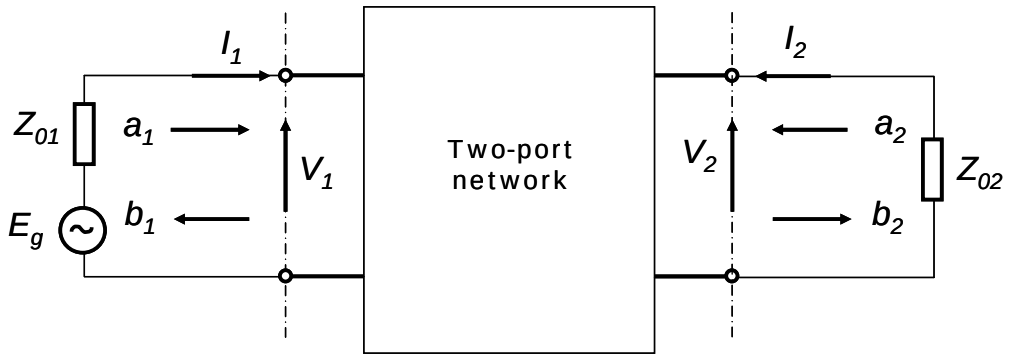

Fig. 2.24. Network variables of a two-port network.

Scattering (S) parameters represent a much more useful way to describe these microwave devices. In fact, the natural way to represent a waveguide is in terms of the amplitude of its modes propagating in forward and backward directions. The S-parameters of a device is the matrix relating the incident and reflected amplitudes of the modes at the waveguide ports of the device. It will depend on the frequency. In addition, they can be calculated using network analysis techniques and measured by network analyzers.

On the other hand, the concepts of voltage and currents, Y and Z matrices, more natural at low frequencies, require a suitable definition for waveguides. In any case, the link between both formulations of amplitudes and voltage-current waves can be expressed in terms of the two port device in Fig. 2.24:

$$V_n = \sqrt{Z_{0n}}\left(a_n + b_n\right) \quad ; \quad I_n = \frac{1}{\sqrt{Z_{0n}}}\left(a_n - b_n\right) \tag{2.41}$$

$$a_n = \frac{1}{\sqrt{8}}\left(\frac{V_n}{\sqrt{Z_{0n}}} + \sqrt{Z_{0n}}\, I_n\right) \quad ; \quad b_n = \frac{1}{\sqrt{8}}\left(\frac{V_n}{\sqrt{Z_{0n}}} - \sqrt{Z_{0n}}\, I_n\right) \ . \tag{2.42}$$

It is possible now to define S parameters depending on these variables as follows:

$$\begin{aligned} S_{11} &= \left.\frac{b_1}{a_1}\right|_{a_2=0} \qquad S_{12} = \left.\frac{b_1}{a_2}\right|_{a_1=0} \\ S_{21} &= \left.\frac{b_2}{a_1}\right|_{a_2=0} \qquad S_{22} = \left.\frac{b_2}{a_2}\right|_{a_1=0} \end{aligned} \ . \tag{2.43}$$

In matrix form, Eq. 2.43 becomes:

$$\begin{bmatrix} b_1 \\ b_2 \end{bmatrix} = \begin{bmatrix} S_{11} & S_{12} \\ S_{21} & S_{22} \end{bmatrix} \begin{bmatrix} a_1 \\ a_2 \end{bmatrix} \ . \tag{2.44}$$

The matrix containing the S-parameters is called the scattering matrix or simply the S-matrix. In this case, S_{11} and S_{22} are reflection coefficients, while S_{12} and S_{21} are

transmission coefficients. Some useful parameters related to them are the return and insertion losses, defined respectively as:

$$L_A = -20\log|S_{mn}|\,dB \quad m,n = 1,2 \ (m \neq n) \tag{2.45}$$

$$L_R = -20\log|S_{mm}|\,dB \quad m = 1,2\ . \tag{2.46}$$

S-parameters have interesting properties that makes them quite useful for network analysis. Reciprocal networks have $S_{12} = S_{21}$. If the network holds physical symmetry, $S_{11} = S_{22}$. In addition, for loss-free networks, transmitted and reflected power must equal incident power, which for S-parameters resumes in:

$$\begin{aligned} |S_{21}|^2 + |S_{11}|^2 &= 1 \\ |S_{12}|^2 + |S_{22}|^2 &= 1 \end{aligned} \ . \tag{2.47}$$

These parameters are complex quantities, i.e. $S_{mn} = |S_{mn}|e^{j\phi_{mn}}$. Measurement of phase between input and output quantities presents a greater difficulty than measurement of magnitude and phase of an input impedance or a reflection coefficient. For that reason, the measure has to be accomplished by modern vector network analyzers.

All these definitions also hold for multiport networks (i.e., networks with more than two ports, as the Turnstile junction or the OMT studied in next chapters). Generally, for M-port networks:

$$\begin{bmatrix} b_1 \\ b_2 \\ \vdots \\ b_M \end{bmatrix} = \begin{bmatrix} S_{11} & S_{12} & \cdots & S_{1M} \\ S_{21} & S_{22} & \cdots & S_{2M} \\ \vdots & \vdots & & \vdots \\ S_{M1} & S_{M2} & \cdots & S_{MM} \end{bmatrix} \begin{bmatrix} a_1 \\ a_2 \\ \vdots \\ a_M \end{bmatrix} \ . \tag{2.48}$$

It is important to note that many modes may be present within a waveguide (either propagating or evanescent modes). Therefore, each one of them should be represented by a single electrical port, increasing the number of elements of the S-matrix with respect to the number of physical ports. When the S-matrix includes parameters relating evanescent modes, it is called Generalized Scattering Matrix. The classic properties of the S-matrix [Col01, Ch. 4] for circuits may not hold for the Generalized Scattering Matrix.

2.10 Polarization

The details of the following analysis can be found in [PC83]. The concept of polarization is related to the time variation of the electromagnetic field vectors at any point of the space. For a monochrome wave propagating in the $\hat{\boldsymbol{z}}$ direction:

$$\overline{\mathrm{E}}(\bar{r},t) = \mathrm{Re}\left[\left(\overline{\mathrm{E}}_\mathrm{r} + j\overline{\mathrm{E}}_\mathrm{i}\right)e^{j\omega t - \gamma z}\right] = e^{-\alpha z}\left[\overline{\mathrm{E}}_\mathrm{r}\cos(\omega t - \beta z) - \overline{\mathrm{E}}_\mathrm{i}\sin(\omega t - \beta z)\right] . \tag{2.49}$$

As $\overline{\mathrm{E}}_\mathrm{r}$ and $\overline{\mathrm{E}}_\mathrm{i}$ are not generally perpendicular to each other, it is not possible to determine an exact location for the end of the electric field vector. As the scalar product

$\overline{\mathrm{E}}_\mathrm{r} \cdot \overline{\mathrm{E}}_\mathrm{i} = 0$ is not always zero, $\overline{\mathrm{E}}_\mathrm{o} \cdot \overline{\mathrm{E}}_\mathrm{o}$ with $\overline{\mathrm{E}}_\mathrm{o} = \overline{\mathrm{E}}_\mathrm{r} + j\overline{\mathrm{E}}_\mathrm{i}$ is generally a complex scalar. Defining 2ψ as its argument:

$$\overline{\mathrm{E}}_\mathrm{o} \cdot \overline{\mathrm{E}}_\mathrm{o} = \left|\overline{\mathrm{E}}_\mathrm{o} \cdot \overline{\mathrm{E}}_\mathrm{o}\right| e^{j2\psi} = \overline{\mathrm{E}}_\mathrm{r} \cdot \overline{\mathrm{E}}_\mathrm{r} - \overline{\mathrm{E}}_\mathrm{i} \cdot \overline{\mathrm{E}}_\mathrm{i} + 2j\,\overline{\mathrm{E}}_\mathrm{r} \cdot \overline{\mathrm{E}}_\mathrm{i} \ , \tag{2.50}$$

$$\tan(2\psi) = \frac{2\overline{\mathrm{E}}_\mathrm{r} \cdot \overline{\mathrm{E}}_\mathrm{i}}{\overline{\mathrm{E}}_\mathrm{r} \cdot \overline{\mathrm{E}}_\mathrm{r} - \overline{\mathrm{E}}_\mathrm{i} \cdot \overline{\mathrm{E}}_\mathrm{i}} \ . \tag{2.51}$$

Now it is possible to obtain the desired geometric location by defining a new complex vector named $\vec{b}$ and defined by

$$\overline{b} = \overline{b}_1 + j\overline{b}_2 = \overline{\mathrm{E}}_\mathrm{o} e^{-j\psi} \tag{2.52}$$

with $\overline{b}_1$ and $\overline{b}_2$ real vectors. The product $\overline{b} \cdot \overline{b}$ now yields

$$\overline{b} \cdot \overline{b} = \overline{b}_1 \cdot \overline{b}_1 - \overline{b}_2 \cdot \overline{b}_2 + 2j\,\overline{b}_1 \cdot \overline{b}_2 = \overline{\mathrm{E}}_\mathrm{o} \cdot \overline{\mathrm{E}}_\mathrm{o}\ e^{-j2\psi} = \left|\overline{\mathrm{E}}_\mathrm{o} \cdot \overline{\mathrm{E}}_\mathrm{o}\right| = real \geq 0 \ , \tag{2.53}$$

and therefore $\overline{b}_1 \cdot \overline{b}_2 = 0$ and $\overline{b}_1 \cdot \overline{b}_1 \geq \overline{b}_2 \cdot \overline{b}_2$ which implies $\overline{b}_1$ and $\overline{b}_2$ being perpendicular vectors with $\left|\overline{b}_1\right| \geq \left|\overline{b}_2\right|$.

Now it is possible to express electric field depending on these two vectors as

$$\overline{\mathrm{E}}(\overline{r},t) = \mathrm{Re}\left[\left(\overline{b}_1 + j\overline{b}_2\right)e^{jwt - \gamma z + j\psi}\right] = \overline{b}_1 e^{-\alpha z}\cos(\omega t - \beta z + \psi) - \overline{b}_2 e^{-\alpha z}\sin(\omega t - \beta z + \psi) \ , \tag{2.54}$$

$$\overline{b}_1 = \overline{\mathrm{E}}_\mathrm{r}\cos\psi + \overline{\mathrm{E}}_\mathrm{i}\sin\psi \ , \tag{2.55}$$

$$\overline{b}_2 = -\overline{\mathrm{E}}_\mathrm{r}\sin\psi + \overline{\mathrm{E}}_\mathrm{i}\cos\psi \ , \tag{2.56}$$

with a new coordinate system defined by *x'* and *y'* as in Fig. 2.25:

$$\overline{\mathrm{E}}(\overline{r},t) = \overline{\mathrm{E}}_{\mathrm{x}'}(\overline{r},t)\hat{\mathrm{x}}' + \overline{\mathrm{E}}_{\mathrm{y}'}(\overline{r},t)\hat{\mathrm{y}}' \ , \tag{2.57}$$

$$\overline{\mathrm{E}}_{\mathrm{x}'}(\overline{r},t) = \left|\overline{b}_1\right| e^{-\alpha z}\cos(wt - \beta z + \psi) \ , \tag{2.58}$$

$$\overline{\mathrm{E}}_{\mathrm{y}'}(\overline{r},t) = -\left|\overline{b}_2\right| e^{-\alpha z}\sin(wt - \beta z + \psi) \ , \tag{2.59}$$

Rearranging from above expressions yields,

$$\left(\frac{\overline{\mathrm{E}}_{\mathrm{x}'}(\overline{r},t)}{\left|\overline{b}_1\right| e^{-\alpha z}}\right)^2 + \left(\frac{\overline{\mathrm{E}}_{\mathrm{y}'}(\overline{r},t)}{\left|\overline{b}_2\right| e^{-\alpha z}}\right)^2 = 1 \ , \tag{2.60}$$

which is the equation for an ellipse. That means the end of the electric vector of a monochromatic wave generally describes an ellipse in time with axis *x'* and *y'*. As $\left|\overline{b}_1\right| \geq \left|\overline{b}_2\right|$, $\left|\overline{b}_1\right| e^{-\alpha z}$ corresponds to the semi major axis and $\left|\overline{b}_2\right| e^{-\alpha z}$ to the semi minor axis.

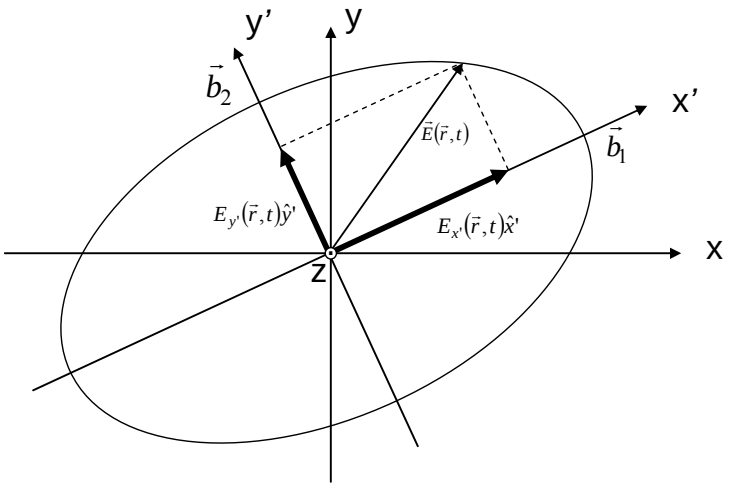

Fig. 2.25. Coordinate system for the polarization section.

Though an ellipse is the general state of the polarization for a monochromatic wave, it is possible to find some variations depending on the properties of both $\bar{b}_1$ and $\bar{b}_2$:

- If $|\bar{b}_1| = |\bar{b}_2|$ the ellipse degenerates into a circumference of radius $|\bar{b}_1|e^{-\alpha z} = |\bar{b}_2|e^{-\alpha z}$, and the wave is said to be "circularly polarized".
- If $\bar{b}_2 = 0$ (note $\bar{b}_1$ can not be zero because of the $|\bar{b}_1| \geq |\bar{b}_2|$ property), the ellipse degenerates into a segment of constant direction, and the wave is said to be "linearly polarized".

2.11 Conclusions

Some basic notions of electromagnetic theory and waveguides analysis have been presented in this chapter. They will be very useful to understand the upcoming chapters.

The analysis has been focused on rectangular and circular waveguides, as they will be used in the design of the OMT. It should be noted that these are not the only types of waveguides, as there are also ridged or elliptical waveguides, for example, but they will not be treated during the design of the OMT presented in this document.

Chapter 3 will represent a first contact with the OMTs. A short definition will be presented and then the reader will be introduced to the different types of OMTs that can be found on the literature.

Chapter 3

OMTs Introduction and Survey of Different Configurations

Orthomode Transducers (OMTs) are passive microwave devices with three physical ports: a common port linked to the antenna (for instance a horn) and two single-mode ports. They act as polarization discriminators in many applications. In receivers, they separate the incoming dual-polarized signal at the common port into two single signals at the output channels. In transmitters, they combine the two signals fed at the single-mode ports into two orthogonally polarized signals at the common port. Therefore, the signals with different polarization remain uncoupled (at least that is the goal of ideal OMTs), and the information carried by those signals can be discriminated. The block diagram of a typical OMT is represented in Fig. 3.1.

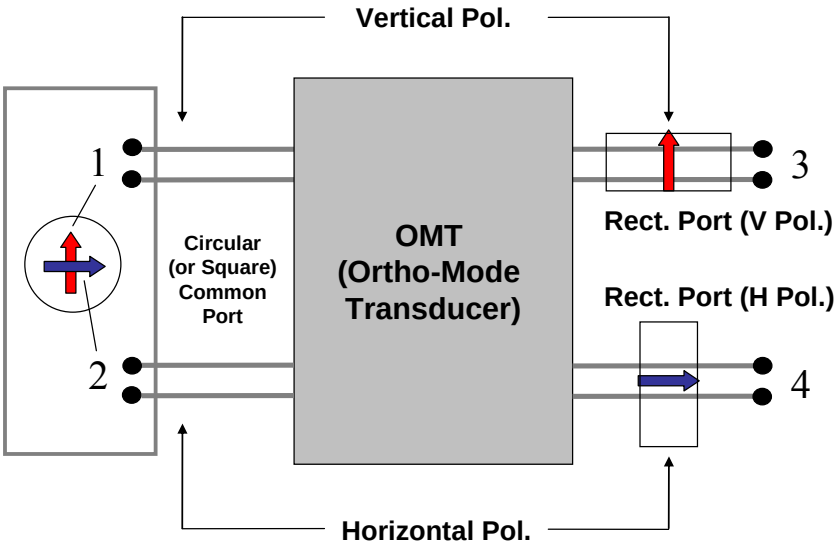

Fig. 3.1. Block diagram of a typical OMT.

Satellite telecommunications and radio astronomy are typical environments where OMTs are found. In radio astronomy, the frequency range can span even to hundred of GHz. In telecommunication, the growing bandwidth demand has originated the need of a more efficient use of the available spectrum. OMTs double the number of channels that can be served in a given frequency range (different signals can be transmitted/received in the same frequency range, as long as they use orthogonal polarizations), so the problem is partially alleviated. OMTs for telecommunication systems are usually found in satellite applications, in a range typically from 1 GHz up to 30 Ghz. A typical scenario can be seen in Fig. 1.1, where the telecommunication system has been designed to operate over two frequency bands. The incoming dual-polarized signal reaches the OMT, which discriminates between both polarizations (vertical and horizontal) and then subsequent diplexers discriminate between both frequency bands. Therefore, the overall system will be serving four independent signals.

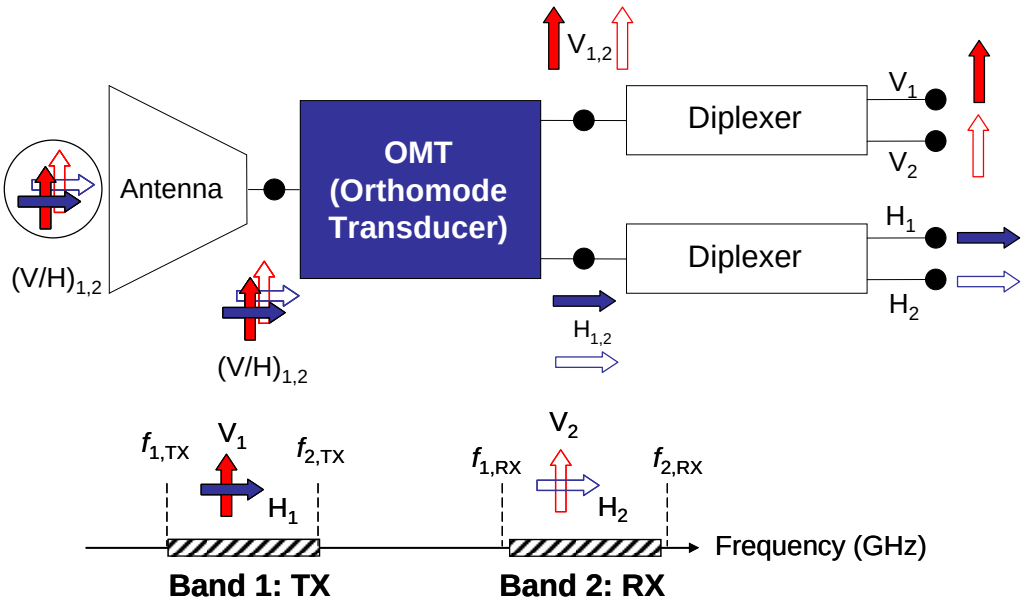

Fig. 3.2. Location of the OMT in a typical RF feed chain system operating over two frequency bands.

In comparison with OMTs for communication systems, radio astronomy applications generally need less stringent specifications in terms of insertion and return losses and isolations. On the other hand, in radio astronomy, the OMTs are designed to operate in a full-wideband, not in two small sub-bands with wide separation (as in Fig. 3.2). The goal of radio astronomy OMTs is to detect the polarization state of incoming signals from background space radiation in order to extract relevant information about fundamental cosmological parameters. Again, OMTs provide a solution for this application avoiding the presence of two different antennas to detect both polarizations separately.

Physically, an OMT is a three-port device. As said before, it has a common port and two single-mode ports dedicated to the fundamental mode of the waveguide. Electrically, it is not a three-port but a four-port device, as two modes incide at the common port, one for each polarization. From now on, these modes at the common port will be labeled as port 1 for the vertical polarization and port 2 for the horizontal one. Ports allocated for the vertical and horizontal polarizations will be port 3 and port 4, respectively. As many other waveguide structures, OMTs are completely characterized by means of its scattering matrix, which for an ideal OMT is given by the following expression with α and β real constants:

$$\mathbf{S} = \begin{bmatrix} 0 & 0 & e^{j\alpha} & 0 \\ 0 & 0 & 0 & e^{j\beta} \\ e^{j\alpha} & 0 & 0 & 0 \\ 0 & e^{j\beta} & 0 & 0 \end{bmatrix}, \tag{3.1}$$

As it can be seen, all the power that reaches port 3 comes from port 1. That means no power would ideally been transfered to the other single-mode port. It is the same for ports 4 and 2 since the device is reciprocal. The design of these structures requires good comprehension of those concepts that have been described in Ch. 2 (e.g. higher-order mode generation, mode symmetry, symmetry planes…).

One of the main handicaps designing OMTs is that this type of structures are not widely dealt with on the literature. Bøifot *et al.* first presented an inventory of different OMTs in [BLS90], although more configurations have been proposed after that work. They classified OMTs into a) simple narrowband OMTs and those based on b) Bøifot or c) Turnstile junctions that will be described later in this document. In [Bøi91], Bøifot classifies them into five main groups: four groups containing OMTs based on waveguide-to-waveguide transitions and a fifth one based on OMTs with waveguide-to-coax transitions. Later, in [UBR93] Uher *et al.* classified them in three main groups: narrowband, wideband and multiband OMTs, with the latter representing combiners made up of OMTs, multiplexers and other structures. A great source of figures and explanations of several architectures is found there. It also refers to the Turnstile junction, although it specifically does not give design methods.

This lack of information concerning OMTs has motivated this section, which consists of a survey of different architectures for the OMT with examples of designs. Some of them have already been manufactured and are found in books and technical papers. The section begins with some narrowband designs followed by those involving more complex structures as the Bøifot or Turnstile junctions mentioned above.

3.1 Narrowband OMTs

These structures represent the easiest way for polarization diplexing. They are widely used in commercial communications systems that require high performance over a narrow band covering usually less than a 10% fractional bandwidth (although some designs can be close to 30%). As it will be seen in the next subsections, these structures hold only one (or even none) symmetry planes, which reduces their theoretical fractional bandwidth to a maximum 34.3% for those using a square common waveguide (generation of TE_{11}/TM_{11} higher-order modes) and 26.6% for those using a circular common waveguide instead (generation of TM_{01} higher-order mode). However, their low physical complexity is an advantage for mass production. An interesting collection of narrowband OMTs can be found in [UBR93]. This section mainly describes these OMTs with some examples from other documents.

3.1.1 Taper/Branching OMT

Fig. 3.3 shows different narrowband designs of this type. They present a longitudinal taper or transition between the circular or square waveguide to the standard rectangular waveguide allocated for one of the polarizations, usually called the axial or vertical polarization. A waveguide branching is placed perpendicular to the longitudinal axis with its broad dimension alligned to the taper axis. Where to place this branching waveguide is a matter of critical importance. There is a particular plane, perpendicular to the propagation direction from which the TE_{01} mode becomes evanescent. As it can be seen in Fig. 3.3, an inductive iris is placed centered at this specific point reducing rectangular aperture and improving matching properties for this path of the OMT.

The analysis of the modes coupled by the two orthogonal modes at the common port is done as follows: as the TE_{10} travels through the guide, only modes with a PMW at the *yz*-plane (vertical plane) are excited. These modes are under cutoff regarding the branching waveguide (the TE_{10} fundamental mode of this waveguide is not excited), so they can only be reflected back to the common port or coupled to the TE_{10} mode

towards its allocated port. This is essentially the same for the TE_{01} but now only modes with a PEW at the *yz*-plane are excited. That includes the TE_{10} fundamental mode of the branching waveguide which allows power coupling between ports 2 and 4 (see Fig. 3.5). Fig. 3.6 shows two designs from [Enc05] referred as sidearm-coupled OMTs. They are basic configurations of these type of OMTs and they only differ in their H or E-plane based coupling properties.

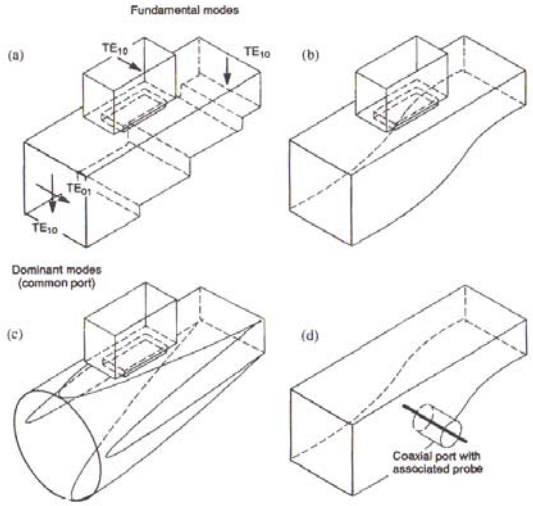

Fig. 3.3. Narrowband taper/branching OMT designs. Images from [UBR93].

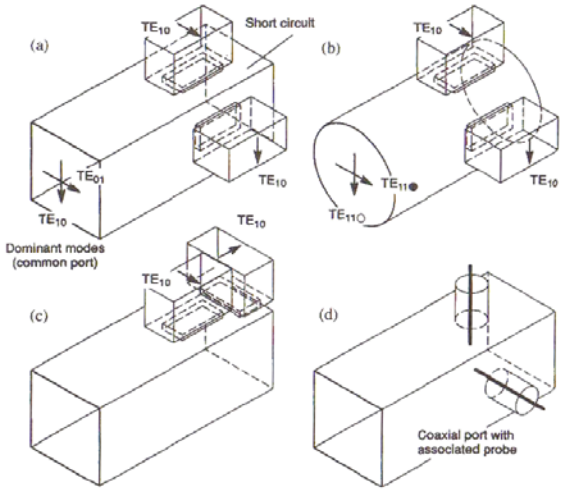

Fig. 3.4. Narrowband OMT designs with short circuited common waveguide. Images from [UBR93].

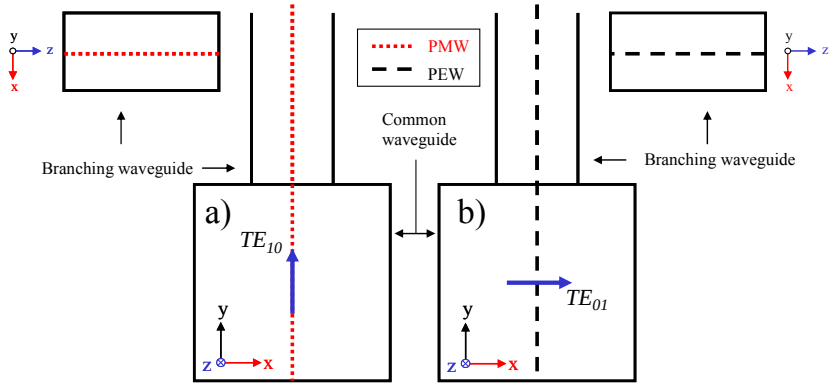

Fig. 3.5. Symmetry properties for the modes excited at the branching waveguide a) vertical polarization; b) horizontal polarization.

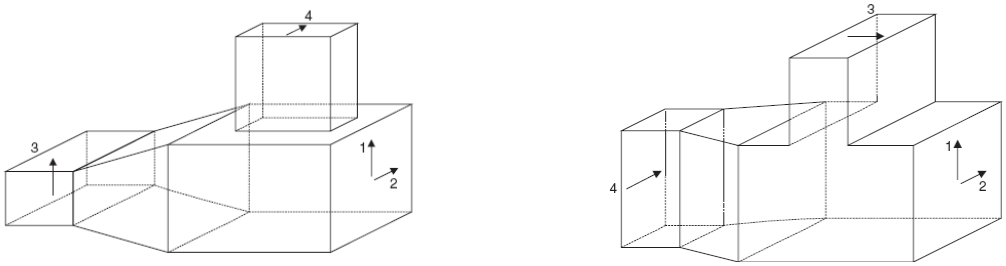

Fig. 3.6. H-plane and E-plane sidearm-coupled OMT: basic configuration. Image from [Enc05].

3.1.2 Short Circuited Common Waveguide OMT

Another option is to use a short circuited common waveguide, as it is shown in Fig. 3.4. In this case both rectangular branching waveguides must be placed at a fixed distance from the short circuit plane, determined by

$$l_{1,2} = \frac{\lambda_{g1,2}}{4}, \tag{3.2}$$

with $\lambda_{g1,2}$ representing the common waveguide wavelength of each of the fundamental modes at the center frequency of the operating band (f_0). That implies there could be different locations for each of the branchings if the common waveguide were not a square one. In Fig. 3.4-a and Fig. 3.4-b, single signal ports are situated at perpendicular side walls, while in Fig. 3.4-c they are located at the same wall. For this latter case, one of the ports is placed right at the short circuit while the other one follows the rule stated at the beginning of this paragraph. These ports have a perpendicular alignment of their cross sections.

3.1.3 Septum/Branching OMT

Another way to separate the two polarizations is to include a septum region into a waveguide of constant cross section (see Fig. 3.8). The branching region must be placed this time right after this section or partially overlapping it, again with its broad dimension alligned to the common waveguide axis. The TE_{01} of the common port becomes evanescent within this region as the septum divides it into two rectangular sections which are seen by this mode as two half height waveguides. The septum region should be long enough to achieve at least a 50 dB rejection for the TE_{01} mode.

This design can be improved in terms of matching by using a shaped septum (Fig. 3.8-b) and with a capacitive discontinuity at the wall facing the branching waveguide (Fig. 3.8-d). The transition between the common circular or rectangular waveguide to the standard waveguide for the TE_{10} can be obtained with a taper or a stepped transformer as in Sec. 3.1.1, or by using the septum section twice. In that case, the second section acts as an H-plane bend for the TE_{10} (Fig. 3.8-e).

The design from [RMR06] sketched in Fig. 3.7 introduces a second septum which enhances the performance of the OMT in two interrelated aspects: first, it contributes to reduce the size of the axial branch of the OMT preventing the power transfer between horizontal modes at the axial and common ports; second, it facilitates the matching of the horizontal polarization between the lateral and common ports. This double-septum configuration results in a very compact design.

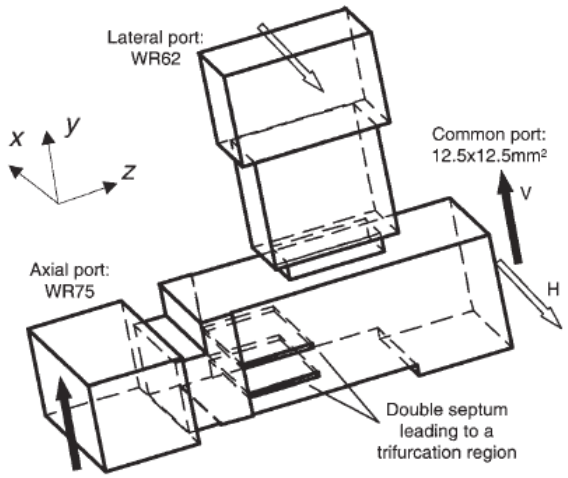

Fig. 3.7. Narrowband OMT with double-septum configuration. Image from [RMR06].

3.1.4 Acute Angle or Longitudinal OMT Branching

Fig. 3.9 shows another type of narrow band OMTs. Two branches with generally equal cross sections ramify under an acute angle from the common waveguide. Each of this branches are allocated to one of the polarizations, thus they are equipped with the necessary septum to make the other one evanescent within its region.

As it happened with the previous type of OMT, a taper or a stepped transformer follows the septum to obtain the standard interface for each mode. This separation technique can be made longitudinally, as it is shown in Fig. 3.9-c.

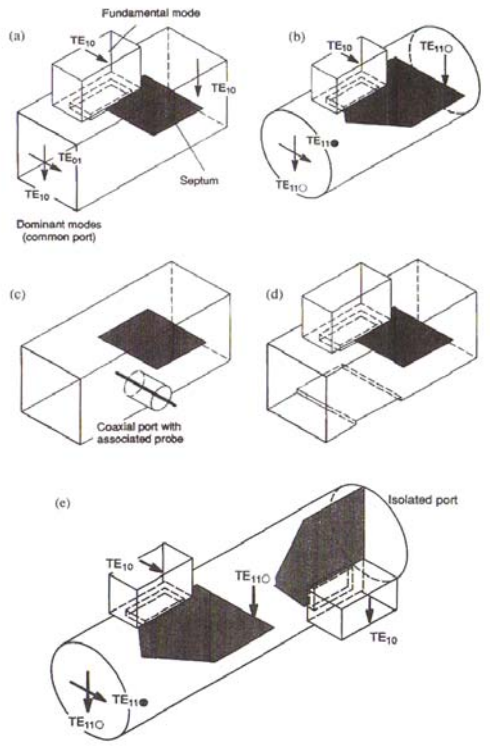

Fig. 3.8. Narrowband septum/branching OMT designs. Images from [UBR93].

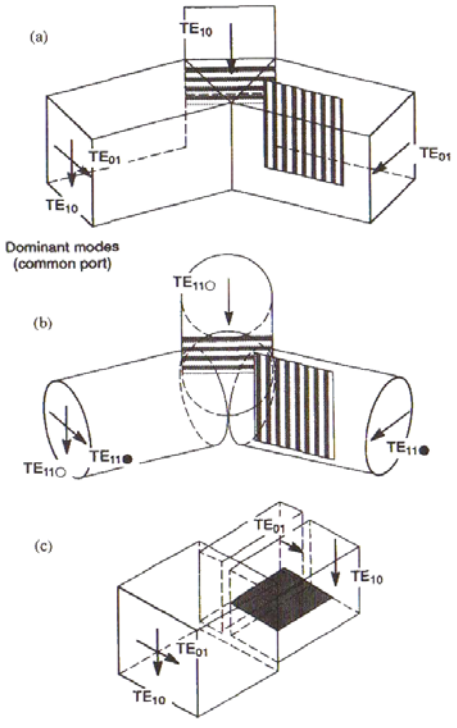

Fig. 3.9. Narrowband OMT designs: acute angle branching (a) and (b); longitudinal branching (c). Images from [UBR93].

3.2 Wideband OMTs

For wideband performance it is necessary to include in the OMT an in-nature broadband structure. Their symmetry properties or energy confination method grant an appropiate treatment of unwanted higher-order modes and, thus, increasing single-mode bandwidth. Four examples are presented in this section: the Bøifot junction, the Turnstile junction, the finline OMT and the Quad-Ridged OMT.

3.2.1 Bøifot junction

This architecture sketched in Fig. 3.10 and Fig. 3.11 was first presented in [BLS90] by Bøifot *et al*. Some examples of OMTs based on this junction can be found in [RMR06], [WGK02] or [BLV05]. See Fig. 3.11 for the port numbers relation that will be followed in this subsection. The dual-polarized signal at the common port (1,2) is split into four single signals (ports 4a and 4b for the horizontal polarization and ports 3a and 3b for the vertical one). Each of these four signals carry half the power of the polarized wave (vertical or horizontal), respectively, if the junction is properly designed. A thin septum is necessary in order to achieve a good performance, as it favours wave splitting and overall matching. The design of this septum is the main drawback of this architecture because of its complexity. It is usual to add one or two metallic posts at both side arms, to help improve matching at some frequencies. Manufacturing these septums and posts at high frequencies (i.e., hundreds of GHz) is quite critical, as they become too small and mechanically unstable. That is the reason for some modified designs as in [BVL05], where the posts are removed, the septum is a little bit thicker and matching is achieved by using a pair of symmetrical E-plane steps at ports 3a and 3b as it can be seen in Fig. 3.12.

The whole OMT also implies signal recombination. Signals at ports 3a and 3b are always combined after the septum, so these ports are generally treated as a unique "through port" and the Bøifot junction is often electrically described as a 5 port structure. Signals at both side arms (4a, 4b) can be recombined by means of E or H-plane bends. By using the first ones, full symmetry over two planes is achieved but the recombination must be carried out behind the through port, which should be prolonged by an E-plane, as in Fig. 3.15 and Fig. 3.16. This method avoids the excitation of the first unwanted higher-order modes TE_{11} / TM_{11} increasing single-mode bandwidth. H-plane bends may reduce overall size, but keeping just one plane of symmetry (Fig. 3.13 and Fig. 3.14) and allowing the excitation of more higher-order modes than the previous option which could degrade overall performance.

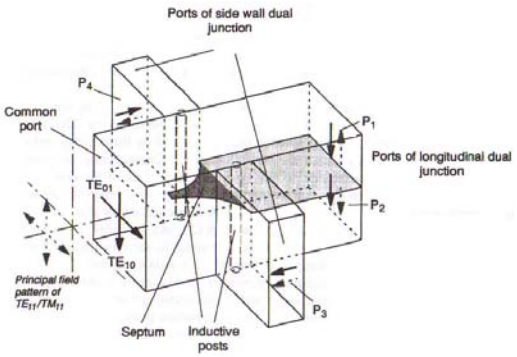

Fig. 3.10. Bøifot junction. Image from [UBR93].

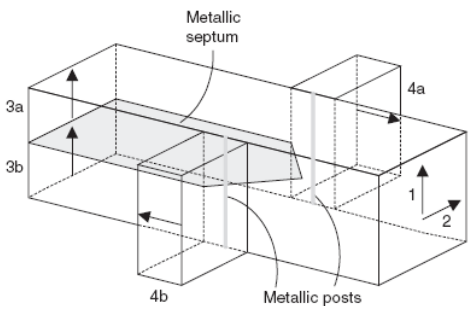

Fig. 3.11. Bøifot junction. Image from [Enc05].

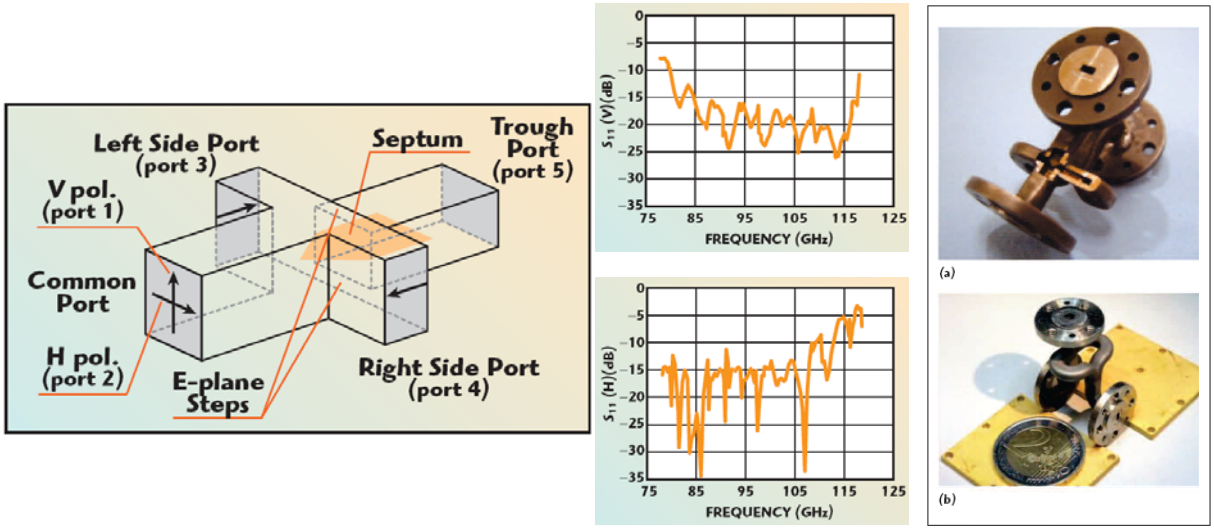

Fig. 3.12. Modified Bøifot junction with E-plane steps at the septum region and complete OMT. Images and results from [BVL05].

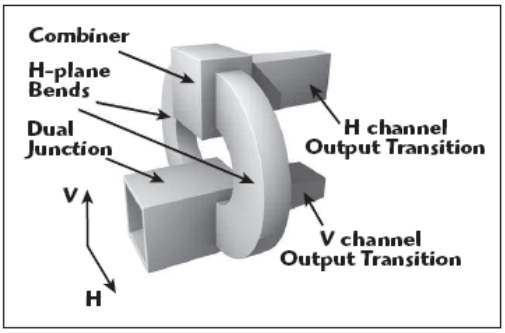

Fig. 3.13. Description of a Bøifot junction based OMT with H-plane recombination. Image from [BVL05].

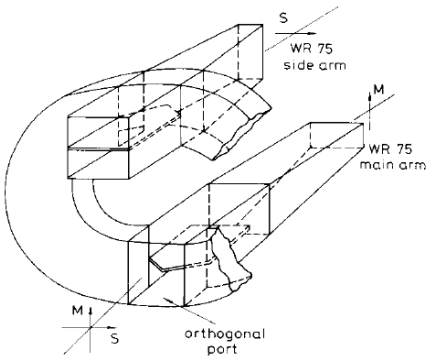

Fig. 3.14. Description of a Bøifot junction based OMT with H-plane recombination. Image from [Bra78].

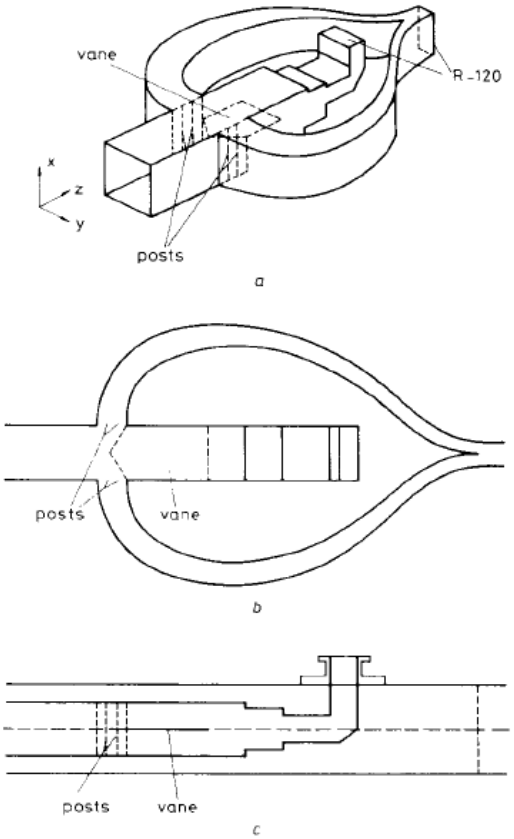

Fig. 3.15. Views of a Bøifot junction based OMT with E-plane recombination: a) perspective b) *yz*-cut c) *xz*-cut. Images from [BLS90].

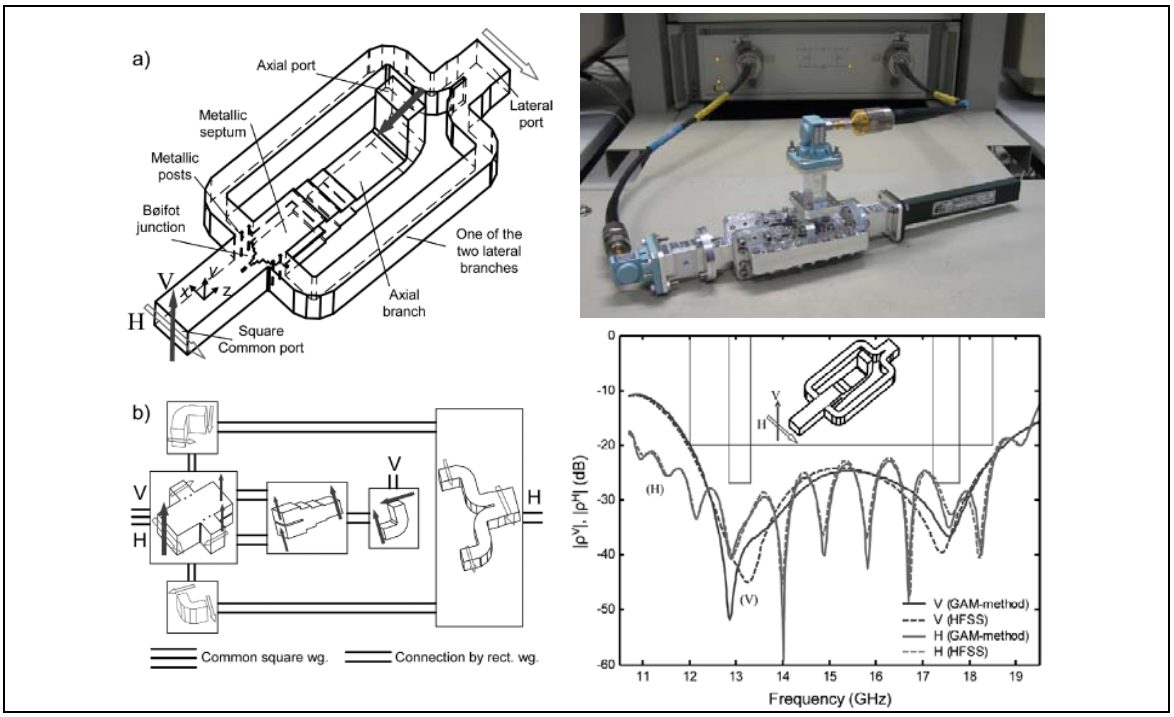

Fig. 3.16. Bøifot junction based OMT. Images and results from [RMR06]. Prototype image with the setup for measuring the vertical polarization courtesy of EADS-CASA.

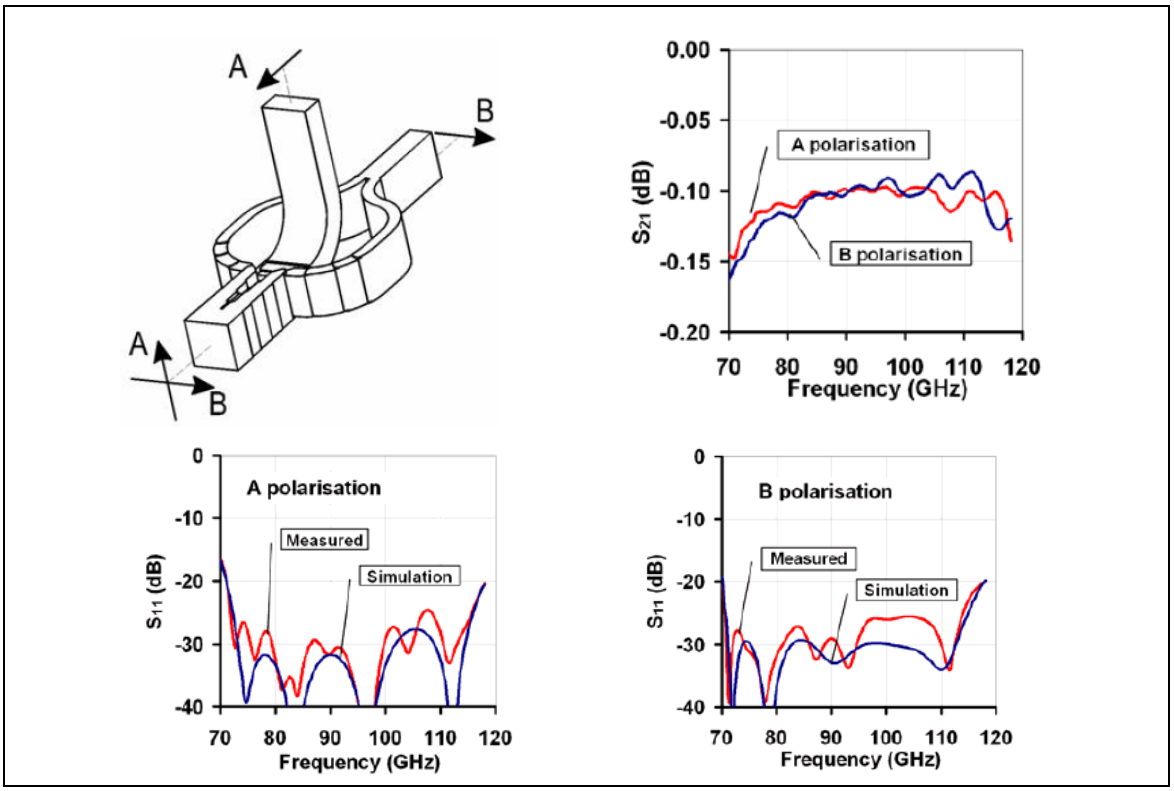

Fig. 3.17. Bøifot junction based OMT with a square to double-ridged transition at the common port. Images and results from [MBD06].

Other Bøifot-based designs use a square to double-ridged transition at the common port instead of the septum-posts option. Fig. 3.17 shows an example of these designs from [MBD06]. The use of a double-ridged waveguide allows a direct transition to the rectangular waveguide which eliminates the necessity of posts or irises at the rectangular side branches.

The twofold symmetry of the Bøifot junction avoids the generation of the TE_{11}/TM_{11} and TE_{20}/TE_{02} modes at the square common waveguide. The first higher-order modes that are excited in this structure are the $TE_{12}/TM_{12}/TE_{21}/TM_{21}$, which represents a 76.4% theoretical fractional bandwidth for the OMTs based on this junction.

3.2.2 Turnstile junction

The Turnstile junction will be deeply treated in Ch. 6. The main difference with the Boifot junction lies in its identical behaviour for both polarizations, which provides a fourfold symmetry. Neither septum nor posts are required to achieve good performance over a wide band. An internal obstacle in the wall that faces the common guide helps wave splitting and matching for broadband performance. It is widely treated in [MDP65] and some interesting applications are discussed in [MG55]. Below are some examples of actual designs which make use of this junction, with computed and measured data. They essentially differ in the way of recombining the signals separated by the Turnstile and the shape of the internal matching obstacle. Figs 3.18-3.21 show some examples of these structures.

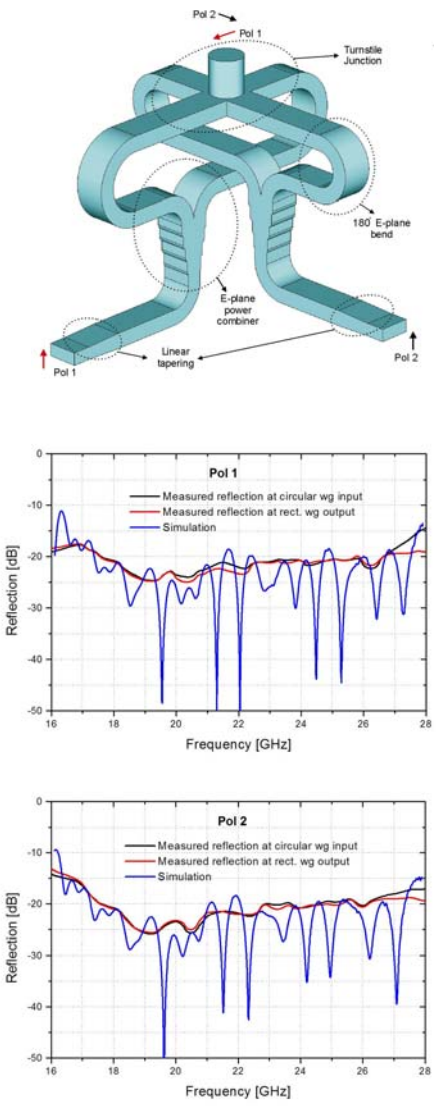

Fig. 3.18. Turnstile junction based OMT. Images and results from [NP06].

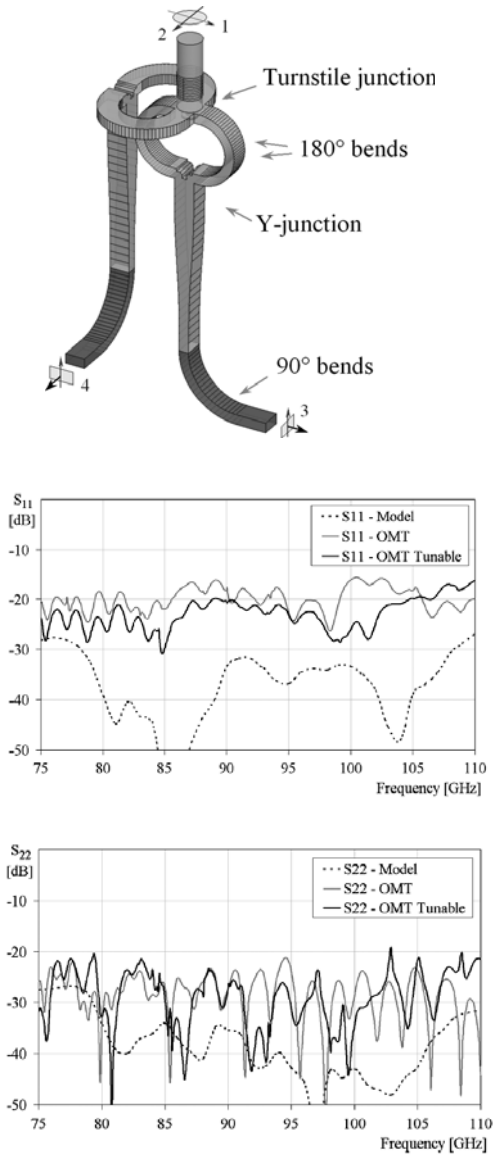

Fig. 3.19. Turnstile junction based OMT. Images and results from [PPI07].

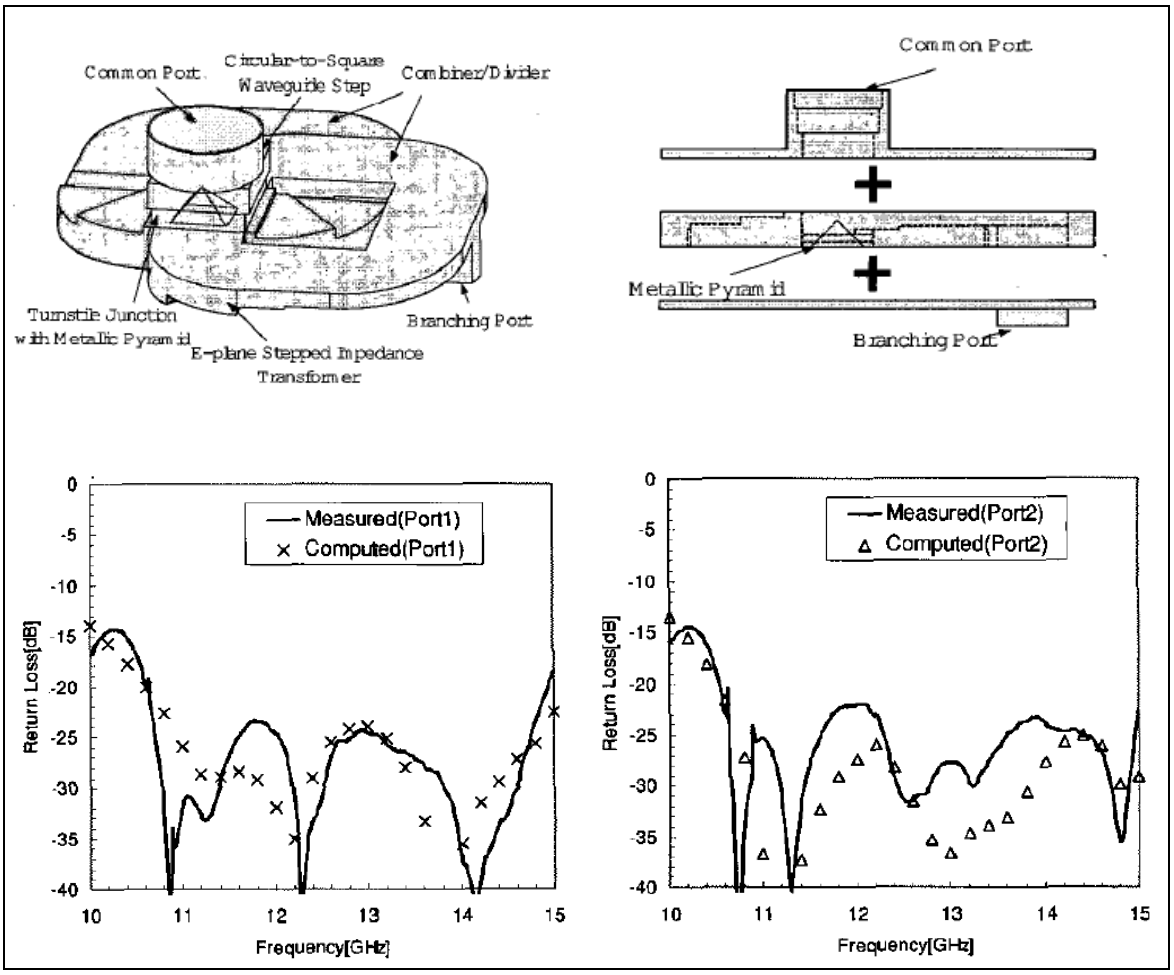

Fig. 3.20. Turnstile junction based OMT. Images and results from [AYM03].

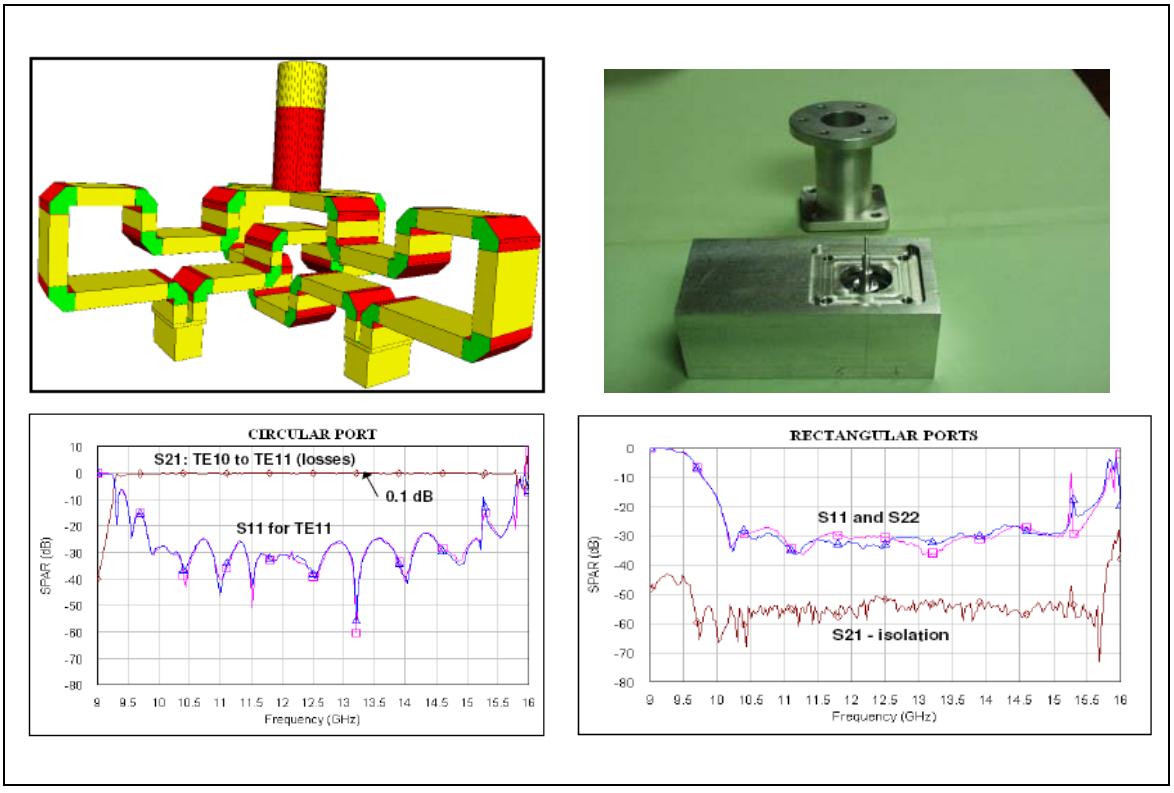

Fig. 3.21. Turnstile junction based OMT. Images and results from [TMF08].

Similarly to what happened with the Bøifot junction, if the Turnstile junction is designed with a square common waveguide, its fourfold symmetry avoids the generation of the TE_{11}/TM_{11} and TE_{20}/TE_{02} square modes, which represents a 76.4% theoretical fractional bandwidth. In case the Turnstile junction is designed with a circular common waveguide, the first higher-order mode excited is the TM_{11}, leading to a 70.17% theoretical fractional bandwidth.

3.2.3 Finline OMT

The finline OMT concepts were first presented by Robertson in [Rob56]. Later, Skinner *et al*. [SJ91] applied these concepts towards the development of a wideband OMT with good performance over the *X*-band (8.2-12.4 GHz).

Basically, the finline OMT consists of a square or circular waveguide with two diametrically opposite thin tapered metallic fins inside. These fins confine the electric energy of the TE_{01} mode to the gap between them and remove it from the waveguide by a bend which is normally of 90º. On the other hand, the TE_{10} passes through the waveguide the same way it was described for the septum/branching OMTs or the Bøifot junction based ones.

See Fig. 3.22 for the relations between signals and port numbers. They are the same that were stated for the narrowband OMTs in Sec. 3.1.1 and so is the higher-order modes analysis. The TE_{10} mode finds a discontinuity which has symmetry at the horizontal plane. Therefore, only modes with a PEW at the vertical plane (i.e. rows 2 and 3 from Table 2.3) will be excited at the branching waveguide (port 4). The TE_{10} fundamental mode of this branching waveguide is not included there, so no propagating modes are excited in port 4 for this case. The TE_{01} mode sees an E-plane bend so only modes with a PMW at the vertical plane (i.e. rows 1 and 4 from Table 2.3) are excited which includes the fundamental mode of the branching waveguide. The finline waveguide is broadband in nature but a resistive card placed at the end of the fins and parallel to them is necessary to suppress these unwanted higher-order modes excited by the bend.

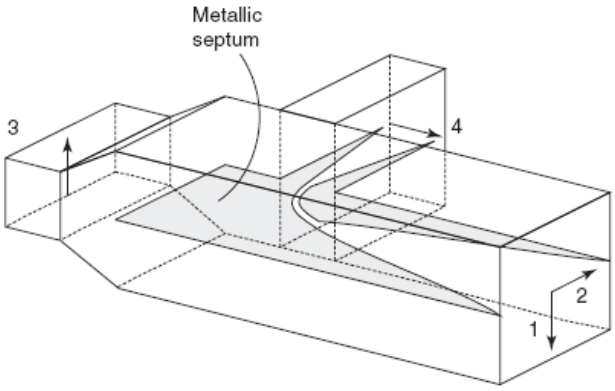

Fig. 3.22. Finline based OMT. Image from [Enc05].

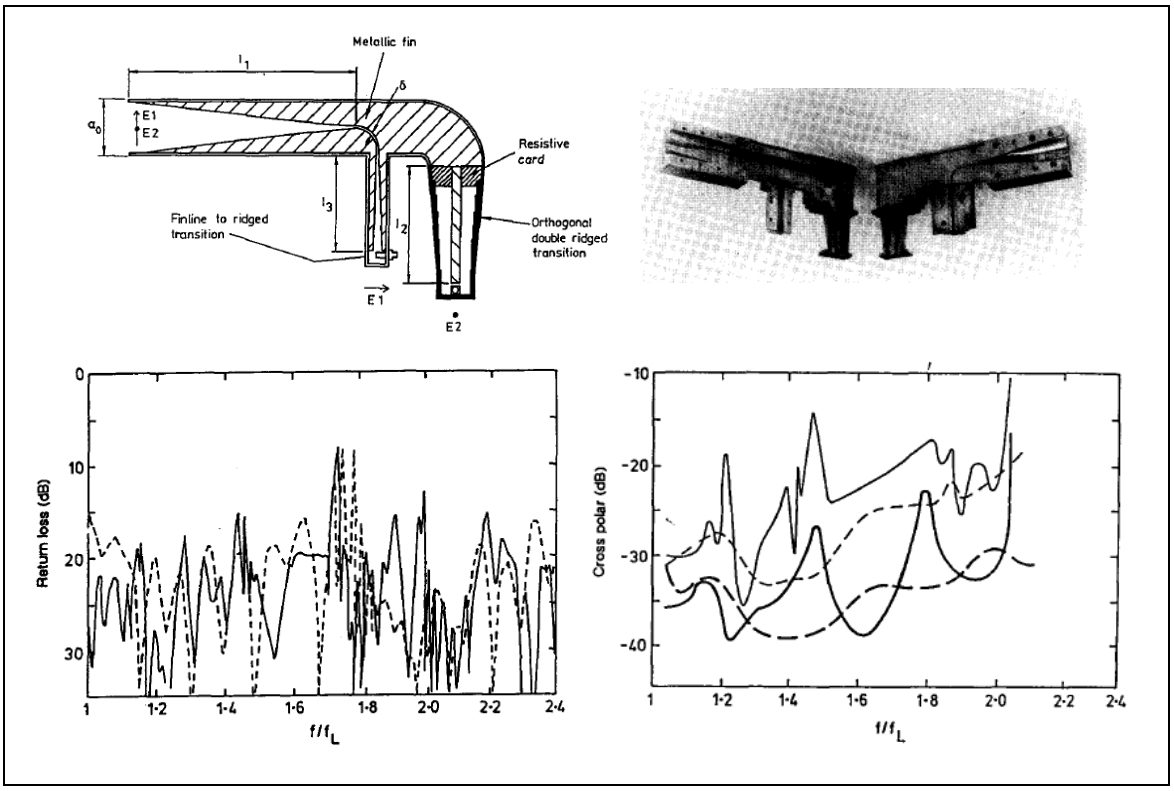

Fig. 3.23. Finline based OMT. Images and results from [SJ91].

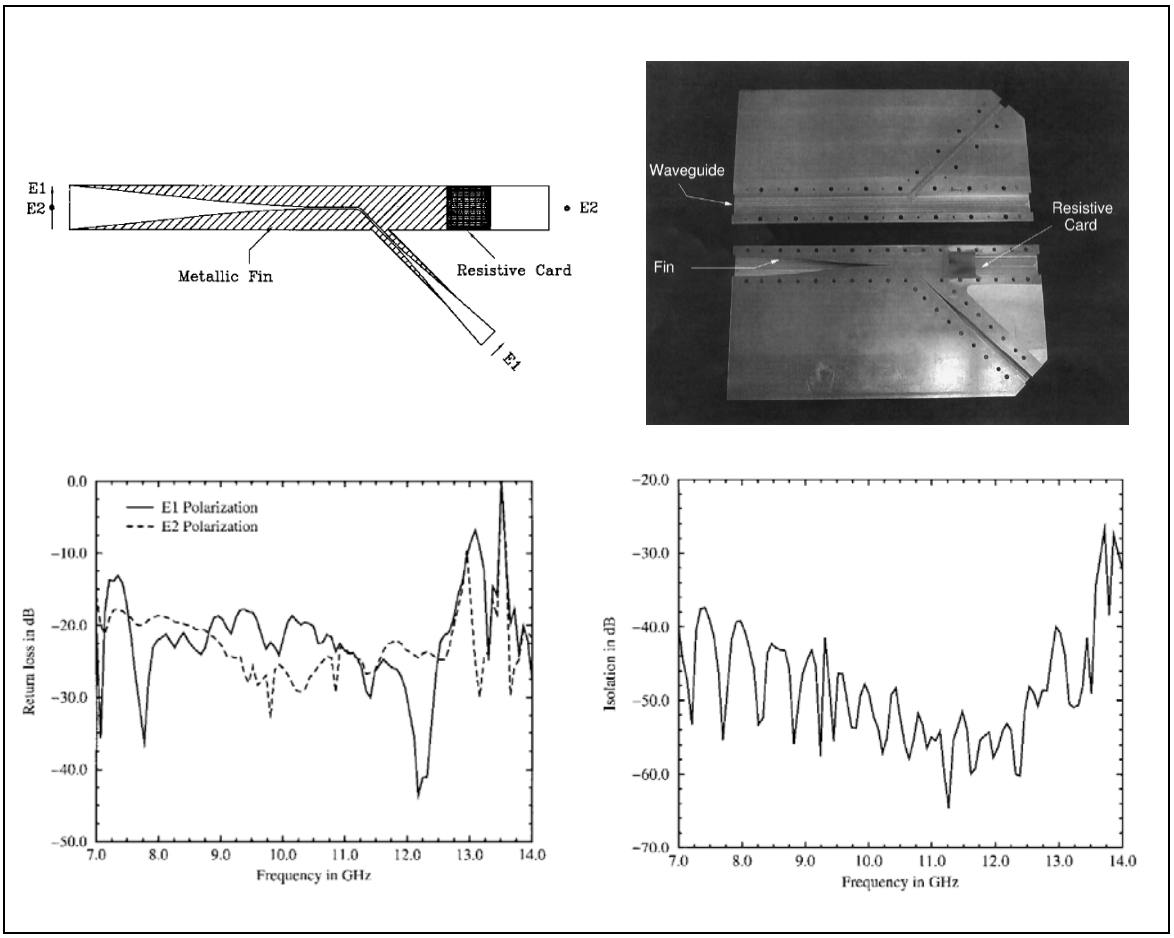

Fig. 3.24. Finline based OMT with 45º bend instead of the common 90º bend. Images and results from [CC99].

3.2.4 Double-Ridged OMT

The double-ridged OMT concentrates one of the polarizations between two ridges in the centre of a square waveguide and then removes its power by a coaxial line. The other polarization is not affected by these ridges and passes through a square-to-rectangular transition after which its power is extracted again with a coaxial line. An example of this OMT can be found in [Dun02] and it is shown in Fig. 3.25.

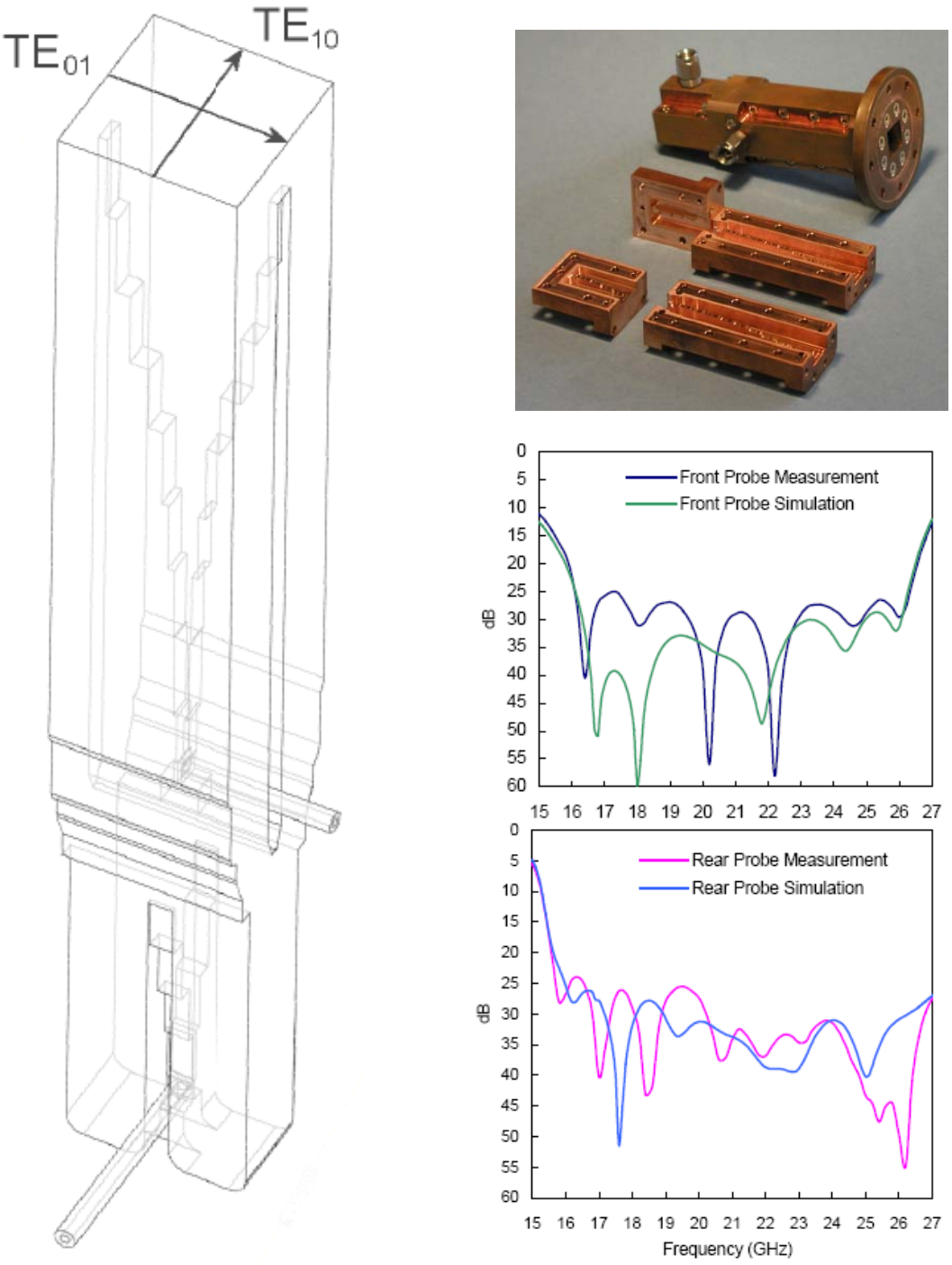

Fig. 3.25. Double-Ridged OMT. Images and results from [Dun02].

3.2.5 Quad-Ridged OMT

The Quad-Ridged OMT is a slight variation of the finline OMT. Now, two orthogonal pairs of finlines or ridges concentrate the field of both fundamental modes in the center of the guide. More information about ridged waveguides can be found in [RWV93], [Enc05], [Mar53] or [UBR93]. The ridges of these structures expand the single-mode bandwidth as they increase separation between the cutoff frequencies of the fundamental mode and the first higher-order modes.

Normally, two coaxial lines that pass through the center of the ridges extract the energy from the orthogonal fields. As it is stated in [SJ91], these designs have two main drawbacks: a) they require an efficient design of the transition from the circular to the quad-ridged waveguide and b) it is necessary an accurate matching of the coaxial probes over the working band.

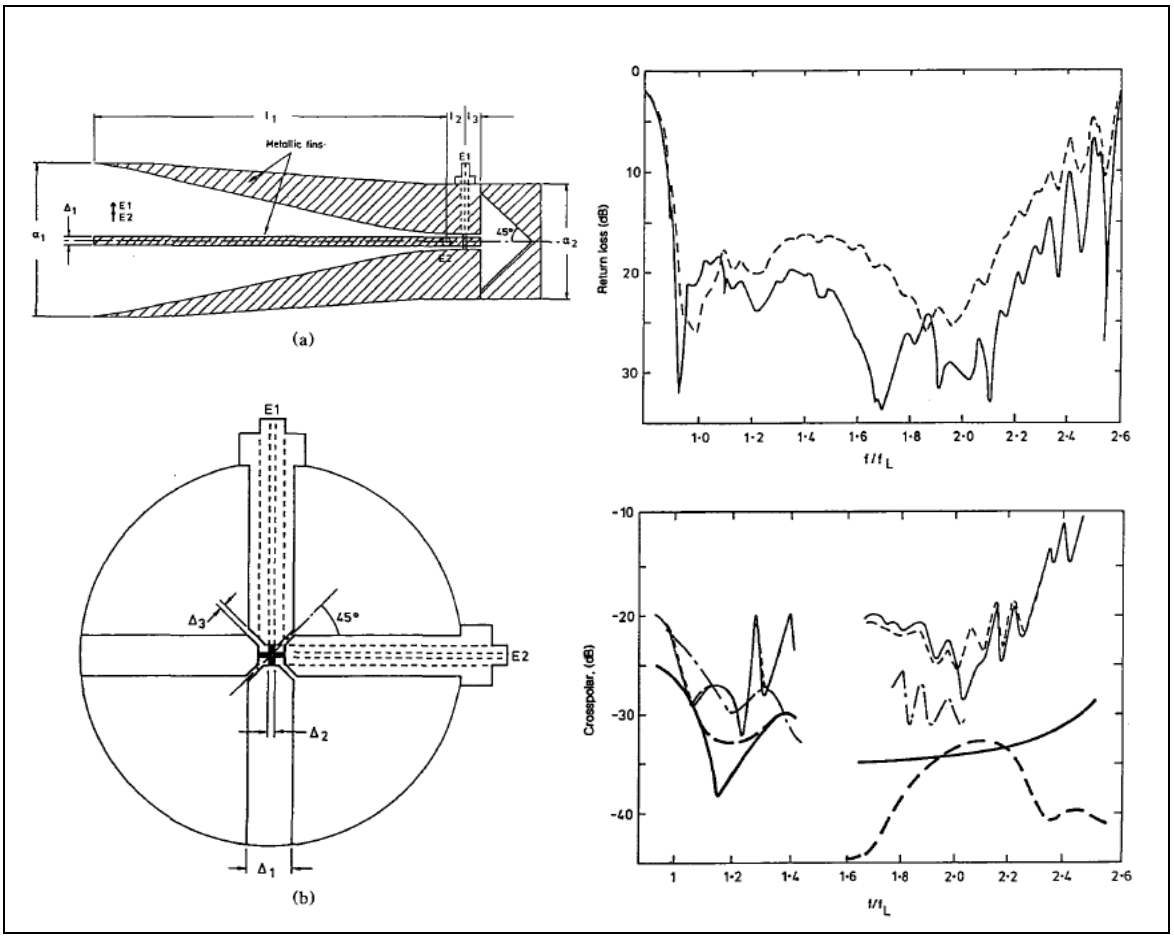

Fig. 3.26. Quad-Ridged OMT. Images and results from [SJ91].

3.2.6 OMT based on the Turnstile junction of this project.

Fig. 3.27 represents the segmentation of the specific OMT that will be designed for this project. It is based on the Turnstile junction, like the OMTs described in Sec. 3.2.2 and its main difference with these OMTs will lie in the design of the internal obstacle of the Turnstile junction and the recombining method for the side branches. This latter feature will be similar to that described in [PPI07] but using well-known routing structures widely used in microwave circuitry.

Ch. 4 will show the design cycle which has been followed through the design and optimization of all the structures that compose the whole OMT. The OMT elements will be presented in Ch. 5 (routing structures) and Ch. 6 (Turnstile junction). Later, Ch. 7 will be focused on the interconnection of all these parts in order to complete the design of two OMTs.

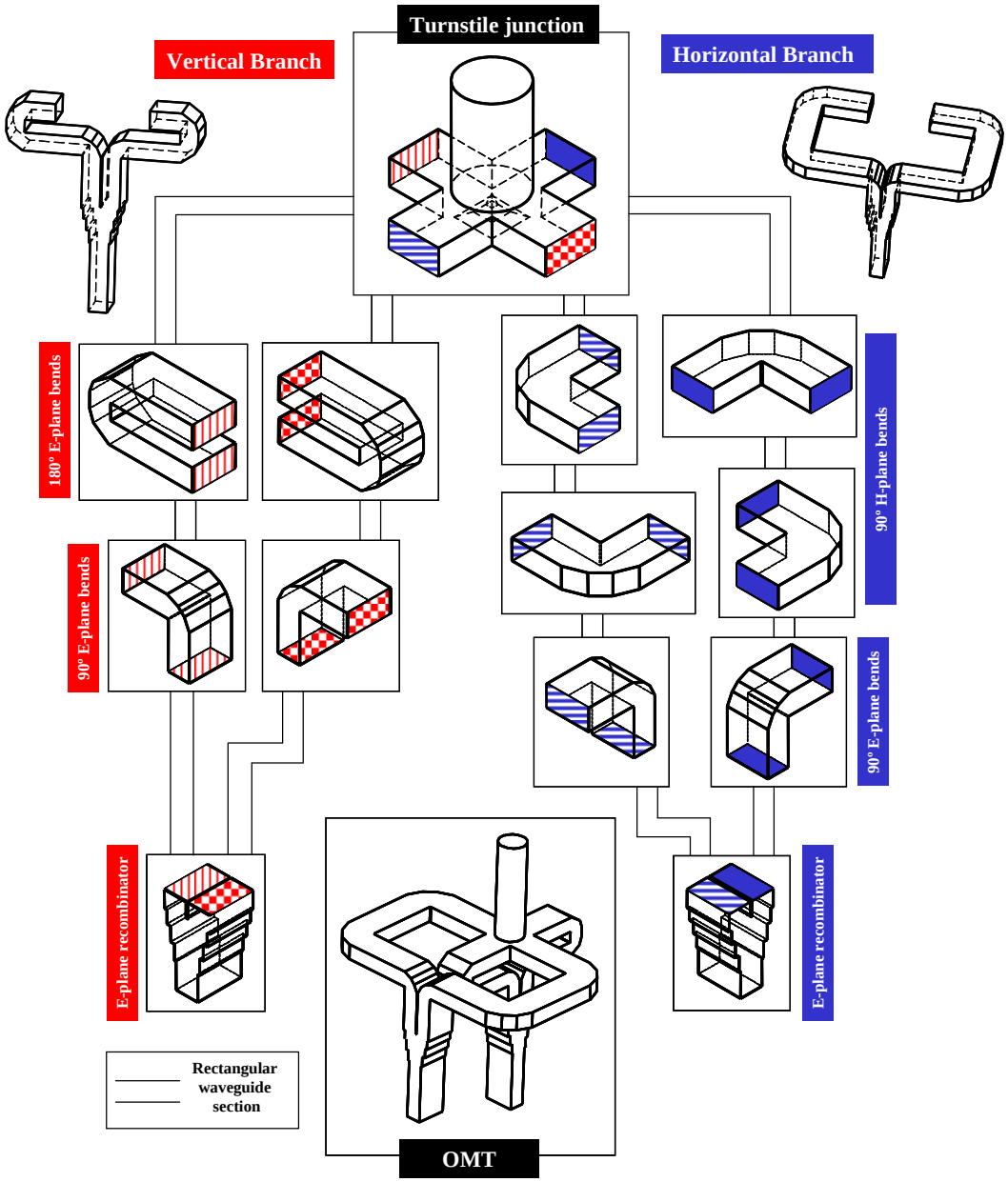

Fig. 3.27. Sketch of the parts that compose the OMT of this project and its interconnection.

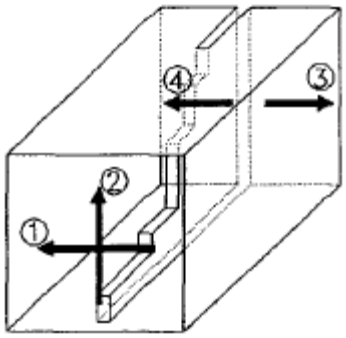

Fig. 3.28. Septum OMT polarizer. Image from [ER92]

3.3 OMT / Polarizers

It is important to note that all these OMTs mainly operate over linearly polarized waves. If circular polarization is required, a proper polarizer should be placed between the antenna horn and the OMT to transform between both polarization states. The design of these polarizers is out of the scope of this project. Some common configurations of these devices can be found in [UBR93].

On the other hand, some structures can carry out both tasks at a time: they act as OMTs and polarizers, reducing overall size and weight. However, they do not offer the same performance as using them separately (typically they are narrowband). Fig. 3.28 shows an example of these devices from [ER92].

3.4 Conclusions.

The general concepts related to OMTs have been presented in this chapter. Since these structures have been developed continuously over the last decades, there has been a high number of contributions and architectures which sometimes are scattered through the technical literature.

An attempt to summarize most of the OMT types has been done in this chapter, where several OMT configurations have been presented and analyzed. They basically can be classified into narrowband and wideband structures by the way that higher-order modes are excited within them. This is a key factor for its operational bandwidth. Narrowband OMTs generally have only one plane of symmetry, while wideband OMTs preserve at least two of them.

If circular polarization is required by the application, a polarizer should be placed between the antenna and the OMT. Some devices can provide both polarization and discrimination at a time. Some examples of these structures have also been presented.

So far, chapters 1 to 3 aimed to present the reader some notions about OMTs as well as basic concepts about electromagnetism. The next chapters will be focused on the design of an OMT based on the Turnstile junction (introduced in Sec. 3.2.2), which is the aim of this project.

Chapter 4

Analysis and Design Techniques

The purpose of this short chapter is to describe the analysis and design process of all the structures that compose the whole OMT. As it has been stated in the previous sections, there is a lack of analytical tools for a straight design of these structures; many parts have to be designed by numerical optimization. Nevertheless, the optimization process is always driven by the knowledge and comprehension of the structure to design.

4.1 Full-wave analysis tools

For an accurate design of a microwave device, the analysis of the structure must solve the Maxwell's equations inside the geometric model of the problem, trying to avoid approximations as much as possible. In this way, when the solution of the Maxwell's equations is carried out rigorously, it is said that is a full-wave analysis.

The full-wave analysis of the structures with complicate geometry of this project have been done with the commercial software HFSS (High Frequency Structure Simulator, http://www.ansoft.com), based on the FEM (Finite Element Method), and with the CST Microwave Studio (Computer Simulation Technology, http://www.cst.com), based on the FIT (Finite Integration Technique, although it has other solvers). Some other parts (mainly the routing system) could be done by home-made Mode-Matching tools (see [UBR93] for basic details on this analysis technique or [RMR06], [RMR08]). However, the whole device has been analyzed with HFSS and CST to include the complex matching elements of the Turnstile junction.

The FEM and FIT are some of the available numerical methods for addressing the full-wave analysis of complex 3-D structures. They involve a discretization of the problem: a mesh of the geometry under analysis. The accuracy of the solution provided by these methods increases with the refinement of that mesh, which is usually adaptive (the mesh is progressively more refined in the zones where the field has more variations and amplitude). A finer mesh provides better results, at the expense of more computation time.

The basic steps to simulate a structure in full-wave simulator software (such as HFSS or CST) are:

- To plot its geometry: a model built of boxes, cylinders…
- To specify the symmetry boundary conditions (e.g., a Perfect Magnetic Wall, finite conductivity walls, etc.).
- To specify the ports of the structure, the number of modes present in the analysis and, if necessary, to set an integration line to polarize electric field or a certain characteristic impedance.

- To set the parameters of the analysis: solution frequency, maximum number of passes for the adaptive mesh solutions, frequency sweeps…
- To perform the analysis and to plot results (S parameters, field reports…).

4.2 Matlab – Full-wave software

The HFSS user interface has not been used directly. In fact, it has been called from the Matlab environment. For this project, several .m-files have been developed through Matlab. These functions are able to control the HFSS. They control geometry, simulation properties and design variables by calling special functions gathered on an API (Application Programming Interface). The same strategy can also be used with CST.

The optimization process has also been controlled from Matlab. The use of Matlab in combination with the full-wave simulator allows the designer to draw the structure, to optimize its dimensions and to observe and interpret results all in a much more efficient way.

4.3 Optimization: Simplex and Simulated Annealing

Two optimization algorithms were chosen for the design cycle. The first one, ***Simplex,*** is suitable for simple structures like the bends and transformers designed in this project. It quickly finds minimums that may result in good enough performances. It does not need the computation of the derivatives of the cost function.

The second one is ***Simulated Annealing***, which will be used for more complex structures like the Turnstile junction and the whole OMT. This method is suitable for large-scale optimization problems where the desired global minimum may be hidden among many other local ones. The technical definition of this optimization technique has an analogy with thermodynamics. When a liquid is slowly cooled, its molecules gradually lose their thermal mobility until they reach a natural minimum energy state, forming an ordered pure crystal. Similarly, the annealing algorithm incorporates these physical principles into numerical calculations.

More information of these optimization algorithms can be found in [Num92].

4.4 Design cycle

All the components of the OMT have been designed through the common design cycle from Fig. 4.1. The scheme is represented in terms of the HFSS and has been used for designing OMTs, but it would be analogous for other type of microwave device (as filters or couplers) or full-wave simulators as CST.

The first stage of the design starts with the initial dimensions of the structure. This is done with the help of equivalent circuits (if available) or previous designs for similar applications which are modified according to the experience of the designer. These dimensions are passed to a Matlab .m script which generates a .vbs file which executes

the HFSS software. This .vbs contains specific instructions assigned by the API to draw the structure in HFSS and to set and perform the desired analysis.

Once the analysis is done, another instruction exports the information about S parameters to a .m file which is used by Matlab to plot results once HFSS is closed. If the user is performing an optimization process, Matlab calculates the cost function. For example, if the user is optimizing a bend, a suitable cost function would be

$$CF = \sum_i \left| S_{11}^{i)} \right|^2 \quad , \tag{4.1}$$

where $S_{11}^{i)}$ represents the coefficient at each point i of the frequency range of the performed analysis. Then the cost function would be compared to an objective threshold to determine if the optimization is finished or not. If not, the optimization algorithm would decide the new dimensions of the device that will be tested and so on.

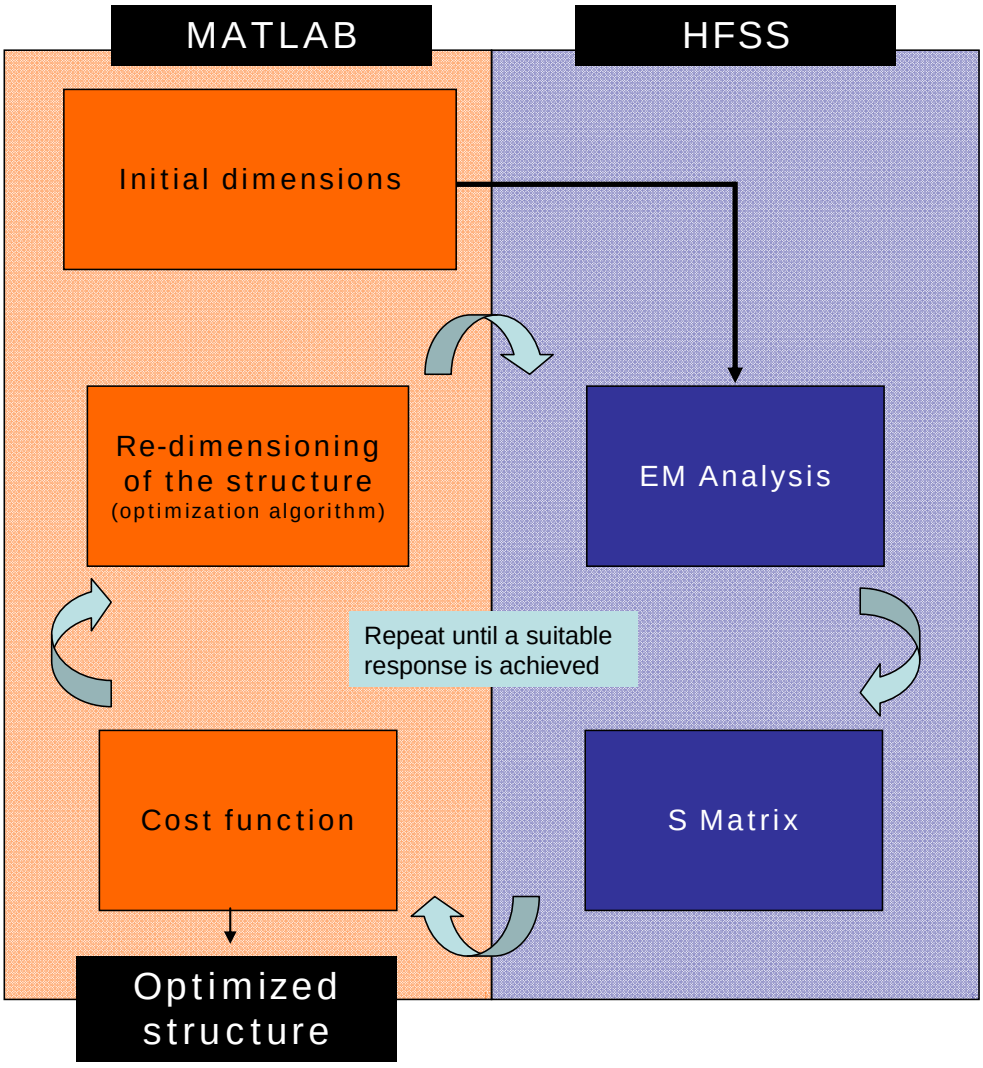

Fig. 4.1. Design cycle.

4.5 Computation Time

Time spent for the analysis may vary depending on computational resources. For this project, the analyses were carried out by a Quad-Core @ 2.4 GHz PC with 8 Gb RAM.

For simple routing structures, like the bends and transformers designed for this project, the full-wave analysis with HFSS or CST takes about 5 minutes (this time is much smaller when the structure is computed by Mode-Matching tools). For the Turnstile, the HFSS or CST take more time, about 10 minutes, using the double symmetry. The analysis of the whole OMT takes about 6 hours. These times also depend on the required accuracy, since accurate results require a higher number of adaptive passes in the full-wave simulator, which implies more computation time.

The duration of the optimization for these structures depends on the number of variables involved on it. For the routing structures, optimum designs with several elements were achieved with just 1 or 2 hours of optimization. The Turnstile junction took more time again, especially when complex internal obstacles were on test. With Mode-Matching (when the structure allows it), these times can be reduced in more than one order of magnitude.

4.6 Conclusions.

The analysis and design techniques used in this project have been described. The design cycle that will be followed in the next chapters has been explained. It is based on the communication between Matlab and the full-wave simulator. The optimization algorithms that will be used during this design cycle have also been described.

Chapter 5 will be the first designing stage: the routing elements of the OMT. Some routing structures will be presented with specific designs developed during this project.

Chapter 5

Waveguide Routing Structures

The term routing structures refers to the waveguide components whose main purpose is to guide the modes between the ports of different elements. For example, a bend may be needed to change wave direction, or a height/width transformer may be necessary in order to match ports with different interfaces. Moreover, in many structures such as the wideband OMTs mentioned in Sec. 3.2.2 it is necessary to use signal recombiners. These three structures will be presented in this section, showing simulated results obtained with designs developed during this project.

5.1 Waveguide bends

Bends are one of the most simple and typical structures found for waveguiding because signals usually need to be routed between ports or places without a straight path linking them. Many devices as OMTs, couplers, filters, Y-branches, etc., include not one but many bends in their topology, which emphasizes the need of optimized structures providing excellent return losses (usually better than 35 dB) over the desired frequency band. Additional restrictions such as low insertion losses and a compact design are usually required. The scattering matrix for a reciprocal, lossless two-port network is

$$\mathbf{S} = \begin{bmatrix} re^{j\varphi_1} & \sqrt{1-r^2}\,e^{j\frac{1}{2}(\varphi_1+\varphi_2+(2n+1)\pi)} \\ \sqrt{1-r^2}\,e^{j\frac{1}{2}(\varphi_1+\varphi_2+(2n+1)\pi)} & re^{j\varphi_2} \end{bmatrix}, \tag{5.1}$$

where r is the magnitude of the S_{11} parameter, φ_1 its phase, φ_2 the phase of the S_{22} parameter and n some integer number (positive or negative) [Col01, Sec. 4.8]. For symmetrical bends with respect to a plane in the middle of the structure: $\varphi_1 = \varphi_2$. For an ideal bend, the S-matrix reduces to

$$\mathbf{S} = \begin{bmatrix} 0 & e^{j\phi} \\ e^{j\phi} & 0 \end{bmatrix}, \tag{5.2}$$

This equation shows that an ideal symmetrical bend is perfectly matched, with a phase delay for the transmission. All the incoming power at one port is fully transmitted to the other one. Unfortunately, in a real design a small fraction of that incoming power is always reflected back to the entrance port, resulting in an S_{11} different from zero, although usually small in magnitude. Of course, there are also small losses related to non-ideal perfect conductor walls (magnitude of the S_{21} a little bit smaller than one), but they will not be considered here.

Among all types of existing bends for different technologies this project is focused on waveguide bends. These bends can differ in their bend angle and the shape of the profile, but basically there are two clearly different types of bends: symmetrical and unsymmetrical bends. The latter change the cross-section of the waveguide besides its direction. Moreover, typical bends can be classified into E-Plane and H-Plane bends. Fig. 5.1 shows an example of each bend. For an E-Plane bend the width remains constant while for an H-plane bend the height remains the same. Each one holds certain properties that will be analyzed in the next sections.

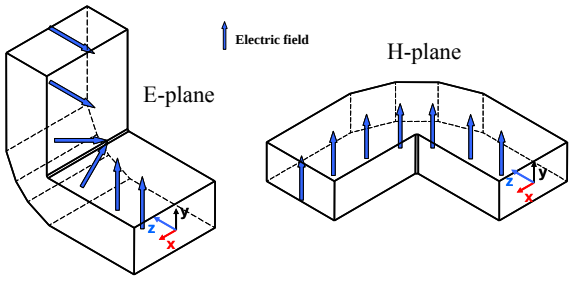

Fig. 5.1. An example of E and H-plane bends.

5.1.1 E and H-plane bends analysis

An E-plane bend holds symmetry regarding *yz*-plane (see again Fig. 5.1 to check coordinate system). Therefore, only modes with a PMW at this plane (rows 1 and 4 from Table 2.3) will be excited by the discontinuity. In this case, TE_{11} / TM_{11} will be the first higher-order modes excited, which gives a 76.4 % theoretical operative bandwidth (f < 2.236 f_c , with f_c being the cutoff frequency of the TE_{10} mode in a rectangular waveguide with $b = a/2$). Reduced height bends will slightly increase this bandwidth, at the expense of increasing insertion losses by non-perfect conductors. Above these frequencies TE_{11} and TM_{11} can freely propagate inside the waveguide. See again Fig. 2.5 for the relation between cutoff frequencies of the modes in a rectangular waveguide.

H-Plane bends hold symmetry regarding *xz*-plane, so only modes with a PEW at this plane (rows 2 and 3 from Table 2.3) will be excited. That means a reduction of the theoretical operative bandwidth (f < 2 f_c, 66.67%) because of the TE_{20} mode excitation (assuming as usual that $b <= a/2$).

5.1.2 Comparison between mitered bends

Several designs of these bends can be found on the literature. Uher *et al.* in [UBR93] present great results using truncated corners on both E-plane and H-plane bends for different bend angles, like those shown in Fig. 5.1.

The study of these structures is one of the first steps in the comprehension of the OMT routing. Full optimization of some waveguide bends was one of the initial stages of this project. They would be later added to the design of the overall OMT, in case reasonable results were achieved. As mitered bends are proved as great performance structures over wide bands, the study begun by checking how this performance was progressively improving on 90 degrees E-plane bends as the number of miters increased. A total of 7 designs were tested. Bends with circular shapes can be found in the literature, though they offer similar performance than that of mitered ones at the expense of a more difficult manufacture.

Of course, these curves can be translated to any frequency range and waveguide size with proper scaling, but in order to make comparison easier, all the bends were designed for the band between 10 and 19 GHz, using the standard WR-62 waveguide dimensions ($a \times b$: 0.622 x 0.311 inches, 15.8 x 7.9 mm). That includes the whole Ku band (12-18 GHz). Dimensions and design variables used for optimization of the structures are also shown on the following figures and tables:

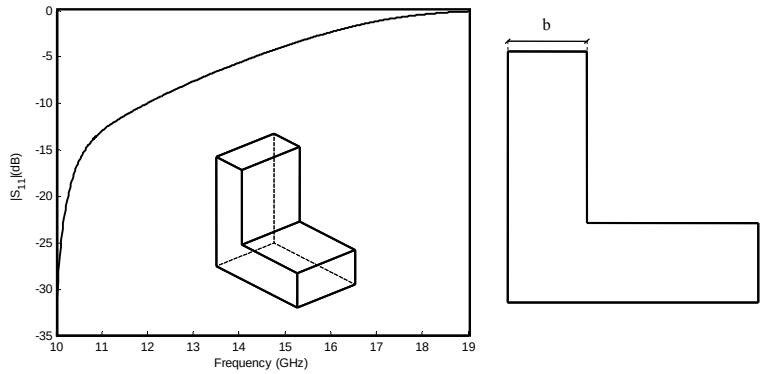

Fig. 5.2. Simulated return losses and topology of a 90º E-plane waveguide bend. Version 1.

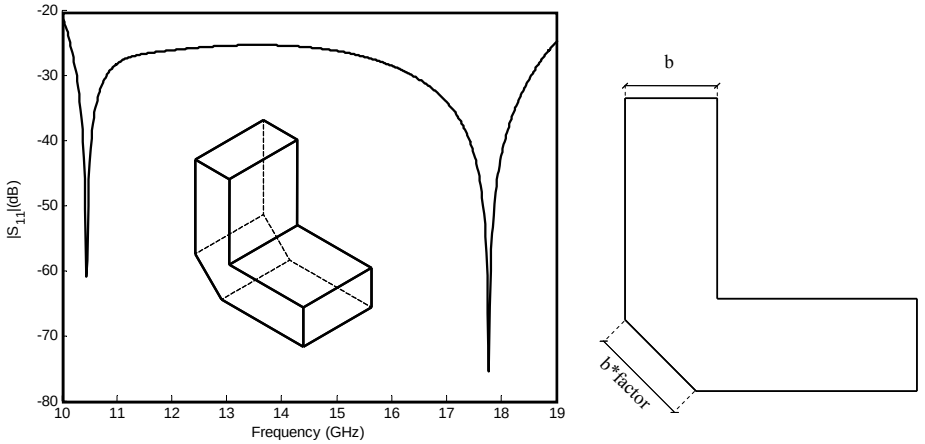

Fig. 5.3. Simulated return losses and topology of a 90º E-plane waveguide bend. Version 2.

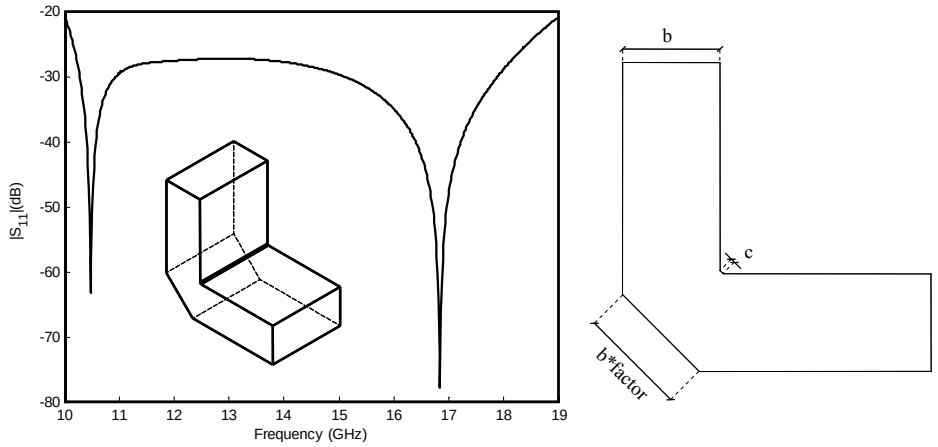

Fig. 5.4. Simulated return losses and topology of a 90º E-plane waveguide bend. Version 3.

- **Version 1:** This is the simplest bend as it has no cuts. It yields poor performance and a very low transmission coefficient, so it seems to be the worst option.
- **Version 2:** The second version adds a cut at the outer corner, yielding much better results. This design presents return losses better than 25 dB over almost a 60% bandwidth (10.15 to 18.95 GHz).
- **Version 3:** Adding a small cut at the inner corner slightly increases performance.

Version 2	*factor = 1.089*
Version 3	*factor = 1.109 ; c = 0.366 mm*

Table 5.1. Dimensions of the 90º E-plane bends from Fig. 5.3 and Fig. 5.4.

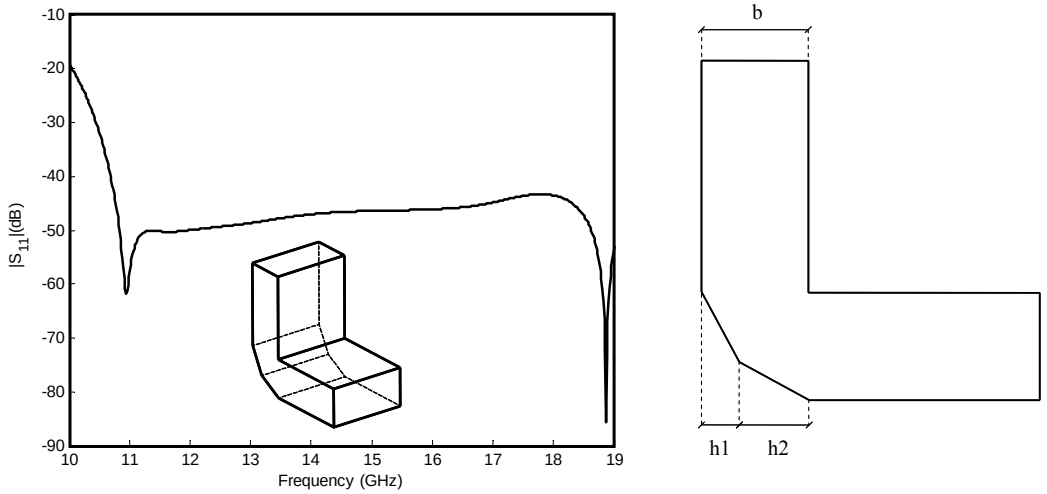

Fig. 5.5. Simulated return losses and topology of a 90º E-plane waveguide bend. Version 4.

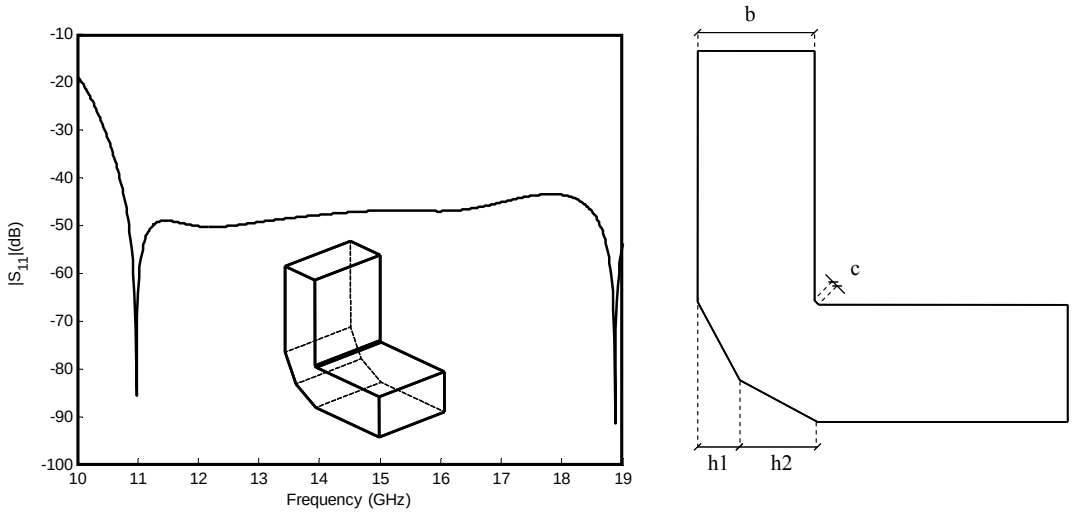

Fig. 5.6. Simulated return losses and topology of a 90º E-plane waveguide bend. Version 5.

- **Version 4:** The improvement on the results is quite significant by just adding a second cut in the structure.
- **Version 5 :** Again, the small cut at the inner corner gives a slight improvement.

Version 4	*h1 = 2.807 ; h2 = 5.166 (mm)*
Version 5	*h1 = 2.831 ; h2 = 5.271 ; c = 0.387 (mm)*

Table 5.2. Dimensions of the 90º E-plane bends from Fig. 5.5 and Fig. 5.6.

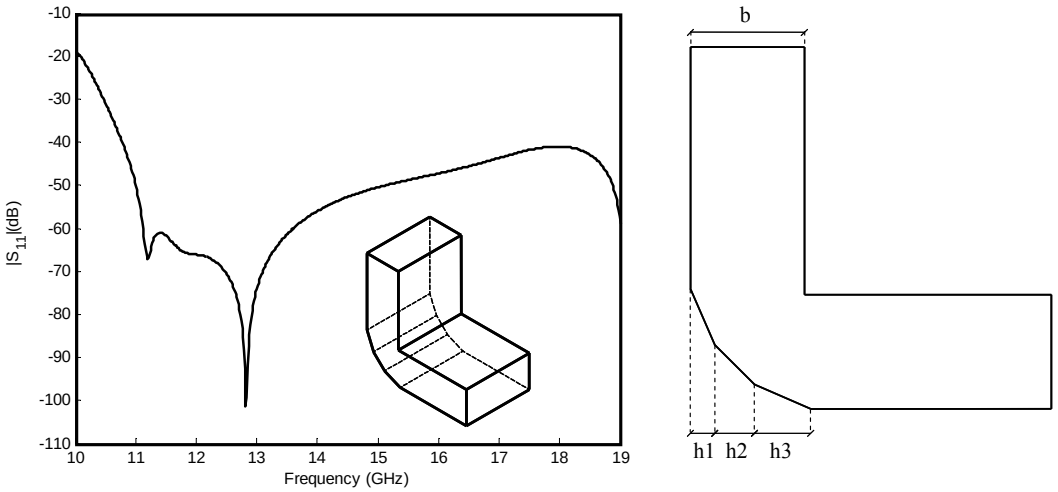

Fig. 5.7. Simulated return losses and topology of a 90º E-plane waveguide bend. Version 6.

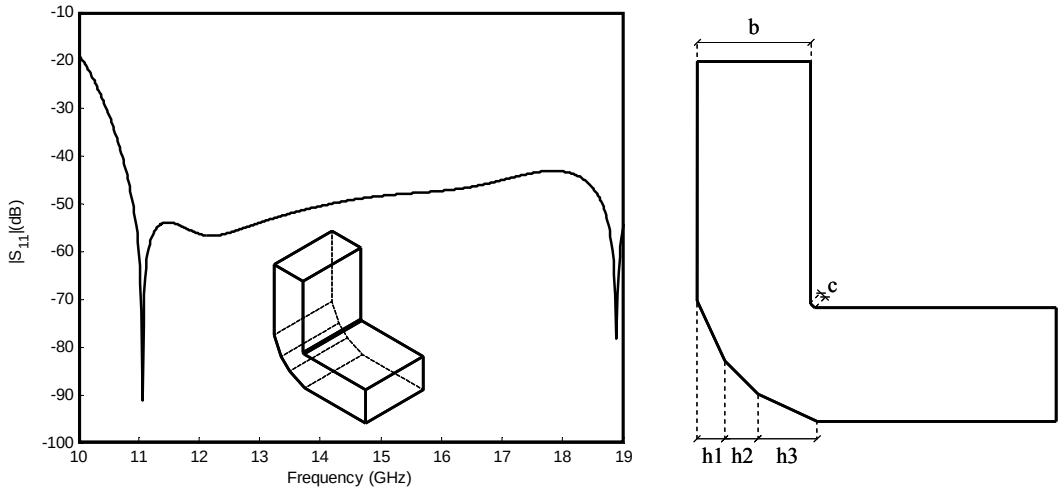

Fig. 5.8. Simulated return losses and topology of a 90º E-plane waveguide bend. Version 7.

- **Version 6:** Three symmetrical cuts offer a great result. These mitered bends are easy to manufacture. Adding more cuts may just result in a slight improvement on the performance of the bend, though it seems unnecessary as it would increase manufacturing difficulty.

- **Version 7 :** This is the final version. A small cut is also added to the bend like in versions 3 and 5. Return losses better than 40 dB are achieved by this design over more than a 50% fractional band, which is more than enough for almost any application.

Version 6	*h1 = 1.68 ; h2 = 2.761 ; h3 = 3.89 (mm)*
Version 7	*h1 = 1.917 ; h2 = 2.31 ; h3 = 4.143 ; c = 0.385 (mm)*

Table 5.3. Dimensions of the 90º E-plane bends from Fig. 5.7 and Fig. 5.8.

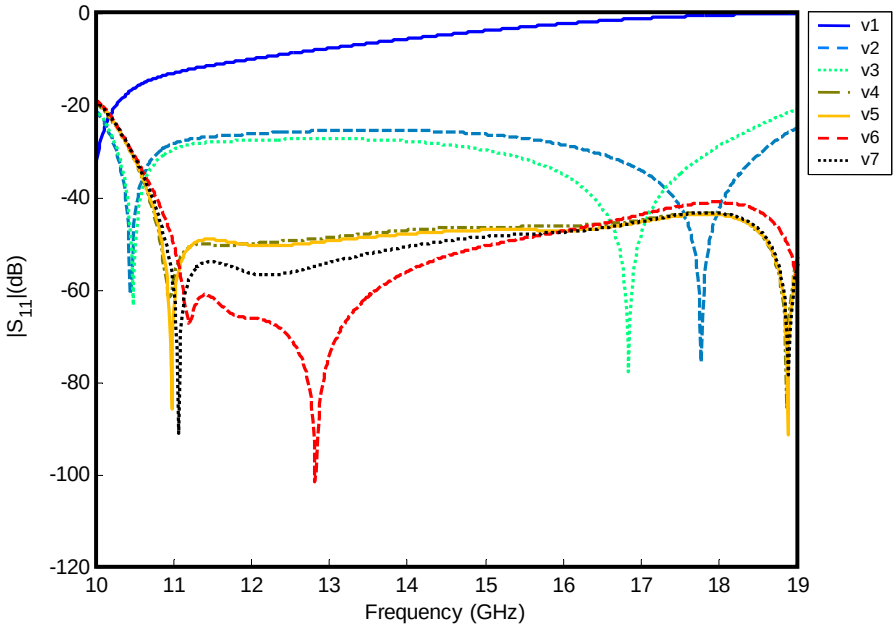

Fig. 5.9. Compared simulated return losses of the seven 90º E-plane bends versions analyzed for this project.

Fig. 5.9 shows combined return losses for all the versions. As it has already been mentioned, it is possible to achieve great performance over a wide band with just two or three symmetrical cuts at the corner of the bend. This is of utmost importance for the reasons stated at the beginning of this chapter.

The same procedure was followed with H-plane bends, yielding similar results. Fig. 5.10 shows a 90º H-plane bend with three cuts. This version will be used for the design of the complete OMT in Ch. 7.

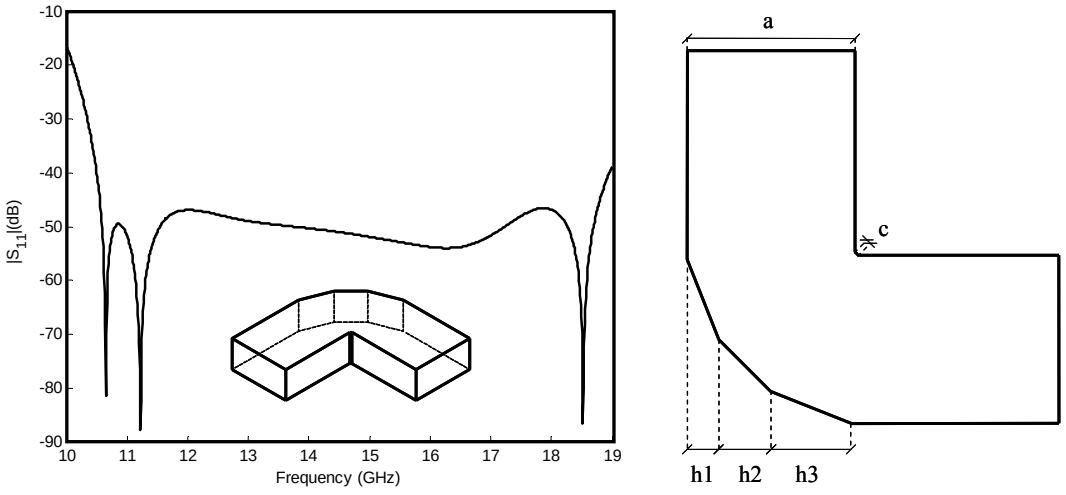

Fig. 5.10. Simulated return losses and topology of a 90º H-plane waveguide bend.

Version 7	*h1 = 1.917 ; h2 = 2.31 ; h3 = 4.143 ; c = 0.385 (mm)*

Table 5.4. Dimensions of the 90º H-plane bend from Fig. 5.10.

5.1.3 Other designs

The angle of the bends is not restricted to be 90 degrees, of course. Different angles may be needed for some designs, so more bends were designed during this project.

- **180º E-plane bend**

A 180 degrees bend can sometimes be understood as the combination of two adjacent 90 degrees bends, but with a little effort on designing it is possible to reduce the intermediate length of the bend. Fig. 5.11 and Fig. 5.12 show the results obtained for two 180 degrees E-plane bend designed during this project. First one has full-height ($b = 7.9$ mm) while the second one is a modified version where the height is modified ($b = 7.631$ mm) because of the topology of the OMT with angled branches that will be described in Ch. 7.

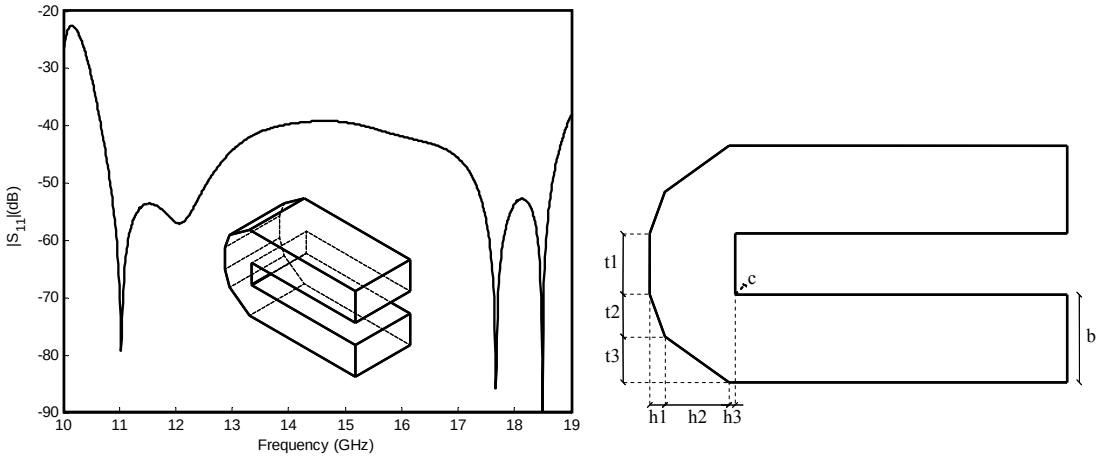

Fig. 5.11. Simulated return losses and topology of a full-height 180º E-plane waveguide bend.

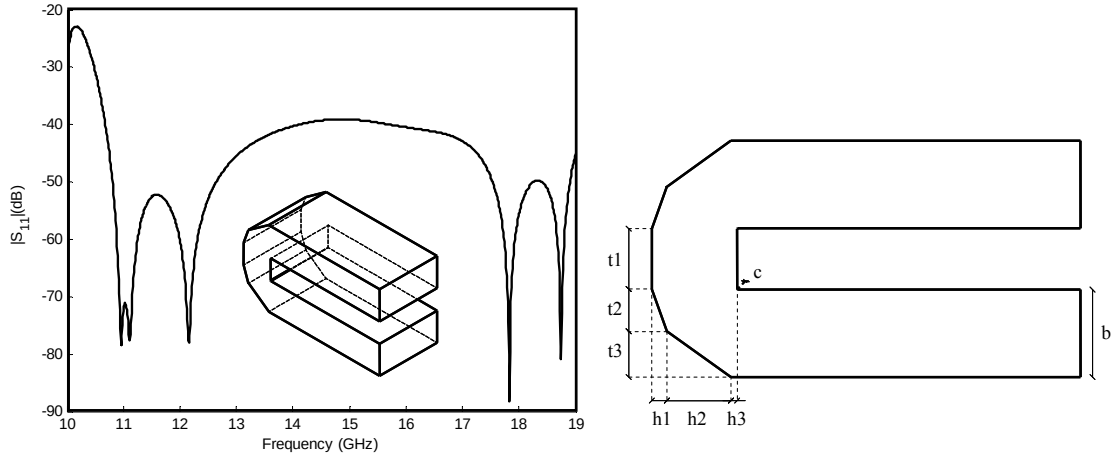

Fig. 5.12. Simulated return losses and topology of a reduced-height 180º E-plane waveguide bend.

Full-height	*h1 = 1.37 ; h2 = 5.787 ; h3 = 0.561 ;* *t1 = 5.455 ; t2 = 3.82 ; t3 = 4.125 ;* *c = 0.1 ; b = 7.9 (mm)*
Reduced-height	*h1 = 1.323 ; h2 = 5.59 ; h3 = 0.542 ;* *t1 = 5.269 ; t2 = 3.69 ; t3 = 3.984 ;* *c = 0.1 ; b = 7.631 (mm)*

Table 5.5. Dimensions of the 180º E-plane bends from Fig. 5.11 and Fig. 5.12.

- **105º and 120º E-plane bends**

These bends were designed at full-height first to test bends with more than 90 degrees. They proved to be very useful later while designing the OMT with angled branches in Ch. 7.

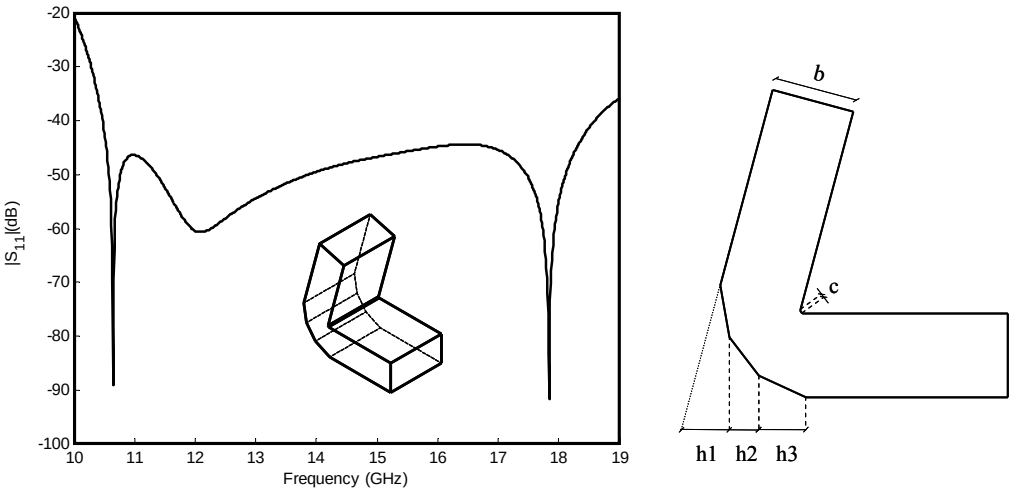

Fig. 5.13. Simulated return losses and topology of a 105º E-plane waveguide bend.

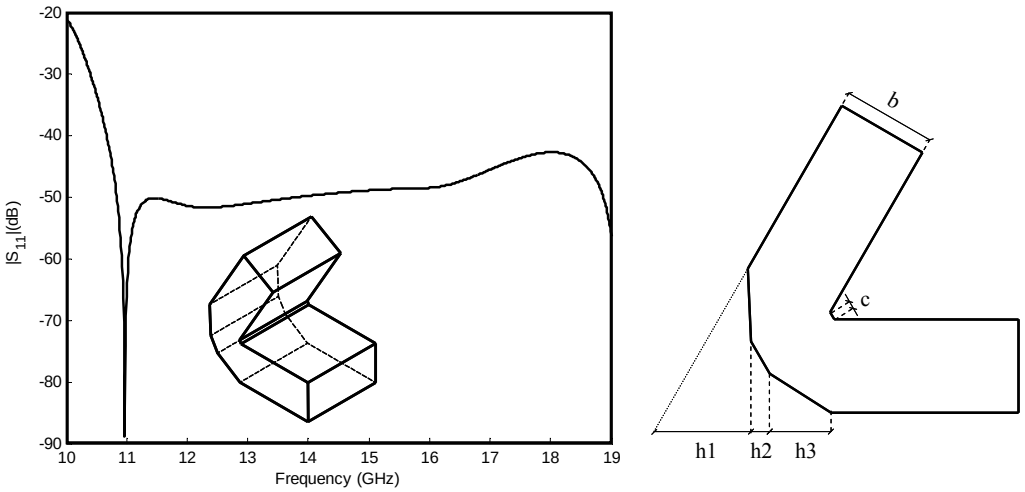

Fig. 5.14. Simulated return losses and topology of a 120º E-plane waveguide bend.

105º	*b = 7.9 ; h1 = 3.674 ; h2 = 2.768 ; h3 = 4.481 ; c = 0.325 (mm)*
120º	*b = 7.9 ; h1 = 7.296 ; h2 = 1.59 ; h3 = 5.204 ; c = 0.673 (mm)*

Table 5.6. Dimensions of the 105º and 120º E-plane bends from Fig. 5.13 and Fig. 5.14.

5.2 Waveguide transformers

A waveguide transformer is a structure with only two ports facing each other with different cross sections. See again Eq. 5.1 for the S-matrix of a two-port network. Since the interfaces of the input and the output will be different, the structure will not have a symmetry plane in the middle of the structure, and the phase of the S_{11} and S_{22} may be different. The S-matrix for an ideal transformer reduces to

$$\mathbf{S} = \begin{bmatrix} 0 & e^{j\phi} \\ e^{j\phi} & 0 \end{bmatrix}. \tag{5.2}$$

The design of some waveguide transformers can be carried out following the classic theory of stepped impedance transformers based on transmission lines, which is stated in many books as in [MYJ64] or in [Poz05, Ch. 5]. Specifically, this project is focused on multisection wideband transformers, which can be easily synthesized to present a Butterworth or Chebyshev frequency response. These books also contain tabulated impedance values for certain number of sections. As the characteristic impedance of a waveguide depends on the mode propagating inside, and there may be many of them above cutoff, it is necessary to establish the dimension of variation as the parameter needed to retrieve the solutions for the transformer sections, i.e., the value obtained will be the dimension of each section. For example, if a transformation between a half-height WR62 waveguide with dimensions 15.8 x 3.95 and the standard waveguide of 15.8 x 7.9 is needed, height will be chosen as the characteristic impedance and then heights of the sections will be obtained applying classic formulas.

The results of this method are not optimum because of the evanescent mode excitation at the discontinuities. As it was stated before, the electromagnetic field inside a waveguide is the result of the superposition of many modes propagating through many hypothetical transmission lines and a full wave analysis is necessary to completely calculate fields within the waveguide. In any case, data obtained from impedance tables are good starting points for optimization. Further optimizations using any optimization algorithm like Simplex or Simulated Annealing (both briefly introduced in Chapter 4) will yield optimum designs for the transformers.

5.2.1 Classification of waveguide transformers.

There are different types of transformers depending on i) the dimension that varies between the sections, ii) the symmetry of the whole structure or iii) their frequency response.

Concerning i) homogeneous and inhomogeneous transformers can be distinguished. The sections of an homogeneous transformer have the same characteristic impedance and internal wavelength, i.e., there is no width change along the direction of propagation. On the contrary, inhomogeneous transformers have different width between the sections, which results in different cutoff frequencies for the fundamental modes of the different sections. Though it may not be desirable to work with the latter, they usually provide better performances with an appropriate design. Homogeneous transformers are also called height transformers or E-plane transformers, while inhomogeneous ones can either be width transformers (H-plane transformers) or a combination of both.

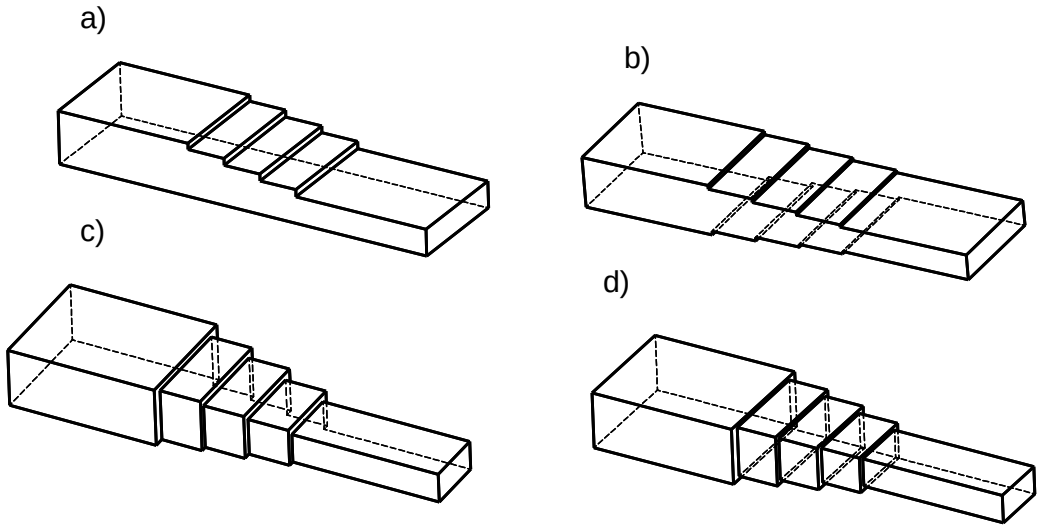

Fig. 5.15. Different transformers: homogeneous with a) 1 plane and b) 2 planes of symmetry; inhomogeneous with c) 1 plane and d) 2 planes of symmetry.

Regarding ii) there are transformers holding two planes of symmetry while some of them only keep one. Different higher-order modes are excited inside them.

Finally, in iii) many types of responses can be designed. The most common of them are Butterworth and Chebyshev transformers.

Fig. 5.15 shows four examples of the transformers described in i) and ii).

This project focuses on homogeneous transformers with two planes of symmetry. That prevents the structure from generating certain higher-order modes (only a subset of $TE/TM_{1n,\ n\ even}$ modes from the first row in Table 2.3 is excited). Fig. 5.16 and Fig. 5.17 show two transformers with 3 and 5 sections designed during this project.

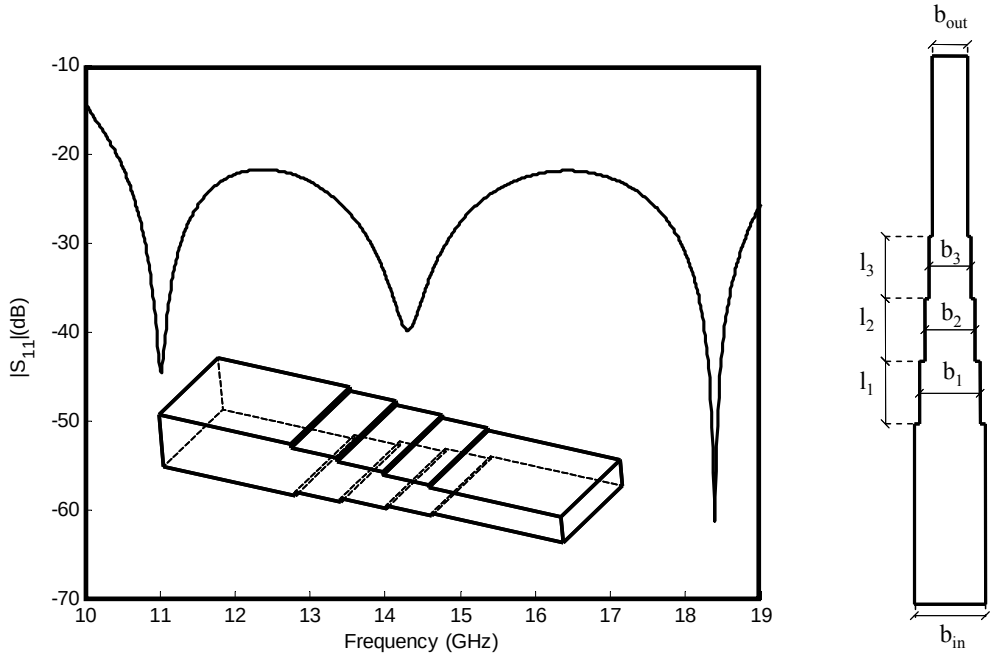

Fig. 5.16. Simulated return losses of a three section homogeneous transformer with 2 planes of symmetry.

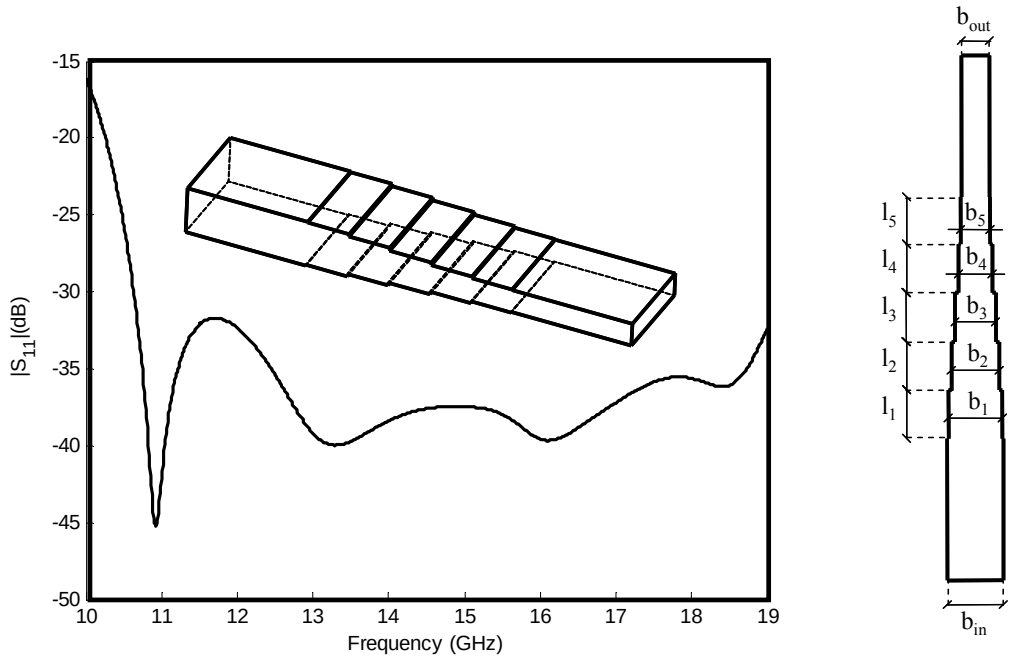

Fig. 5.17. Simulated return losses of a five section homogeneous transformer with 2 planes of symmetry.

3 sections	$l_{1\text{-}3}$=[6.955 , 6.946 , 6.911] ; $b_{1\text{-}3}$=[6.745 , 5.585 , 4.673] ; b_{in} = 7.9 ; b_{out} = 3.95 ; (mm)
5 sections	$l_{1\text{-}5}$=[6.878 , 6.763 , 6.947 , 6.802 , 6.674] ; $b_{1\text{-}5}$=[7.614 , 6.743 , 5.751 , 4.774 , 4.16] ; b_{in} = 7.9 ; b_{out} = 3.95 ; (mm)

Table 5.7. Dimensions of the 3 and 5 sections homogeneous transformers from Fig. 5.16 and Fig. 5.17.

5.3 Waveguide recombiners.

This kind of structures is very similar to the transformers stated above but with the implication of joining two separate waves. Specifically, in an OMT with the Turnstile junction each of these waves carry half the power of the original wave, so they must be rejoined somehow before reaching the single-mode port. The recombiners used in this project are physically and electrically three-port devices (see Fig. 5.18 for the port numbers relation). The complete S-matrix for this three-port network is

$$\mathbf{S} = \begin{bmatrix} S_{11e} & \frac{S_{12e}}{\sqrt{2}} & \frac{S_{12e}}{\sqrt{2}} \\ \frac{S_{21e}}{\sqrt{2}} & \frac{S_{22e}+\rho_m}{2} & \frac{S_{22e}-\rho_m}{2} \\ \frac{S_{21e}}{\sqrt{2}} & \frac{S_{22e}-\rho_m}{2} & \frac{S_{22e}+\rho_m}{2} \end{bmatrix}, \tag{5.3}$$

with $S_{ij,e}$ being the S-parameters of the two-port network which results from the e-problem (PEW boundary condition at the symmetry plane of the three-port network)

and ρ_m representing the reflection coefficient which corresponds to the *m*-problem (PMW symmetry). Check Appendix-A for more information on solving N-port networks applying the Bartlett's Theorem. For an ideal recombiner, $S_{11e} = S_{22e} = 0$, $S_{12e} = S_{21e} = e^{j\phi_e}$, $\rho_m = e^{j\phi_m}$ and the S-matrix reduces to

$$\mathbf{S} = \frac{1}{\sqrt{2}} \begin{bmatrix} 0 & e^{j\phi_e} & e^{j\phi_e} \\ e^{j\phi_e} & \frac{e^{j\phi_m}}{\sqrt{2}} & \frac{-e^{j\phi_m}}{\sqrt{2}} \\ e^{j\phi_e} & \frac{-e^{j\phi_m}}{\sqrt{2}} & \frac{e^{j\phi_m}}{\sqrt{2}} \end{bmatrix} . \tag{5.4}$$

Moreover, as this design is intended to be part of the OMT, it should be noted that $a_2 = a_3$, and the reflected waves from the recombiner will only involve the problem with PEW at the symmetry plane:

$$\begin{bmatrix} b_1 \\ b_2 \\ b_3 \end{bmatrix} = \begin{bmatrix} S_{11e} & \frac{S_{12e}}{\sqrt{2}} & \frac{S_{12e}}{\sqrt{2}} \\ \frac{S_{21e}}{\sqrt{2}} & \frac{S_{22e}+\rho_m}{2} & \frac{S_{22e}-\rho_m}{2} \\ \frac{S_{21e}}{\sqrt{2}} & \frac{S_{22e}-\rho_m}{2} & \frac{S_{22e}+\rho_m}{2} \end{bmatrix} \begin{bmatrix} a_1 \\ a_2 \\ a_2 \end{bmatrix} , \quad \begin{aligned} b_1 &= (S_{11e})a_1 + \left(\frac{S_{12e}}{\sqrt{2}}\right)a_2 + \left(\frac{S_{12e}}{\sqrt{2}}\right)a_2 = (S_{11e})a_1 + \left(\sqrt{2}S_{12e}\right)a_2 \\ b_2 &= \left(\frac{S_{21e}}{\sqrt{2}}\right)a_1 + \left(\frac{S_{22e}+\rho_m}{2}\right)a_2 + \left(\frac{S_{22e}-\rho_m}{2}\right)a_2 = \left(\frac{S_{21e}}{\sqrt{2}}\right)a_1 + (S_{22e})a_2 \\ b_3 &= \left(\frac{S_{21e}}{\sqrt{2}}\right)a_1 + \left(\frac{S_{22e}-\rho_m}{2}\right)a_2 + \left(\frac{S_{22e}+\rho_m}{2}\right)a_2 = \left(\frac{S_{21e}}{\sqrt{2}}\right)a_1 + (S_{22e})a_2 \end{aligned} , \tag{5.5}$$

which implies $b_2 = b_3$.

There is a slight difference between the topologies of a transformer and a recombiner. As it is shown in Fig. 5.19 and Fig. 5.20, the new dimensions for the transformer itself depend on the separation of the two branches that arrive to the structure. The first section may start before the end of this narrow separation for some designs.

Within the complete OMT structure, the modes which will excite port 2 and 3 must be in phase, so that means these ports must have the same electrical path from the Turnstile junction to the recombiner. This will be further explained in Ch. 6. For this chapter, this condition implies that the recombiner must be physically symmetrical with respect to the *xz*-plane. The electromagnetic field will have a PEW at that plane. In addition, this also implies that the two-port structure made up of ports 1 and 2 (or alternatively 3) with PEW in the *xz*-plane, behaves like a simple transformer, thus having the ideal scattering matrix from Eq. 5.1. Two designs were developed for this project, with three and five sections for the recombiner.

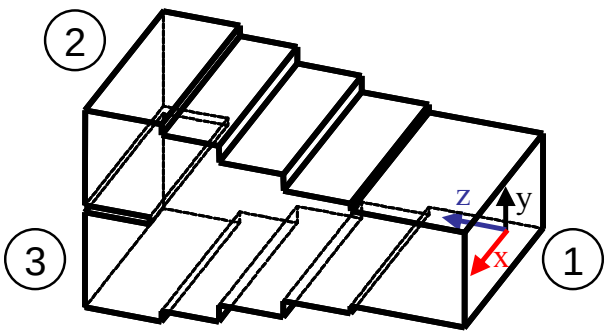

Fig. 5.18. Port numbers and reference system for a recombiner.

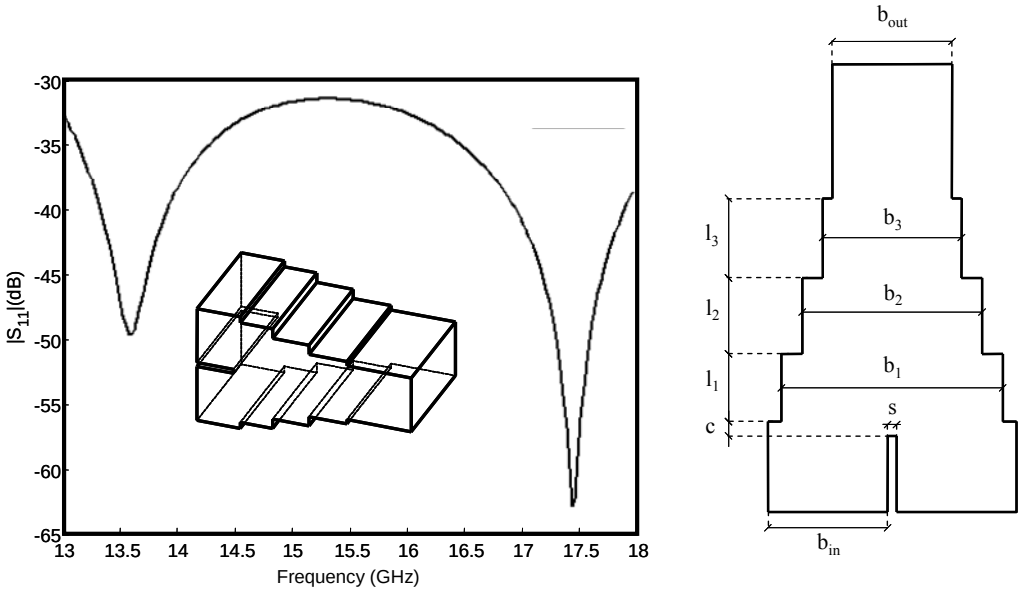

Fig. 5.19. Simulated return losses of a five section homogeneous recombiner with 2 planes of symmetry.

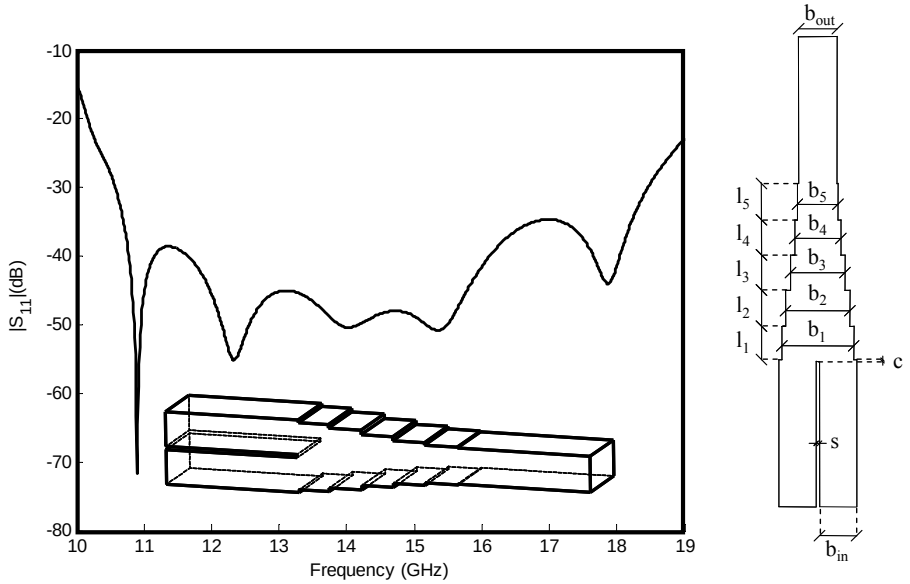

Fig. 5.20. Simulated return losses of a five section homogeneous recombiner with 2 planes of symmetry.

3 sections	$l_{1\text{-}3}$=[4.46 , 4.989 , 5.227] ; $b_{1\text{-}3}$=[14.613 , 11.863 , 9.152] ; b_{in} = 7.9 ; b_{out} = 7.9 ; c = 0.939 ; s = 0.592 (mm)
5 sections	$l_{1\text{-}5}$=[6.792 , 7.384 , 7.149 , 7.161 , 7.41] ; $b_{1\text{-}5}$=[14.727 , 13.157 , 11.158 , 9.391 , 8.298] ; b_{in} = 7.631 ; b_{out} = 7.9 ; c = 0.378 ; s = 0.702 (mm)

Table 5.7. Dimensions of the 3 and 5 sections homogeneous recombiners from Fig. 5.19 and Fig. 5.20.

5.4 Conclusions

The importance of routing structures in microwave devices has been stated in this chapter. They can be found in many designs carrying out the task of routing the waves between non-facing ports of the devices.

Bends are the most typical routing structures. In particular, mitered bends represent one of the most simple and efficient devices in microwave circuitry. Several designs have been designed for this project, including those that will compose the whole OMT design.

Stepped transformers theory has been developed over decades. Waveguide transformers and recombiners support on this theory, yielding great results in wide bands. A classification of these structures has been presented in this chapter, along with the designs developed during this project.

Chapter 6 will be focused on the Turnstile junction, which is the key structure of the OMT presented in this document.

Chapter 6

Turnstile Junction

6.1 Introduction

The so-called Turnstile junction is the key component of the OMT presented in this document. Physically, it is a five-port structure composed of a common port and four single-mode ports (see Fig. 6.1). The S-matrix of the ideal Turnstile junction is:

$$\mathbf{S} = \left[\begin{array}{cc|cccc} 0 & 0 & \varepsilon & \varepsilon & 0 & 0 \\ 0 & 0 & 0 & 0 & \varepsilon & \varepsilon \\ \hline \varepsilon & 0 & 0 & 0 & \gamma & -\gamma \\ \varepsilon & 0 & 0 & 0 & -\gamma & \gamma \\ 0 & \varepsilon & \gamma & -\gamma & 0 & 0 \\ 0 & \varepsilon & -\gamma & \gamma & 0 & 0 \end{array}\right], \text{ with } |\varepsilon|^2 = |\gamma| = 1/2 \tag{6.1}$$

The device works in the same way for both polarizations: it separates each one into two halves of equal power which are routed through dedicated ports situated facing each other. The operation principle can be explained according to Fig. 6.2. Taking vertical polarization with its electric field polarized regarding *x* axis, only modes with Perfect Magnetic Wall (PMW) at *xy*-plane and Perfect Electric Wall (PEW) at *yz*-plane are coupled. These latter modes are under cutoff on guides 5 and 6 so no power is transmitted to them. Therefore, all the power will be divided between ports 3 and 4. As said before, this behavior holds for horizontal polarization because of Turnstile's fourfold symmetry.

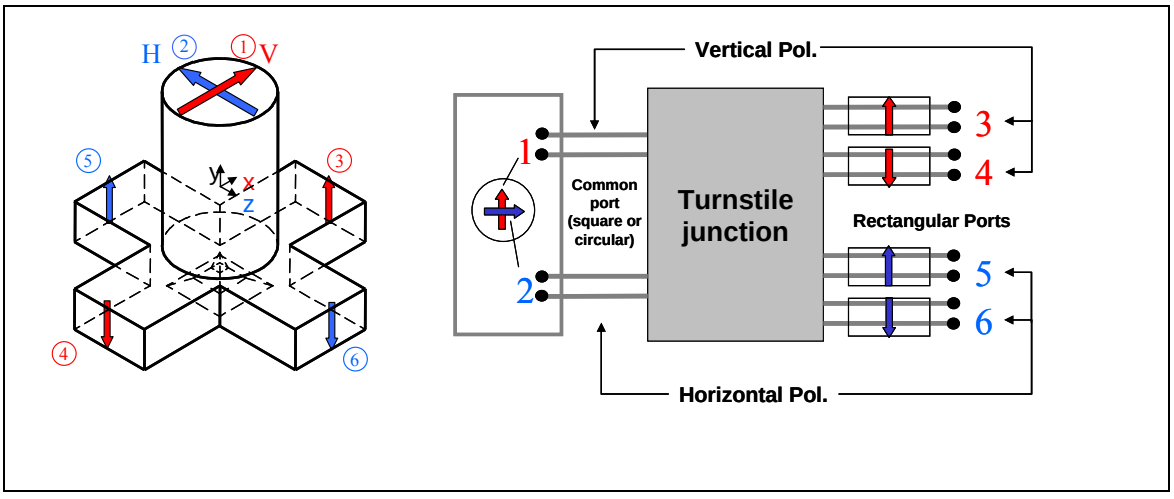

Fig. 6.1. Sketch of electric and physical ports of the Turnstile junction

It should be noted that the complete S-matrix of a six-port network with two planes of physical symmetry (*xy* and *yz*-planes, see again Fig. 6.1 for the relation of port numbers and phases) is

$$\mathbf{S}=\begin{bmatrix} S_{11em} & 0 & \frac{S_{12em}}{\sqrt{2}} & \frac{S_{12em}}{\sqrt{2}} & 0 & 0 \\ 0 & S_{11me} & 0 & 0 & \frac{S_{21me}}{\sqrt{2}} & \frac{S_{21me}}{\sqrt{2}} \\ \frac{S_{21em}}{\sqrt{2}} & 0 & \frac{S_{22em}+S_{11mm}}{2} & \frac{S_{22em}-S_{11mm}}{2} & \frac{S_{12mm}}{2} & \frac{-S_{12mm}}{2} \\ \frac{S_{21em}}{\sqrt{2}} & 0 & \frac{S_{22em}-S_{11mm}}{2} & \frac{S_{22em}+S_{11mm}}{2} & \frac{-S_{12mm}}{2} & \frac{S_{12mm}}{2} \\ 0 & \frac{S_{21me}}{\sqrt{2}} & \frac{S_{21mm}}{2} & \frac{-S_{21mm}}{2} & \frac{S_{22me}+S_{22mm}}{2} & \frac{S_{22me}-S_{22mm}}{2} \\ 0 & \frac{S_{21me}}{\sqrt{2}} & \frac{-S_{21mm}}{2} & \frac{S_{21mm}}{2} & \frac{S_{22me}-S_{22mm}}{2} & \frac{S_{22me}+S_{22mm}}{2} \end{bmatrix}. \tag{6.2}$$

Check Appendix A for more information on solving this six-port network. The matrix of Eq. 6.1 is obtained by introducing $S_{ij,e,m}=0$, $i=j$ and $S_{ij,e,m}=1$, $i\neq j$ in Eq. 6.2. In the OMT, the junction will operate with $a_3=a_4$ and $a_5=a_6$, which leads to only need to compute the two-port problem with PEW and PMW at the symmetry planes (*em*-problem defined in A.2):

$$\begin{aligned} b_1 &= S_{11em}a_1+\sqrt{2}S_{12em}a_3 \\ b_2 &= S_{11em}a_1+\sqrt{2}S_{21em}a_3 \\ b_3 &= b_4=\frac{S_{21em}}{\sqrt{2}}a_1+S_{22em}a_3 \\ b_5 &= b_6=\frac{S_{21em}}{\sqrt{2}}a_1+S_{22em}a_3 \end{aligned} \quad \text{, under } a_3=a_4 \text{ and } a_5=a_6 . \tag{6.3}$$

Fig. 6.3 and Fig. 6.4 show cutoff frequencies for the first higher-order modes excited at the common port of the Turnstile junction for both circular and square waveguides. It can be seen that the theoretical operative bandwidth is slightly increased by using a square common port. However, a circular to square transition will be needed in this case as the antenna horn inputs are usually cast in circular waveguide.

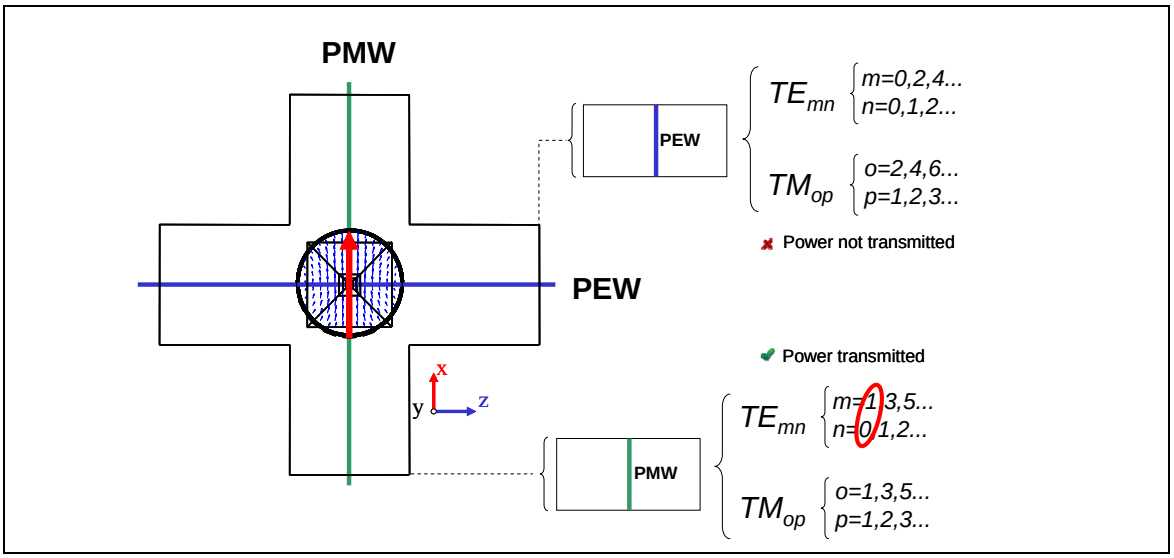

Fig. 6.2. Symmetry properties of the Turnstile junction and higher-order modes generation at rectangular ports. Example for one of the polarizations.

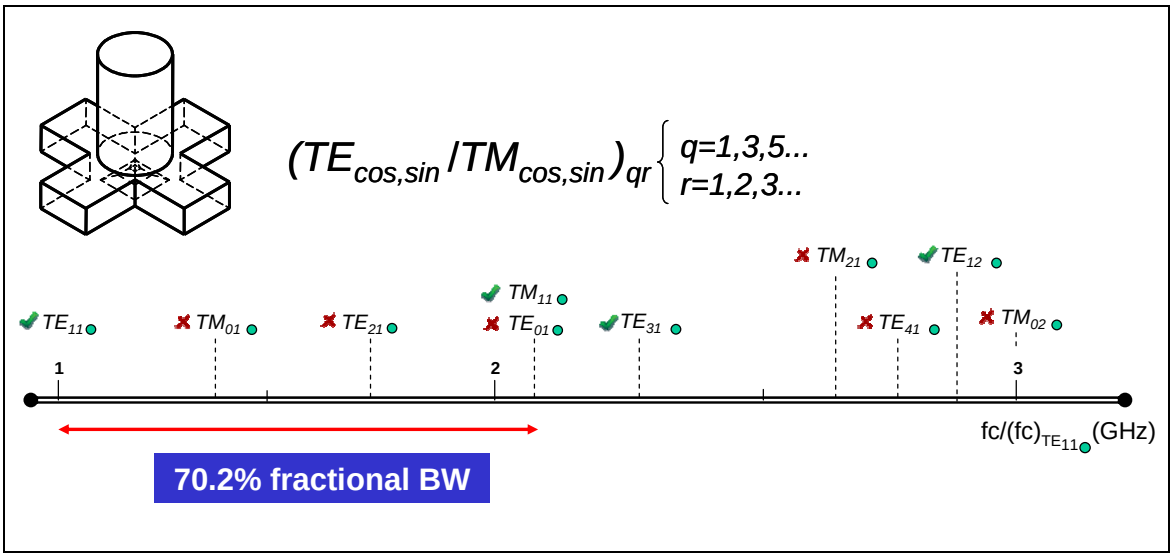

Fig. 6.3. Cutoff frequencies for the modes excited at the common circular port of a Turnstile junction.

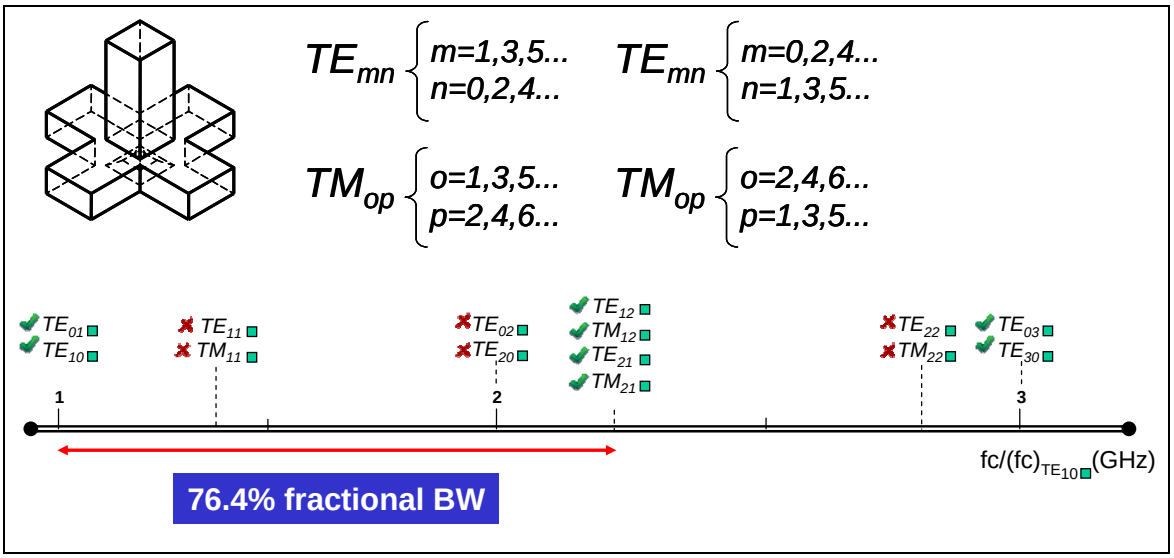

Fig. 6.4. Cutoff frequencies for the modes excited at the common square port of a Turnstile junction.

6.2 Design parameters

Some important parameters concerning the design of a Turnstile junction will be discussed in this section.

6.2.1 Rectangular waveguide cross section

The dimensions of the waveguide branchings determine the cutoff frequencies for the modes inside them. This is important in order to establish a short circuit reference plane for the mode of the common port for which the waveguide is not allocated, i.e., to avoid coupling of unwanted modes which may be above cutoff inside these branchings. Moreover, reducing height will increase some higher-order modes cutoff frequencies, which could be helpful in order to increase bandwidth. In the other hand, a reduced height for the branches may increase losses by non-perfect conductors.

6.2.2 Common port radius / dimension

If the design is not restricted by the radius of the antenna horn and there is enough space in the footprint it is convenient to match cutoff frequencies of circular TE_{11} / square TE_{10}/TE_{01} and rectangular TE_{10} fundamental modes. This will increase operational bandwidth in some cases by choosing appropriate dimensions.

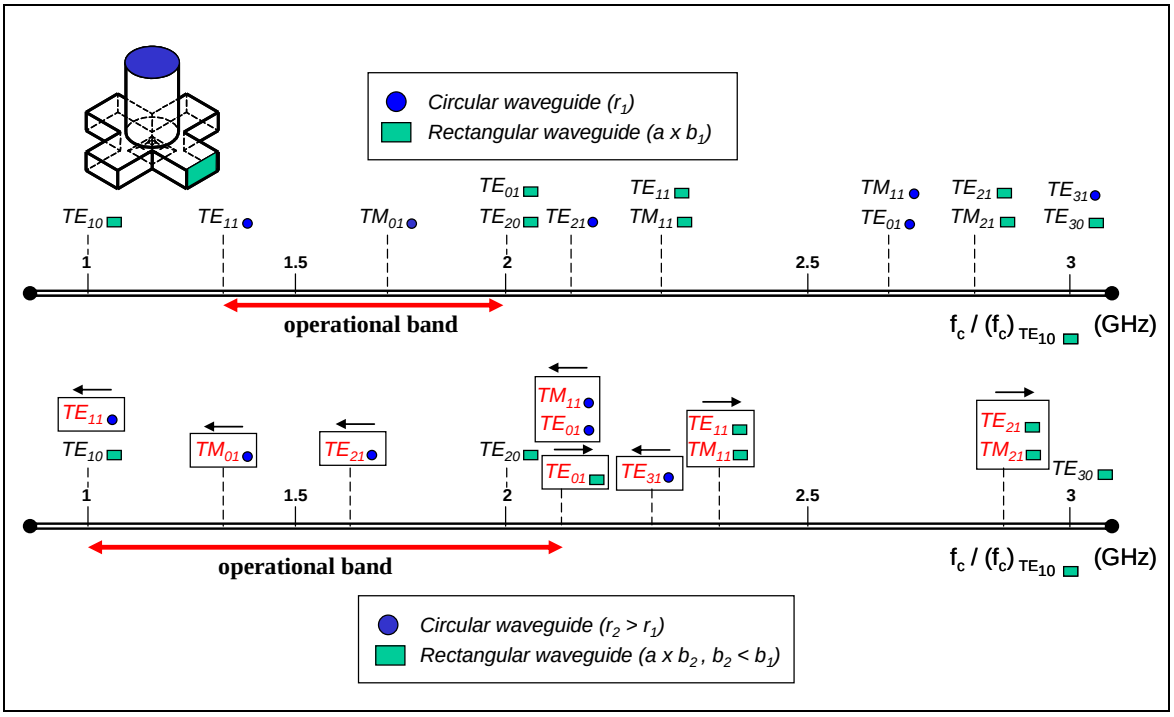

Fig. 6.5. Operational band of a Turnstile junction with common circular port and a method to expand it. In this case a= 15.8 mm, r_1= 6.99 mm, r_2= 9.25 mm, b_1= 7.9 mm and b_2=7.631 mm.

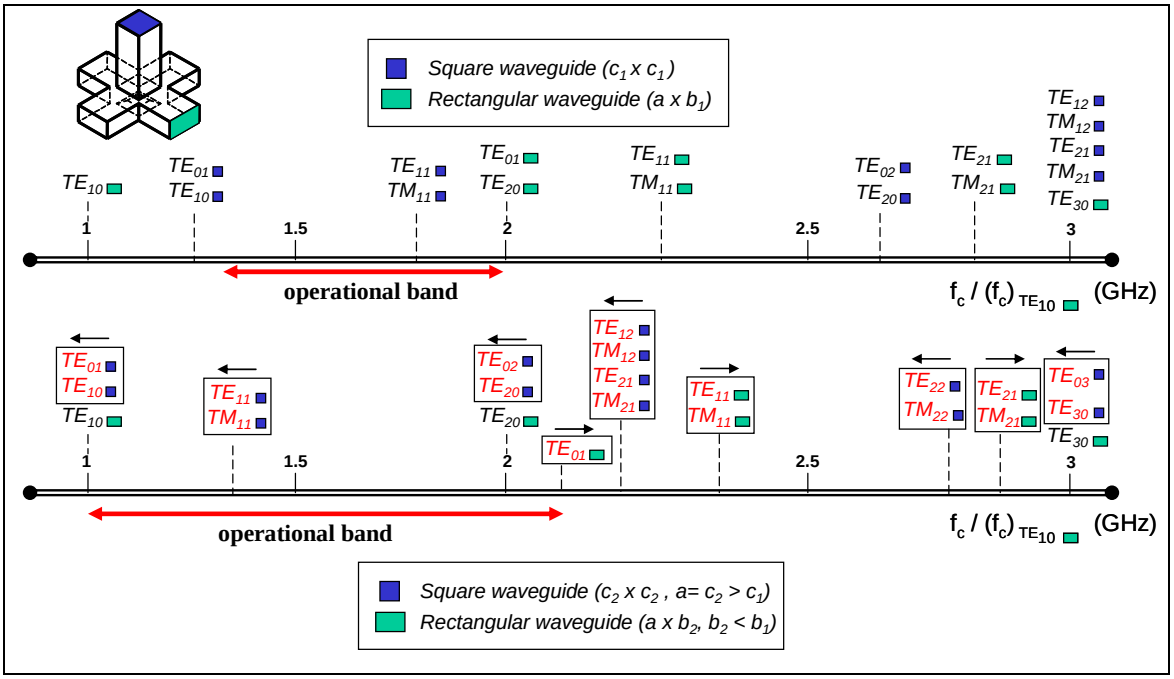

Fig. 6.6. Operational band of a Turnstile junction with common square port and a method to expand it. In this case a= 15.8 mm, c_1= 12 mm, c_2= 15.8 mm, b_1= 7.9 mm and b_2=7.631 mm.

Fig. 6.5 and Fig. 6.6 show the result of applying concepts from Sec. 6.2.1 and Sec. 6.2.2. By this method it is possible to enlarge operational bandwidth from the TE_{11} (circular) and TE_{10} (rectangular) cutoff frequencies to the first unwanted higher-order modes that will be excited in the structure. If a common circular port is used, the TE_{01} from the rectangular waveguide or the TM_{11} from the circular waveguide will be the first modes to be excited, depending on the height of the branches. The same way, if a common square port is used, the TE_{01} from the rectangular waveguide or the TE_{21}/TM_{21}/ TE_{12}/TM_{12} from the square waveguide will limit operative bandwidth. They all have cutoff frequencies of around 2.08 times the TE_{10} rectangular fundamental mode. Excitation of TM_{01} / TE_{21} modes from the circular waveguide is avoided by the fourfold symmetry of the Turnstile as it happens with the TE_{11}/TM_{11} and TE_{20}/TE_{02} from the square waveguide.

6.2.3 Circular to rectangular transition

It is also desirable to include this transition right after the main body of the Turnstile. It improves matching properties at the lower frequencies of the operation band by canceling some unwanted modes reflected back to the common port.

6.2.4 Internal obstacle

Latest Mode-Matching techniques allow an easy and efficient design of Turnstile junctions without internal obstacles, or with obstacles of canonical shape. Unfortunately these obstacles help improving matching properties and broadband operation, so they are often included and another analysis method is needed like that used by HFSS (FEM, Finite Element Method). These obstacles will be deeply treated in Sec 6.3.

6.2.5 Angle of the branches

The four branches of the Turnstile junction generally form a 90-degree bend with the common waveguide. One of the ideas that came out during this project was to test some modified designs with different angles for the branches. Intuitively, better return losses could be achieved if the angle of the bend is less than 90º. As it will be discussed in the next chapter, these designs would also offer a more compact solution for the OMT as well as a natural method to reduce the height of the branches.

6.3 Internal obstacle of the Turnstile junction

An internal obstacle is placed inside the junction in order to improve matching properties for incident modes. Different shapes of this obstacle yield different results for return losses, transmission coefficients, etc. An improved performance can be achieved with just a prism, although more complex structures like two concentric cylinders allow to operate over a wider band with even better performance. Figs 6.7-6.12 show some of this obstacles which have been tested for this project using a Turnstile with fixed radius (9.25 mm) and standard rectangular cross section (WR62, 15.8×7.9 mm) and return losses obtained between 10 and 19 GHz

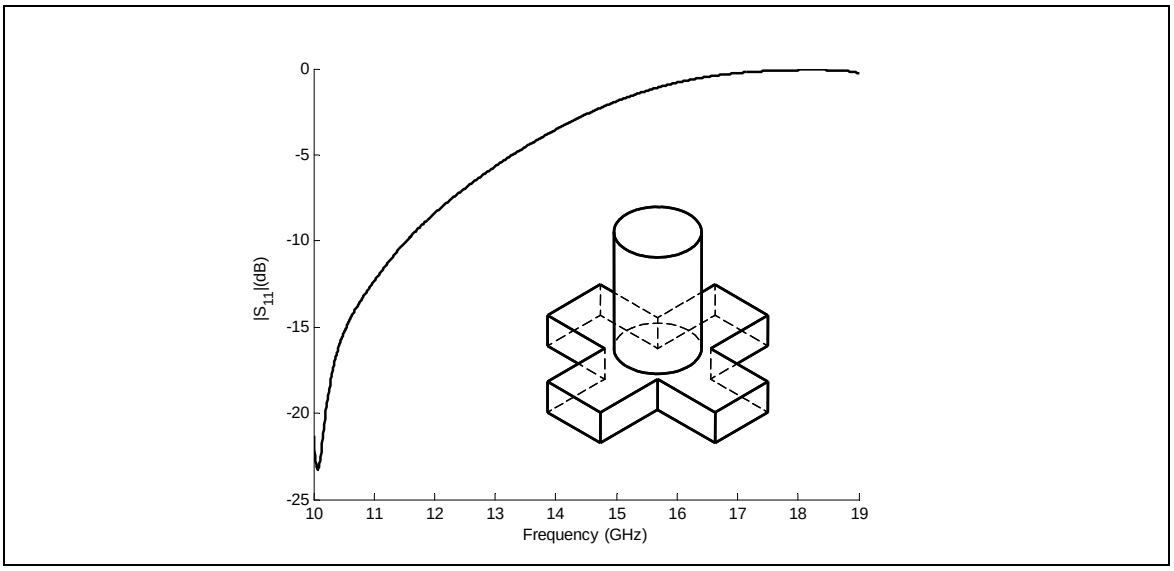

Fig. 6.7. Return losses at the common port of the Turnstile junction without internal obstacle (*r=9.25 mm* ; *a x b=15.8 x 7.9 mm*).

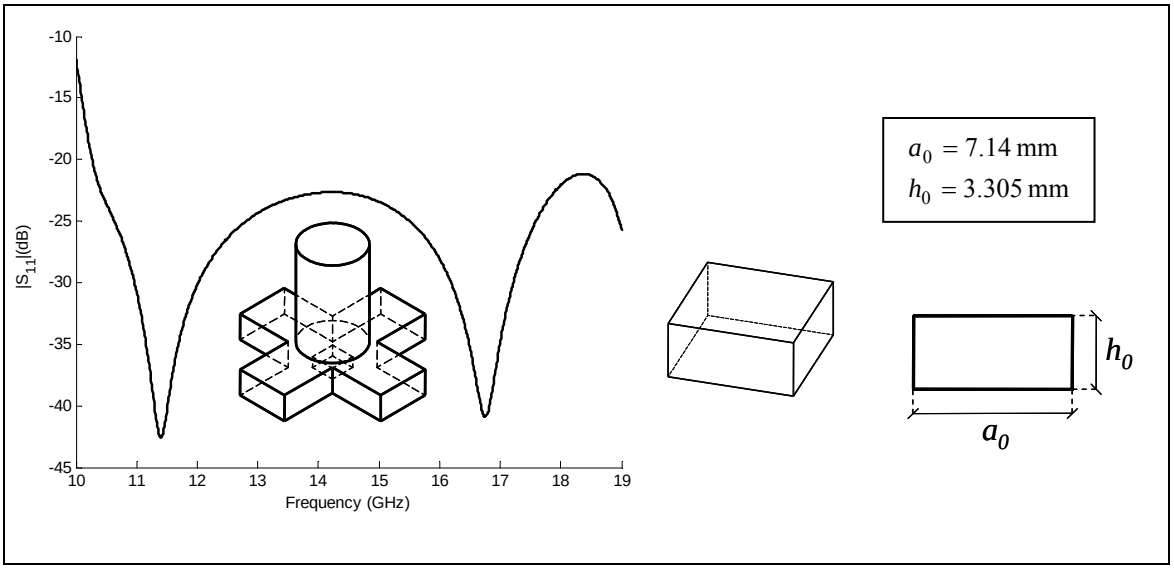

Fig. 6.8. Return losses at the common port of the Turnstile junction with a rectangular prism as internal obstacle and its design variables (*r=9.25 mm* ; *a x b=15.8 x 7.9 mm*).

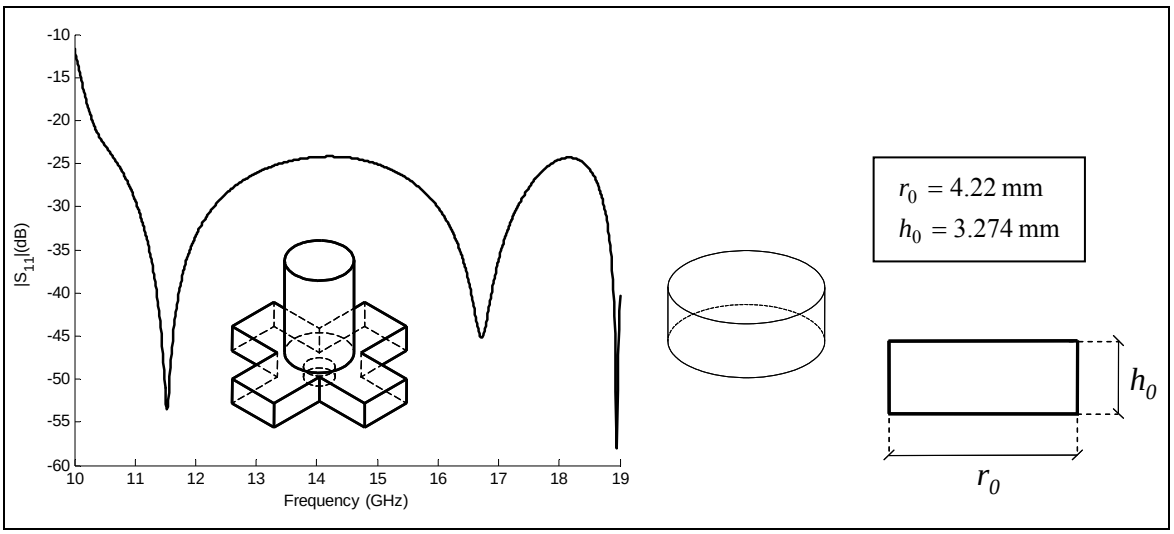

Fig. 6.9. Return losses at the common port of the Turnstile junction with a cylinder as internal obstacle and its design variables (*r=9.25 mm* ; *a x b=15.8 x 7.9 mm*).

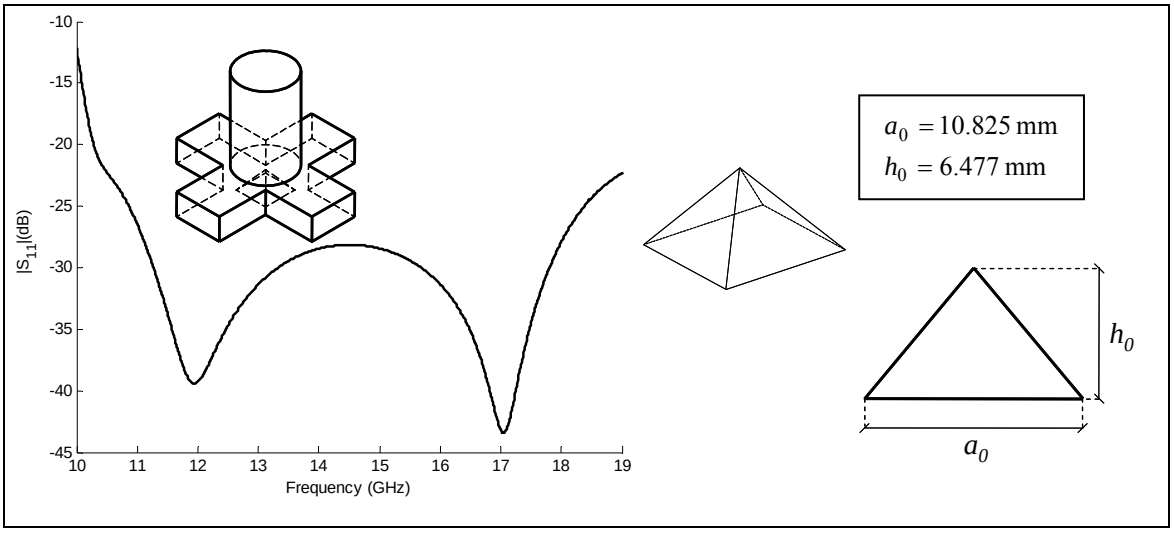

Fig. 6.10. Return losses at the common port of the Turnstile junction with a pyramid as internal obstacle and its design variables (*r=9.25 mm* ; *a x b=15.8 x 7.9 mm*).

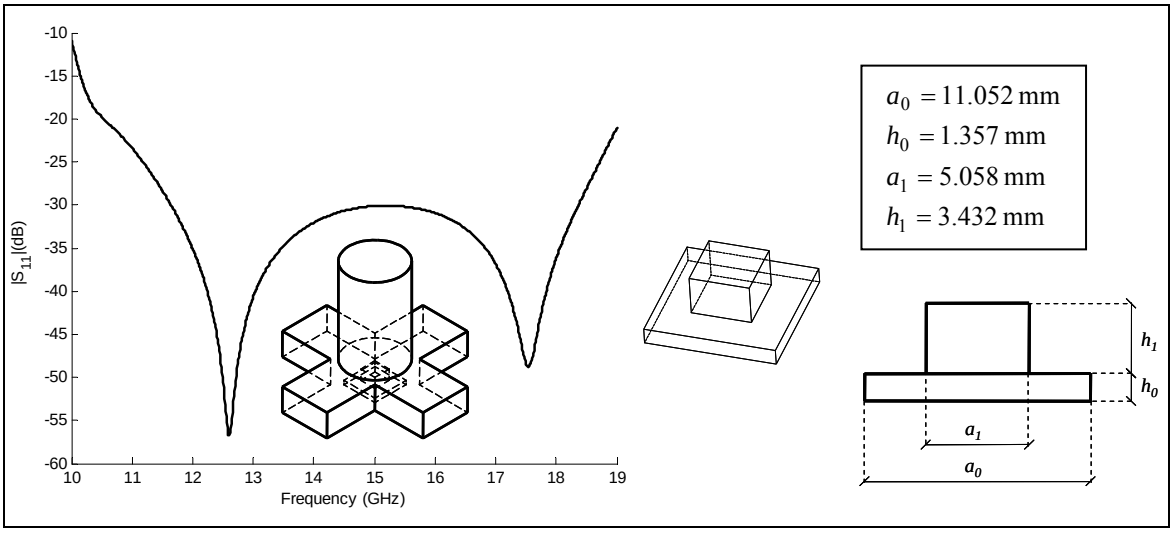

Fig. 6.11. Return losses at the common port of the Turnstile junction with two rectangular prisms as internal obstacle and its design variables (*r=9.25 mm* ; *a x b=15.8 x 7.9 mm*).

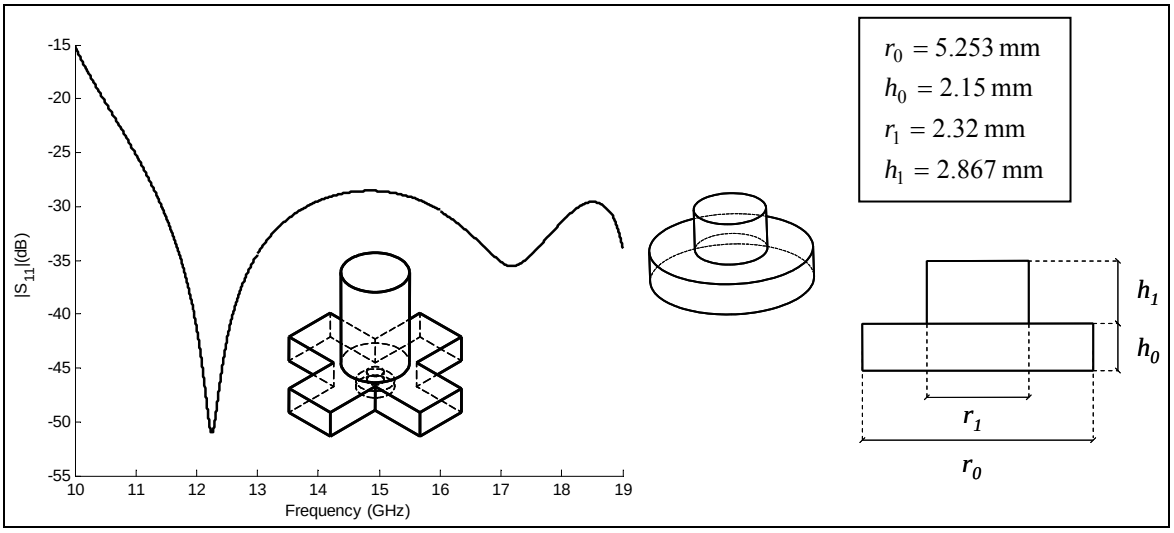

Fig. 6.12. Return losses at the common port of a Turnstile junction with two cylinders as internal obstacle and its design variables (*r=9.25 mm* ; *a x b=15.8 x 7.9 mm*).

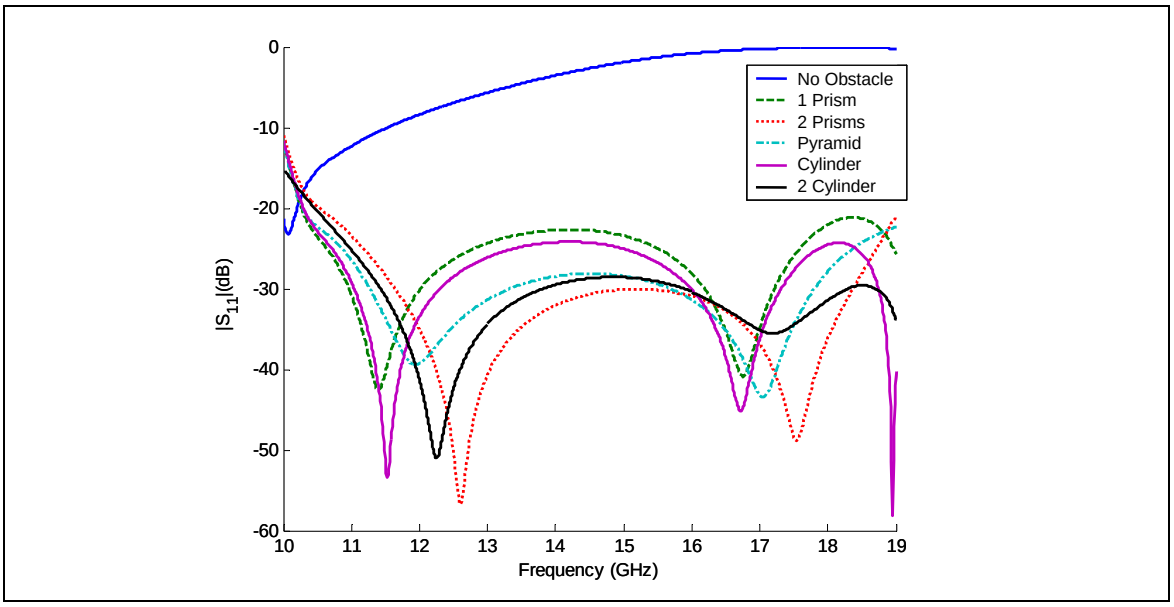

Fig. 6.13. Comparison of return losses for common obstacles of a Turnstile junction.

It can be seen that return losses better than 30 dB can be obtained over a wide band with just two prisms or cylinders.

6.4 Previous designs

Some designs of Turnstile junctions can be extracted from Ch. 2. Navarrini and Plambeck in [NP06] present a Turnstile junction with an internal obstacle with the shape shown in Fig. 6.14. It achieves return losses above 26 dB over the entire band of interest (18-26 GHz, K-band, about 36.4% fractional bandwidth).

Aramaki *et al.* in [AYM03] show how a circular-to-square waveguide step improves the performance in the lower band of interest (see Fig. 6.15). They use a Turnstile junction with a pyramid as internal obstacle. Their fabricated junction presents return losses above 23 dB over the frequency range between 10.7 and 15 GHz (33.5% fractional bandwidth).

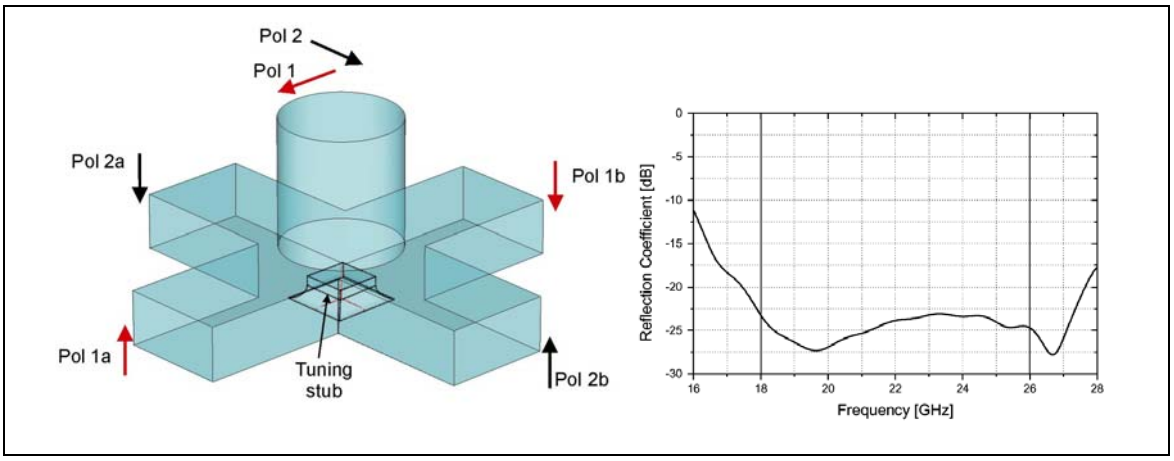

Fig. 6.14. Turnstile junction with tuning stub. From [NP06].

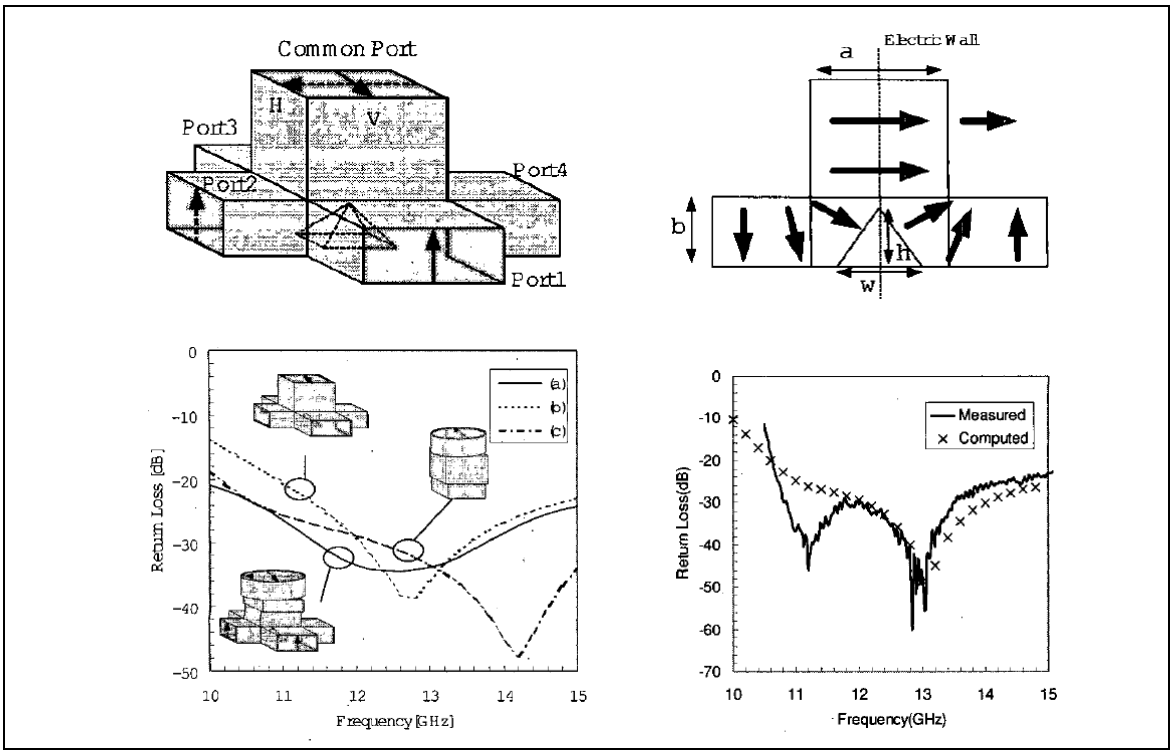

Fig. 6.15. Turnstile junction with pyramid as internal obstacle. From [AYM03]

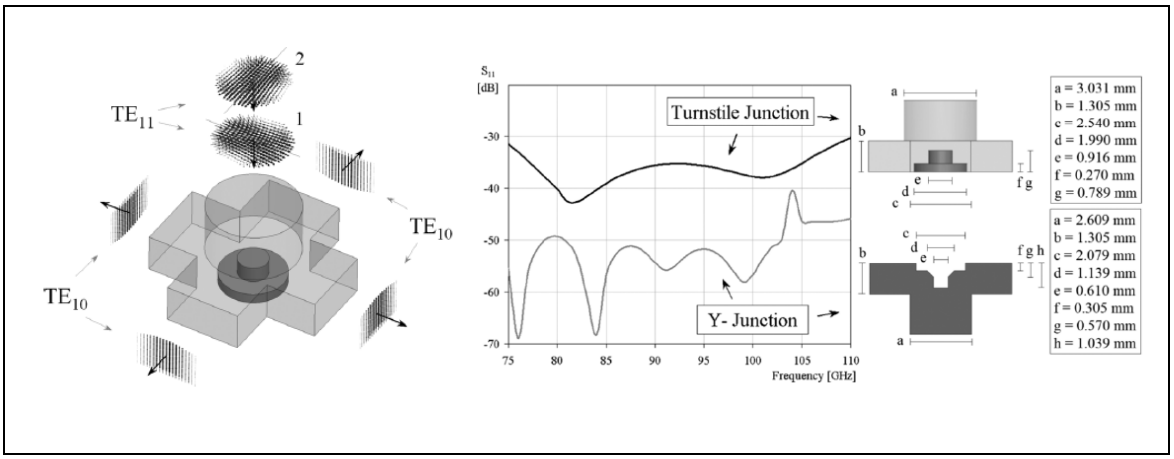

Fig. 6.16. Turnstile junction with two cylinders as internal obstacle. From [PPI07].

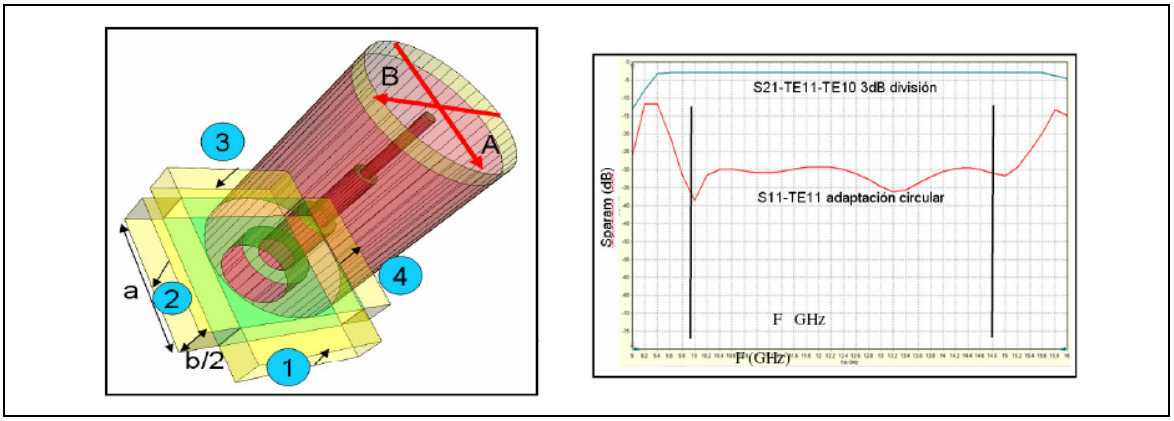

Fig. 6.17. Turnstile junction with four cylinders as internal obstacle. From [TMF08].

The Turnstile junction described in [PPI07] (see Fig. 6.16) with two concentric cylinders as internal obstacle and the one described in [TMF08] (see Fig. 6.17) with four cylinders are the best designs that have been observed so far during this project. The first one presents return losses better than 30 dB in the band between 75 and 110 GHz (WR10, W-band), which represents a 37.8 % fractional band. The second one presents return losses better than 28 dB from 9.8 to around 15.2 GHz (43.2 % fractional band). This design is based on reduced height branches for the Turnstile. As it was stated in Sec. 6.2.1 this may increase bandwidth at the expense of increased return losses.

6.5 Proposal of a new obstacle

During the study of the Turnstile junction and all the internal obstacles stated before, came out the idea of developing a new obstacle different from the structures found in the literature, as far as the author knowledge. The origin of its topology lies in the results obtained for bends with three symmetrical cuts, like those presented in Ch.5. It seems natural to try to emulate the path the wave follows inside a bend but this time inside a Turnstile junction. For this reason, the original structure proposed for this project as internal obstacle had the shape shown in Fig. 6.18.

The obstacle can be understood as the superposition of three square pyramids of different heights and base dimension. This obstacle turned into a bigger structure sketched in Fig. 6.19 after some optimization. The radius of the circular common port for this first design was smaller (6.99 mm) than the radius of the Turnstile junctions compared in Sec. 6.2 (9.25 mm), as it was meant to be part of the design of an OMT with certain restrictions on its dimensions, including this radius. It presents return losses above 26 dB in the band from 13 to 18 GHz (32.3% fractional bandwidth), although its topology may require longer reference planes in the circular waveguide in order to avoid unwanted higher-order modes from reaching the antenna attached to the common port. This consideration has been taken into account during the analysis.

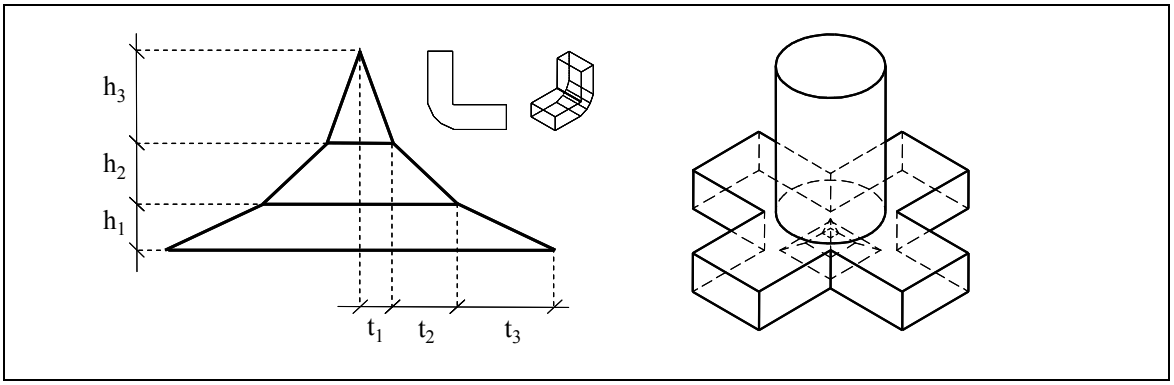

Fig. 6.18. Original dimensions of the internal obstacle proposed in this document and its related Turnstile junction.

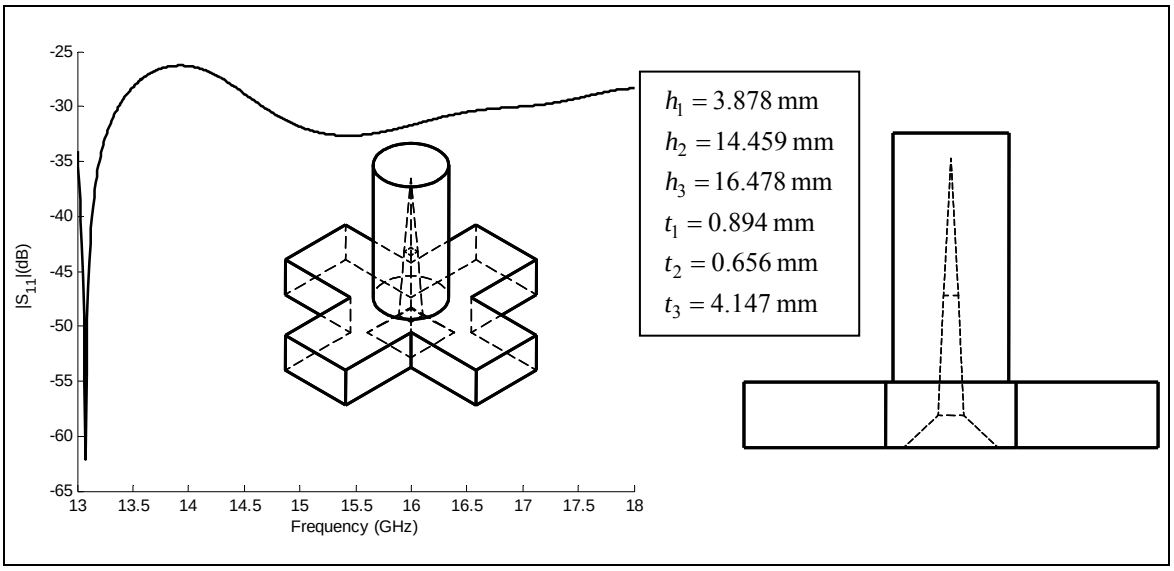

Fig. 6.19. Turnstile junction with the obstacle proposed in this document. (*r=6.99 mm* ; *a x b=15.8 x 7.9 mm*).

6.6 Angled Branches

This is the latest attempt to improve existing Turnstile junctions that will be presented in this document. The idea is to increase the angle between the common circular waveguide and the rectangular branches. The topology that turned out from this idea has two interesting features: first, it would reduce the size of the overall OMT with proper recombinations for both polarizations; second, the height of the rectangular branches is slightly reduced from the original design, which has the effect stated in Sec. 6.2, i.e., it slightly increases bandwidth at the expense of increased losses by non-perfect conductors. This latter feature, along with the possibility of setting a bigger radius for the common waveguide allows us to work over the widest band possible taking up even less space than that from previous designs. Moreover, the obstacle includes a cut (*1 x 1 mm*) at the top thinking of mechanical tolerance.

A sketch of this new obstacle can be seen in Fig. 6.20 along with the results obtained for this Turnstile junction in Fig. 6.21, which includes a circular-to-square transition.

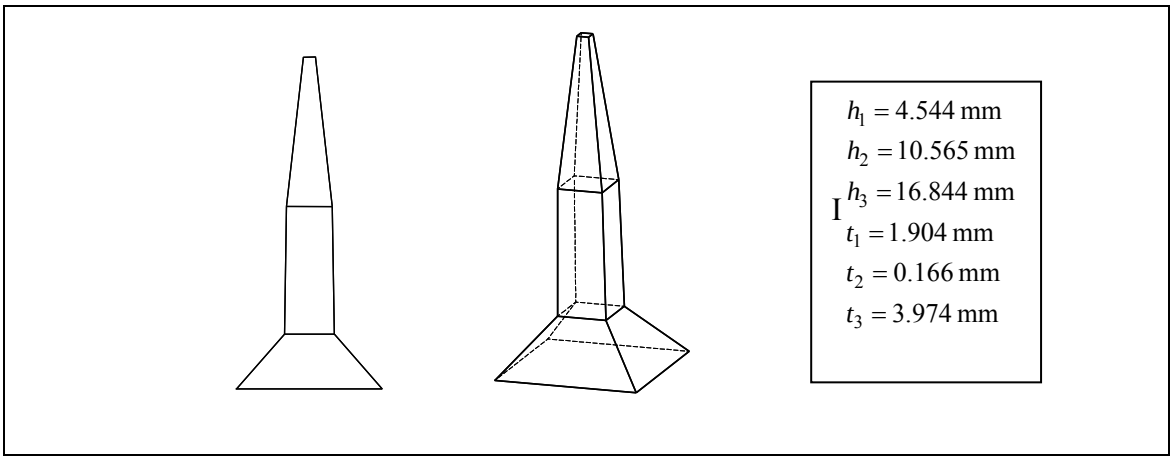

Fig. 6.20. Internal obstacle for the Turnstile junction with angled branches.

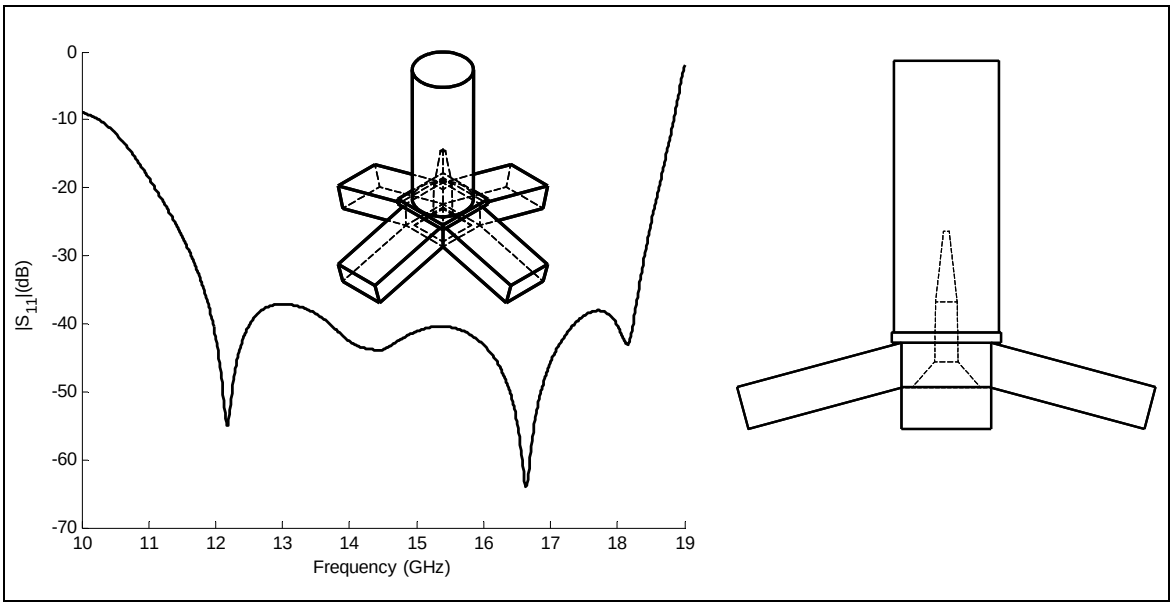

Fig. 6.21. Turnstile junction with angled branches. (*r=9.25 mm*; *a x b=15.8 x 7.9 mm*). Dimensions of the circular-to-square transition (*19.263 x 19.263 x 1.83 mm*)

This Turnstile junction presents return losses above 30 dB from 11.64 to 18.4 GHz (45% fractional bandwidth). This is a great improvement over the previous design, and even over the junctions presented in this chapter.

6.7 Conclusions

The Turnstile junction has been deeply characterized throughout this chapter. Its fourfold symmetry grants broadband performance. The design of its internal obstacle is the only challenge, although it is possible to achieve great performance with a simple prism.

For this project, a new internal obstacle has been designed. It is inspired by waveguide bends with three symmetrical cuts. A first design using this new obstacle presents good return losses above 26 dB in the band between 13-18 GHz.

As an attempt to improve the performance of Turnstile junctions, a new topology has been presented. It makes use of angled branches for the Turnstile which intuitively should result in a better performance, along with a natural way to reduce the height of the branches. A second design using this Turnstile and an optimized version of the internal obstacle sketched before presents great return losses above 37 dB from 11.88 to 18.28 GHz.

The next chapter will focus on the interconnection of all the components designed during chapters 5 and 6 to complete the design of the OMT.

Chapter 7

Design of an OMT based on the Turnstile Junction

7.1 Introduction

Finally, the last step of this project is to address the design of an OMT based on the Turnstile junction described in Ch. 6. The first goal is to present the results of an OMT using some of the structures which have already been presented in this document.

One of the most important details to bear in mind in the process of designing this kind of OMTs is to decide a suitable recombination for the signals previously separated by the Turnstile junction. Some designs, like that presented in [NP06] or [TMF08] and sketched in Fig. 7.1 and Fig. 7.2 choose a full E-plane solution which requires different path lengths for each of the signals, as their phase must be the same at the recombiner. These lengths must be carefully calculated. The OMT of Fig. 7.3 from [AYM03] is based in a double H-plane configuration for the branches combined with E-plane stepped impedance transformers to avoid its superposition. This design is very compact regarding the axis direction of the common port. However, H-plane bends excite TE_{20} mode from the rectangular waveguide, which can degrade its performance if the bend is not far enough from the junction.

The option chosen for this project is to use a mixed solution like that of Fig. 7.4 used in [PII07], i.e., a path made up of E-plane bends for the vertical polarization and another one made up of H-plane bends for the horizontal one. Both paths need a last E-plane recombination. It avoids superposition of the branches and it still keeps one plane of symmetry.

Following these guidelines two OMT designs have been successfully completed. All the bends, recombinators and Turnstile junctions which are part of these OMTs have been properly designed to present matching properties above specifications in order to prevent possible degradation caused by their interconnection.

Figs. 7.1-7.4 also show some information about the four designs stated above. The results obtained for the OMTs presented in this chapter will be compared with these reference works.

The four-port S-matrix of an OMT is given by (see Fig. 3.1 for port numbers):

$$\mathbf{S} = \begin{bmatrix} S_{11} & S_{12} & S_{13} & S_{14} \\ S_{21} & S_{22} & S_{23} & S_{24} \\ S_{31} & S_{32} & S_{33} & S_{34} \\ S_{41} & S_{42} & S_{43} & S_{44} \end{bmatrix} \tag{7.1}$$

For the type of OMT under analysis (see for instance Fig. 7.7), as long as one plane of symmetry is preserved, both polarizations are uncoupled, i.e.:

$$\mathbf{S} = \begin{bmatrix} S_{11} & 0 & S_{13} & 0 \\ 0 & S_{22} & 0 & S_{24} \\ S_{31} & 0 & S_{33} & 0 \\ 0 & S_{42} & 0 & S_{44} \end{bmatrix} \tag{7.2}$$

If the OMT has no losses,

$$\mathbf{S} = \begin{bmatrix} r_1 e^{j\phi_1} & 0 & \sqrt{1-r_1^2}\, e^{j\frac{1}{2}(\phi_1+\phi_3+\pi+2n\pi)} & 0 \\ 0 & r_1 e^{j\phi_2} & 0 & \sqrt{1-r_2^2}\, e^{j\frac{1}{2}(\phi_2+\phi_4+\pi+2n\pi)} \\ \sqrt{1-r_1^2}\, e^{j\frac{1}{2}(\phi_1+\phi_3+\pi+2n\pi)} & 0 & r_1 e^{j\phi_3} & 0 \\ 0 & \sqrt{1-r_2^2}\, e^{j\frac{1}{2}(\phi_2+\phi_4+\pi+2n\pi)} & 0 & r_2 e^{j\phi_4} \end{bmatrix} \tag{7.3}$$

This means that the whole OMT can be fully characterized with only the reflection coefficient for both polarizations. If the OMT has losses (real conductors), the magnitude of the transmission coefficients are no longer related to the magnitude of the reflection coefficients as in the previous equation, and it has to be measured. Moreover, if the symmetry is broken by the manufacturing tolerances, the isolation between polarizations (typically defined as the magnitude of one of these parameters: S_{12}, S_{14}, S_{34} or S_{23}) will not be perfect and has to be carefully computed/measured.

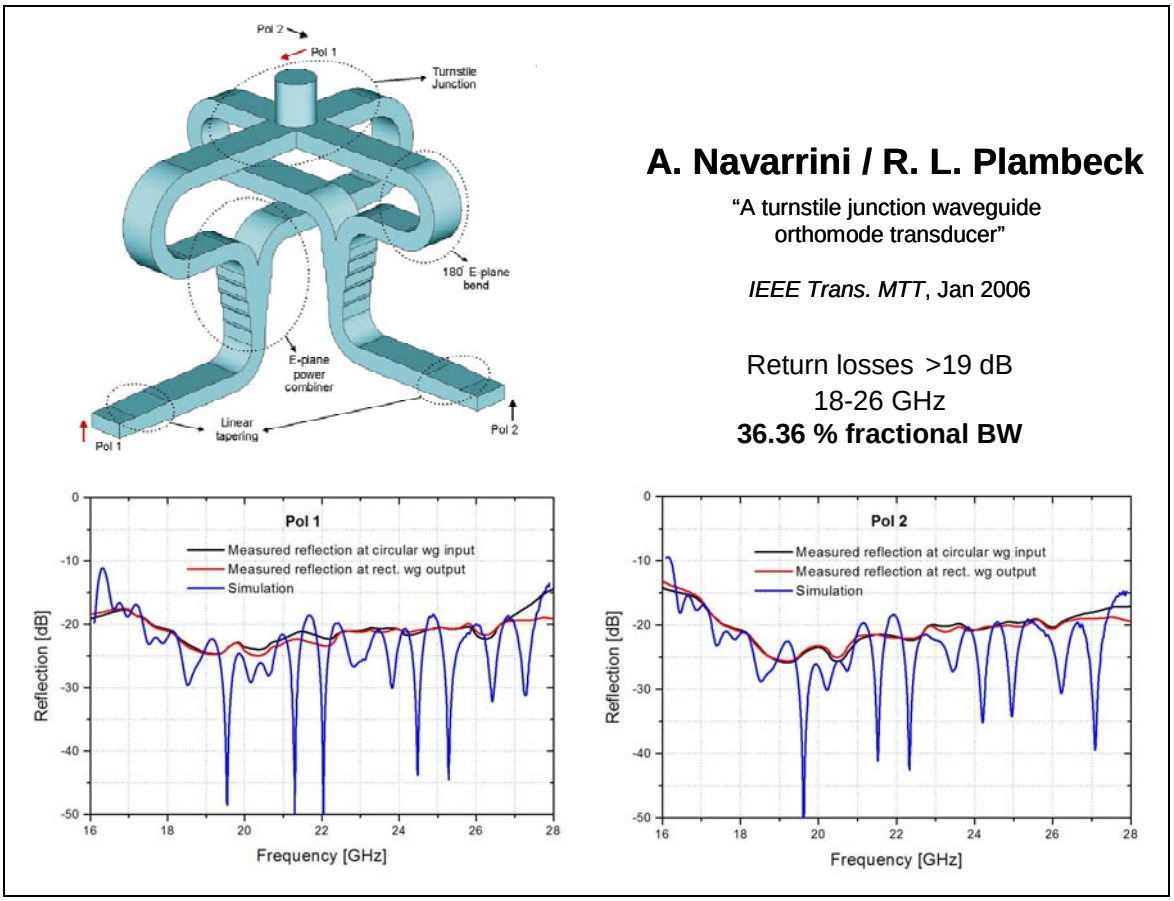

Fig. 7.1. OMT with a double E-plane configuration for the branches. Images and results from [NP06].

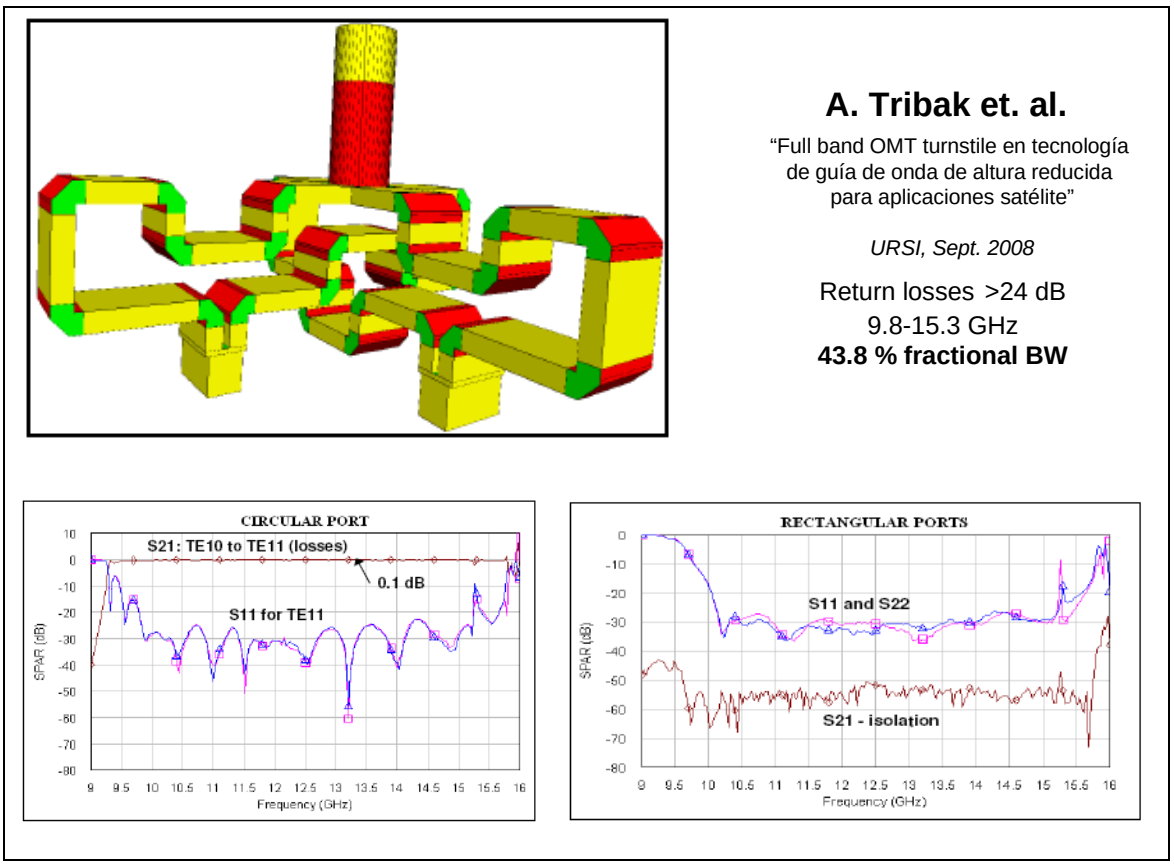

Fig. 7.2. OMT with a double E-plane configuration for the branches and reduced height. Images and results from [TMF08].

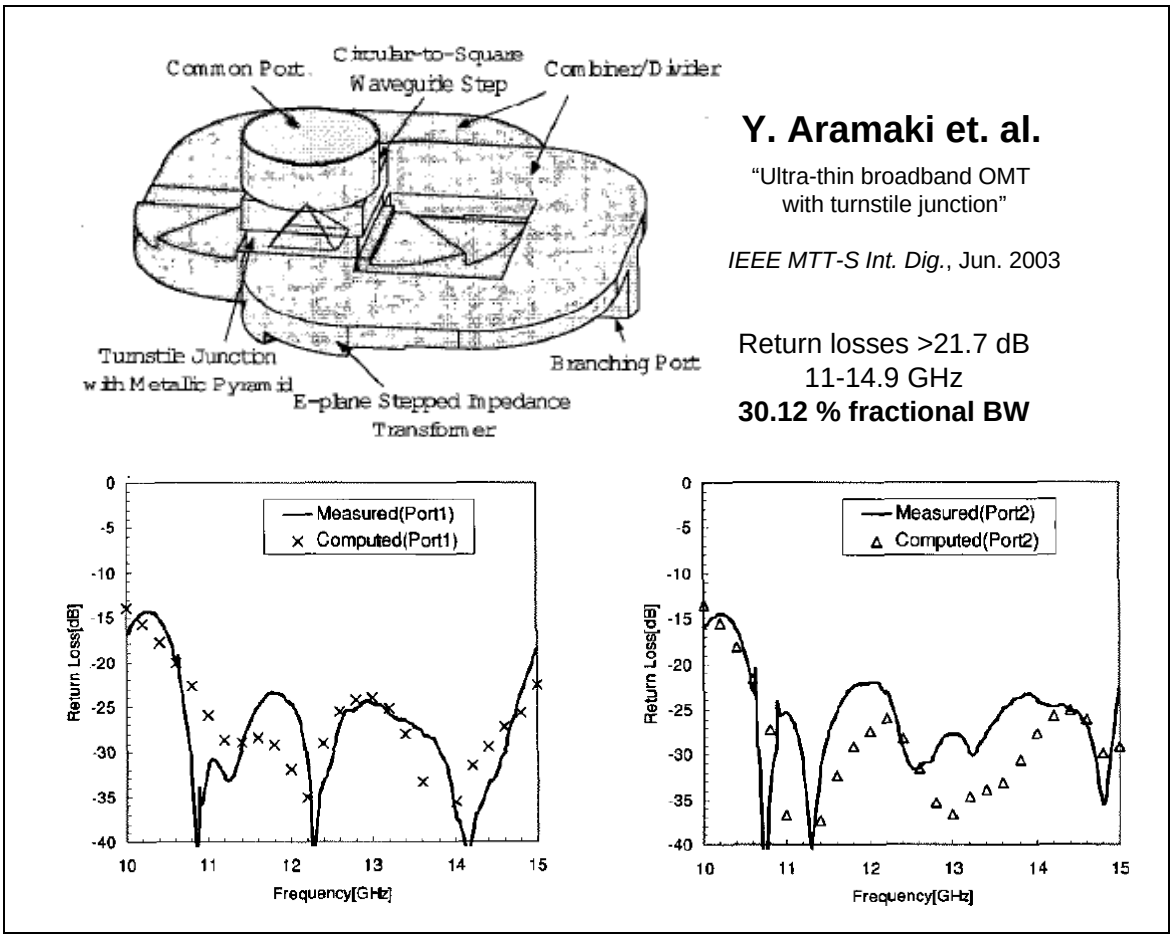

Fig. 7.3. OMT with a double H-plane configuration for the branches. Images and results from [AYM03].

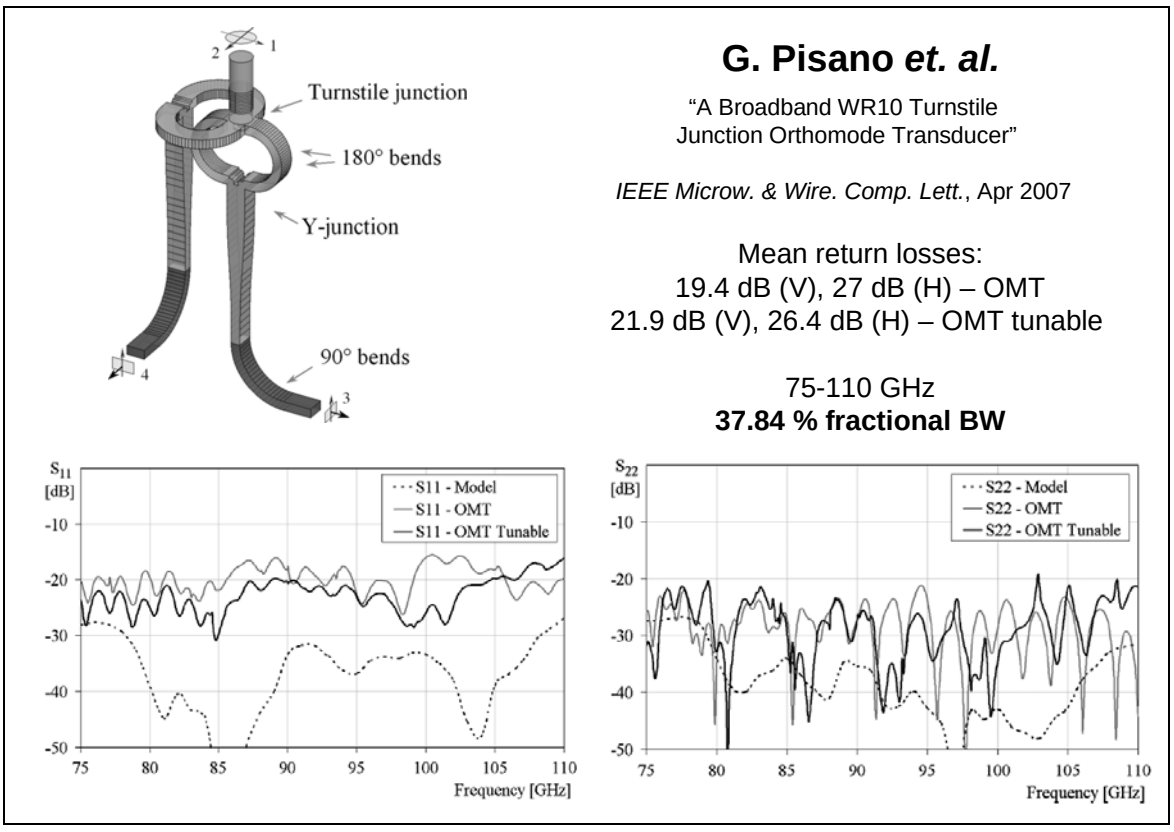

Fig. 7.4. OMT with a mixed E and H-plane configuration for the branches. Images and results from [PPI07].

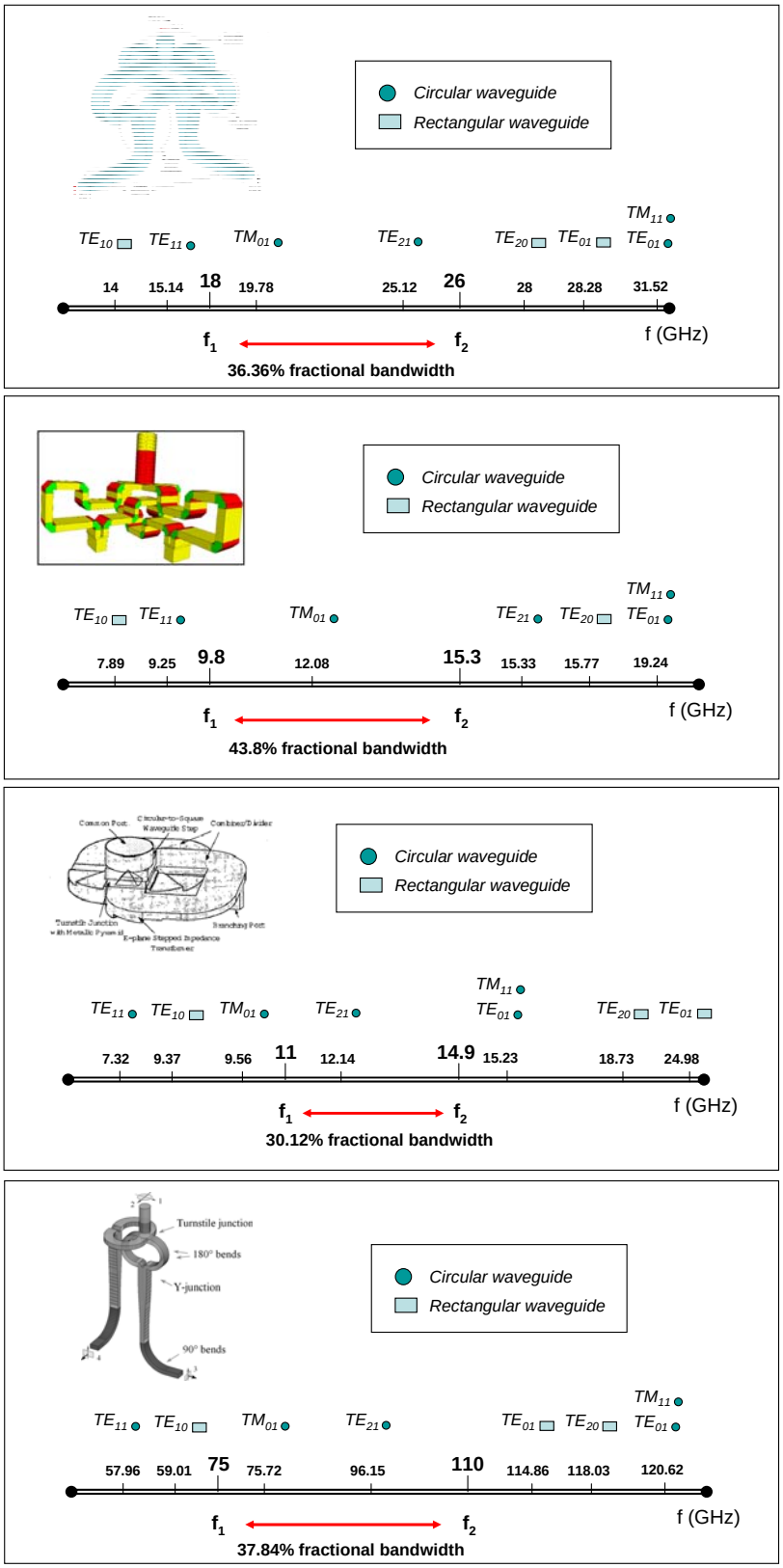

Fig. 7.5. Frequency mapping for the four reference works from Fig. 7.1-7.4. The fractional bandwidth is between points of return loss levels defined in Fig. 7.1-7.4, respectively (which can be different for each design).

7.2 First design

Table 7.1 shows specifications for the first design.

Dimensions	V-H ports → 15.8 mm x 7.9 mm.	Common port radius → 6.99 mm
Polarization	**Frequency Band (GHz)**	**Return losses for the common port**
Vertical and Horizontal	13-18	22 dB

Table 7.1. Specifications for the first design of the OMT.

Common port radius and rectangular waveguide cross-section are fixed dimensions here. Therefore, Sec. 6.1.2 idea of a bigger radius for the common port to match rectangular TE_{10} and circular TE_{11} modes cutoff frequencies can not be applied here. Fig. 7.6 shows cutoff frequencies for the first modes that will be excited within the waveguides in this design.

It can be seen that the structure is limited by the TE_{01}/TE_{20} modes of the rectangular ($b = a/2$) waveguide. The TE_{01} mode is excited by any of the polarizations in the side branches of the opposite polarization. The TE_{20} mode is excited by the H-plane bends of the horizontal branch. Therefore, this structure presents only about a 40% fractional bandwidth.

Fig. 7.7 shows a sketch of the different parts that compose the OMT and Fig. 7.8 shows the routing scheme of this OMT.

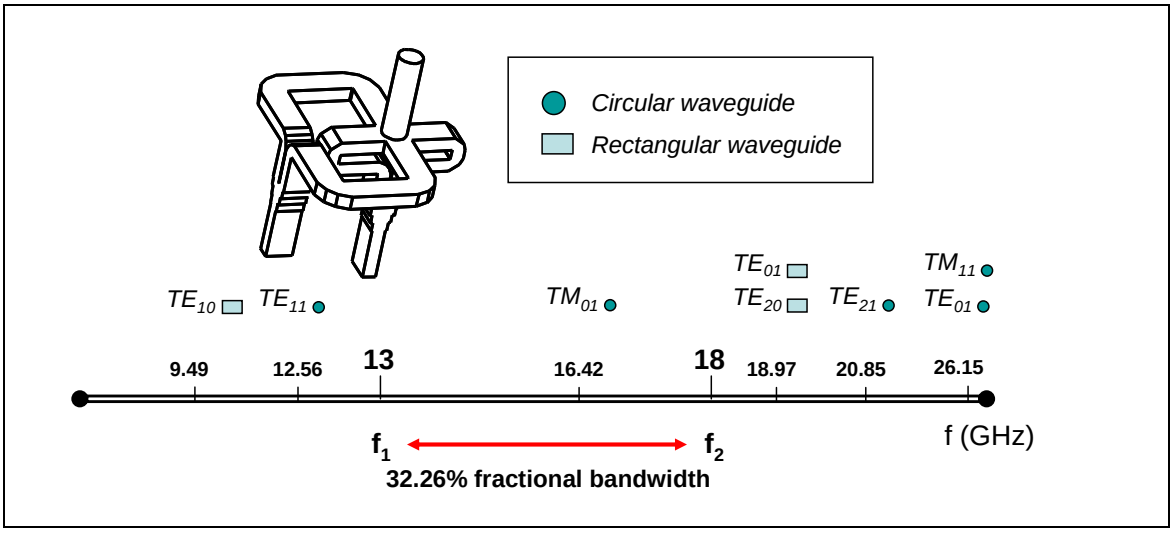

Fig. 7.6. Frequency mapping for the first design of the OMT. (*r=6.99 mm , a x b=15.8 x 7.9 mm*)

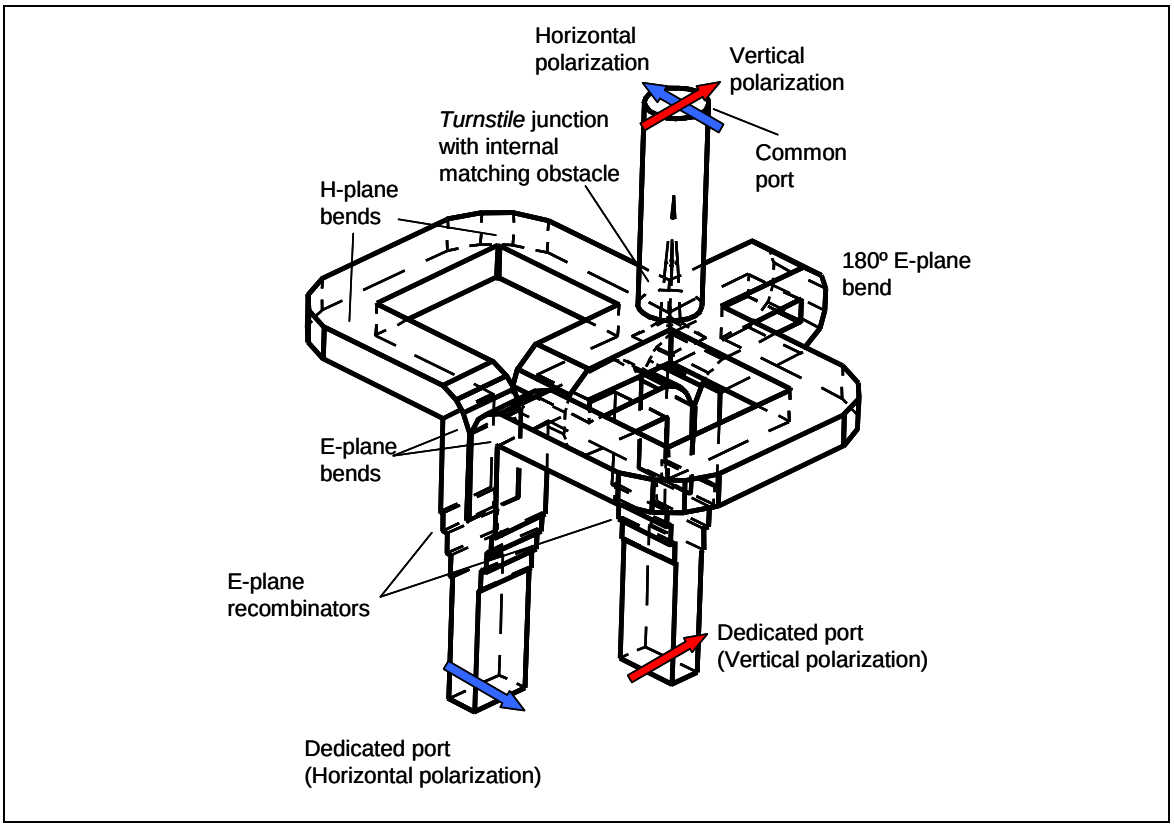

Fig. 7.7. Sketch of the parts that compose the first design of the OMT.

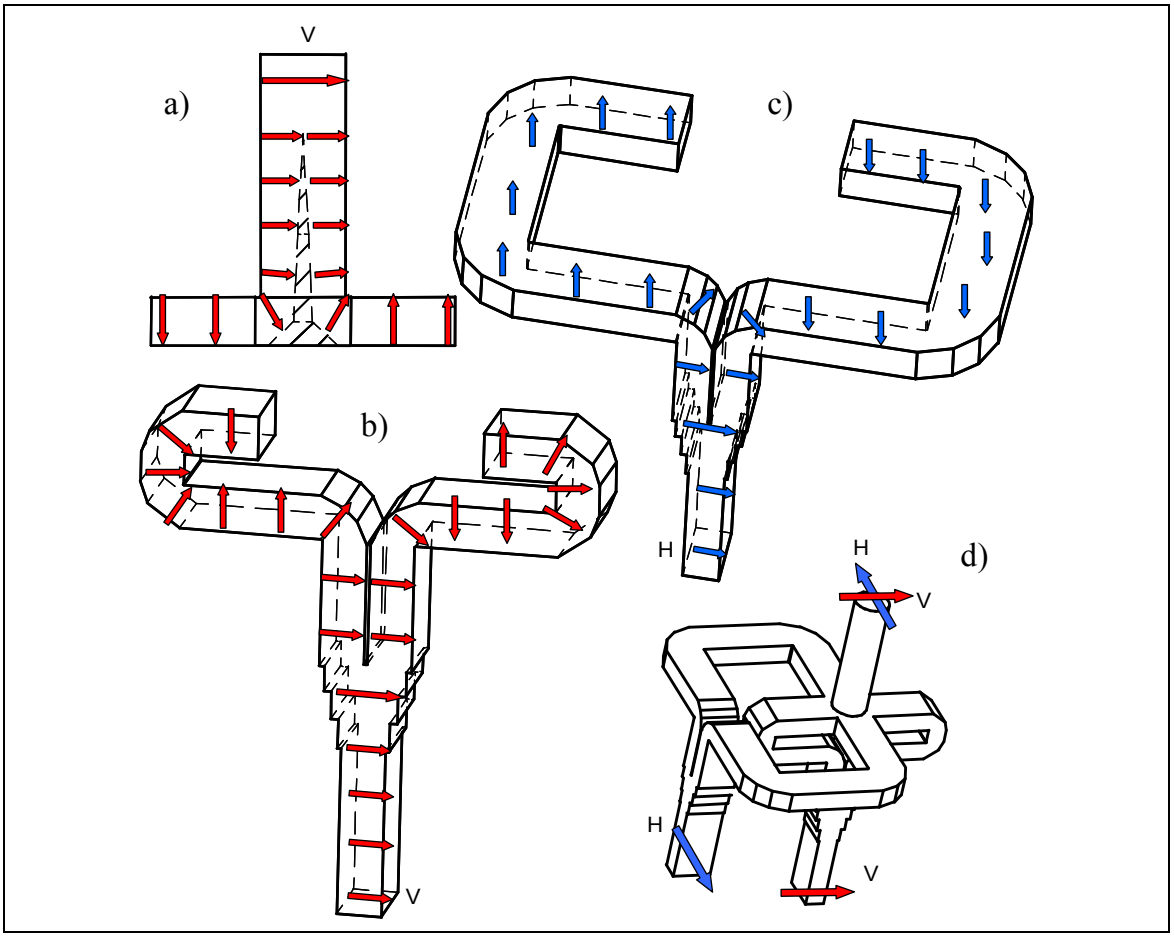

Fig. 7.8. Routing scheme of the first design of the OMT. a) Turnstile junction; b) Vertical branch; c) Horizontal branch; d) OMT.

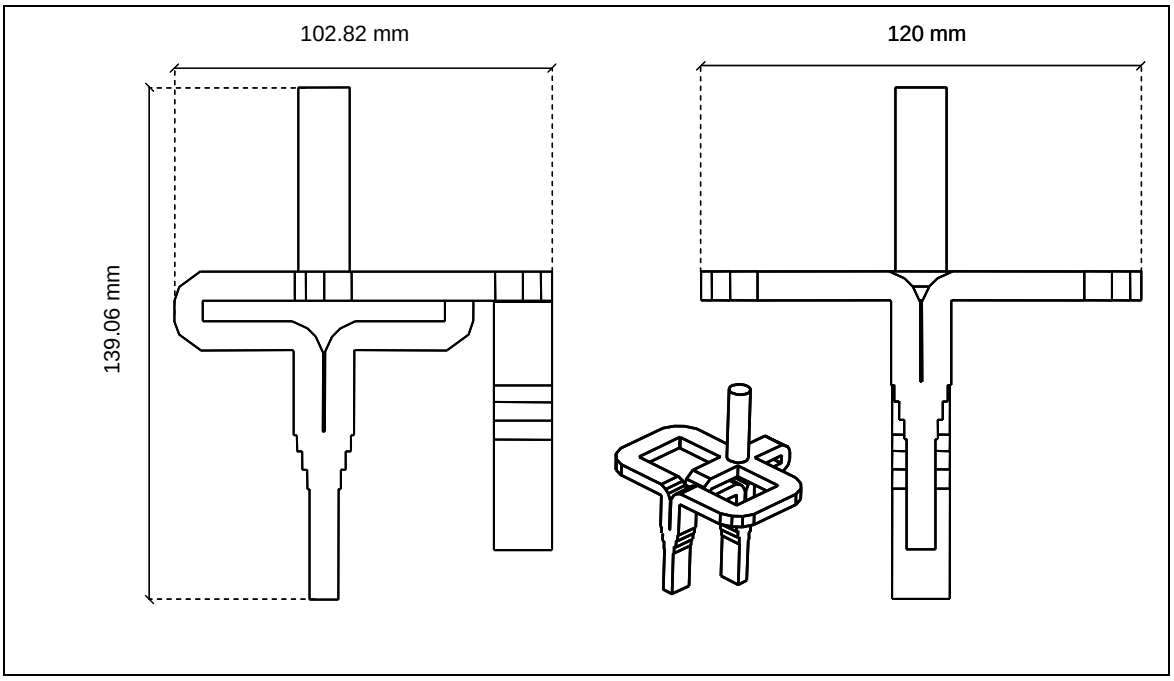

Fig. 7.9. Overall dimensions for the first design of the OMT.

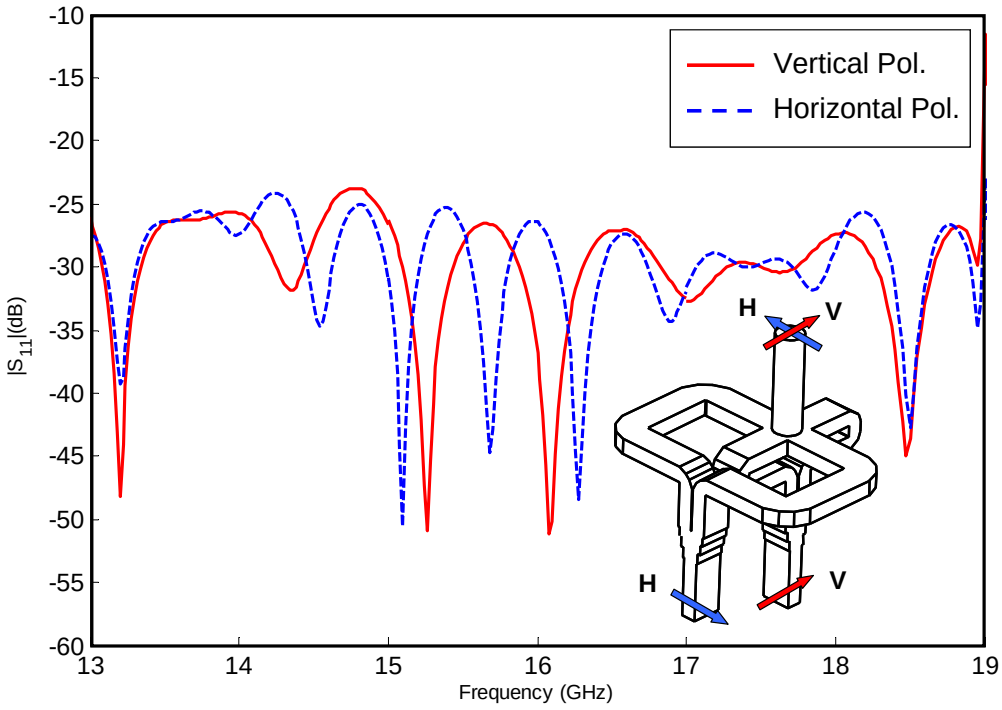

Fig. 7.10. Simulated return losses for the first design of the OMT (*r=6.99 mm , a x b=15.8 x 7.9 mm*).

The overall OMT presents the dimensions of Fig. 7.9 and expected return losses above 24 dB for all the prescribed band (13-18 GHz, 32.26% fractional bandwidth, although it covers until 19 GHz, which is approximately a 37%). This performance is shown in Fig. 7.10. Therefore, the design fulfills the initial specifications. It is remarked here that the OMT has 34 variables involved in its design, carefully obtained for providing the desired performance. The results for this OMT have been published in [IR08]. The text of this article can be found in Appendix B.

7.3 Second design

The results obtained for the Turnstile junction with angled branches motivated this second OMT. This Turnstile junction had a great performance over the band between 10 and 19 GHz (see again Fig. 6.21), so it was worth to make a little effort to design better routing structures expecting an increase in bandwidth and performance for the overall OMT.

Common port radius is not restricted to a fixed value this time, so it is recalculated to match the frequency of the TE_{11} circular mode to that of the TE_{10} rectangular fundamental mode. The result is a radius of 9.25 mm (see Fig. 7.11 for the cutoff frequencies of the modes for this design). The topology used for the Turnstile junction also involves reduced heights for the rectangular side branches (7.631 mm). This design also includes two more sections for the recombiner as an attempt to increase bandwidth. Fig. 7.12 shows the routing scheme of this OMT.

The results obtained for this second design of the OMT are shown in Fig. 7.14. It presents return losses better than 30 dB for the band between 11.8 and 18.48 GHz, which represents a 44.12% fractional bandwidth. The design is more compact than the first one, as it can be seen in Fig. 7.13.

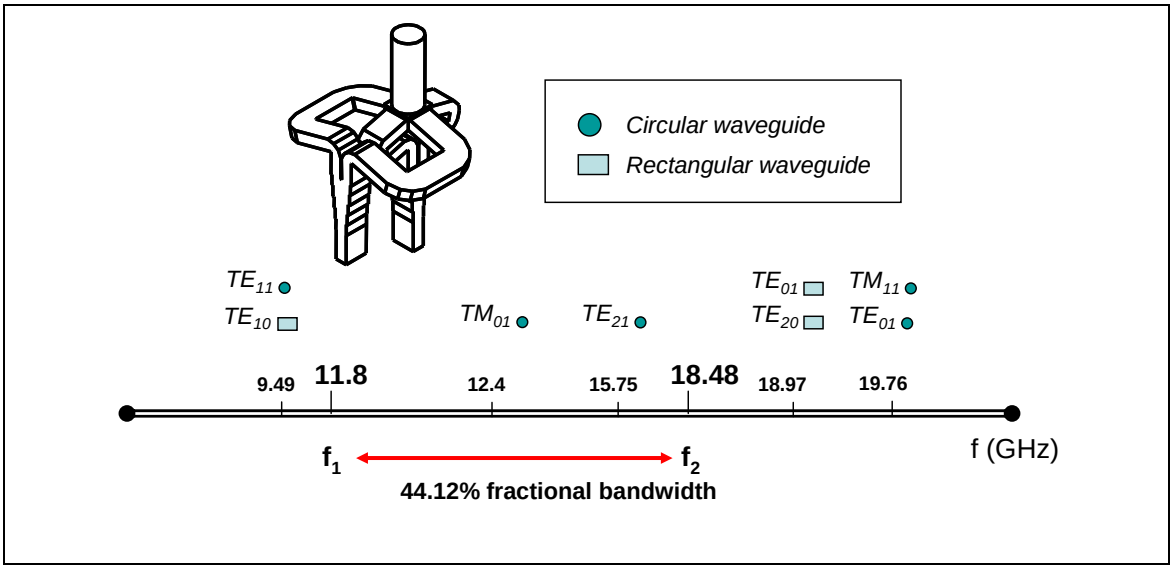

Fig. 7.11. Frequency mapping for the second design of the OMT (*r=9.25 mm , a x b=15.8 x 7.9 mm*).

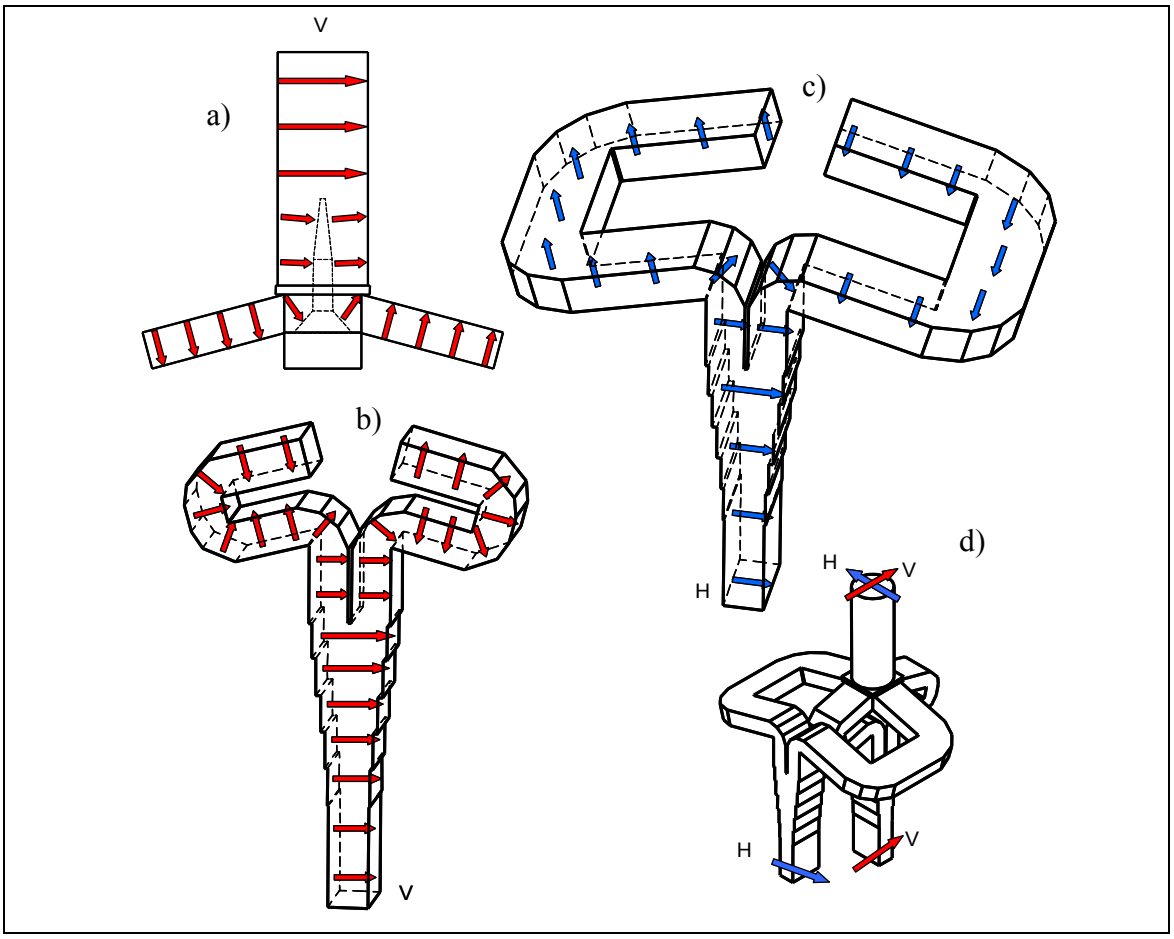

Fig. 7.12. Routing scheme of the second design of the OMT. a) Turnstile junction; b) Vertical branch; c) Horizontal branch; d) OMT.

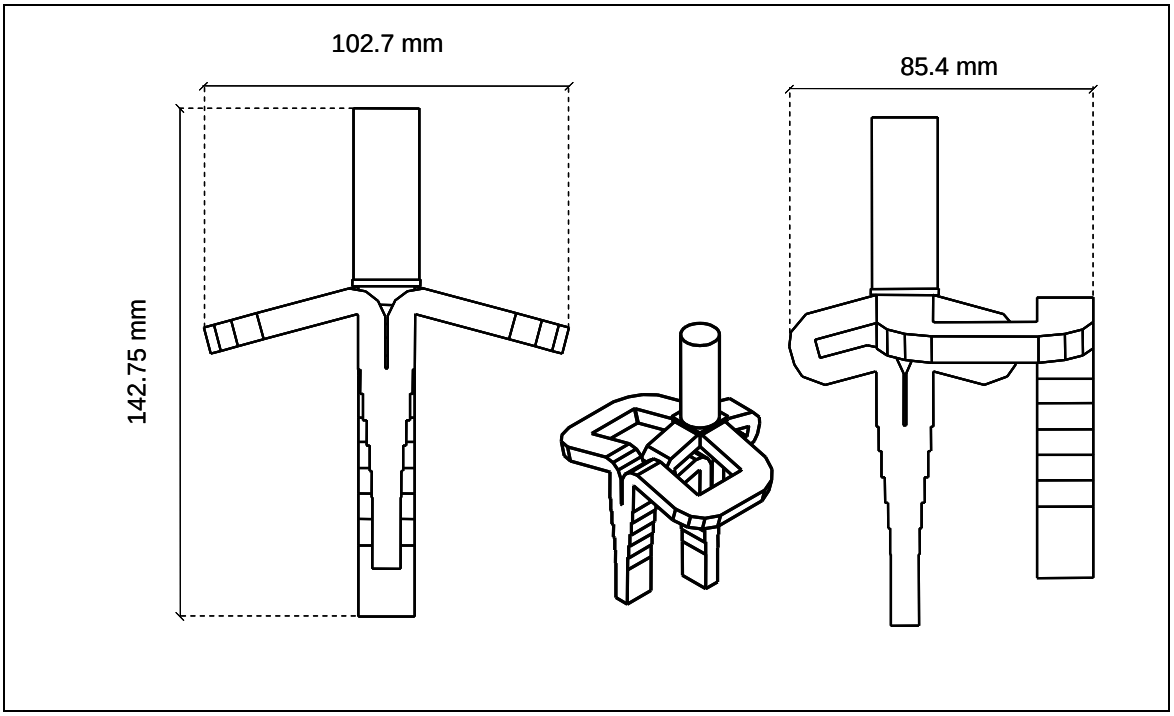

Fig. 7.13. Overall dimensions for the second design of the OMT.

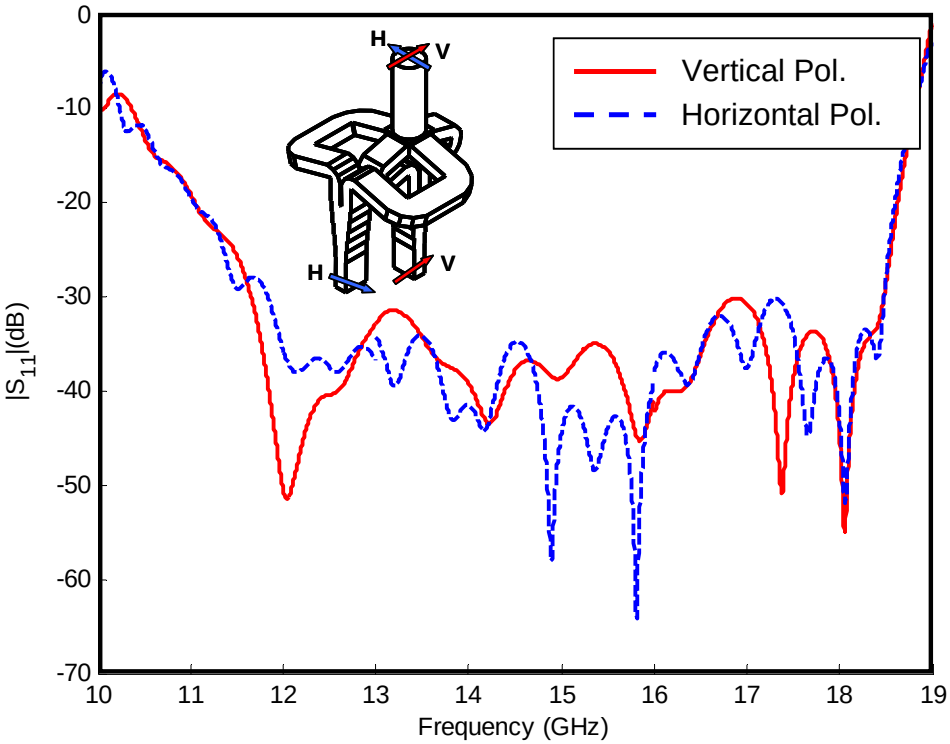

Fig. 7.14. Simulated return losses for the second design of the OMT (*r=9.25 mm , a x b=15.8 x 7.9 mm*)

7.4 Other simulations for the second design

The effect of a finite conductivity of $\sigma = 58 \cdot 10^6$ S/m (typical value for the copper metal) for the conductors is also approximated now. Fig. 7.15 shows the insertion losses for both polarizations when non-perfect copper conductors are used in the waveguides.

The second design has been further analyzed with the HFSS to see the effect on the simulations when higher-order modes are included in the ports. The conductors are again assumed to be perfect. Fig. 7.16 shows the two different analysis that have been performed when the TM_{01} (f_c=12.4 GHz) and the $TE_{21,cos,sin}$ (f_c=15.75 GHz) modes are included in the simulation. It should be noted that S-parameters are referred to the plane labeled A in these analyses, which is 30 mm away from the first discontinuity (the internal matching object of the Turnstile junction). Fig. 7.17 and Fig. 7.18 show the results obtained for these analyses. The parameters for these modes are computed with less accuracy than for the fundamental ones, resulting in a high variation and absolute value which can differ from other full-wave simulators as CST-MWS. Nevertheless, it is interesting to include these graphs for seeing their trend.

Finally, the effect of the manufacturing tolerances has been also considered. Fig. 7.19 shows the computations of the HFSS when the internal matching obstacle of the Turnstile junction is misaligned in 0.05 mm with respect to the axis of the common port in both the *x* and *z* directions (check the coordinate system in Fig. 7.16). This misalignment breaks the symmetry of the problem and couples the polarizations. The isolations which are perfect in the symmetric problem are now reduced to the values shown in the graphs. Its computed value and variation changes a lot with the adaptive pass and they can only be used as an estimation. On the other hand, the return losses are almost not affected.

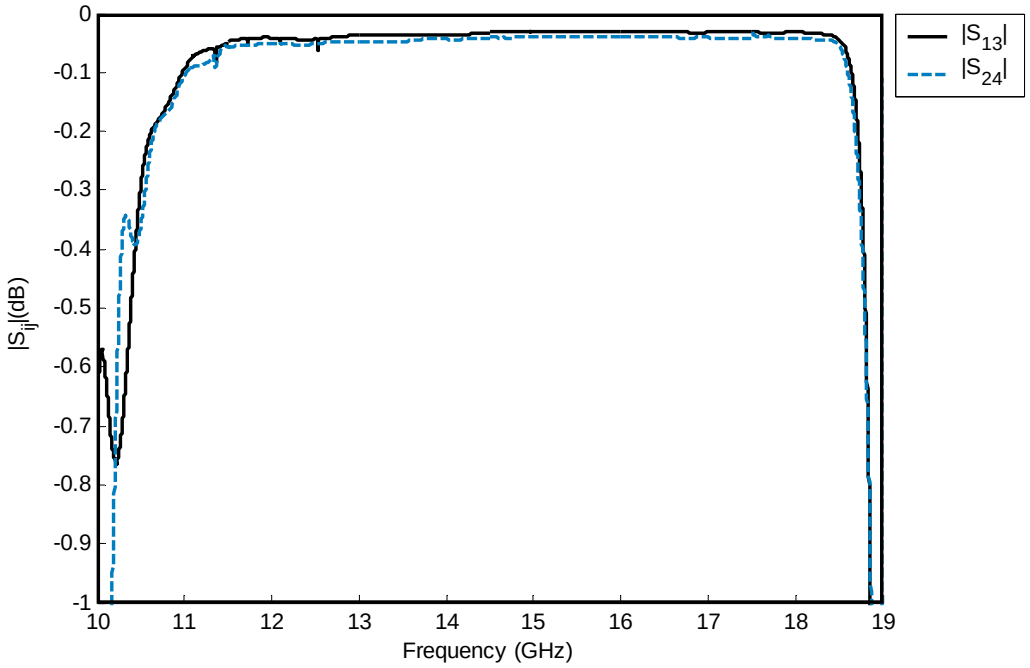

Fig. 7.15. Insertion losses for both polarizations of the second design of the OMT when non-perfect copper conductors are used in the waveguides ($\sigma = 58 \cdot 10^6$ S/m).

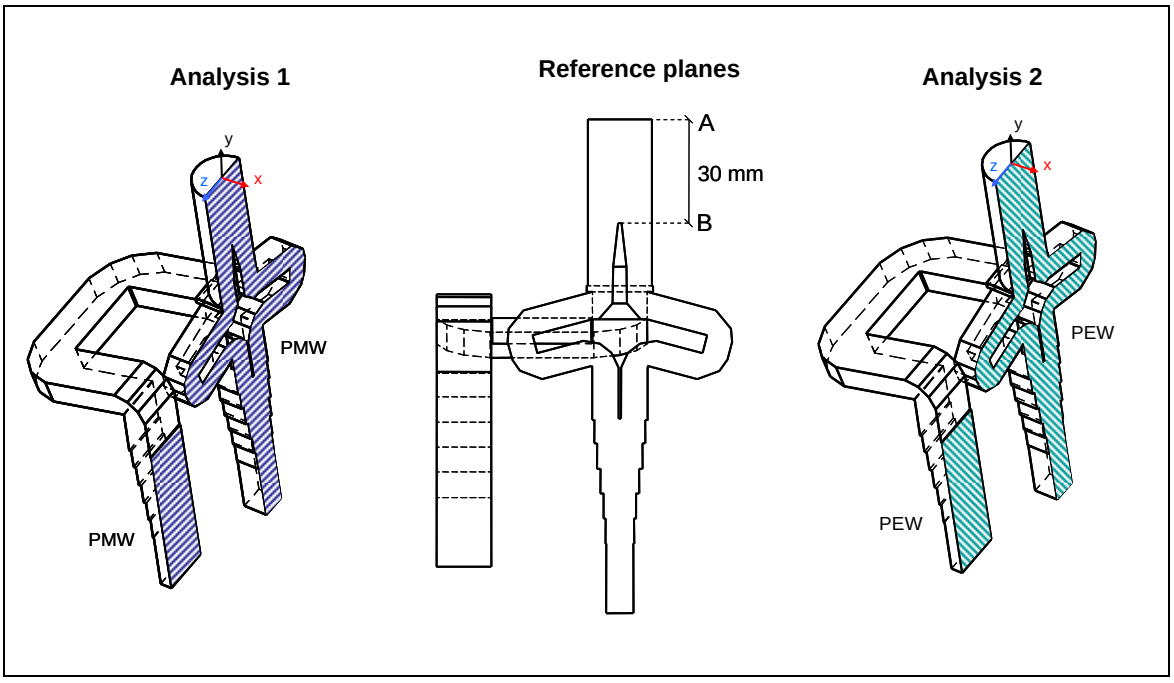

Fig. 7.16. Sketch of the two analysis performed when the TM_{01} and the $TE_{21,cos,sin}$ modes are included in the simulation. Coordinate system and reference planes are indicated.

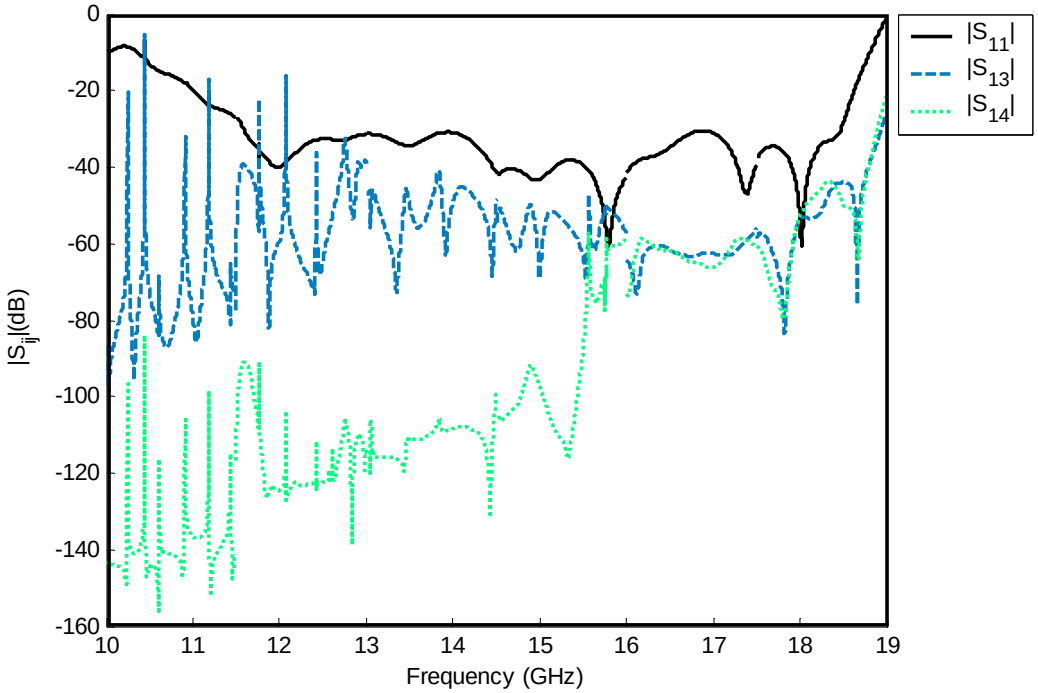

Fig. 7.17. Results for the first analysis from Fig. 7.16. Electric ports: 1 (vertical circular $TE_{11,cos}$), 2 (rectangular TE_{10}, vertical pol.), 3 (circular TM_{01}) and 4 (circular $TE_{21,sin}$).

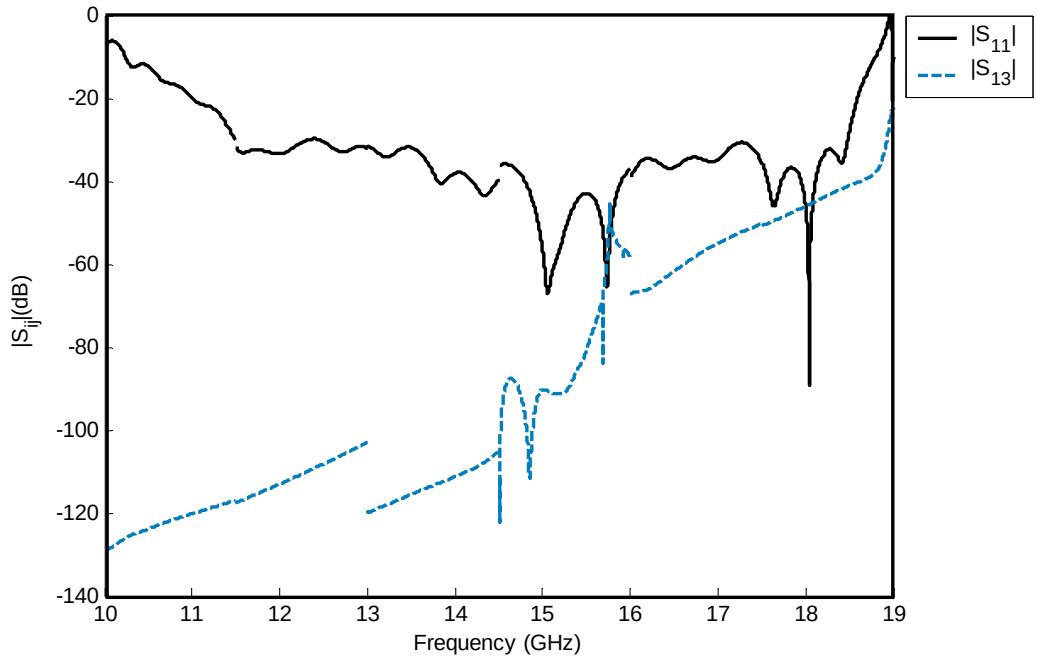

Fig. 7.18. Results for the second analysis from Fig. 7.16. Electric ports: 1 (horizontal circular $TE_{11,sin}$), 2 (rectangular TE_{10}, horizontal pol.) and 3 (circular $TE_{21,cos}$).

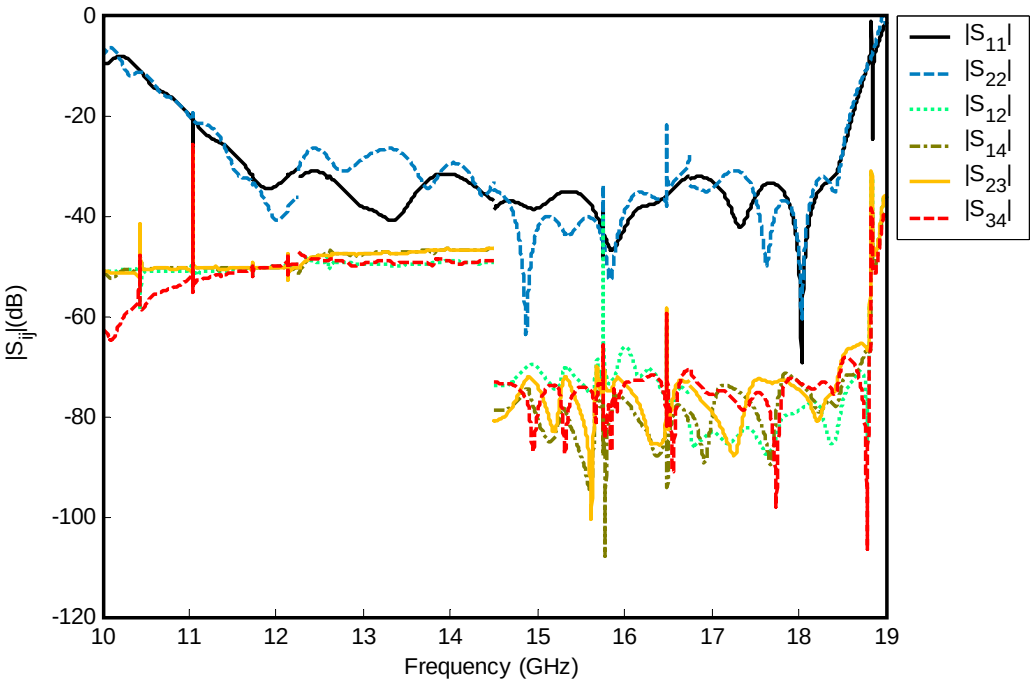

Fig. 7.19. Results for the analysis considering misalignment of 0.05 mm in the manufacturing of the internal matching obstacle of the Turnstile junction. Electric ports: 1 (vertical circular $TE_{11,cos}$), 2 (horizontal circular $TE_{11,sin}$), 3 (rectangular TE_{10}, vertical pol.) and 4 (rectangular TE_{10}, horizontal pol.).

7.5 Conclusions

The results of two OMT designs based on the Turnstile junction have been presented in this chapter. Different configurations for the branches have been discussed: a mixed E and H-plane option has been chosen for this project.

The first design was motivated by the excellent results previously obtained during the study of bends, transformers and Turnstile junctions. It had to fulfill certain specifications: return losses better than 22 dB over the band between 13-18 GHz using fixed common port and rectangular waveguide dimensions. The developed OMT had return losses better than 24 dB over the desired band (actually a 37% of fractional bandwidth fulfilled this specification)

The second design was an attempt to improve existing OMTs based on Turnstile junctions. It was motivated by the excellent results obtained with the Turnstile junction with angled branches, which also improved the compactness of the OMT. Some slight modifications had to be done to the routing structures because of the reduced height of the branches of the Turnstile junction. A five sections recombiner was included in this design to increase bandwidth. The results obtained for this second design had a 44.12% bandwidth with return losses better than 30 dB, which are comparable (even better in some aspects) to the reference works mentioned in this chapter.

Chapter 8

Final Conclusions and Future Work

8.1 Final conclusions

Throughout this project a design method for wideband OMTs based on the Turnstile junction has been developed.

It can be divided into a) the study of basic notions related to electromagnetism, waveguides, waves propagation and polarization, b) the application of these concepts into a first stage of design where some basic routing structures like bends, transformers and recombinators are studied, c) an in-depth study of the Turnstile junction with a test of internal obstacles for the junction and d) the appropriate interconnection of all these structures to complete the design of a wideband OMT.

The importance of a good comprehension of certain electromagnetic concepts has been stated. For example, the understanding of higher-order modes generation in the vicinities of a waveguide discontinuity plays a fundamental role. Moreover, the usefulness of the S-matrix as a powerful tool to characterize microwave devices has been proved.

All the knowledge gathered throughout the first stages of this project has resulted in an efficient design of many waveguide routing structures. The basic steps needed to design three of these structures (bends, transformers and recombinators) have been presented along with the simulation results obtained for some of them designed during this project.

Furthermore, the Turnstile junction has been proved as a suitable structure to be part of the design of a wideband OMT. A comparison between some Turnstile junctions with different internal obstacles has been carried out. In addition, a new internal obstacle never previously seen in the literature, to the best of the author's knowledge, has been proposed. The results of the simulation for a Turnstile junction with this new obstacle have been presented. Moreover, a new topology for the Turnstile junction has also been proposed, which includes angled rectangular branches. The optimized design using this topology that has been presented in this document has return losses better than 30 dB from 11.64 to 18.4 GHz (45% fractional bandwidth), which is a great improvement with regard to the previous designs.

Two OMT designs have been successfully completed following the aforementioned design method. Both are based on an option for the routing branches which consists of E-plane bends for the vertical polarization and H-plane bends for the horizontal polarization. Both require an E-plane recombinator to join the individual signals before they reach their allocated single-signal port. These two OMTs are composed of some of the structures designed during this project and presented in this document.

The first design had fixed specifications. It had to present return losses above 22 dB for both polarizations in the band between 13 and 18 GHz. Circular waveguide radio and rectangular cross section were fixed dimensions. The expected return losses for this first design were above 24 dB for all the band, so it fulfilled specifications. The results obtained for this OMT have been published in [IR08].

The second design was more of a challenge than a primary goal. Previous results during the study of Turnstile junctions with angled branches motivated the design of appropriate routing structures for a hypothetical OMT composed of them. It did not have any restrictions on waveguides dimensions but the aim was to achieve better results than those of the first design even with a more compact structure. The expected return losses for this OMT were above 30 dB for the band between 11.7 and 18.3 GHz, which represents a 44% fractional bandwidth.

Moreover, a survey of narrowband and wideband OMTs found in papers and books has been carried out, providing a great source of information and figures.

8.2 Future work

There are several research lines that can be followed from the results presented in this document.

- There was no opportunity to manufacture any of the structures developed during this project and, thus, present measures from physical devices. It would be very interesting to compare computed and measured return losses, transmission coefficients, etc. for these structures.

- It would also be interesting to test different angles for the Turnstile branches apart from the 15º used in this project. They might yield even better return losses than those obtained here, moreover in wider bandwidths.

- Another challenge would be to find new topologies for the internal obstacle apart from the topology proposed in this document, which could offer advantageous results.

[AYM03] Y. Aramaki, N. Yoneda, M. Miyazaki, and T. Horie, "Ultra-thin broadband OMT with turnstile junction," 2003 IEEE MTT-S International Microwave Symposium Digest, vol. 1, pp. 47-50, June 2003.

[BLS90] A.M. Boifot, E. Lier, and T. Schaug-Pettersen, "Simple and broadband orthomode transducer (antenna feed)," IEE Proceedings H Microwaves, Antennas and Propagation, vol. 137, nº. 6, pp. 396-400, Dec 1990.

[Bøi91] A. M. Bøifot, "Classification of ortho-mode transducers," Europ. Trans. Telecom. and Related Technologies, vol. 2, nº. 5, pp. 503–510, Sept. 1991.

[Bra78] Brain, J.R., "The design and evaluation of a high performance 3 m antenna for satellite communication," *The Marconi Review,* 1978, Fourth Quarter, pp. 218-236

[BVL05] R. Banham, G. Valsecchi, L. Lucci, G. Pelosi, S. Selleri, V. Natale, R. Nesti, and G. Tofani, "Electroformed front-end at 100 GHz for radio-astronomical applications," Microwave Journal, vol. 48, nº. 8, pp. 112-122 2005.

[CC99] G. Chattopadhyay, and J.E. Carlstrom, "Finline ortho-mode transducer for millimeter waves," IEEE Microwave and Guided Wave Letters, vol. 9, nº. 9, pp. 339-341, Sep 1999.

[Col91] R.E. Collin. "Field theory of guided waves". IEEE Press, 1991.

[Col01] R.E. Collin. "Foundations for Microwave Engineering". IEEE Press, 2001.

[Dun02] A. Dunning, "Double ridged orthogonal mode transducer for the 16-26 GHz microwave band," Proceedings of the Workshop on the Applications of Radio Science 2002.

[Enc05] Kai Chang (Editor), "Encyclopedia of RF and Microwave Engineering," 6-Volume Set, John Wiley & Sons, Inc. 5832p. Apr. 2005.

[ER92] J. Esteban, J. M. Rebollar, "Field Theory C.A.D. of Septum OMT-Polarizers", 1992

[IR08] I. Izquierdo Martínez, J. A. Ruiz-Cruz, "Diseño de OMTs (Ortho-Mode Transducers) con la unión Turnstile", Actas del Simposium Nacional URSI 2008, pp. 1-4, Sept. 2008.

[Mar53] N. Marcuvitz, Waveguide Handbook. New York: McGraw-Hill, 1953.

[MBD06] G. Moorey, R. Bolton, A. Dunning, R. Gough, H. Kanoniuk, and L. Reilly, "A 77-117 Ghz Cryogenically Cooled Receiver For Radioastronomy," Proceedings of the Workshop on the Applications of Radio Science 2006.

[MDP65] Montgomery, C.G., Dicke, R.H., and Purcell, E.M., "Principles of microwave circuits," Dover Publications, Inc. New York, 1965.

[MG55] M.A. Meyer, and H.B. Goldberg, “Applications of the Turnstile Junction,” IRE Transactions on Microwave Theory and Techniques, vol. 3, nº. 6, pp. 40-45, December 1955.

[MYJ64] G. Matthaei, L.Young, and E.M.T.Jones, “Microwave Fillers, Impedance-Matching Networks, and Coupling Structures”, Artech House, 1964

[NP06] Navarrini, and R.L. Plambeck, “A Turnstile Junction Waveguide Orthomode Transducer,” IEEE Transactions on Microwave Theory and Techniques, vol. 54, nº. 1, pp. 272-277, Jan. 2006.

[Num92] W. H. Press, B. P. Flannery, S. A. Teukolsky, W. T. Vetterling, “Numerical Recipes in Fortran 77,” Second Edition (1992)

[Pag83] J.E. Page. “Propagación de ondas guiadas”. Serv. Publ. ETSIT-Madrid, 1983.

[PC83] J.E. Page, C. Camacho. “Ondas Planas”. Serv. Publ. ETSIT-Madrid, 1983.

[Poz05] D.M. Pozar. “Microwave Engineering”. New York, John Wiley & Sons Inc., 2005.

[PPI07] G. Pisano, L. Pietranera, K. Isaak, L. Piccirillo, B. Johnson, B. Maffei, and S. Melhuish, “A Broadband WR10 Turnstile Junction Orthomode Transducer,” IEEE Microwave and Wireless Components Letters, vol. 17, nº. 4, pp. 286-288, April 2007.

[RMR06] J. A. Ruiz-Cruz, J. R. Montejo-Garai, J.M. Rebollar, C.E. Montesano, and M.J. Martın, "Very compact ortho-mode transducers with double septum configuration," *Microwave and Optical Technology Letters,* vol. 48, nº. 4, pp. 765-767, Apr. 2006.

[RMR08] J. A. Ruiz-Cruz, J. R. Montejo-Garai, J. M. Rebollar, “Full-Wave Modeling and Optimization of Bøifot Junction Ortho-Mode Transducers,” *Int. J. RF Microw. Comput.-Aided Eng.,* 18, 4 (Jul 2008), pp. 303-313.

[Rob56] S. D. Robertson, “Recent advances in finline circuits,” *IRE Trans. Microwave Theory Tech.*, vol. MTT-4, pp. 263–267, 1956.

[RWV93] S. Ramo, J.R. Whinnery, T. Van Duzer, *Fields and Waves in Communication Electronics*, John Wiley & Sons, Inc. 3rd Edition, 1993

[SJ91] S.J. Skinner, and G.L. James, “Wide-band orthomode transducers,” IEEE Transactions on Microwave Theory and Techniques, vol. 39, nº. 2, pp. 294-300, Feb 1991.

[TMF08] A. Tribak, A. Mediavilla, N. Fernández, M. Boussouis, M. Chaibi, “Full-band OMT turnstile en tecnología de guía de onda de altura reducida para aplicaciones satélite”, Actas del Simposium Nacional URSI 2008, pp. 1-4, Sept. 2008.

[UBR93] J. Uher, J. Bornemann, and U. Rosenberg, “Waveguide components for antenna feed systems: Theory and CAD,” Chapter 3, Boston, Artech House, 1993.

[WGK02] E.J. Wollack, W. Grammer, and J. Kingsley, "The Boifot Orthomode Junction," , vol. 425 2002.

Appendix A

Symmetries of the S-matrix

This document explains the symmetries of the S-matrix for the three-port (recombiner) and six-port (Turnstile junction) circuits described in Ch. 5 and Ch. 6 of this document, respectively.

A.1 Three-port network (recombiner).

Fig. A.1 shows the three-port network. Its S-parameters are defined as

$$\begin{bmatrix} b_1 \\ b_2 \\ b_3 \end{bmatrix} = \begin{bmatrix} S_{11} & S_{12} & S_{13} \\ S_{21} & S_{22} & S_{23} \\ S_{31} & S_{32} & S_{33} \end{bmatrix} \begin{bmatrix} a_1 \\ a_2 \\ a_3 \end{bmatrix}, \ \mathbf{b} = \mathbf{S}\,\mathbf{a} \ . \tag{A.1}$$

Based on the linearity of the network, the S-parameters can be calculated solving two problems that will be called *e*- and *m*-problem:

- *e*-problem. The excitations are:

$$a_1, \frac{a_2 + a_3}{2}, \frac{a_2 + a_3}{2} \tag{A.2}$$

by ports 1,2 and 3 respectively. The reflected waves for this problem will be named as b_{1e}, b_{2e}, b_{3e}.

- *m*-problem. The excitations are:

$$0, \frac{a_2 - a_3}{2}, \frac{-a_2 + a_3}{2} \tag{A.3}$$

by ports 1,2 and 3 respectively. The reflected waves for this problem will be named as b_{1m}, b_{2m}, b_{3m}.

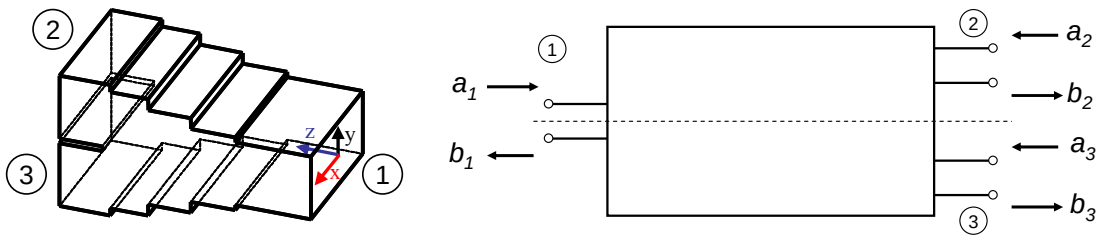

Fig. A.1. Three-port symmetrical network (recombiner) with coordinate system and with excitations, reflected waves and ports definition.

It is clear that summing up the *e*- and *m*-excitations it is possible to make up any arbitrary incident excitation

$$\begin{bmatrix} a_1 \\ a_2 \\ a_3 \end{bmatrix} = \begin{bmatrix} a_1 \\ \frac{a_2+a_3}{2} \\ \frac{a_2+a_3}{2} \end{bmatrix} + \begin{bmatrix} 0 \\ \frac{a_2-a_3}{2} \\ \frac{-a_2+a_3}{2} \end{bmatrix}, \tag{A.4}$$

with the reflected waves being the sum of that of the *e*- and *m*-problems:

$$\begin{bmatrix} b_1 \\ b_2 \\ b_3 \end{bmatrix} = \begin{bmatrix} b_{1e} \\ b_{2e} \\ b_{3e} \end{bmatrix} + \begin{bmatrix} b_{1m} \\ b_{2m} \\ b_{3m} \end{bmatrix} . \tag{A.5}$$

Although this approach can be followed for any three-port network, it only leads to simplifications in symmetric problems. In this case, the recombiner described in Ch. 5 is symmetric with respect to the *xz*-plane shown in Fig. A.1. Therefore, $b_{2e} = b_{3e}$, $b_{2m} = -b_{3m}$ and $b_{1m} = 0$. By defining $2a_{2e} = a_2 + a_3$ and $2a_{2m} = a_2 - a_3$, the incident and reflected waves can be written as:

$$\begin{bmatrix} a_1 \\ a_2 \\ a_3 \end{bmatrix} = \begin{bmatrix} a_1 \\ \frac{a_2+a_3}{2} \\ \frac{a_2+a_3}{2} \end{bmatrix} + \begin{bmatrix} 0 \\ \frac{a_2-a_3}{2} \\ \frac{-a_2+a_3}{2} \end{bmatrix} = \begin{bmatrix} a_1 \\ a_{2e} \\ a_{2e} \end{bmatrix} + \begin{bmatrix} 0 \\ a_{2m} \\ -a_{2m} \end{bmatrix} \tag{A.6}$$

$$\begin{bmatrix} b_1 \\ b_2 \\ b_3 \end{bmatrix} = \begin{bmatrix} b_{1e} \\ b_{2e} \\ b_{2e} \end{bmatrix} + \begin{bmatrix} b_{1m} \\ b_{2m} \\ -b_{2m} \end{bmatrix} . \tag{A.7}$$

A.1.1 The *e*-problem

In the *e*-problem, a Perfect Electric Wall (PEW) is created in the symmetry plane (see Fig. A.2 and Fig. A.3). The waves of the complete port 1 (without any division) are:

$$a_1 = \frac{v_1 + Z_{o1} i_1}{\sqrt{8 Z_{o1}}} \;,\; b_{1e} = \frac{v_1 - Z_{o1} i_1}{\sqrt{8 Z_{o1}}} . \tag{A.8}$$

It should be noted that in this problem the area of port 1 is divided by 2 and, thus:

$$a_{1d} = \frac{v_1/2 + (Z_{o1}/2) i_1}{\sqrt{8 Z_{o1}/2}} = \frac{a_1}{\sqrt{2}} \;,\; b_{1d} = \frac{v_1/2 - (Z_{o1}/2) i_1}{\sqrt{8 Z_{o1}/2}} = \frac{b_{1e}}{\sqrt{2}} . \tag{A.9}$$

The network with ports 1d and 2 is a classical two-port network, defined by a two-port S-matrix $\mathbf{S}_e$:

$$\begin{bmatrix} b_{1d} \\ b_{2e} \end{bmatrix} = \begin{bmatrix} S_{11e} & S_{12e} \\ S_{21e} & S_{22e} \end{bmatrix} \begin{bmatrix} a_{1d} \\ a_{2e} \end{bmatrix} \tag{A.10}$$

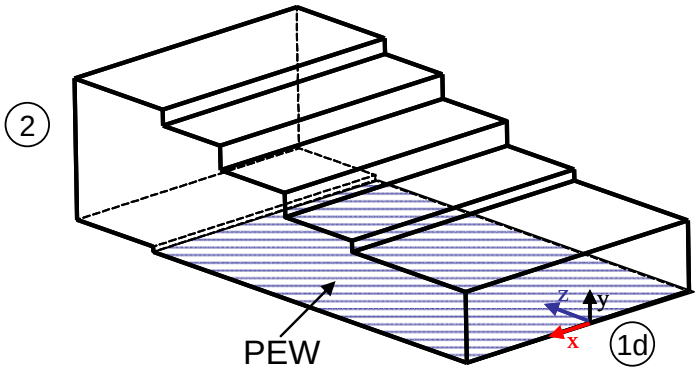

Fig. A.2. Sketch of the recombiner (a half of the structure) with PEW symmetry at *xz*-plane.

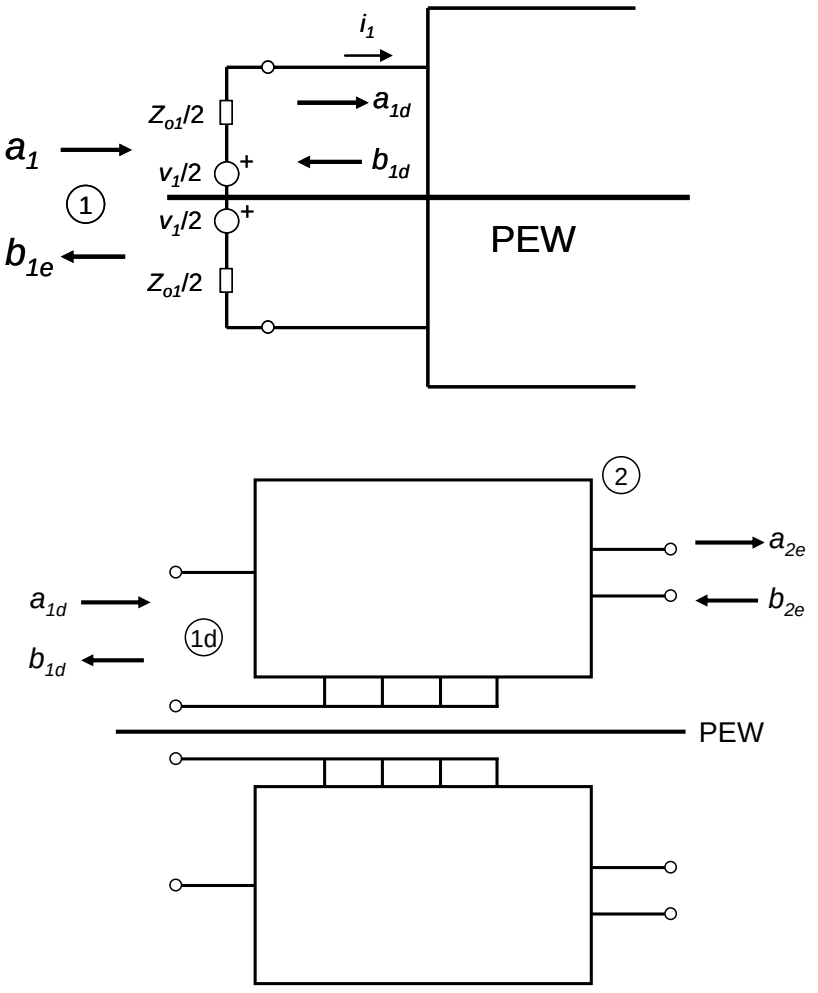

Fig. A.3. Excitation of the *e*-problem in the three-port symmetrical network.

If the circuit is reciprocal and lossless, $\mathbf{S}_e$ verifies $\mathbf{S}_e = \mathbf{S}_e^t$, $\mathbf{S}_e\mathbf{S}_e^{t^*} = I$, respectively. Coming back to the original variables,

$$\frac{b_{1e}}{\sqrt{2}} = b_{1d} = S_{11e}\frac{a_1}{\sqrt{2}} + S_{12e}a_{2e} \quad , \quad b_{2e} = S_{21e}\frac{a_1}{\sqrt{2}} + S_{22e}a_{2e} \quad , \tag{A.11}$$

and, therefore:

$$\begin{bmatrix} b_{1e} \\ b_{2e} \end{bmatrix} = \begin{bmatrix} S_{11e} & \sqrt{2}S_{12e} \\ \frac{S_{21e}}{\sqrt{2}} & S_{22e} \end{bmatrix} \begin{bmatrix} a_1 \\ a_{2e} \end{bmatrix} . \tag{A.12}$$

A.1.2 The *m*-problem

In the *m*-problem, a Perfect Magnetic Wall (PMW) is created in the symmetry plane (see Fig. A.4 and Fig. A.5). In this case, there is no signal transmitted to port 1 (the first mode there is evanescent). The resultant network has one port and is defined by a reflection coefficient ρ_m:

$$b_{2m} = \rho_m a_{2m} \quad . \tag{A.13}$$

For a lossless circuit $|\rho_m| = 1$.

A.1.3 Combination of the *e*- and *m*-problems.

By summing up the contributions of the two problems, it is obtained:

$$\begin{bmatrix} b_1 \\ b_2 \\ b_3 \end{bmatrix} = \begin{bmatrix} b_{1e} \\ b_{2e} \\ b_{2e} \end{bmatrix} + \begin{bmatrix} b_{1m} \\ b_{2m} \\ -b_{2m} \end{bmatrix} = \begin{bmatrix} S_{11e}a_1 + \sqrt{2}S_{12e}a_{2e} \\ \frac{S_{21e}}{\sqrt{2}}a_1 + S_{22e}a_{2e} \\ \frac{S_{21e}}{\sqrt{2}}a_1 + S_{22e}a_{2e} \end{bmatrix} + \begin{bmatrix} 0 \\ \rho_m a_{2m} \\ -\rho_m a_{2m} \end{bmatrix} . \tag{A.14}$$

Using a_1, a_{2e}, a_{2m} as excitation vector:

$$\begin{bmatrix} b_1 \\ b_2 \\ b_3 \end{bmatrix} = \begin{bmatrix} S_{11e} & \sqrt{2}S_{12e} & 0 \\ \frac{S_{21e}}{\sqrt{2}} & S_{22e} & \rho_m \\ \frac{S_{21e}}{\sqrt{2}} & S_{22e} & -\rho_m \end{bmatrix} \begin{bmatrix} a_1 \\ a_{2e} \\ a_{2m} \end{bmatrix} . \tag{A.15}$$

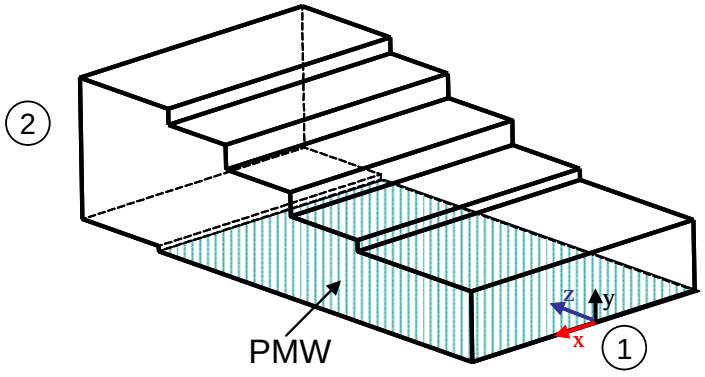

Fig. A.4. Sketch of the recombiner (a half of the structure) with PMW symmetry at *xz*-plane.

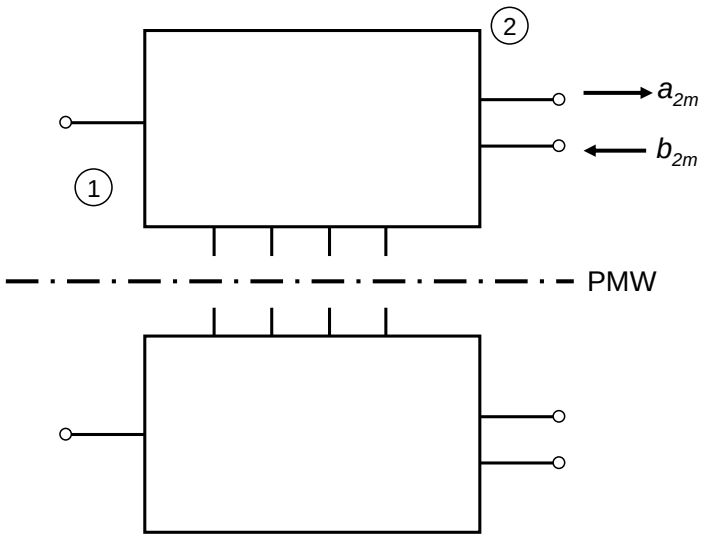

Fig. A.5. Excitation of the *m*-problem in the three-port symmetrical network.

Since

$$\begin{bmatrix} a_1 \\ a_{2e} \\ a_{2m} \end{bmatrix} = \begin{bmatrix} 1 & 0 & 0 \\ 0 & \frac{1}{2} & \frac{1}{2} \\ 0 & \frac{1}{2} & -\frac{1}{2} \end{bmatrix} \begin{bmatrix} a_1 \\ a_2 \\ a_3 \end{bmatrix}, \tag{A.16}$$

the complete S-matrix of the three-port network is:

$$\begin{bmatrix} b_1 \\ b_2 \\ b_3 \end{bmatrix} = \begin{bmatrix} S_{11e} & \frac{S_{12e}}{\sqrt{2}} & \frac{S_{12e}}{\sqrt{2}} \\ \frac{S_{21e}}{\sqrt{2}} & \frac{S_{22e}+\rho_m}{2} & \frac{S_{22e}-\rho_m}{2} \\ \frac{S_{21e}}{\sqrt{2}} & \frac{S_{22e}-\rho_m}{2} & \frac{S_{22e}+\rho_m}{2} \end{bmatrix} \begin{bmatrix} a_1 \\ a_2 \\ a_3 \end{bmatrix} \tag{A.17}$$

It is easy to show that $\mathbf{S} = \mathbf{S^t}$, provided that $\mathbf{S_e} = \mathbf{S_e^t}$. If $\mathbf{SS_e^{t*}} = \mathbf{I}$ and $|\rho_m| = 1$, it is easy to see that the diagonal of $\mathbf{SS^t}$ is all ones. There is a dual of the presented three-port formulation, where the connection is in parallel, instead of series (it can be applied, for instance, to H-plane recombiners).

A.2 Six-port network (Turnstile junction).

Fig. A.6 shows the six-port network (Turnstile junction) described in Ch. 6 of this document. It has two planes of physical symmetry (*xy*- and *yz*-planes) which will be of interest for solving the network. In this case, an arbitrary excitation can be decomposed as

$$\begin{bmatrix} a_1 \\ a_2 \\ a_3 \\ a_4 \\ a_5 \\ a_6 \end{bmatrix} = \begin{bmatrix} a_1 \\ 0 \\ \frac{a_3+a_4}{2} \\ \frac{a_3+a_4}{2} \\ 0 \\ 0 \end{bmatrix} + \begin{bmatrix} 0 \\ 0 \\ \frac{a_3-a_4}{2} \\ \frac{-a_3+a_4}{2} \\ 0 \\ 0 \end{bmatrix} + \begin{bmatrix} 0 \\ a_2 \\ 0 \\ 0 \\ \frac{a_5+a_6}{2} \\ \frac{a_5+a_6}{2} \end{bmatrix} + \begin{bmatrix} 0 \\ 0 \\ 0 \\ 0 \\ \frac{a_5-a_6}{2} \\ \frac{-a_5+a_6}{2} \end{bmatrix} =$$

$$= \underbrace{\begin{bmatrix} a_1 \\ 0 \\ a_{3p} \\ a_{3p} \\ 0 \\ 0 \end{bmatrix}}_{(yz,xy)=(e,m)} + \underbrace{\begin{bmatrix} 0 \\ 0 \\ a_{3n} \\ -a_{3n} \\ 0 \\ 0 \end{bmatrix}}_{(yz,xy)=(m,m)} + \underbrace{\begin{bmatrix} 0 \\ a_2 \\ 0 \\ 0 \\ a_{5p} \\ a_{5p} \end{bmatrix}}_{(yz,xy)=(m,e)} + \underbrace{\begin{bmatrix} 0 \\ 0 \\ 0 \\ 0 \\ a_{5n} \\ -a_{5n} \end{bmatrix}}_{(yz,xy)=(m,m)}, \tag{A.18}$$

where $2a_{3p} = a_3 + a_4$, $2a_{3n} = a_3 - a_4$, $2a_{5p} = a_5 + a_6$, $2a_{5n} = a_5 - a_6$. The reflected waves, because of the symmetry, have the form

$$\begin{bmatrix} b_1 \\ b_2 \\ b_3 \\ b_4 \\ b_5 \\ b_6 \end{bmatrix} = \begin{bmatrix} b_1 \\ 0 \\ b_{3em} \\ b_{3em} \\ 0 \\ 0 \end{bmatrix} + \begin{bmatrix} 0 \\ 0 \\ b_{33mm} \\ -b_{33mm} \\ b_{35mm} \\ -b_{35mm} \end{bmatrix} + \begin{bmatrix} 0 \\ b_2 \\ 0 \\ 0 \\ b_{5me} \\ b_{5me} \end{bmatrix} + \begin{bmatrix} 0 \\ 0 \\ b_{53mm} \\ -b_{53mm} \\ b_{55mm} \\ -b_{55mm} \end{bmatrix} \tag{A.19}$$

each term being the corresponding response to the *(e,m), (m,m), (m,e)* and *(m,m)* excitation. In fact, the two *(m,m)* problems can be gathered:

$$\begin{bmatrix} a_1 \\ a_2 \\ a_3 \\ a_4 \\ a_5 \\ a_6 \end{bmatrix} = \underbrace{\begin{bmatrix} a_1 \\ 0 \\ a_{3p} \\ a_{3p} \\ 0 \\ 0 \end{bmatrix}}_{(yz,xy)=(e,m)} + \underbrace{\begin{bmatrix} 0 \\ a_2 \\ 0 \\ 0 \\ a_{5p} \\ a_{5p} \end{bmatrix}}_{(yz,xy)=(m,e)} + \underbrace{\begin{bmatrix} 0 \\ 0 \\ a_{3n} \\ -a_{3n} \\ a_{5n} \\ -a_{5n} \end{bmatrix}}_{(yz,xy)=(m,m)} \tag{A.20}$$

$$\begin{bmatrix} b_1 \\ b_2 \\ b_3 \\ b_4 \\ b_5 \\ b_6 \end{bmatrix} = \underbrace{\begin{bmatrix} b_1 \\ 0 \\ b_{3em} \\ b_{3em} \\ 0 \\ 0 \end{bmatrix}}_{(yz,xy)=(e,m)} + \underbrace{\begin{bmatrix} 0 \\ b_2 \\ 0 \\ 0 \\ b_{5me} \\ b_{5me} \end{bmatrix}}_{(yz,xy)=(m,e)} + \underbrace{\begin{bmatrix} 0 \\ 0 \\ b_{3mm} \\ -b_{3mm} \\ b_{5mm} \\ -b_{5mm} \end{bmatrix}}_{(yz,xy)=(m,m)} \tag{A.21}$$

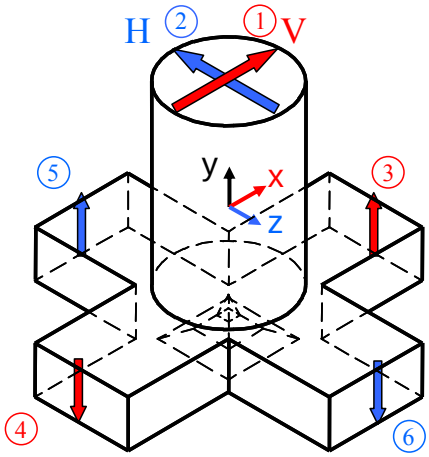

Fig. A.6. Sketch of the Turnstile junction with coordinate system and ports definition.

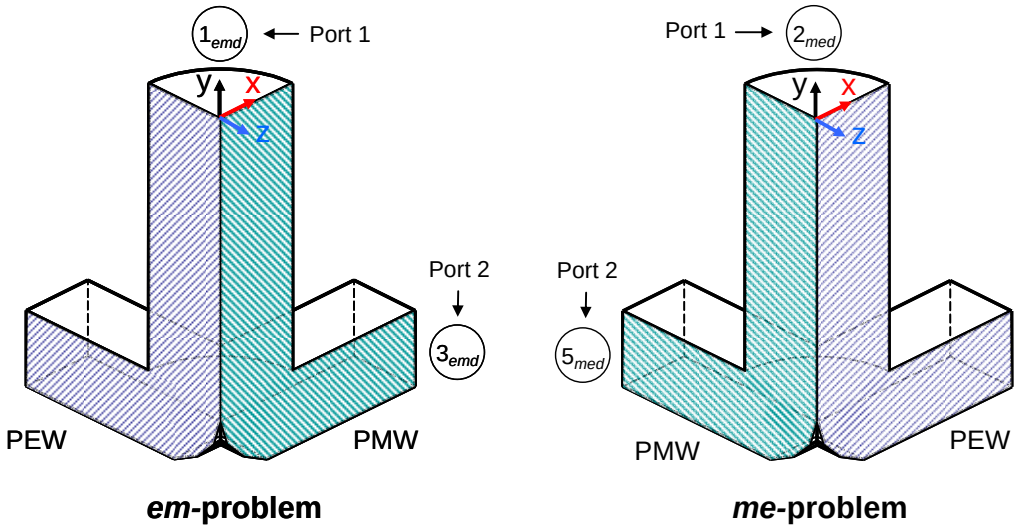

Fig. A.7. Sketch of the Turnstile junction (a quarter of the structure) with symmetries definition for the *em*- and *me*-problems.

A.2.1 The *em*- and *me*-problems.

The *em*-problem is a two-port network with PEW at the *yz*-plane and PMW at the *xy*-plane. The structure to analyze is one quarter of the whole Turnstile junction. For this analysis, port 5 is evanescent, and ports 4 and 6 are not in the structure (See. Fig. A.7). The resultant problem is defined by a two-port (port one is the Turnstile junction common port with mode 1 and port two is the Turnstile port 3) S-matrix $\mathbf{s}_{em}$:

$$\begin{bmatrix} b_{1emd} \\ b_{3emd} \end{bmatrix} = \begin{bmatrix} S_{11em} & S_{12em} \\ S_{21em} & S_{22em} \end{bmatrix} \begin{bmatrix} a_{1emd} \\ a_{3emd} \end{bmatrix} \tag{A.22}$$

If the circuit is reciprocal and lossless, $\mathbf{S}_{em}$ verifies $\mathbf{S}_{em}=\mathbf{S}_{em}^{t}$, $\mathbf{S}\mathbf{S}_{em}^{t*}=\mathbf{I}$, respectively. Since in the two-port network, port one has a quarter of the area of the corresponding Turnstile port 1, and port two has half the area of the Turnstile port 3, the original amplitudes are related to the amplitudes of the one-quarter problem by:

$$\begin{aligned} a_{1emd}&=\frac{a_1}{2},\ b_{1emd}=\frac{b_1}{2} \\ a_{3emd}&=\frac{a_{3p}}{\sqrt{2}},\ b_{3emd}=\frac{b_{3em}}{\sqrt{2}} \end{aligned} \quad . \tag{A.23}$$

Coming back to the original variables,

$$\begin{aligned} b_1&=2S_{11em}\frac{a_1}{2}+2S_{12em}\frac{a_{3p}}{\sqrt{2}} \\ b_{3em}&=\sqrt{2}S_{21em}\frac{a_1}{2}+\sqrt{2}S_{22em}\frac{a_{3p}}{\sqrt{2}} \end{aligned} \quad , \tag{A.24}$$

leading to:

$$\begin{aligned} b_1&=S_{11em}a_1+\sqrt{2}S_{12em}a_{3p} \\ b_{3em}&=\frac{1}{\sqrt{2}}S_{21em}a_1+S_{22em}a_{3p} \end{aligned} \quad . \tag{A.25}$$

The results for the me-problem would be similar. The problem in this case has two-ports (port one is the Turnstile common port with mode 2 and port two is the Turnstile port 5):

$$\begin{aligned} b_2&=S_{11me}a_2+\sqrt{2}S_{12me}a_{5p} \\ b_{5me}&=\frac{1}{\sqrt{2}}S_{21me}a_2+S_{22me}a_{5p} \end{aligned} \quad . \tag{A.26}$$

If the structure is rotated around the *y*-axis 90º and the same problem is obtained (which is the case for Fig. A.6), it follows that $\mathbf{S}_{em}=\mathbf{S}_{me}$.

A.2.2 The *mm*-problem.

The *mm*-problem is a two port network with PMW at both the *yz*- and *xy*-planes. The structure to analyze is one quarter of the whole Turnstile junction. For this analysis, Turnstile common port is evanescent for both modes 1 and 2 (See Fig. A.8). The resultant problem is defined by a two-port (port one is the Turnstile port 3 and port two the Turnstile port 5) S-matrix $\mathbf{S}_{mm}$:

$$\begin{bmatrix} b_{3mmd} \\ b_{5mmd} \end{bmatrix}=\begin{bmatrix} S_{11mm} & S_{12mm} \\ S_{21mm} & S_{22mm} \end{bmatrix}\begin{bmatrix} a_{3mmd} \\ a_{5mmd} \end{bmatrix} \quad . \tag{A.27}$$

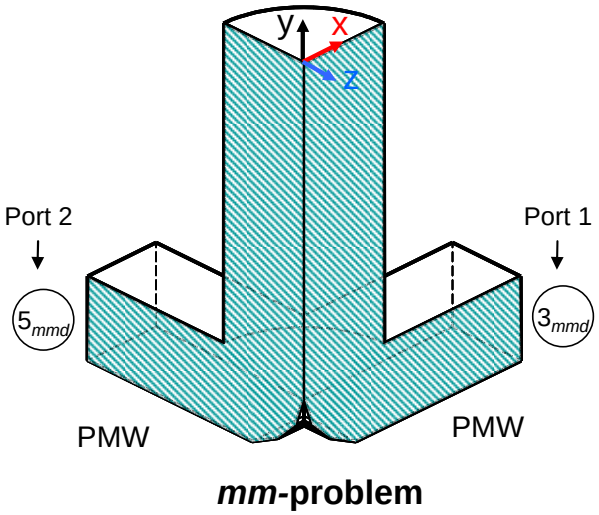

Fig. A.8. Sketch of the Turnstile junction (a quarter of the structure) with symmetries definition for the *mm*-problem.

Since in the two-port network, port one has half of the area of the corresponding Turnstile port 3, and port two has half of the area of the corresponding Turnstile port 5, the original amplitudes are related to the amplitudes of the one-quarter problem by:

$$\begin{aligned} a_{3mmd} &= \frac{a_{3n}}{\sqrt{2}},\ b_{3mmd} = \frac{b_{3mm}}{\sqrt{2}} \\ a_{5mmd} &= \frac{a_{5n}}{\sqrt{2}},\ b_{5mmd} = \frac{b_{5mm}}{\sqrt{2}} \end{aligned} . \tag{A.28}$$

The result is

$$\begin{aligned} b_{3mm} &= \sqrt{2}S_{11mm}\frac{a_{3n}}{\sqrt{2}} + \sqrt{2}S_{12mm}\frac{a_{5n}}{\sqrt{2}} \\ b_{5mm} &= \sqrt{2}S_{21mm}\frac{a_{3n}}{\sqrt{2}} + \sqrt{2}S_{22mm}\frac{a_{5n}}{\sqrt{2}} \end{aligned} , \tag{A.29}$$

leading to:

$$\begin{aligned} b_{3mm} &= S_{11mm}a_{3n} + S_{12mm}a_{5n} \\ b_{5mm} &= S_{21mm}a_{3n} + S_{22mm}a_{5n} \end{aligned} . \tag{A.30}$$

A.2.3 Combination of the *em*-, *me*- and *mm*-problems.

By summing up the contributions of the three problems, it is obtained:

$$\begin{bmatrix} b_1 \\ b_2 \\ b_3 \\ b_4 \\ b_5 \\ b_6 \end{bmatrix} = \begin{bmatrix} b_1 \\ 0 \\ b_{3em} \\ b_{3em} \\ 0 \\ 0 \end{bmatrix} + \begin{bmatrix} 0 \\ b_2 \\ 0 \\ 0 \\ b_{5me} \\ b_{5me} \end{bmatrix} + \begin{bmatrix} 0 \\ 0 \\ b_{3mm} \\ -b_{3mm} \\ b_{5mm} \\ -b_{5mm} \end{bmatrix} =$$

$$= \begin{bmatrix} S_{11em}a_1 + \sqrt{2}S_{12em}a_{3p} \\ 0 \\ \frac{1}{\sqrt{2}}S_{21em}a_1 + S_{22em}a_{3p} \\ \frac{1}{\sqrt{2}}S_{21em}a_1 + S_{22em}a_{3p} \\ 0 \\ 0 \end{bmatrix} + \begin{bmatrix} 0 \\ S_{11me}a_2 + \sqrt{2}S_{12me}a_{5p} \\ 0 \\ 0 \\ \frac{1}{\sqrt{2}}S_{21me}a_2 + S_{22me}a_{5p} \\ \frac{1}{\sqrt{2}}S_{21me}a_2 + S_{22me}a_{5p} \end{bmatrix} + \begin{bmatrix} 0 \\ 0 \\ S_{11mm}a_{3n} + S_{12mm}a_{5n} \\ -S_{11mm}a_{3n} - S_{12mm}a_{5n} \\ S_{21mm}a_{3n} + S_{22mm}a_{5n} \\ -S_{21mm}a_{3n} - S_{22mm}a_{5n} \end{bmatrix} \tag{A.31}$$

This leads to:

$$\begin{bmatrix} b_1 \\ b_2 \\ b_3 \\ b_4 \\ b_5 \\ b_6 \end{bmatrix} = \begin{bmatrix} S_{11em} & 0 & \sqrt{2}S_{12em} & 0 & 0 & 0 \\ 0 & S_{11me} & 0 & 0 & \sqrt{2}S_{21me} & 0 \\ \frac{S_{21em}}{\sqrt{2}} & 0 & S_{22em} & S_{11mm} & 0 & S_{12mm} \\ \frac{S_{21em}}{\sqrt{2}} & 0 & S_{22em} & -S_{11mm} & 0 & -S_{12mm} \\ 0 & \frac{S_{21me}}{\sqrt{2}} & 0 & S_{21mm} & S_{22me} & S_{22mm} \\ 0 & \frac{S_{21me}}{\sqrt{2}} & 0 & -S_{21mm} & S_{22me} & -S_{22mm} \end{bmatrix} \begin{bmatrix} a_1 \\ a_2 \\ a_{3p} \\ a_{3n} \\ a_{5p} \\ a_{5n} \end{bmatrix} \tag{A.32}$$

Since

$$\begin{bmatrix} a_1 \\ a_2 \\ a_{3p} \\ a_{3n} \\ a_{5p} \\ a_{5n} \end{bmatrix} = \begin{bmatrix} 1 & 0 & 0 & 0 & 0 & 0 \\ 0 & 1 & 0 & 0 & 0 & 0 \\ 0 & 0 & \frac{1}{2} & \frac{1}{2} & 0 & 0 \\ 0 & 0 & \frac{1}{2} & \frac{-1}{2} & 0 & 0 \\ 0 & 0 & 0 & 0 & \frac{1}{2} & \frac{1}{2} \\ 0 & 0 & 0 & 0 & \frac{1}{2} & \frac{-1}{2} \end{bmatrix} \begin{bmatrix} a_1 \\ a_2 \\ a_3 \\ a_4 \\ a_5 \\ a_6 \end{bmatrix}, \tag{A.33}$$

the complete S-matrix of the six-port network is:

$$\begin{bmatrix} b_1 \\ b_2 \\ b_3 \\ b_4 \\ b_5 \\ b_6 \end{bmatrix} = \begin{bmatrix} S_{11em} & 0 & \frac{S_{12em}}{\sqrt{2}} & \frac{S_{12em}}{\sqrt{2}} & 0 & 0 \\ 0 & S_{11me} & 0 & 0 & \frac{S_{21me}}{\sqrt{2}} & \frac{S_{21me}}{\sqrt{2}} \\ \frac{S_{21em}}{\sqrt{2}} & 0 & \frac{S_{22em}+S_{11mm}}{2} & \frac{S_{22em}-S_{11mm}}{2} & \frac{S_{12mm}}{2} & \frac{-S_{12mm}}{2} \\ \frac{S_{21em}}{\sqrt{2}} & 0 & \frac{S_{22em}-S_{11mm}}{2} & \frac{S_{22em}+S_{11mm}}{2} & \frac{-S_{12mm}}{2} & \frac{S_{12mm}}{2} \\ 0 & \frac{S_{21me}}{\sqrt{2}} & \frac{S_{21mm}}{2} & \frac{-S_{21mm}}{2} & \frac{S_{22me}+S_{22mm}}{2} & \frac{S_{22me}-S_{22mm}}{2} \\ 0 & \frac{S_{21me}}{\sqrt{2}} & \frac{-S_{21mm}}{2} & \frac{S_{21mm}}{2} & \frac{S_{22me}-S_{22mm}}{2} & \frac{S_{22me}+S_{22mm}}{2} \end{bmatrix} \begin{bmatrix} a_1 \\ a_2 \\ a_3 \\ a_4 \\ a_5 \\ a_6 \end{bmatrix} \tag{A.34}$$

Appendix B

Text of the Published Article

Diseño de OMTs (Ortho-Mode Transducers) con la unión Turnstile

Ignacio Izquierdo Martínez[(1)], Jorge A. Ruiz Cruz[(1)]
ignacio.izquierdo@estudiante.uam.es, jorge.ruizcruz@uam.es
[(1)] Escuela Politécnica Superior, Universidad Autónoma de Madrid, C/ Francisco Tomás y Valiente 11, Madrid 28049, España

Abstract.- **This paper presents the design of an orthomode transducer (OMT) based on the Turnstile junction with two main characteristics: a) the routing branches for each polarization are made in both *E*- and *H*-plane configuration, and b) the used Turnstile junction has an optimized internal profile inspired on mitered bends. These branches are made up of well-known waveguide elements, such as *E*- and *H*-plane bends and height transformers, which can be efficiently analyzed by specialized codes or available commercial software. The proposed structures are illustrated with the design of a complete OMT. The numerical simulations of the OMT elements and the performance of the overall structure in the band 13-19 GHz are presented in this communication, obtaining return losses better than 24dB in a 37% fractional bandwidth for both polarizations.**

I. INTRODUCCIÓN

Los Transductores de Modos Ortogonales (OMTs u Ortho-Mode Transducers) son dispositivos pasivos de microondas que se componen de tres puertas físicas. Su misión es discriminar las señales independientes que se usan en sistemas de alimentación de antenas de doble polarización. En recepción, el OMT separa las dos componentes ortogonales de las señales polarizadas y encamina cada una de ellas hasta la puerta dedicada a la polarización correspondiente. En transmisión, combina en la puerta común dos modos ortogonales, cada uno asociado a una excitación independiente en las puertas dedicadas a cada polarización [1],[2] (ver Figs. 1 y 2).

Estos dispositivos se usan en sistemas de comunicación por satélite y en aplicaciones radioastronómicas. En los primeros, el OMT duplica la capacidad de tráfico del enlace gracias al empleo de la doble polarización. En radioastronomía, permite mejorar las características del receptor en una amplia banda del espectro [3-6].

En [1],[2],[7] se catalogan diversas configuraciones empleadas para realizar la función de los OMTs, donde se hace mención especial a las simetrías físicas de la estructura y a la distinción entre OMTs de banda estrecha y de banda ancha. Las prestaciones a comparar son las pérdidas de retorno, las pérdidas de inserción y el aislamiento entre polarizaciones, que está asociado a las especificaciones de polarización cruzada del sistema conjunto antena más alimentador. Generalmente, los OMTs con un sólo plano de simetría física se diseñan para aplicaciones de menor ancho de banda que los que tienen doble simetría, aunque los primeros suelen ser mucho más compactos. La simetría es una cuestión clave en el diseño de OMTs, puesto que determina los modos de orden superior que se van a generar en la estructura y por tanto el ancho de banda de trabajo. Si el OMT tiene una sola simetría, el primer modo de orden superior que se generará tendrá frecuencia de corte menor que en una estructura de doble simetría. De ahí que para OMT´s de banda ancha se suelan usar estructuras con doble simetría como la que se utiliza en este trabajo.

Este trabajo ha sido financiado por los proyectos TEC2007-64556 (MEC-CICYT) y CCG07-UAM/TIC-1794 (C. Madrid-Univ. Autónoma de Madrid).

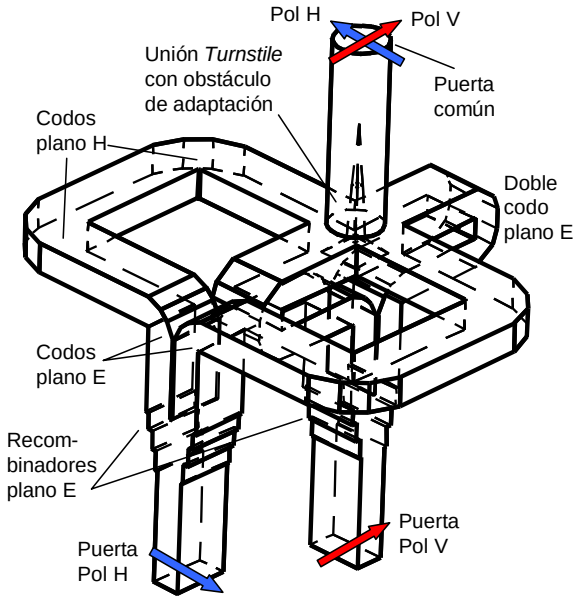

Fig. 1. OMT (Orthomode Transducer o Transductor de Modos Ortogonales) basado en la unión *Turnstile* y con redes de encaminamiento de señal en configuración mixta plano *E* y *H*. La unión Turnstile tiene un elemento interior de adaptación optimizado.

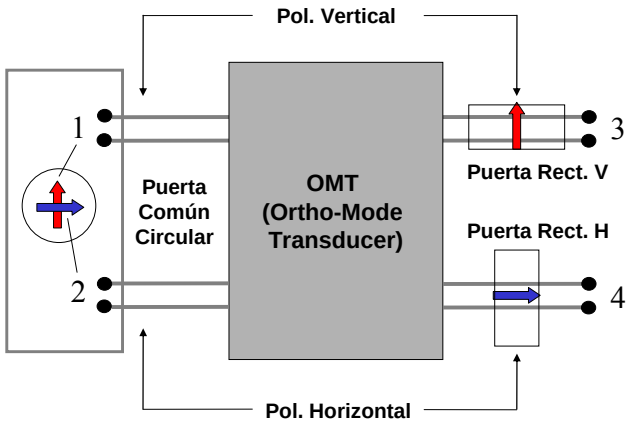

Fig. 2. Esquema de puertas físicas y eléctricas del OMT.

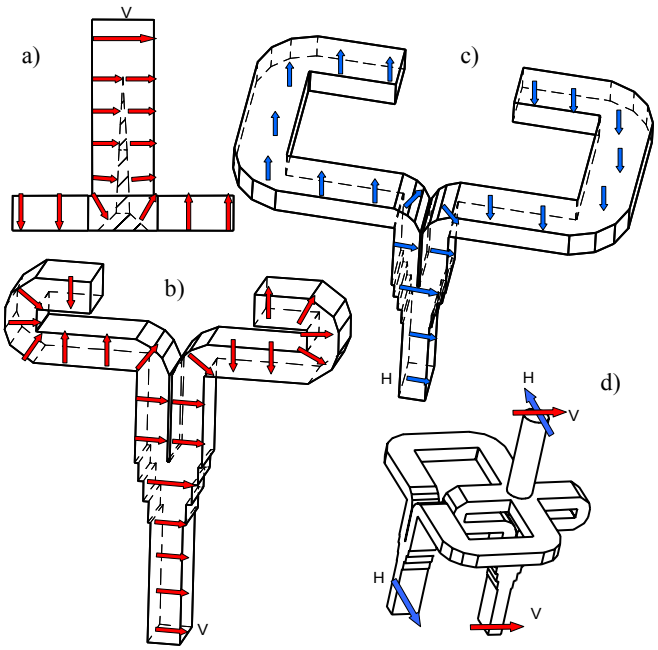

Fig. 3. Caminos recorridos por las señales individuales: a) unión Turnstile para la polarización vertical (para la horizontal se tendría el mismo esquema debido a la simetría); b) encaminamiento para la polarización vertical; c) encaminamiento para la polarización horizontal; d) vista del OMT completo.

Dentro de las estructuras con doble simetría, existen dos configuraciones básicas: las que cuentan con una unión idéntica para ambas polarizaciones, como la unión conocida como *Turnstile* [3],[4]; y las que presentan un procedimiento distinto para cada una, cuyo máximo exponente es la unión propuesta por Bøifot en [8] y usada en [5],[6],[9].

En concreto, en esta comunicación se describe el diseño de un OMT de banda ancha basado en la unión *Turnstile*. Se propone una configuración para la recombinación de las señales que utiliza una configuración distinta a las de [3],[4], utilizando una red mixta plano *E* y *H* que es una alternativa adicional a considerar dependiendo de la disposición física de los interfaces a los que vaya conectado el OMT. Adicionalmente, se presenta un diseño de la unión Turnstile con un perfil interno optimizado en base a la analogía con codos truncados. También se presentan los resultados obtenidos para las simulaciones tanto de los elementos individuales como del OMT completo en la banda de 13 a 18 GHz.

II. Teoría

A. *Descripción del funcionamiento del OMT.*

Eléctricamente, el OMT se trata de un dispositivo de cuatro puertas, cuyo comportamiento ideal se describe mediante la siguiente matriz de scattering:

$$\mathbf{S} = \begin{bmatrix} 0 & 0 & e^{j\alpha} & 0 \\ 0 & 0 & 0 & e^{j\beta} \\ e^{j\alpha} & 0 & 0 & 0 \\ 0 & e^{j\beta} & 0 & 0 \end{bmatrix}, \quad (1)$$

con α y β fases reales. La numeración de las puertas es la indicada en la Fig. 2.

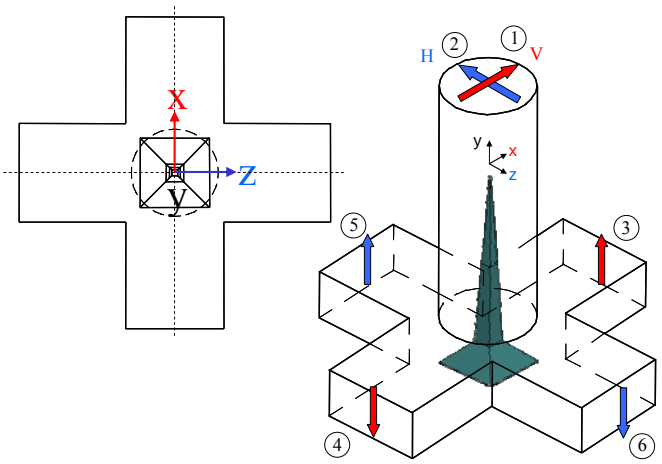

Fig. 4. Principio de funcionamiento de la unión Turnstile.

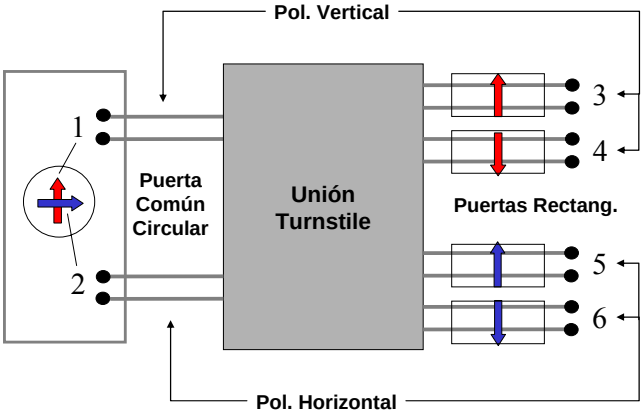

Fig. 5. Esquema de puertas físicas y eléctricas de la unión Turnstile.

El OMT de la Fig. 1 está formado por los siguientes elementos: una unión Turnstile; cuatro ramas laterales, dedicadas a encaminar las cuatro componentes resultantes de la división provocada por dicha unión y dos recombinadores. Éstos últimos elementos combinan en fase las dos componentes correspondientes a cada una de las polarizaciones, formando el modo fundamental que llega a cada una de las puertas rectangulares de la estructura.

Uno de los elementos fundamentales en el diseño de este tipo de OMTs es la manera en que se recombinan las señales que son separadas por la unión Turnstile. Algunos diseños, como el descrito en [4], ofrecen una solución íntegramente en plano *E* que requiere una gran precisión en el diseño debido a la necesidad de igualar la longitud eléctrica recorrida por cada señal antes de recombinarse. En el diseño presente en esta comunicación se opta por una solución mixta de codos plano *E* para la polarización vertical y codos plano *H* para la horizontal, con posterior recombinación en plano *E* en ambos casos. En la Fig. 3 se muestra el camino eléctrico de cada polarización al completo.

El diseño del OMT se ha llevado a cabo de manera que cumpla las especificaciones de la Tabla I. Todos los elementos presentes en la configuración del OMT propuesta (unión Turnstile, codos y recombinadores) se diseñan con una adaptación mejor que la de las especificaciones para prevenir la degradación provocada por la interconexión de las diferentes partes del OMT.

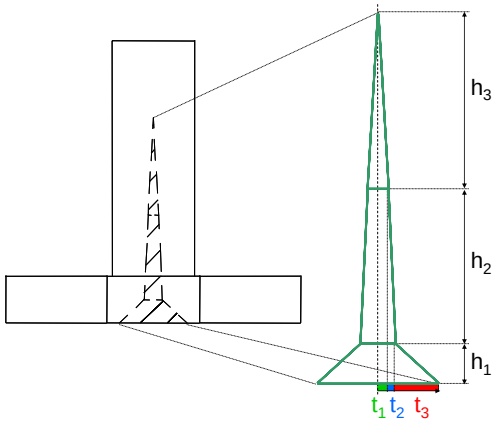

Fig. 6. Perfil y variables del obstáculo interno empleado en la unión Turnstile, basado en la analogía con codos truncados.

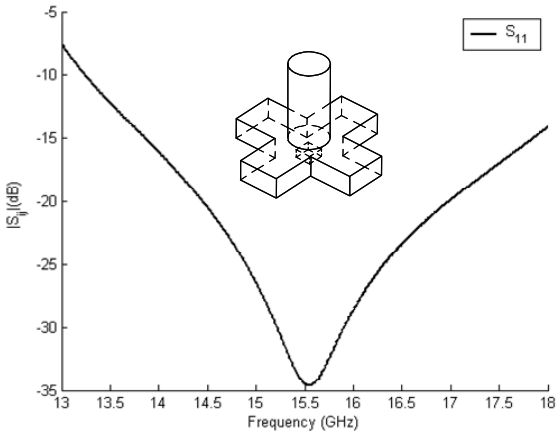

Fig. 7. Pérdidas de retorno de la unión Turnstile con un obstáculo rectangular simple.

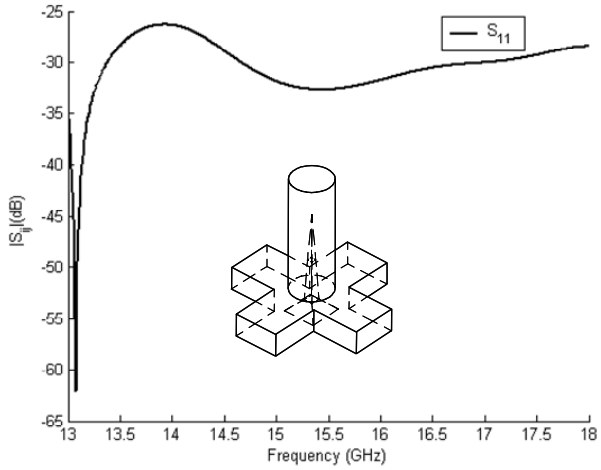

Fig. 8. Pérdidas de retorno de la unión Turnstile con el obstáculo propuesto.

Tabla I. Especificaciones del OMT con unión Turnstile.		
Puertas V-H: 15.8mm x 7.9mm. Puerta Común: r=6.99mm		
Polarización	Banda de frecuencia (GHz)	Pérdidas de retorno en la puerta común
V y H	13 – 18	22 dB

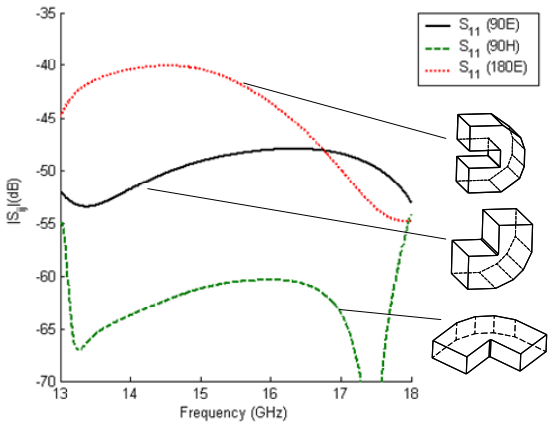

Fig. 9. Pérdidas de retorno de los codos empleados en el diseño del OMT.

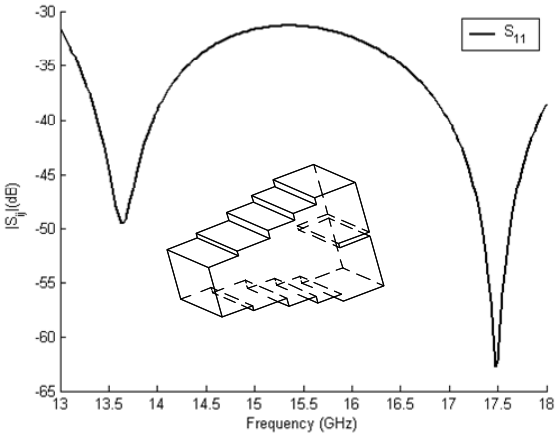

Fig. 10. Pérdidas de retorno del recombinador/bifurcación plano *E* de 3 secciones (pared eléctrica perfecta en el plano de simetría).

B. Descripción del funcionamiento de la unión Turnstile.

La unión Turnstile es un dispositivo de 5 puertas físicas con 6 puertas eléctricas. El comportamiento ideal de la unión [10] se describe mediante la siguiente matriz de scattering, cuya relación entre numeración de puertas y fases se definen en las Figs. 4 y 5 ($|\varepsilon|^2=|\gamma|=1/2$):

$$\mathbf{S}=\left[\begin{array}{cc|cccc} 0 & 0 & \varepsilon & \varepsilon & 0 & 0 \\ 0 & 0 & 0 & 0 & \varepsilon & \varepsilon \\ \hline \varepsilon & 0 & 0 & 0 & \gamma & -\gamma \\ \varepsilon & 0 & 0 & 0 & -\gamma & \gamma \\ 0 & \varepsilon & \gamma & -\gamma & 0 & 0 \\ 0 & \varepsilon & -\gamma & \gamma & 0 & 0 \end{array}\right]. \qquad (2)$$

En la puerta común (puertas eléctricas 1 y 2) inciden los dos modos asociados a cada polarización. El dispositivo se comporta de manera idéntica para las dos polarizaciones: separa cada una de ellas en dos mitades de igual potencia que se encaminan hacia las puertas correspondientes a cada polarización, situadas una frente a la otra. El principio de funcionamiento se explica de acuerdo a la Fig. 4. Tomando como ejemplo la polarización vertical con el campo eléctrico polarizado según el eje *x*, en la unión se generan los modos con simetría de pared magnética perfecta en el plano *xy* y pared eléctrica perfecta en el plano *yz*. Estos últimos modos

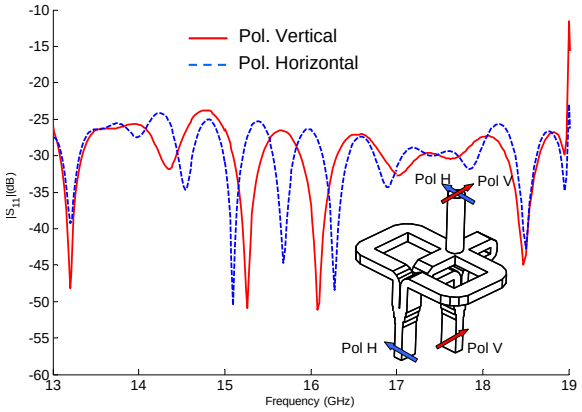

Fig. 11. Perdidas de retorno del OMT basado en la unión Turnstile para ambas polarizaciones.

están al corte en las guías 5 y 6, por lo que no se transmite potencia hacia esas puertas y sí hacia las otras dos. Si se consigue adaptar el modo incidente, toda la potencia se dividirá entre las puertas 3 y 4. El comportamiento es idéntico para la otra polarización debido a la simetría.

El obstáculo interno que se suele situar en la unión mejora la adaptación de los modos incidentes. En esta comunicación se presenta un diseño para dicho obstáculo cuyo perfil se puede observar en la Fig. 6, junto con las variables que lo definen. Pretende emular la función de un codo truncado para cada polarización, favoreciendo el encaminado de cada una de ellas hasta su puerta correspondiente. Los resultados obtenidos para la unión Turnstile, tanto para un prisma rectangular como para el obstáculo propuesto se pueden comparar observando las Figs. 7 y 8. En ambos casos el radio de la guía circular y las dimensiones de las guías laterales son las mismas.

C. Diseño de los elementos de las ramas laterales

El diseño de los codos es un campo ampliamente tratado. Se pueden obtener prestaciones excelentes en banda ancha con codos de fabricación simple, como ocurre con los codos truncados empleados en este diseño. Además, su análisis y optimización se puede hacer de forma muy eficiente por distintos métodos numéricos. En la Fig. 9 se pueden observar las pérdidas de retorno de los 3 tipos de codos diseñados para el OMT. Para el diseño del recombinador (que también puede verse como una bifurcación) se ha optado por emplear un transformador plano *E* de tres secciones, cuyas pérdidas de retorno se muestran en la Fig. 10.

III. Resultados

La optimización de la unión Turnstile es fundamental, y tiene una gran relevancia en la respuesta del OMT completo. Una de las claves para dicha optimización es el diseño de su obstáculo interno, que en este caso ha sido realizado manejando las variables que se muestran en la Fig. 6. Como puede verse en la Fig. 8, la Turnstile presenta pérdidas de retorno mejores de 26 dB para toda la banda. Estos resultados podrían mejorarse incluyendo más grados de libertad en la estructura.

Respecto a los elementos de las ramas laterales, los tres codos empleados tienen una respuesta por debajo de 40 dB, mientras que el transformador de tres secciones presenta unas pérdidas de retorno mejores de 30 dB, lo que supone un margen aceptable para prevenir la mencionada degradación que supone la interconexión de los elementos del OMT.

Todos los elementos individuales mencionados se han empleado en el diseño del OMT presentado en la Fig. 1, cuya respuesta está en la Fig. 11. El OMT diseñado tiene unas pérdidas de retorno por debajo de 24 dB para toda la banda de funcionamiento (y hasta casi 19GHz, que es aproximadamente un 37% de banda fraccional) y para ambas polarizaciones. El análisis de la estructura completa presentado en la Fig. 11 se ha realizado mediante el software comercial HFSS (High Frequency Structural Simulator), basado en el método de los elementos finitos.

IV. Conclusiones

Se han presentado las ideas principales del diseño de un OMT basado en la unión Turnstile con una nueva red conjunta plano *E* y *H*. La estructura se puede dividir en una serie de elementos cuyo diseño individual puede realizarse en una primera fase de manera aislada. Para que la respuesta global del OMT cumpla unas especificaciones fijadas de antemano, las especificaciones de estos elementos deben ser mas exigentes. Dentro de esta línea, el elemento fundamental de la estructura es la unión Turnstile. El diseño de su elemento interno es un factor clave para mejorar sus prestaciones. Todas estas características se han plasmado en el diseño de un OMT con pérdidas de retorno mejores de 24 dB en la banda de 13 a 18 GHz cuyos simulaciones parciales y del dispositivo total se han presentado en este trabajo.

Referencias

[1] J. Uher, J. Bornemann, and U. Rosenberg, “Waveguide components for antenna feed systems: Theory and CAD,” Chapter 3, Boston, Artech House, 1993.

[2] G. Pelosi, R. Nesti and G.G. Gentili, “Orthomode transducers”, Encyclopedia of RF and microwave engineering, Wiley, New York, 2005.

[3] G. Pisano, L. Pietranera, K. Isaak, L. Piccirillo, B. Johnson, B. Maffei, S. Melhuish, “A Broadband WR10 Turnstile Junction Orthomode Transducer,” *IEEE Microw. and Wireless Comp. Lett.*, vol. 17, no. 4, pp. 286-288, Apr 2007

[4] A. Navarrini and R.L. Plambeck, “A turnstile junction waveguide orthomode transducer,” *IEEE Trans. Microw. Theory Techn.*, vol. 54, no. 1, pp. 272-277, Jan 2006

[5] E.J. Wollack, W. Grammer and J. Kingsley, “The Bøifot orthomode junction”, Atacama Large Millimeter Array (ALMA) Report #425, 05/22/02. Available at www.alma.nrao.edu/memos/html-memos/alma425/memo425.pdf

[6] R. Banham, G. Valsecchi, L. Lucci, G. Pelosi, S. Selleri, V. Natale, R. Nesti, and G. Tofani, “Electroformed front-end at 100 GHz for radio-astronomical applications,” Microw. J., vol. 48, pp. 112–122, Aug. 2005.

[7] A. M. Bøifot, “Classification of ortho-mode transducers,” Europ. Trans. Telecommunications and Related Technologies, vol. 2, no. 5, pp. 503–510, Sept. 1991.

[8] A. Bøifot, E. Lier, and T. Schaug-Pettersen, “Simple and broadband orthomode transducer,” *IEE Proc. Microwaves, Ant. and Prop.*, vol. 137, no. 6, pp. 396-400, Dec. 1990.

[9] J. A. Ruiz-Cruz, J. R. Montejo-Garai, J. M. Rebollar, C. E. Montesano, M. J. Martín, M. Naranjo-Masi, “Computer Aided Design of Wideband Orthomode Transducers based on the Bøifot Junction,” *Proc. 2006 IEEE IMS-MTT-s Dig. (in CD), San Francisco, June 2006.*

[10] C. G. Montgomery, R. H. Dicke and E. M. Purcell, “Principles of Microwaves Circuits,” Chapter 12, MIT Radiation Laboratory Series, McGraw-Hill, 1948.

PRESUPUESTO

1) Ejecución Material

- Compra de ordenador personal (Software incluido)..... ..... 2.000 €
- Material de oficina ..... 150 €
- Total de ejecución material ..... 2.150 €

2) Gastos generales

- 16 % sobre Ejecución Material ..... 344 €

3) Beneficio Industrial

- 6 % sobre Ejecución Material ..... 129 €

4) Honorarios Proyecto

- 640 horas a 15 € / hora ..... 9600 €

5) Material fungible

- Gastos de impresión ..... 60 €
- Encuadernación ..... 200 €

6) Subtotal del presupuesto

- Subtotal Presupuesto ..... 12010 €

7) I.V.A. aplicable

- 16% Subtotal Presupuesto ..... 1921.6 €

8) Total presupuesto

- Total Presupuesto ..... 13931,6 €

Madrid, Noviembre de 2008

El Ingeniero Jefe de Proyecto

Fdo.: Ignacio Izquierdo Martínez
Ingeniero Superior de Telecomunicación

PLIEGO DE CONDICIONES

Este documento contiene las condiciones legales que guiarán la realización, en este proyecto, del diseño de un Ortomodo de banda ancha basado en la unión Turnstile. En lo que sigue, se supondrá que el proyecto ha sido encargado por una empresa cliente a una empresa consultora con la finalidad de realizar dicho sistema. Dicha empresa ha debido desarrollar una línea de investigación con objeto de elaborar el proyecto. Esta línea de investigación, junto con el posterior desarrollo de los programas está amparada por las condiciones particulares del siguiente pliego.

Supuesto que la utilización industrial de los métodos recogidos en el presente proyecto ha sido decidida por parte de la empresa cliente o de otras, la obra a realizar se regulará por las siguientes:

Condiciones generales

1. La modalidad de contratación será el concurso. La adjudicación se hará, por tanto, a la proposición más favorable sin atender exclusivamente al valor económico, dependiendo de las mayores garantías ofrecidas. La empresa que somete el proyecto a concurso se reserva el derecho a declararlo desierto.

2. El montaje y mecanización completa de los equipos que intervengan será realizado totalmente por la empresa licitadora.

3. En la oferta, se hará constar el precio total por el que se compromete a realizar la obra y el tanto por ciento de baja que supone este precio en relación con un importe límite si este se hubiera fijado.

4. La obra se realizará bajo la dirección técnica de un Ingeniero Superior de Telecomunicación, auxiliado por el número de Ingenieros Técnicos y Programadores que se estime preciso para el desarrollo de la misma.

5. Aparte del Ingeniero Director, el contratista tendrá derecho a contratar al resto del personal, pudiendo ceder esta prerrogativa a favor del Ingeniero Director, quien no estará obligado a aceptarla.

6. El contratista tiene derecho a sacar copias a su costa de los planos, pliego de condiciones y presupuestos. El Ingeniero autor del proyecto autorizará con su firma las copias solicitadas por el contratista después de confrontarlas.

7. Se abonará al contratista la obra que realmente ejecute con sujeción al proyecto que sirvió de base para la contratación, a las modificaciones autorizadas por la superioridad o a las órdenes que con arreglo a sus facultades le hayan comunicado por escrito al Ingeniero Director de obras siempre que dicha obra se haya ajustado a los preceptos de los pliegos de condiciones, con arreglo a los cuales, se harán las modificaciones y la valoración de las diversas unidades sin que el importe total pueda exceder de los presupuestos aprobados. Por consiguiente, el número de unidades que se consignan en el proyecto o en el presupuesto, no podrá servirle de fundamento para entablar reclamaciones de ninguna clase, salvo en los casos de rescisión.

8. Tanto en las certificaciones de obras como en la liquidación final, se abonarán los trabajos realizados por el contratista a los precios de ejecución material que figuran en el presupuesto para cada unidad de la obra.

9. Si excepcionalmente se hubiera ejecutado algún trabajo que no se ajustase a las condiciones de la contrata pero que sin embargo es admisible a juicio del Ingeniero Director de obras, se dará conocimiento a la Dirección, proponiendo a la vez la rebaja de precios que el Ingeniero estime justa y si la Dirección resolviera aceptar la obra, quedará el contratista obligado a conformarse con la rebaja acordada.

10. Cuando se juzgue necesario emplear materiales o ejecutar obras que no figuren en el presupuesto de la contrata, se evaluará su importe a los precios asignados a otras obras o materiales análogos si los hubiere y cuando no, se discutirán entre el Ingeniero Director y el contratista, sometiéndolos a la aprobación de la Dirección. Los nuevos precios convenidos por uno u otro procedimiento, se sujetarán siempre al establecido en el punto anterior.

11. Cuando el contratista, con autorización del Ingeniero Director de obras, emplee materiales de calidad más elevada o de mayores dimensiones de lo estipulado en el proyecto, o sustituya una clase de fabricación por otra que tenga asignado mayor precio o ejecute con mayores dimensiones cualquier otra parte de las obras, o en general, introduzca en ellas cualquier modificación que sea beneficiosa a juicio del Ingeniero Director de obras, no tendrá derecho sin embargo, sino a lo que le correspondería si hubiera realizado la obra con estricta sujeción a lo proyectado y contratado.

12. Las cantidades calculadas para obras accesorias, aunque figuren por partida alzada en el presupuesto final (general), no serán abonadas sino a los precios de la contrata, según las condiciones de la misma y los proyectos particulares que para ellas se formen, o en su defecto, por lo que resulte de su medición final.

13. El contratista queda obligado a abonar al Ingeniero autor del proyecto y director de obras así como a los Ingenieros Técnicos, el importe de sus respectivos honorarios facultativos por formación del proyecto, dirección técnica y administración en su caso, con arreglo a las tarifas y honorarios vigentes.

14. Concluida la ejecución de la obra, será reconocida por el Ingeniero Director que a tal efecto designe la empresa.

15. La garantía definitiva será del 4% del presupuesto y la provisional del 2%.

16. La forma de pago será por certificaciones mensuales de la obra ejecutada, de acuerdo con los precios del presupuesto, deducida la baja si la hubiera.

17. La fecha de comienzo de las obras será a partir de los 15 días naturales del replanteo oficial de las mismas y la definitiva, al año de haber ejecutado la provisional, procediéndose si no existe reclamación alguna, a la reclamación de la fianza.

18. Si el contratista al efectuar el replanteo, observase algún error en el proyecto, deberá comunicarlo en el plazo de quince días al Ingeniero Director de obras, pues transcurrido ese plazo será responsable de la exactitud del proyecto.

19. El contratista está obligado a designar una persona responsable que se entenderá con el Ingeniero Director de obras, o con el delegado que éste designe, para todo relacionado con ella. Al ser el Ingeniero Director de obras el que interpreta el proyecto, el contratista deberá consultarle cualquier duda que surja en su realización.

20. Durante la realización de la obra, se girarán visitas de inspección por personal facultativo de la empresa cliente, para hacer las comprobaciones que se crean oportunas. Es obligación del contratista, la conservación de la obra ya ejecutada hasta la recepción de la misma,

por lo que el deterioro parcial o total de ella, aunque sea por agentes atmosféricos u otras causas, deberá ser reparado o reconstruido por su cuenta.

21. El contratista, deberá realizar la obra en el plazo mencionado a partir de la fecha del contrato, incurriendo en multa, por retraso de la ejecución siempre que éste no sea debido a causas de fuerza mayor. A la terminación de la obra, se hará una recepción provisional previo reconocimiento y examen por la dirección técnica, el depositario de efectos, el interventor y el jefe de servicio o un representante, estampando su conformidad el contratista.

22. Hecha la recepción provisional, se certificará al contratista el resto de la obra, reservándose la administración el importe de los gastos de conservación de la misma hasta su recepción definitiva y la fianza durante el tiempo señalado como plazo de garantía. La recepción definitiva se hará en las mismas condiciones que la provisional, extendiéndose el acta correspondiente. El Director Técnico propondrá a la Junta Económica la devolución de la fianza al contratista de acuerdo con las condiciones económicas legales establecidas.

23. Las tarifas para la determinación de honorarios, reguladas por orden de la Presidencia del Gobierno el 19 de Octubre de 1961, se aplicarán sobre el denominado en la actualidad “Presupuesto de Ejecución de Contrata” y anteriormente llamado ”Presupuesto de Ejecución Material” que hoy designa otro concepto.

Condiciones particulares

La empresa consultora, que ha desarrollado el presente proyecto, lo entregará a la empresa cliente bajo las condiciones generales ya formuladas, debiendo añadirse las siguientes condiciones particulares:

1. La propiedad intelectual de los procesos descritos y analizados en el presente trabajo, pertenece por entero a la empresa consultora representada por el Ingeniero Director del Proyecto.

2. La empresa consultora se reserva el derecho a la utilización total o parcial de los resultados de la investigación realizada para desarrollar el siguiente proyecto, bien para su publicación o bien para su uso en trabajos o proyectos posteriores, para la misma empresa cliente o para otra.

3. Cualquier tipo de reproducción aparte de las reseñadas en las condiciones generales, bien sea para uso particular de la empresa cliente, o para cualquier otra aplicación, contará con autorización expresa y por escrito del Ingeniero Director del Proyecto, que actuará en representación de la empresa consultora.

4. En la autorización se ha de hacer constar la aplicación a que se destinan sus reproducciones así como su cantidad.

5. En todas las reproducciones se indicará su procedencia, explicitando el nombre del proyecto, nombre del Ingeniero Director y de la empresa consultora.

6. Si el proyecto pasa la etapa de desarrollo, cualquier modificación que se realice sobre él, deberá ser notificada al Ingeniero Director del Proyecto y a criterio de éste, la empresa consultora decidirá aceptar o no la modificación propuesta.

7. Si la modificación se acepta, la empresa consultora se hará responsable al mismo nivel que el proyecto inicial del que resulta el añadirla.

8. Si la modificación no es aceptada, por el contrario, la empresa consultora declinará toda responsabilidad que se derive de la aplicación o influencia de la misma.

9. Si la empresa cliente decide desarrollar industrialmente uno o varios productos en los que resulte parcial o totalmente aplicable el estudio de este proyecto, deberá comunicarlo a la empresa consultora.

10. La empresa consultora no se responsabiliza de los efectos laterales que se puedan producir en el momento en que se utilice la herramienta objeto del presente proyecto para la realización de otras aplicaciones.

11. La empresa consultora tendrá prioridad respecto a otras en la elaboración de los proyectos auxiliares que fuese necesario desarrollar para dicha aplicación industrial, siempre que no haga explícita renuncia a este hecho. En este caso, deberá autorizar expresamente los proyectos presentados por otros.

12. El Ingeniero Director del presente proyecto, será el responsable de la dirección de la aplicación industrial siempre que la empresa consultora lo estime oportuno. En caso contrario, la persona designada deberá contar con la autorización del mismo, quien delegará en él las responsabilidades que ostente.